ISSN: 0128-7680

Pertanika Journal of

SCIENCE & TECHNOLOGY

VOLUME 11 NO.2
JULY 2003

A scientific journal published by Universiti Putra Malaysia Press

Pertanika Journal of Science & Technology

About the Journal

Pertanika, the pioneer journal of UPM, began publication in 1978. Since then, it has established itself as one of the leading multidisciplinary journals in the tropics. In 1992, a decision was made to streamline Pertanika into three journals to meet the need for specialised journals in areas of study aligned with the strengths of the university. These are **(i) Pertanika Journal of Tropical Agricultural Science (ii) Pertanika Journal of Science & Technology (iii) Pertanika Journal of Social Science & Humanities.**

Aims and Scope

Pertanika Journal of Science & Technology welcomes full papers and short communications in English or Bahasa Melayu in the fields of chemistry, physics, mathematics, and statistics, engineering, environmental control and management, ecology and computer science. It is published twice a year in January and July.

Articles must be reports of research not previously or simultaneously published in other scientific or technical journals.

Communications are notes of a significant finding intended spaced typewritten pages and must be accompanied by a letter from the author justifiying its publication as a communication.

Reviews are critical appraisals of literature in areas that are of interest to a board specturm of scientist and researchers. Review papers will be published upon invitation.

Submission of Manuscript

Three complete clear copies of the manuscript are to be submitted to

The Chief Editor
Pertanika Journal of Science & Technology
Universiti Putra Malaysia
43400 UPM, Serdang, Selangor Darul Ehsan
MALAYSIA
Tel: 03-89468854; Fax: 03-89416172

Proofs and Offprints

Page proofs, illustration proofs and the copy-edited manuscript will be sent to the author. Proofs must be checked very carefully within the specified time as they will not be proofread by the Press editors.

Authors will receive 20 offprints of each article and a copy of the journal. Additional copies can be ordered from the Secretary of the Editorial Board.

Published by Universiti Putra Malaysia Press
ISSN No. 0128-7680

Pertanika Journal of Science & Technology

Volume 11 No. 2, 2003

Contents

Pertanika J. Sci. & Technol. 11(2): 145 - 155 (2003)
ISSN: 0128-7680

Modelling of Saltwater Intrusion into a Discharging Well in a Non-Homogeneous Unconfined Aquifer

Abdul Halim Ghazali[1], Jong Tze Yong[2], Suleyman Aremu Muyibi[3], Salim Said[3] & Aziz F. Eloubaidy[3]

[1]Department of Civil Engineering
[2 & 3]Department of Civil Engineering,
Faculty of Engineering, Universiti Putra Malaysia,
43400 UPM, Serdang, Selangor, Malaysia

Received: 30 October 2000

ABSTRAK

Kaedah unsur terhingga berdasarkan teknik Galerkin digunakan untuk membentuk penyelesaian bagi pergerakan air masin di dalam satu akuifer ke arah telaga pengepaman. Jenis akuifer adalah tak terkurung, bukan homogen dan isotropik. Persamaan bagi aliran air bumi dan olakan-serakan telah ditukar bentuk kepada dua persamaan kebezaan separa bukan linear untuk menghasilkan nilai-nilai turus piezometrik dan kepekatan air masin pada titik-titik dan masa yang berlainan. Persamaan-persamaan itu telah diselesaikan dengan model Argus-ONE™ SUTRA. Prestasi model berangka telah dibandingkan dengan data yang diperoleh daripada satu model uji kaji di makmal. Perbandingan yang baik telah diperoleh di antara dua model tersebut, dengan perbezaan yang ditunjukkan bagi kepekatan dan turus piezometrik adalah masing-masing 10% dan 11%.

ABSTRACT

Finite element method based on the Galerkin technique was used to formulate the solution for simulating a two-dimensional transient movement of saltwater in a stratified aquifer under pumping conditions. The aquifer system was unconfined, non-homogeneous and isotropic. The groundwater flow and convection-dispersion equations were transformed into two non-linear coupled partial differential equations to yield the values of the corresponding piezometric head and saltwater concentration at various points and times. These two equations were solved by Argus- ONE™ SUTRA model that employs the finite element method. The performance of the numerical model is compared with the data observed from a laboratory experimental model. Good agreement has been achieved between the numerical and experimental models for the concentration and hydraulic head as comparison showed the maximum differences of only 10% and 11% respectively.

Keywords: Non-homogenous aquifer, saltwater intrusion, mathematical modelling, experimental model, validation

INTRODUCTION

Water resource engineers have always been interested in optimising the use of groundwater reservoirs, not only through making the maximum use of the quantity of water available but also by managing the quality of water in the

system. Efforts that were done or currently underway include predicting and controlling the movement of a salt water - fresh water interface and mass transport in the flowing groundwater, and predicting quality changes in an aquifer due to changing irrigation patterns and irrigation efficiency. Human activities, such as groundwater abstraction, land reclamation and land drainage have resulted in a drawdown of the groundwater table and piezometric level, and in stratified groundwater reservoirs, a displacement of the saltwater into freshwater zone, which directly influences the quality of water pumped from the well. This leads to the necessity of developing techniques for groundwater utilisation from such reservoirs to meet the desired water quality constraints.

Basic studies have been conducted to explain the pattern of movement and mixing between freshwater and saltwater, and the factors that influence these processes. Many researchers have worked in this field and several of them presented numerical solutions for the flow and convective-dispersion problems. Huyakorn (1987) developed a three-dimensional finite element model for the simulation of saltwater intrusion in single and multiple coastal aquifer systems with either a confined or phreatic top aquifer. Before that, Pickens and Lennox (1976) used the finite element method based on Galerkin technique to formulate the simulation of the two-dimensional transient movement of conservative or non-conservative wastes in a steady state saturated groundwater flow system. Batu (1984) developed a finite element dual mesh to calculate the horizontal and vertical Darcy velocity components in a highly non-homogeneous and anisotropic aquifer of constant porosity under steady flow conditions. The Galerkin method of approximation in conjunction with the finite element was also used by Pinder (1973) as a method of analysis to simulate the movement of groundwater contaminants. For the development of analytical solutions, Gupta and Yapa (1982) used an approach considering both analytical and numerical models for assessing the saltwater encroachment phenomenon in an aquifer in Thailand. Guvanasen and Volker (1982) presented two analytical solutions for a problem of solute transport in transient flow in an unconfined aquifer. Kipp (1973) developed a realistic theoretical solution to the problem of unsteady flow to a single, partially penetrating well of finite radius in an unconfined aquifer.

Rahem (1991) had conducted a very detailed study on selective withdrawal from the density-stratified unconfined groundwater reservoirs. He had employed a finite difference method in solving the governing flow and solute transport equations, as well as preparing sandbox model to simulate the physical problem in order to achieve the verification purposes. However, he used homogeneous porous media in contrast to this study, in which a non-homogeneous and isotropic soil had been used in the experimental set-up.

More recently, Gordon *et al.* (2000) developed an optimisation model for a confined aquifer in which the groundwater flow and Darcy's law are solved by finite element method, while the salinity transport equation is solved by the streamline-upwind Petrov-Galerkin (SUPG) method. Feehley *et al.* (2000) demonstrated that a dual-domain mass transfer approach is more practical for

modelling of solute transport in highly heterogeneous aquifers compared to the classical Fickian advection-dispersion model.

NUMERICAL MODELLING

A general form of the equation describing the two-dimensional flow of an incompressible fluid in a non-homogeneous, isotropic aquifer may be derived by combining Darcy's Law with the continuity equation (Rahem 1991). The general groundwater flow equation may be written as:

$$\frac{\partial}{\partial r}\left(\rho\frac{\partial}{\partial r}\right)+\frac{\partial}{\partial z}\left(\rho\frac{\partial h}{\partial z}\right)=\frac{S\rho}{K}\frac{\partial h}{\partial t} \tag{1}$$

where S is the specific storage coefficient; K represents the hydraulic conductivity; h stands for the piezometric head in the aquifer; r and z are the radial and vertical axis respectively; and ρ denotes the water density. Meanwhile, the generalised form of the solute transport equation is:

$$\rho\frac{\partial c}{\partial t}+\frac{\partial}{\partial r}\left(v_r\rho c\right)+\frac{\partial}{\partial z}\left(v_z\rho c\right)=\frac{\partial}{\partial r}\left(D_{rr}\rho\frac{\partial c}{\partial r}\right)+\frac{\partial}{\partial z}\left(D_{zz}\rho\frac{\partial c}{\partial z}\right) \tag{2}$$

where c is the concentration of solute in the aquifer; v_r and v_z represent the seepage velocities in the aquifer in r and z direction; ρ is the water density; and D_{rr} and D_{zz} are coefficients of dispersion in r and z direction respectively. The components of the dispersive coefficient for two-dimensionals are expressed by Bear and Verruijt (1990) as

$$D_{rr} = a_T V : D_{zz} a_L V \tag{3}$$

where a_T is the transverse dispersivity; and a_L is the longitudinal dispersivity; and V is the average velocity of the pore fluid.

The Galerkin technique was used to determine an approximate solution to Equations (1) and (2) under appropriate boundary conditions. A saline intrusion model, SUTRA that employed the finite element method to solve the governing equations was utilised. The SUTRA (which is named from the acronym Saturated Unsaturated Transport) was published by the United States Geological Survey (Voss 1984). The model is two-dimensional and can be applied either aerially or in cross section to establish a salinity profile. The coordinate system may be either Cartesian or radial, which makes it possible to simulate phenomena such as saline up-coning beneath a pumped well. In this study, the software package used is the combination of the USGS-developed code that interfaces SUTRA with Argus ONE™, a commercial software product developed by Argus Interware. The Argus ONE™ (Argus Open Numerical Environment), is a programmable system with geographic-information-system-like (GIS-like) functionality that

includes automated gridding and meshing capabilities for linking geo-spatial information with finite element numerical model discretizations. The Graphical-User Interface (GUI) for SUTRA is based on a public-domain Plug-In Extension (PIE) that automates the use of Argus ONE™ to automatically create the appropriate geo-spatial information coverage (information layers) for SUTRA, provide menus and dialogues for inputting geo-spatial information and simulation control parameters for SUTRA, and allow visualisation of SUTRA simulation results.

MATERIALS AND METHODS

Saltwater Source

A solution of sodium chloride (NaCl) was selected to represent the saltwater for modelling the concentration distribution in the aquifer. Saltwater has been found to be easily monitored, safe and easily available. In this investigation, saltwater with a concentration of 0.04 by weight was used in order to produce an approximate density of 1028 kg/m^3, which is equivalent to the concentration of seawater.

Porous Media

For an isotropic and non-homogeneous porous media, it must have a coefficient of uniformity of more than 4. In this study coarse sand was mixed with gravel, which gave a uniformity coefficient of 6 and grain size d_{50} of 1 mm using sieve analysis.

Piezometric Taps

Four piezometric taps were fixed on the floor of the model in a radial line. *Fig. 1(a)* shows the arrangement of the taps. Each tap was connected to a manometer board through a flexible tubing. The water elevation in each tube on the manometer board represents the hydraulic head at that particular tap location.

Conductivity Probes

The concentration of the saltwater tracer was measured using specially constructed probes. The probes had been calibrated by determining the resistance in ohms of different concentrations of saltwater. The probes were installed at locations shown in *Fig. 1(b)*. The probes were identified as Probes 1, 2 and 3, with Probe 1 located nearest to the interface and Probe 3, furthest.

Determination of Parameters

The parameters required in the numerical model viz. longitudinal and lateral apparent dispersivity coefficients, storage coefficient, hydraulic conductivity, porosity and compressibility of soil and water were determined using empirical

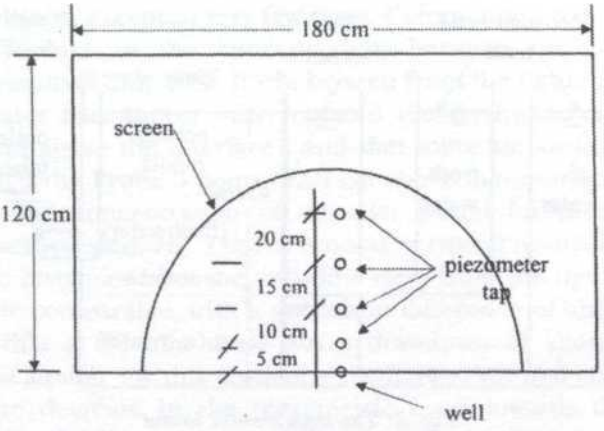

Fig. 1(a): Locations of the piezometer taps (in plan)

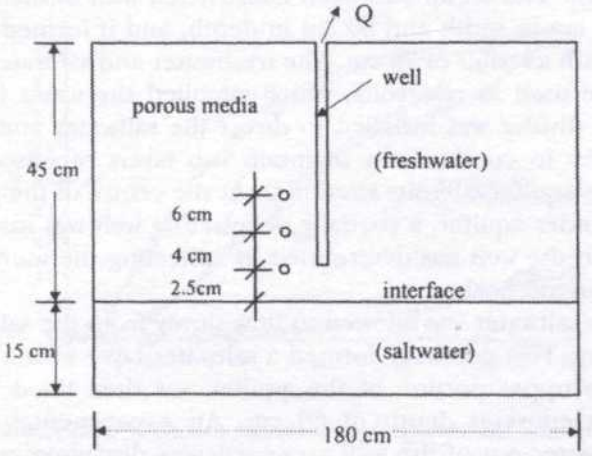

Fig. 1(b): Locations of the conductivity probes (elevation)

formulae and laboratory analysis as well as results from previous studies. The values of the various parameters were as follows: the hydraulic conductivity of the porous medium was determined using Breyer's formula (Kresic 1997) and its value was 0.071 cm/s, the porosity of the porous medium was 0.21, the compressibility of water 4.69×10^{-8} cm^2/g (Kashef 1987), the compressibility of coarse-fine sand 0.35×10^{-6} cm^2/g (Kashef 1987), the specific storage coefficient 3.52×10^{-4}/s^2, and the longitudinal and transverse dispersivity 0.16 cm and 0.0016 cm respectively (Rahem 1991).

Experimental Procedure

The schematic diagram in *Fig. 2* shows the experimental set-up used in conducting tests on the distributions of hydraulic head and concentration of a conservative tracer (saltwater) in two-dimensional flow towards a partially

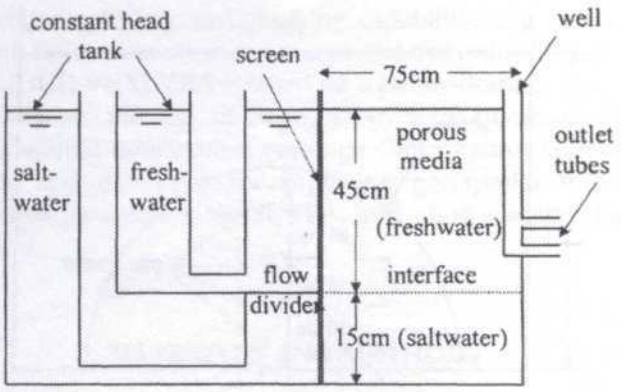

Fig. 2: The experimental layout

penetrating well. The set-up had been constructed with dimensions of 180 cm in length, 120 cm in width and 60 cm in depth, and it formed an aquifer of a half-cylinder with a radius of 75 cm. The freshwater and saltwater constant head chambers were used as reservoirs, which supplied the water into the porous media. A flow divider was installed to direct the saltwater and the freshwater into the aquifer to continuously maintain two layers of water with different densities in the aquifer (density stratified). At the centre of the plane boundary of the half-cylinder aquifer, a partially penetrating well was installed. The rate of flow through the well was determined by collecting the water from the well by using volumetric beaker.

Initially the saltwater was allowed to flow slowly from the saltwater chamber into the aquifer. This gradually formed a saltwater layer with a constant depth of 15 cm. The upper portion of the aquifer was then filled with freshwater gradually to a constant depth of 60 cm. An experimental run started by pumping the water out of the well at a particular discharge rate. This caused a flow through the aquifer towards the well to occur. The pressure head and saltwater concentration variations were noted at different times from the devices installed. The test was repeated for a different discharge rate. Another set of tests was conducted for the same discharge rates but at a different well penetration.

RESULTS AND DISCUSSION

Theoretical model validation was conducted by comparison between the numerical solutions and the experimental test results for two different sets of well penetration (40.0 cm and 35.0 cm) and pumping rates (6.0 cm^3/s and 4.8 cm^3/s). All tests were carried out over a duration of 120 min. Comparison between the concentration ratios (the ratio of the existing concentration to the initial saltwater concentration) of numerical and experimental solution for concentration and piezometric head distributions were shown in *Figs. 3* and *4* respectively. *Fig. 3* shows that the numerical results are almost the same as the

experimental results, except in very few cases. Computation has shown that the maximum difference in the concentration between the numerical and experimental results is only 10%. It can be seen from the figure also that at 120 min the saltwater had almost fully replaced the freshwater at the Probe 1 location (2.5 cm above the interface), and that some amount of the saltwater had also reached the Probe 3 point (12.5 cm above the interface). It could be expected that the concentration of saltwater would increase at the latter location as time increased. *Fig. 4* shows two sets of typical results for piezometric head at various distances from the well. It is clear from the figure that the two results are quite comparable, with a maximum difference of about 11%. It can also be seen that at 60 min there was a drawdown of about 0.5 to 2 cm throughout the aquifer for this particular discharge rate (6.0 cm^3/s). This also means that the decrease in the piezometric head towards the well is not significant at this discharge rate.

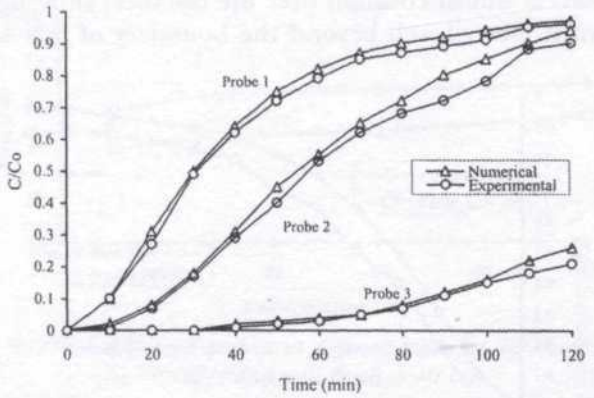

Fig. 3: Comparison between numerical and experimental solutions for concentration ratios at probe locations 1, 2 and 3 for well depth = 40.0 cm and discharge rate = 6.0 cm^3/s

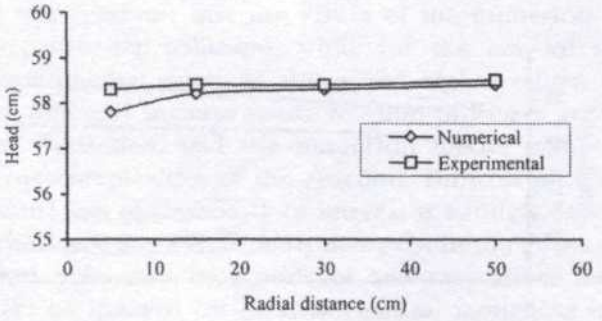

Fig. 4: Comparison between numerical and experimental solutions for piezometric heads at various distances from the well at time = 60 min for well depth = 40.0 cm and discharge rate = 6.0 cm^3/s

The following discussion will use only the numerical results, since it was shown that these results were comparable with the experimental results. For the shallower well, it was found that the saltwater concentrations at a particular location (Probe 1) and at various times were lower when compared to the deeper well (*Fig. 5*). The differences in concentrations resulting from the two well depths are also shown to be quite constant. In the case of the piezometric head profiles, abstraction using the shallower well resulted in higher heads at the corresponding locations, or in other words, smaller drawdown, compared to the deeper well (*Fig. 6*).

The effect of the different discharge rates is shown in *Fig. 7*. As expected, the lower discharge induced less saltwater into the well. Nevertheless, for this particular aquifer system, salt water intrusion has occurred with these discharge rates.

The lowering of the water table due to the constant discharge rate over a certain lapse of time is shown in *Fig. 8*. The amount of reduction in the piezometric heads is almost constant over the distance, showing that the point of no drawdown is located well beyond the boundary of this aquifer system.

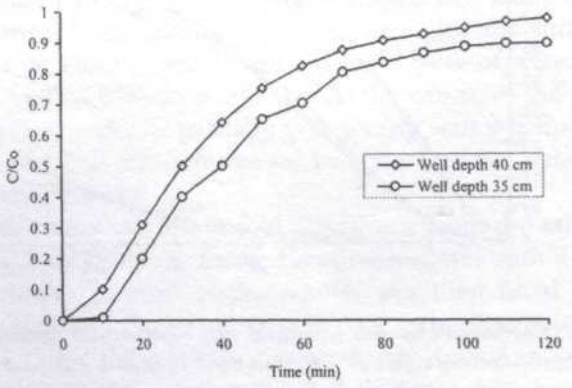

Fig. 5: Variation of concentration ratios at Probe 1 for different well depths (discharge rate = 6.0 cm³/s)

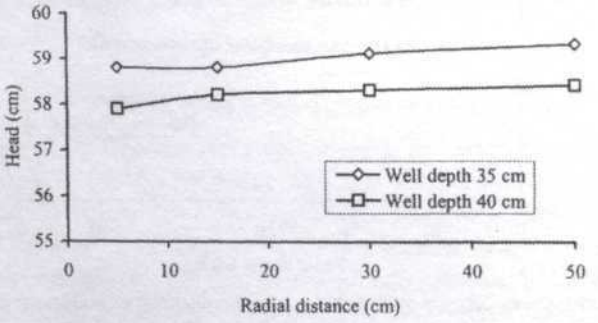

Fig. 6: Piezometric head profiles for different well depths at time = 60 min and discharge rate = 6.0 cm³/s

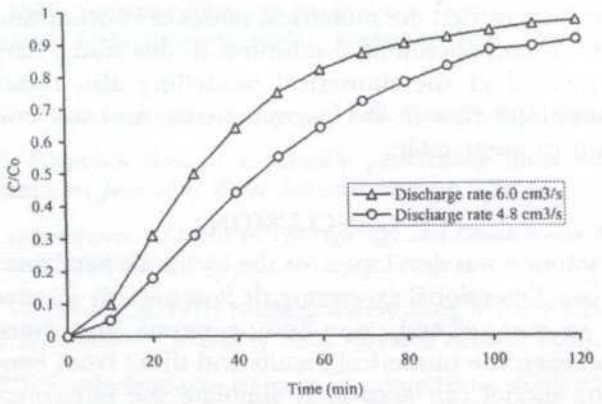

Fig. 7: Variation of concentration ratios at Probe 1 for different discharge rates (well depth = 40 cm)

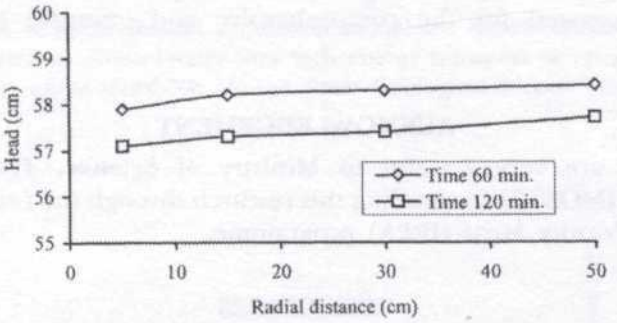

Fig. 8: Piezometric head profiles at different times for discharge rate = 60 cm^3/s and well depth = 40 cm

Although comparison of both solutions had shown the consistency that is needed for the purpose of modelling, it is observed that all these discrepancies need to be investigated further. In this study, for the case of concentration ratio distributions, it was apparent that the values of the numerical solution were greater than experimental solutions, while for the case of pressure head distributions, experimental solutions always had higher values. In reality, the situation may be different because solute reaction processes are neither linear nor equilibrium controlled, and the numerical model may not necessarily represent the true complexities of the reaction. Difficult problems also arise when the concentration of the solute of interest is strongly dependent on the presence of numerous other constituents that exist in the porous media. Here, mineralogical variability may be significant and may affect the rate and of reactions, and yet be ignored in the mathematical modelling instead. At the same time, in many groundwater flow systems, sorption may also cause the retardation of the movement of the contaminants. Sorption refers to the uptake of the dissolved constituents from solution by the porous medium. These

phenomena may have caused the numerical values of concentration distribution becoming greater than experimental solutions in this study. Larger movement of solute experienced in the numerical modelling also meant that higher velocity of groundwater flow in the porous media, and this could generate a bigger drawdown in water table.

CONCLUSION

The numerical solution was developed for the hydraulic head and concentration distributions in two-dimensional axi-symmetric flow towards a partially penetrating well through an unconfined, non-homogeneous and isotropic aquifer. Comparisons between the numerical results and those from experimental tests indicate that the model can accurately simulate the movement of pollutant (saltwater) in the saturated zone of a non-homogeneous unconfined aquifer. Deterministic groundwater simulation model can be a valuable tool for analysing aquifer systems and for predicting responses to specific stresses, and its usage is hereby suggested for the comprehensive and intensive hydro-geologic investigations.

ACKNOWLEDGEMENT

The authors are very grateful to Ministry of Science, Technology and Environment (MOSTE) for funding this research through the Intensification of Research in Priority Areas (IRPA) programme.

REFERENCES

BATU, V. 1984. A finite element dual mesh method to calculate nodal darcy velocities in non-homogeneous and anisotropic aquifers. *Journal of Water Resources Research* **20**: 1705.

BEAR, J. 1979. *Hydraulics of Groundwater.* p. 567. New York: McGraw-Hill.

BEAR, J. and A. VERRUIJT. 1990. *Modeling Groundwater Flow and Pollution.* p. 326-327. D. Reidel Publishing Company.

FEEHLEY, C. E., C. ZHENG and F. J. MOLZ. 2000. A dual-domain mass transfer approach for modelling solute transport in heterogeneous aquifers: Application to the Macrodispersion Experiment (MADE) site. *Water Resources Research* **36(11)**: 2501-2515.

GORDON, E., U. SHAMIR and J. BENSABAT. 2000. Optimal management of a regional aquifer under salinization conditions. *Water Resources Research* **36(11)**: 3193-3203.

GUPTA, A. D. and P. N. N. YAPA. 1982. Saltwater encroachment in an aquifer: A case study. *Journal of Water Resources Research* **18(3)**: 546.

GUVANASEN, V. and R. E. VOLKER. 1982. Solution for solute transport in an unconfined aquifer. *Journal of Hydrology* **58:** 89.

HUYAKORN, P. S. 1987. Saltwater intrusion in aquifers: Development and testing of a three-dimensional finite element model. *Journal of Water Resources Research* **23(2)**: 293.

KASHEF, A. I. 1987. *Groundwater Engineering.* p. 11-12. New York: McGraw-Hill.

KIPP, K. L. 1973. Unsteady flow to a partially penetrating finite radius well in an unconfined aquifer. *Journal of Water Resources Research* **9(2)**: 448.

KRESIC, N. 1997. *Quantitative Solutions in Hydrogeology and Groundwater Modeling.* p. 369. New York: Lewis Publishers.

PICKENS, J. F. and W. C. LENNOX. 1976. Numerical simulation of waste movement in steady groundwater flow systems. *Journal of Water Resources Research* **12(2)**: 171-180.

PINDER, G. F. 1973. A galerkin-finite element of groundwater contamination on Long Island, New York. *Journal of Water Resources Research* **9(6)**: 1657.

RAHEM, A. M. 1991. Selective withdrawal from density-stratified unconfined groundwater reservoirs. Ph.D Thesis, College of Engineering, University of Baghdad, Iraq.

VOSS, C. I. 1984. A finite-element simulation model for saturated-unsaturated, fluid-density-dependent ground-water flow with energy transport or chemically-reactive single-species solute transport. United States Geological Survey, Virginia, U.S.A.

ISSN: 0128-7680
Pertanika J. Sci. & Technol. 11(2): 157 - 171 (2003)

Single Slice Grouping Mechanism for Recognition of Cursive Handwritten Courtesy Amounts of Malaysian Bank Cheques

Md. Nasir Sulaiman & Marzuki Khalid*
Faculty of Computer Science and Information Technology, Universiti Putra Malaysia, 43400 UPM Serdang, Selangor, Malaysia
**Centre for Artificial Intelligence and Robotics (CAIRO), Universiti Teknologi Malaysia, Jalan Semarak, 54100 Kuala Lumpur, Malaysia*
E-mail: nasir@fsktm.upm.edu.my

Received: 24 April 2001

ABSTRAK

Mekanisme mengumpul hiris tunggal untuk pengecaman melibatkan proses memotong secara menegak ke atas imej hiris demi hiris, mengumpul setiap hirisan mengikut lebar tertentu dan kemudiannya diuji untuk dicamkan menggunakan Rangkaian Neural yang sudah terlatih. Imej mengandungi jumlah berangka tulisan tangan dan bersambung yang diperoleh daripada cek-cek bank di Malaysia. Seni bina Rangkaian Neural tiga paras dengan fungsi ralat baru untuk algoritma pembelajaran *Backprogation* digunakan. Pendekatan ini menghasilkan keputusan yang baik untuk mengecam jumlah yang mengandungi dua atau lebih angka-angka yang bercantum secara sambung atau secara sentuh.

ABSTRACT

Mechanism to group single slice for recognition involves the process of cutting vertically across an image slice by slice, group every slice at a certain width and tested for recognition using a trained Neural Network. The image contains cursive handwritten courtesy Amounts of Malaysian bank cheques. A three layer Neural Network architecture with the new error function of Backpropagation learning algorithm is used. This approach yields good recognition results with faster convergence rates.

Keywords: Cursive handwritten courtesy amount, Malaysian bank cheques, recognition, neural networks, backpropagation learning algorithm, error function

INTRODUCTION

Automated bank cheque processing is an active research area involving offline cursive hand written recognition (Knerr *et al.* 1998; Dimauro *et al.* 1997). Due to the different types of cheques and languages, it is rather difficult to use any commercial recognition software to solve bank cheques of a particular country. In Malaysia, bank cheque processing is done manually. To automate such a process in Malaysia requires a huge amount of resources as well as extremely good research. This is due to the fact that Malaysian bank cheques are usually written in two different languages, English and Malay.

At the Center for Artificial Intelligence and Robotics (CAIRO, UTM), research in automated processing of Malaysian bank cheques is currently being carried out. Three different strategies are employed:

1. to automatically find the location of the date, the courtesy amount and the legal amount of a bank cheque,
2. to segment and recognise the legal amount, and
3. to segment and recognise the courtesy amount and date.

In this paper, we discuss the technique of recognising the courtesy amount of Malaysian bank cheques by single slice grouping and recognising it. The pre-processing technique is presented first before the recognition phase. It can be divided into 4 processes: scanning, filtering or removing noise, thresholding and thinning. The effectiveness of this technique is tested on several hundred Malaysian bank cheques from a variety of banks.

EXAMPLE OF THE HAND WRITTEN COURTESY AMOUNT

The courtesy amount is a sequence of handwritten or typewritten digits which may include RM (Ringgit Malaysia), comma, decimal or slash to represent the amount of money written on any Malaysian bank cheques. The styles of handwriting can be categorised as follows:

- unconnected digits.
- joint digits.
- touched digits.
- overlapped digits.

Fig. 1 shows some examples of the styles of handwriting of the courtesy amounts obtained from Malaysian bank cheques.

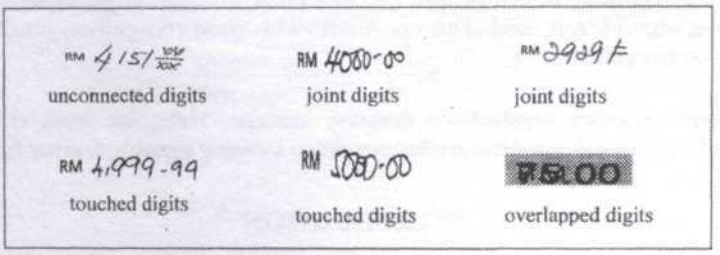

Fig. 1: Examples of the handwritten courtesy amount of Malaysian bank cheques

Due to the large variation of bank cheques in Malaysia which resulted in many levels of difficulty when the images are processed, this research involves only bank cheques that are based on the following assumptions:

- The objects of the image are located and scanned manually.
- The objects of the image are within the box.
- The objects of the image are not mixed with other images such as marking, stamping, etc.

SYSTEM OVERVIEW

The process to recognise off-line cursive handwritten courtesy amount is divided into 2 phases: Pre-processing phase and Recognition phase. The overall process can be illustrated as in *Fig. 2.*

After the recognition phase, the output is expected to contain a list of single characters, i.e., R or M (to represent Ringgit Malaysia), a sequence of single digits which may include comma, or decimal, and slash (to represent end of digit amount). The characters after the slash are omitted as they usually do not indicate any significant value of the courtesy amount.

Pre-processing Phase

The objective of the pre-processing phase is to clean the original image from noise or blur and convert it to binary pixels where the pixel '1' represents the object and the pixel '0' represents the background.

We use Matrox Image language library functions (MIL User Guide 1998) for the following process:

- Filtering/smoothing
  Filtering is used to remove noise such as random noise, which may be caused by the camera, the digitiser or uneven lighting during scanning. The MIL Function *MimConvolve*() with parameters M_SPARPEN2 and M_SMOOTH are used to implement this process.

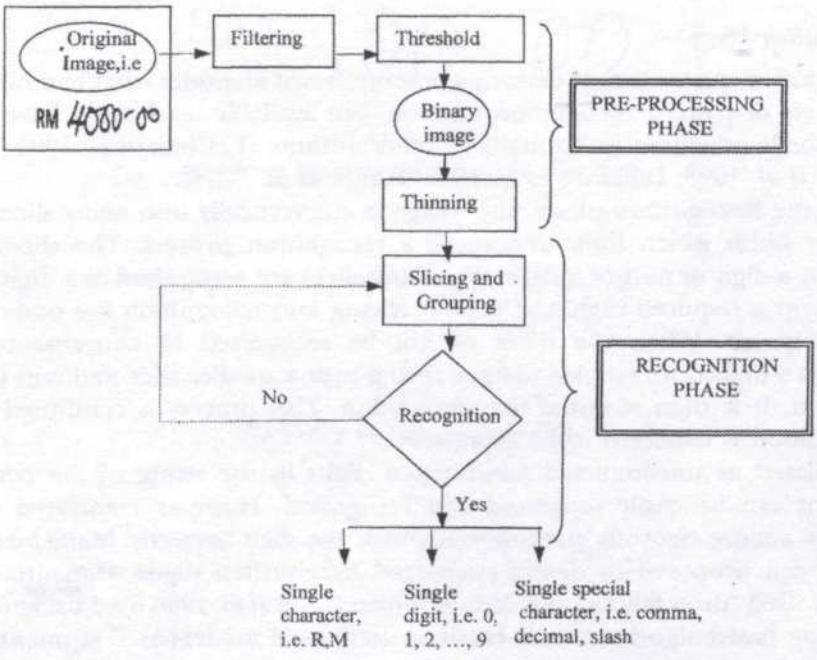

Fig. 2: Process flow to recognise cursive handwritten courtesy amount

- Threshold/binarisation
  To threshold an image means to reduce each pixel to a certain range of values. The MIL Function *MimBinarize*() is used to perform a binarisation operation which reduces a pixel into two scale values (for example, 0 and the maximum value for an 8-bit buffer, 255). A pixel with a 0 value will be seen as black whereas those set to the maximum buffer value will be seen as white.
- Thinning
  The object thickness needs to be reduced to a skeleton size. The purpose of thinning is to simplify the pattern so that analysis such as contour analysis and feature analysis can easily be done. The MIL function *MimThin*() with parameters M_THIN and M_BINARY is used to implement this process.

Fig. 3 shows an example of the pre-processing phase using several MIL functions.

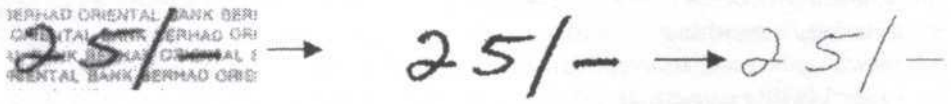

Original image Filter image Thin image

Fig. 3: Example of filtering, binarising and thinning on an image of the figure "25"

Recognition Phase

Recognition is a process of deducing amount/word identities from handwriting. A variety of pattern recognition methods are available, and many have been used for handwritten recognition by other authors (LeChun *et al.* 1990, 1995; Knerr *et al.* 1998; Dimauro *et al.* 1997; Senior *et al.* 1998).

In the Recognition phase, the image is cut vertically into many slices at a certain width which then undergoes a recognition process. The slices may contain a digit or part of a digit. When the slices are recognised as a digit, they represent a required digit and further slicing and recognition are done on a new segment. When the slices cannot be recognised or converge to the unknown object, we employ further slicing with a smaller slice and add to the segment. It is then re-tested for recognition. This process is continued until recognition is expected to be successful.

Isolated or unconnected handwritten digits in the string of the courtesy amount can be easily separated and recognised. However connected digits require a more rigorous method to segment the digit correctly. Many methods have been proposed to detect connected handwritten digits. Dimauro *et al.* (1997) used "drop falling" and "contour-based", Lu *et al.* 1998 used background thinning based algorithm, and Hu *et al.* 1998 used model-based segmentation method for handwritten numeral strings.

To recognise an image, three type of images are considered:

a. When an image contains joint digits as shown in *Fig. 4a.*

b. When an image contains touched digits as shown in *Fig. 4b.*
c. When an image contains what is required to be slant correction as shown in *Fig. 4c.*

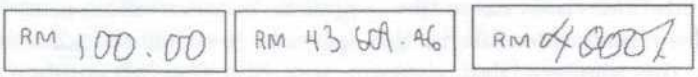

(a) joint digits (b) touched digits (c) image to be slant correction

Fig. 4: Some examples of images to be recognized

Isolated or unconnected digits, characters R and M, a decimal and a slash are not involved in the process of slicing. They can be separated using the blob analysis technique (Sulaiman *et al.* 2001). The process of slicing of *Fig. 4a* is shown in *Fig. 5a.* The process of slicing started from the slice a to the slice b at a certain width, w. The segment ab is then tested for recognition using a recogniser. The recogniser will inform if it is an unknown object and therefore further slicing but with the smaller slices, i.e., from slice *b* to slice *c*, are added to the segment in order to recognise a digit 0. A similar process of slicing is also applied on the second joint digit which started at the slice d and ended at the slice *f* (*Fig. 5b.*).

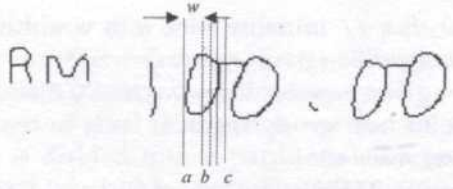

(a) Slicing begins at the first of the joint digit

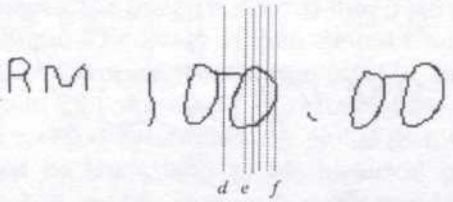

(b) Slicing on the next joint digit

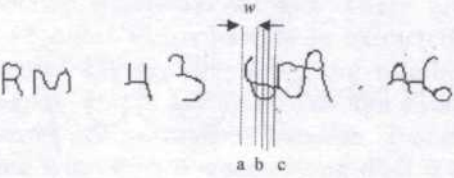

(c) Slicing on the touched digits

Fig. 5: Process of slicing an image RM100.00 and RM43609.46

Fig. 5c shows a similar process of slicing and recognising of the image of *Fig. 4b* which contains the touched digits.

However, when the same process of slicing and recognising is employed on the connected digits of the image of *Fig. 4c*, as shown in *Fig. 6a*, no digit can be identified. This is because the segment between slice *a* and slice *b* is considered an incomplete digit; the segment between slice *a* and slice *c* is considered the segment that contains some portion of another digit. The recogniser will inform that both segments be converge on to the unknown object. Slant correction can then be applied on the connected digits using the following formula:

$$x' = x - (Row - y) \sin \theta \quad (1)$$

$$y' = y \quad (2)$$

where *Row* is the height of the image. The object is sheared horizontally from right to the left as shown in *Fig. 6b* and the similar process of slicing and recognising can be applied on this new image.

Algorithm to recognise on the connected digits is as follows:

Algorithm 1:

READ image

i = 1; // start grouping the slices

REPEAT

group_segmenti = w_slice; // initialise slice with w width

WHILE (NOT *Recognition* (*group_segment*$_i$)) DO

group_segment$_i$ = *group_segment*$_i$ + *smaller_slice*; // add smaller slice

i = i + 1; // move to next group segment

UNTIL (*end_of_courtesy_amount*)

IF (*unrecognised the image*) THEN slant correction and GO TO REPEAT.

(a) Slice b and slice c contain some portion of two digits

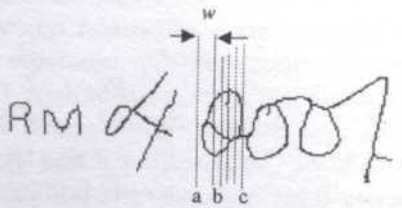

(b) Slant correction is applied on the joint digits at a certain angle

Fig. 6: Example of an image to be slant correction

FEATURE EXTRACTION

Feature extraction is a methodology of extracting features from the images. In other words, the image is represented by a set of numerical features to remove redundancy from the data and reduce its dimension. These features can be categorized as good features if fulfilling the characteristics below:

- Small interclass invariance whereby slightly different shapes with similar general characteristics should have numerically close values.
- Large interclass separation in which features from different classes should be quite different numerically.

There are many techniques for feature extraction (Mehdi *et al.* 1997; Samer *et al.* 1998). These can be classified as local features or global features. Global features depend on the entire shape of an image for the determination of the feature, while local features describe the limited regions of the shape and are affected by other region of the image. Techniques widely used, as global features are moment invariants, *fourier* descriptors, *eigenvector*, structural analysis and heuristic.

The following methods are used to extract the most discriminant features from the image :

- Number of transitions.
- Shapes.
- Moment invariant.

The number of transition and shape are based on local feature extraction whereas moment invariant is based on global features. The number of transition means that the numbers of pixel '1' for each row and column of the image are counted. The image is divided into 5 partitions on row and 5 partitions on column which bring a total of 10 features. For each partition, an average count of pixel '1' is calculated.

To measure the shapes, the image is divided into 5 partitions on its row and 5 partitions on its column. The image is then viewed from the top, horizontal and bottom directions. An average length from pixel '0' until pixel '1' on each view is calculated. About 20 features are extracted where 5 are on each sides.

Moment invariant method determines the global feature of the image. This method was presented by Hu (1962) in his historical paper on the use of moment invariant in 2-D pattern recognition. Shamsuddin *et al.* (2000) has improved the scaled-invariant moment formulation and successfully applied it on unconstrained isolated handwritten digits. There are 9 moment values calculated up to the 4^{th} order which have been extracted from the image.

A total of 39 features (10 features from the number of transitions, 20 features from the shapes, and 9 features from the moment invariants) are extracted. These features are normalised between -1 and 1. The output is a binary number ranging from 0 to 9 representing digit 0 to digit 9.

Table 1 shows the global feature extraction values (9 features) using the moment invariant method, Table 2 shows the local feature extraction values (10

features) based on the number of transitions and Table 3 shows local feature extraction values (20 features) based on the shapes.

TABLE 1
Global feature extractions using moment invariant on the selected image digits

Digits	Moment values								
	η_{02}	η_{03}	η_{11}	η_{12}	η_{13}	η_{21}	η_{22}	η_{30}	η_{31}
0	1.0000	-0.3615	-0.8292	-0.8069	-0.8094	-1.0000	-0.2835	-0.7833	-0.8502
1	0.7582	0.1215	0.9600	0.0184	0.5850	-0.3074	0.6281	-1.0000	1.0000
2	1.0000	-0.4574	-1.0000	-0.1249	-0.9898	-0.4403	0.5157	-0.6984	-0.7552
3	1.0000	-0.6463	0.3114	-0.6584	0.3631	-1.0000	0.3227	-0.4968	-0.0771
4	1.0000	-0.7774	-0.4314	-1.0000	-0.4724	-0.8877	-0.3102	-0.9008	-0.4790
5	1.0000	-0.6340	-0.6550	-1.0000	-0.9176	-0.0473	0.2464	-0.5717	-0.9893

TABLE 2
Local feature extractions based on the transitions of the selected image digits

	Feature extraction method based on the transitions				
Digit 0					
View from the top	-0.333333	-0.111111	-0.111111	-0.111111	-0.333333
View from the bottom	-0.259259	-0.111111	-0.111111	-0.111111	-0.222222
Digit 1					
View from the top	-0.777778	-1.000000	-1.000000	-1.000000	-1.000000
View from the bottom	-0.777778	-0.777778	-0.777778	-0.777778	-0.777778
Digit 2					
View from the top	-0.857143	-0.785714	-0.714286	-0.642857	-0.750000
View from the bottom	-0.809524	-0.857143	-0.857143	-0.857143	-0.857143
Digit 3					
View from the top	-0.878788	-0.81818	-0.575758	-0.696970	-0.797980
View from the bottom	-0.797980	-0.878788	-0.878788	-0.878788	-0.878788
Digit 4					
View from the top	-0.925192	-0.980605	-0.934428	-0.925192	-0.980605
View from the bottom	-0.954746	-0.915957	-0.915957	-0.961211	-0.980605
Digit 5					
View from the top	-0.789474	-0.649123	-0.578947	-0.578947	-0.824561
View from the bottom	-0.859649	-0.859649	-0.859649	-0.672515	-0.859649

NEURAL NETWORK MODEL

We use the popular multilayer Neural Network (NN) trained by the backpropagation (BP) algorithm (Rumelhart *et al.* 1987; LeChun *et al.* 1990) as the recogniser with the new error function (Shamsuddin *et al.* 2001). BP model is basically a gradient descent method and its objective is to minimise the mean square error between the target values and the actual outputs. Thus the mean squared error function (MSE) is defined as:

TABLE 3
Local feature extractions based on the shapes of the selected image digits

Feature extraction method based on the shapes					
Digit 0					
View from the top	0.111111	-1.000000	-0.777778	-0.33333	1.000000
View from the left side	-0.407407	-0.851852	-1.000000	-1.000000	-0.555556
View from the bottom	-0.111111	-1.000000	-1.000000	-0.333333	0.555556
View from the right side	0.481481	-0.55555	-1.000000	-1.000000	0.111111
Digit 1					
View from the top	1.000000	-1.000000	-1.00000	-1.000000	-1.000000
View from the left side	-1.000000	-1.000000	-1.00000	-0.925926	-0.733333
View from the bottom	-0.481481	-1.000000	-1.000000	-1.000000	-1.000000
View from the right side	-0.555556	-0.555556	-0.555556	-0.629630	-0.822222
Digit 2					
View from the top	1.000000	0.071429	-1.000000	-1.000000	-0.821429
View from the left side	-0.190476	0.523810	0.42857	0.142857	-0.500000
View from the bottom	-0.928571	-1.000000	-1.000000	-1.000000	-0.035714
View from the right side	-0.809524	-0.952381	-0.904762	-0.571429	-0.392857
Digit 3					
View from the top	-0.818182	-1.000000	-1.000000	-0.454545	0.292929
View from the left side	-0.878788	-0.393939	-0.515152	-0.151515	-0.099567
View from the bottom	1.000000	0.090909	-1.000000	-0.818182	-0.595960
View from the right side	-0.515152	-0.434343	-0.272727	-0.79798	-0.774892
Digit 4					
View from the top	-0.075522	0.940389	0.968095	0.044541	1.000000
View from the left side	-0.670291	-0.786659	-1.000000	0.002057	0.073668
View from the bottom	0.377020	0.330843	-0.269468	0.303136	0.271231
View from the right side	0.480458	-0.211284	-0.023803	-0.030267	0.292479

$$E = \frac{1}{2}\sum\left(t_{kj} - o_{kj}\right)^2 \tag{3}$$

where t_{kj} is the target output from node k to node j,
o_{kj} is the actual output from node k to node j.

The new error function (E_{new}) is used to increase the convergence rates of BP learning and defined implicitly as (Shamsuddin *et al.* 2001):

$$E_{new} = \sum_{p,j} g_{p,j} \tag{4}$$

with $g_{p,j} = \dfrac{e_{p,j}^2}{1 - a_{p,j}^2}$,

where $e_{p,j} = t_{p,j} - a_{p,j}$,
and $e_{p,j}$ is an error at output unit j for pattern p,

$t_{p,j}$ is the target value of output unit j for pattern p,
$a_{p,j}$ is an activation of output unit j for pattern p.

The derivatives of the improved error function which are used to determine a descent direction are defined in the same way as for the mean square error function.

EXPERIMENTS AND RESULTS

We have experimented on several hundred digits from the selected cursive handwritten courtesy amounts of Malaysian bank cheques. The digits may be unconnected, joint or touched between two or more digits. Appendix A shows some examples of the original images.

We divided the experiments into two parts :

a) Recognition.
b) Slicing and recognition.

Recognition

Firstly, the NN are trained with more than 300 isolated handwritten digits from various samples of selected Malaysian bank cheques. Some examples of the isolated digits served as the training data set are shown in *Fig. 7*. More examples of the training data set are shown in Appendix B.

A three layer NN architecture with the new error function of BP learning algorithm (Shamsuddin *et al.* 2001) is used. The input data for the BP model

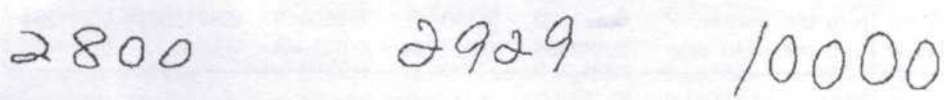

Fig. 7: Some examples of training data set

are the numerical features extracted from the isolated digits. Decimal, comma, and slash are not extracted because they can be detected easily during the programming process.

The input nodes for the network architecture are 39, the hidden layer contains 39 nodes, and the output layer contains 12 nodes. The output nodes are used to represent a binary value for digit 0 to 9, the unknown objects such as the incomplete digits, and the rejected objects such as the objects after slash. All initial weights and biases are set randomly between -1 and 1. For training purposes, the learning and momentum rates are set to 0.01 and 0.9 respectively with a sigmoid activation function. To terminate the training cycles, the minimum sum of errors is set to 0.01.

Further experiment is also carried out to compare the use of the new error function of BP with the standard error of BP and Kalman's BP (Kalman *et al.* 1991) on the recognition of the isolated digits. The same learning and

momentum rates are used for this experiment. The result from the experiment is shown in *Fig. 8*. It can be seen that the new error function of BP gives better results with faster convergence rates compared to the standard BP and Kalman's BP. The new learning rate takes 345 cycles to converge to the solution, compared to the standard BP, which takes 845 cycles, and Kalman's, which takes 1553 cycles.

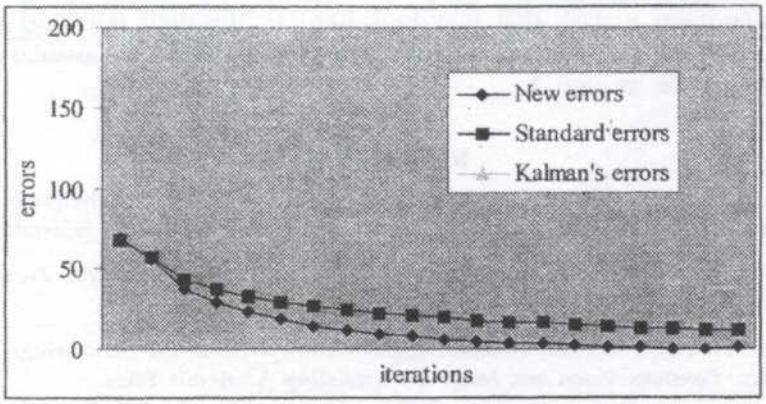

Fig. 8: Comparison of the convergence rates

Slicing and Recognition

About 156 digits from the original courtesy amounts of Malaysian bank cheques are used for testing. These figures are fed into the trained neural network. A 95% recognition rate has been achieved on tested data with 4% classified into the unknown objects and 1% classified as incorrect digits.

Although our method has been successfully tested on quite a number of cursive handwritten courtesy amounts there are still cases where recognition has not been successful. The reasons for not being successfully recognised are:

- The amount contains slash that may look like '1'.
- The digit joint with the decimal.
- Incompletely written digit 0 may be classified into the wrong digit such as digit 2.

There is no direct solution to overcome the above difficulties. However, the percentage of error for the unsuccessful recognition is small which is 5%.

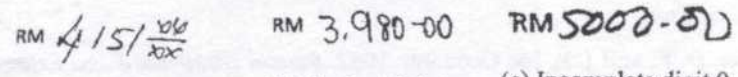

(a) slash like '1' (b) decimal joint with digit (c) Incomplete digit 0

Fig. 9: Some examples of the unrecognised courtesy amounts

CONCLUSION

We have described a technique called grouping single slice segment mechanism to segment and recognise cursive handwritten courtesy amounts of Malaysian bank cheques. We have implemented and tested on more than hundred courtesy amounts of selected Malaysian bank cheques. A 95% recognition rate has been achieved with 4% converge to the unknown images, and 1% converge to the incorrect digits. The reasons for not being successfully recognised are the amount contains a slash that may look like '1', the digit is joined with the decimal, and the incompletely written digit 0 which may be classified into the wrong digit such as digit 2.

REFERENCES

DIMAURO, G., S. IMPEDOVO, G. PIRLO and A. SALZO. 1997. Automatic bankcheque processing: A new engineering system. *Automatic Bank Cheque Processing*, World Scientific, p. 5-42.

HU, M.K. 1962. Visual pattern recognition by moment invariant. *IRE Trans. Inform. Theory*, IT-8: 179-187.

HU, J. and H. YAN. 1998. Model-based segmentation method for handwritten numeral strings. *Computer Vision and Image Understanding*. Academic Press.

KALMAN, B. L. and S. K. KWASNY. 1991. A superior error function for training neural network. *Proceeding of International Joint Conference of Neural Networks* **2**: 45-52.

KNERR, S., E. AUGUSTIN, O. BARET and D. PRICE. 1998. HMM based word recognition and its app. to legal amount reading on French checks. *Computer Vision and Image Understanding* **70(3)**: 404-419.

LECUN, Y., B. BOSER, J. S. DENKER, D. HENDERSON, R. E. HOWARD, W. HUBBARD and D. L. JACKEL. 1990. Handwritten Digit Recognition with a Back-Propagation Network. In *Advances in Neural Information Processing Systems* **2**, ed. D. Touretzky, Morgan Kaufman.

LECUN, Y., L. JACKEL, L. BOTTOU, A. BRUNOT, C. CORTES, J. DENKER, H. DRUCKER, I. GUYON, U. MÜLLER, E. SÄCKINGER, P. SIMARD and V. VAPNIK. 1995. Comparison of Learning Algorithms for Handwritten Digit Recognition. In *International Conference on Artificial Neural Networks*, ed. F. Fogelman and P. Gallinari, p. 53-60, Paris.

LU, Z. and Z. CHI. 1998. Background-thinning based algorithm for separating connected handwritten digit strings. In *Proceeding IEEE Intern. Conf. on Acoustics, Speech and Signal Processing*. p. 1065-1068. USA.

MEHDI, D. and F. KARIM. 1997. Farsi Handwritten Character Recognition with Moment Invariants. In *International Conference of Digital Signal Processing*, p. 507 - 510.

MIL USER GUIDE. 1998. *Matrox Imaging Library User Guide* (version 5.1). Matrox Electronic Systems Ltd.

RUMELHART, D. E. and J. L. MC CLELLAND. 1987. *Parallel Distributed Proc.: Explorations in the Microstructure of Cognition*. MIT Press.

SAMER. M. A., M. N. EDUARDO and C. R. DAVID. 1998. Object Recognition and Orientation via Zernike Moments. In 3rd *Asean Conference on Computer Vision*, p. 386 - 393.

SENIOR, A. W. and A. J. ROBINSON. 1998. An off-line cursive hand writing recognition system. *IEEE Transactions on Pattern Analysis and Machine Intelligence* **20(3)**.

SHAMSUDDIN, M., M. N. SULAIMAN and M. DARUS. 2000. Improved scale-invariant moments for deformation digits. *Intern. J. Computer Math.* **74**: 439-447.

SHAMSUDDIN, S. M., M. N. SULAIMAN and M. DARUS, 2001. An improved error signal for the BP model for classification problems. *Intern. J. Computer Math.* **76**: 297-305.

SULAIMAN, M. N. and M. KHALID. 2001. An offline segmentation technique for the processing of the courtesy amount of Malaysian bank cheques. *ELEKTRIKA* **4(2)**: 1-13.

APPENDIX A:
Some examples of the courtesy amounts taken from Malaysian bank cheques

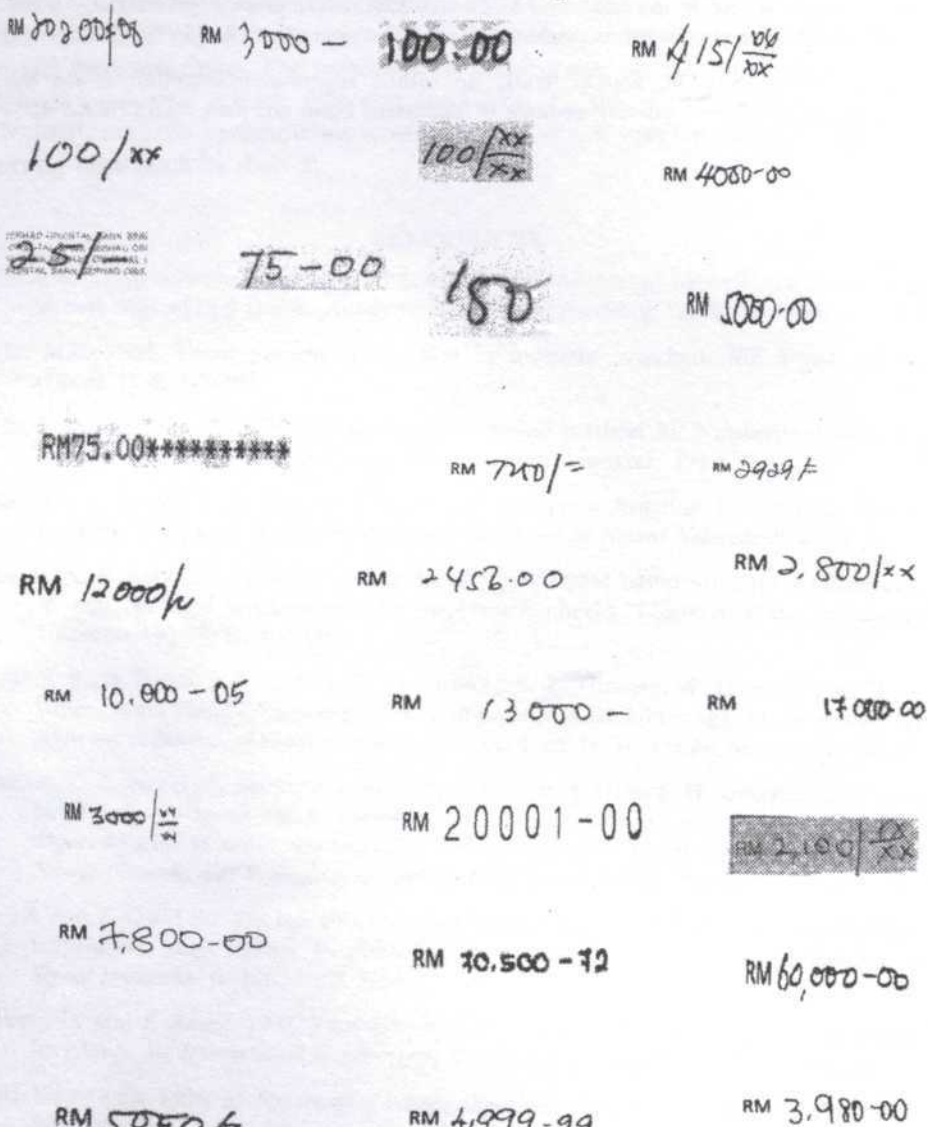

APPENDIX B:
Some examples of images for training data set

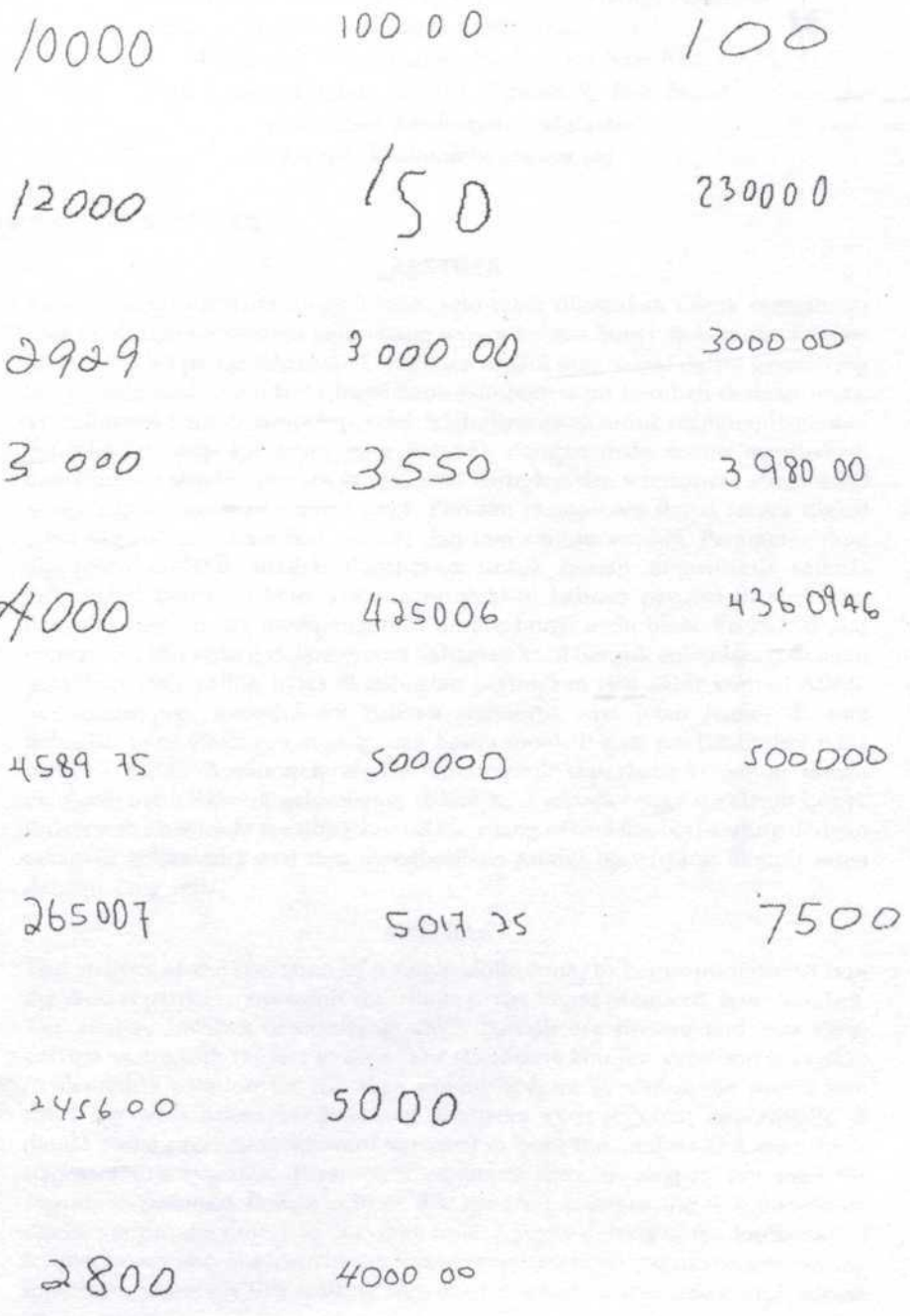

ISSN: 0128-7680
Pertanika J. Sci. & Technol. **11(2)**: 173 - 190 (2003)

Time-Varying Spectral Modelling of the Solo Violin Tone

Ong Bee Suan & Minni K. Ang
Music Department, Faculty of Human Ecology
Universiti Putra Malaysia 43400 UPM Serdang, Malaysia
E-mail: bee_suan_ong@hotmail.com
Musicmall Conservatoire Productions Sdn Bhd
14-2 Jalan Dagang SB 4/1, Taman Sg Besi Indah
43300 Seri Kembangan, Malaysia
E-mail: kimhuai@musician.org

Received: 30 April 2001

ABSTRAK

Analisis spektrum nada tunggal biola solo telah dijalankan untuk memahami kesan pelbagai komponen gelombang separa ke atas bunyi nada biola. Analisis ini melibatkan pengenalpastian komponen separa yang wujud dalam gelombang bunyi nada biola solo, serta bagaimana komponen ini berubah dengan masa. Transformasi Fourier tempoh-pendek telah digunakan untuk mengimplementasi penyelesaian bagi spektrum yang berubah dengan masa secara membahagi bunyi kepada segmen pendek yang digelar tetingkap dan seterusnya menganalisis setiap segmen secara berturut-turut. Perisian memproses signal secara digital telah digunakan dalam fasa analisis dan fasa sintesis semula. Parameter yang diperoleh melalui analisis digunakan untuk tujuan mensintesis semula gelombang bunyi tersebut. Data menunjukkan bahawa perubahan spektrum dengan masa banyak mempengaruhi timbre bunyi nada biola. Frekuensi asas dicerap beralih sedikit dalam semua bahagian kecil bentuk gelombang, dengan peralihan yang paling nyata di bahagian permulaan dan akhir sampul ADSR. Keputusan juga menujukkan bahawa harmonik asas lebih lemah di awal bahagian permulaan gelombang, dan hanya menjadi kuat setelah timbre nada menjadi stabil. Komponen separa inharmonik diperhatikan wujud dalam bahagian akhir bentuk gelombang, dalam julat separa tinggi spektrum bunyi. Proses sintesis semula menjimatkan 93.8% ruang cakera liat berbanding dengan rakaman gelombang asal dan menghasilkan kualiti bunyi yang hampir sama dengan yang asli.

ABSTRACT

The analysis of the spectrum of a single violin tone, to better understand how the various partial components contribute to the sound produced, is undertaken. The analysis involves determining which partials are present and how these partials evolve with respect to time. The short-time Fourier transform is used to implement a solution for the time varying spectra by slicing the sound into short segments called windows and analysing each segment sequentially. A digital signal processing software was used in both the analysis and resynthesis stages of this research. Parameters extracted through analysis are used for resynthesis purposes. Results indicate that spectrum changes over time contribute significantly to the timbre of the violin tone. A slight shifting of the fundamental frequency was also observed in the sound spectrum of all the sub-sections of the waveform, although this shifting was most marked in the attack and release

portions of the ADSR envelope. The results also showed that the intensity of the fundamental harmonic was weaker in the initial attack stage, only dominating when the timbre of the tone stabilised. Within the release portion, inharmonic overtones were shown to occur in the upper partials of the sound spectrum. Finally, the resynthesis process reduces the required hard disk capacity by about 93.8% compared with the sampled waveform, while at the same time producing an audible tone almost indistinguishable from the original.

Keywords: Music synthesis techniques, digital tone generation, computer music, digital music, spectral modelling, violin acoustics

INTRODUCTION

A complete mathematical model of a musical tone consists of periodic and non-periodic functions. Periodic functions are generally modelled as summations of simple sinusoids, according to Fourier's theorem. Non-periodic functions, such as the amplitude envelope, transient sounds and residual noise, contribute towards the realism of the tone.

The periodic function is contributed by the addition of the partials that occur in the sound waveform. This can be shown through the analysis of the sound waveform using spectrum analysis to identify the partials that occur. The sound waveform can be defined as in the Equation 1 below:

$$y = \sum_{n=1}^{N} \sum_{m=1}^{M} a_n \sin\left(2\pi f_n t_m + \phi_n\right) \quad (1)$$

where,

y = the waveform of the sound signal
a_n = the relative amplitude of the n^{th} harmonic
f_n = frequency of the n^{th} harmonic
t_m = the time at which the waveform is captured
ϕ_n = the phase of the n^{th} harmonic

The Fourier Series equation usually assumes that the waveform does not change over time. However, according to the formula above, the waveform does change with time. Therefore, the exact contribution of each of these modes is time varying with respect to the overall sound. This exact contribution needs to be determined through experiment.

The objective of the study is to analyse the spectrum of a single violin tone, to better understand how the various harmonic or partial components contribute to the sound produced. The analysis involves determining which partials are present and how these partials evolve with respect to time. The parameters obtained in this way may then be used for resynthesising the violin tone. The purpose of this resynthesis is to obtain savings in data bandwidth in order to create the same sound using minimal memory requirements.

LITERATURE REVIEW

Spectral modelling synthesis was developed by Xavier Serra and Julius Smith, in 1990 (Vaggione 1996). The spectral modelling synthesis technique is a set of techniques and software implementations for the analysis, transformation and synthesis of musical sounds. Spectral modelling synthesis technique is developed through Fourier analysis, which considers a pitched sound to be made up of various sinusoidal components, where the frequencies of the higher components are integral multiples of the frequency of the lowest component (Miranda 1998). Acoustic characteristics which correspond with physical and behavioural properties of sound sources (such as spectral centroid and inharmonicity) are most important for discrimination of different sounds (Martin 1998). Conclusions drawn from McAdam, Beauchamp and Meneguzzi (1999) indicate that spectral-envelope shape (jaggedness and irregularity in the shape of the spectrum) and spectral flux (change in the shape of the spectral envelope over time) are the most important physical parameters in timbre discrimination. Literature on musical instrument sounds has suggested that there are many other acoustic features that are also useful for instrument identification such as inharmonicity (Benade 1990), spectral centroid (Handel 1995), and intensity (Beauchamp 1982). Most spectral modelling techniques work in two stages: analysis and resynthesis (Miranda 1998). Analysis is a process of digitising sound from a natural musical instrument first and then analysing it to determine the content of partial frequencies and the associated amplitude and frequency envelopes, while resynthesis is the process of synthesising sound on the basis of information derived from the analysis of another sound (Dodge and Jerse 1997).

METHODOLOGY

Recording the Violin Tone to be Used in the Analysis

The violin used in recording the musical instrument tone for this study was a *Charles Buthod* handmade French violin. The violin strings used were *Thomastik "Dominant"* violin strings, and the bow was a *Mirecort* bow. The recording of the violin sound was conducted in a quiet and acoustically dry (non-reverberant) room, with the aim of minimising reverberation and background sounds (which generate energy affecting the recorded spectrum partials). With a sampling rate of 44100 Hz and a resolution of 16 bits, a compact disc quality violin sound was recorded. During the recording, only the monophonic (single melodic line) violin sound was recorded. This was to ensure that successful analysis could be done.

The Analysis Methodology

Spectrum analysis is important for spectral modelling, as samples alone do not inform of the spectral constituents of a sampled sound. There are two categories of spectrum analysis, which have been created to analyse the spectrum of the

sounds. They are harmonic analysis and formant analysis. Harmonic analysis focuses on the identification of the frequencies and amplitudes of the spectrum components, while formant analysis uses the estimation of the overall shape of the spectrum's amplitude envelope.

The Fourier transform decomposes or separates a waveform or function into sinusoids of different frequencies, which sum to the original waveform. It identifies or distinguishes the different frequency sinusoids and their respective amplitudes. The Fast Fourier Transform (FFT) is a Discrete Fourier Transform (DFT) algorithm developed by Tukey and Cooley that reduces the number of computations from the order of N_0^2 to $N_0 \log N_0$. The Short-Time Fourier Transform (STFT) implements a solution for time varying spectra by slicing the sound into short segments called windows and analysing each segment sequentially. It uses FFT to analyse these windows, and plots the analysis of the individual windows in sequence in order to trace the time evolution of the sound. The result of each window analysis is called an FFT frame. Each FFT frame contains two types of information. One is a magnitude spectrum which depicts the amplitudes of every analysed component, and the other one is the phase spectrum that shows the initial phase for every frequency component (Miranda 1998). In this investigation, the phases that occur in the sound spectrum are not considered. This is due to the fact that in determining the timbre or sound quality of the wave the spectral component amplitudes are far more important than their phases (Berg and Stork 1995).

The sample waveform of the recorded violin note is recalled and divided into four main portions: the attack portion, decay portion, sustain portion, and release portion Attack-Decay-Sustain-Release (ADSR) envelope. Each portion is further subdivided into even smaller sections. The minimum duration time of each section was set at 0.1 seconds. (Portions with duration times of less than 0.1 seconds produced significant fluctuation of results when the FFT function was applied). The sections for data analysis are also overlapped to improve the periodogram estimation of the results. Table 1 shows the details for each section of data used for the analysis.

A digital signal processing software was used in both the analysis and resynthesis stages of this research. The Welch power spectrum estimation method was used. It estimates the power spectrum by using the FFT and taking the squared magnitude of the results. In order to perform the FFT, parameters such as the sampling frequency, length of FFT, size of window, number of overlapping samples and type of window need to be specified. Below are the parameters that are used in this paper.

Window type. Different types of windows display various types of frequency graphs. With a suitable window, the spectral leakage is diminished and the width of the spectral peaks is increased. In this study, the Hanning window was used. One of the reasons the Hanning window was chosen is due to its simple implementation. The Hanning window has low side lobes, which makes it easier to pick up major frequency components. Although different functions may be

applied, it is important to choose a suitable window function whose characteristics are best suited to the problem that is being addressed (Brigham 1988).

Size of window. The size of the spectral window affects the variance of the estimation. The narrower the spectral window, the larger the variance of the estimation. In this particular study, the size of the window is set to 65536 or 2^{10} in order to produce a stable and low variance estimate.

Length of the FFT. The length of the FFT is the number of the different frequencies at which the power spectrum is estimated. The length of the FFT has to be a power of two, in order to employ a high-speed radix-2 FFT algorithm. It is due to the characteristic of the radix-2 FFT routine. The Radix-2 FFT routine is optimised to perform a real FFT when the input sequence is purely real, and computes a complex FFT when the input sequence is not. This causes a real power of two FFTs to be 40 percent faster than a complex FFT, although both have the same FFT length. Thus, the length of the FFT, which

TABLE 1
Divisions and subdivisions of the original waveform with respect to time, for the purpose of analysis

ADSR envelope portion	Total time duration (s)	Total sections	Time duration for each section (s)	Sections with or without overlap (s)
Attack	0.00-0.16	4	0.10	0.00-0.10
				0.02-0.12
				0.04-0.14
				0.06-0.16
Decay	0.16-0.40	8	0.10	0.16-0.26
				0.18-0.28
				0.20-0.30
				0.22-0.32
				0.24-0.34
				0.26-0.36
				0.28-0.38
				0.30-0.40
Sustain	0.40-1.83	12	0.10	0.40-0.50
				0.45-0.55
				0.50-0.60
				0.55-0.65
				0.60-0.70
			0.20	0.70-0.90
				0.90-1.10
				1.10-1.30
			0.30	1.30-1.60
			0.10	1.60-1.70
				1.64-1.74
				1.68-1.78
			0.11	1.72-1.83
Release	1.83-2.575	8	0.10	1.83-1.93
				1.91-2.01
				1.99-2.09
				2.07-2.17
				2.15-3.15
				2.23-2.33
			0.10	2.33-2.43
			0.165	2.41-2.575

is a power of two, has the fastest execution time. In order to obtain the fastest execution time, the FFT length is set to 65536 or 2^{10}. When the sequence length is not an exact power of two, an alternate algorithm finds the prime factors of the sequence length and computes the mixed-radix DFT of the shorter sequences.

Sampling frequency. According to the Nyquist Theorem, to digitally encode the desired frequency bandwidth the sampling frequency must be set at least twice as high as the highest desired frequency. As a result, in order to reproduce a signal with an 11 kHz frequency range, a 22 kHz sampling rate has to be selected. Otherwise aliasing (which is caused by having too few samples to show the basic waveform) will occur. Thus, a proper sampling rate will enable the same waveform to be reconstructed.

Number of overlapping samples. This refers to the number of samples in the overlapping sections. In this particular case, the number of overlapping samples is set to zero.

In the analysis section, there are a few rules that have to be followed. The procedures are as below:

1. The size of the window must be less or equal to the length of the FFT.
2. The minimum value of the length of the FFT has to be 2^8, which is equal to 256.
3. Values for NOVERLAP, number of samples overlap and nfft, length of the FFT have to be positive integers.
4. The number of overlapping samples has to be less than the window size.

As explained earlier, the number of the FFT will determine the number of different frequencies at which the power spectrum is estimated. The compromise between small variance and high resolution is the most important issue of the power spectrum estimation. With a small variance, a stable estimation is produced. On the other hand, with a high resolution, one can look into all the fine details in the spectrum. It is thus important to know the main purpose of the experiment and how accurate an estimation is required.

To obtain the relative amplitudes the following equation (2) was used,

$$\text{Relative amplitude of the Harmonic, } \frac{A_n}{A_{peak}} = Anti\log_{10}\frac{PSD_{relative}}{20} \qquad (2)$$

where,

A_n = amplitude of the nth harmonic
A_{peak} = maximum amplitude present among all the harmonics
$PSD_{relative}$ = relative power spectrum density

The Resynthesis Process

In order to resynthesise the original sound, the results obtained from the analysis were inserted back into the Equation 1 according to their time-varying components. All the contributing equations were concatenated, that is appended

one after another according to their time-varying intervals. Through this method, the waveform produced consists of a sound spectrum that changes over time. A comparison between the synthesised sound and the original sound was then carried out. The purpose of resynthesising the sound is to find out how authentically the equation manages to generate the sound compared with the original sound. It also helps in discovering other factors needed to improve the quality of the sound produced.

RESULTS

Fig. 1 below shows a screen snapshot of the recorded violin tone. It is an A4 violin tone recorded on stereo channels using a sampling rate of 44.1 kHz with a resolution of 16-bits. The complete duration of this tone is 2.575 seconds, and is stored in the .wav file format using 221 KB of hard disk space. This A4 violin tone, as explained previously, is divided into four portions according to ADSR parameters. These four portions are the attack, decay, sustain and release portions (*Fig. 1*). The attack portion occurs between time T0 and T1, the decay portion between T1 and T2, the sustain portion between time T2 and T3, and the release portion between T3 and T4. Table 2 presents a summary of all these results.

RESULTS OF THE SPECTRUM ANALYSIS

The Attack Portion

The sound spectrum of all the four sections within the attack portion consists only of harmonic overtones (which are integer multiples of the fundamental harmonic, f). Within the attack portion, there is an occurrence of a weaker intensity on the fundamental harmonic. In the first two sections (which are sections A1 and A2), the fundamental frequency does not contain the highest power spectrum density compared with other partials in the sound spectrum. In fact, the highest power spectrum density focuses on the fifth harmonic, 5f.

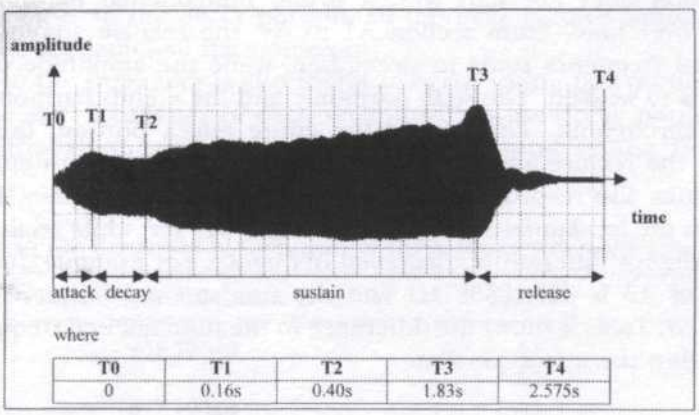

T0	T1	T2	T3	T4
0	0.16s	0.40s	1.83s	2.575s

Fig. 1: Snapshot of the recorded violin tone

TABLE 2
Summary of ADSR parameters for recorded violin tone

Parameter	Value Recorded
Note	A4
Sampling Rate	44.1 KHz
Sampling Resolution	16 bits
Number of Channels	2
Attack time (T1-T0)	0.16 seconds
Decay time (T2-T1)	0.24 seconds
Sustain time (T3-T2)	1.43 seconds
Decay time (T4-T3)	0.745 seconds
Total duration of sample	2.575 seconds
Sample format	.wav
Sample file size	221 KB

It is then followed by the second harmonic and then only the fundamental harmonic. The relative amplitudes of the fundamental harmonic within sections A1 and A2 are only 0.7498 and 0.9469, while the second harmonic records values of 0.9710 and 0.98. The highest power spectrum density in section A1 is –82.23164 decibels which is about 2.501147 decibels louder than the fundamental harmonic, while in section A2 the highest power spectrum density is –80.958757 decibels, which is about 0.473661 decibel louder than the fundamental harmonic. Thus, one can see that the difference between the fundamental harmonic and the second harmonic in these two sections becomes smaller.

Table 3 shows the changes, with respect to time, in the relative amplitudes of the sound spectrum within the attack portion. In section A1, the relative amplitude of the fundamental frequency is only 0.7498. In section A2, the relative amplitude of the fundamental frequency starts to increase and from section A3 onwards the fundamental frequency contains the highest relative amplitude within the sound spectrum. This result indicates that the initial attack portion does not start with a strong fundamental harmonic, but is developed over time. From section A1 to A4, the relative amplitude of the fundamental frequency starts to strengthen, while the amplitude of the fifth partial starts to weaken. The sixth harmonic and the eighth harmonic are very consistent throughout. Throughout the entire attack portion, there are no changes in the relative amplitudes of the sixth and eighth harmonics.

The results also record the occurrence of a shift in frequency. In the first two sections the fundamental frequency is 442.77649 Hz, while sections A3 and A4 have a slightly different fundamental frequency. For example, fundamental frequency of A3 is 442.10358 Hz and the fundamental frequency of A4 is 441.43066 Hz. Table 4 shows the difference in the fundamental frequency of all sections within the attack portion.

TABLE 3
Changes in the relative amplitudes of the sound spectrum over time within the attack portion

Harmonics, f	A1	A1+A2	A1+A2+A3	A1+A2+A3+A4	A2+A3+A4	A3+A4	A4
1.0	0.7	0.8	0.9	1.0	1.0	1.0	1.0
2.0	1.0	1.0	1.0	0.9	0.8	0.7	0.6
3.0	0.4	0.4	0.4	0.4	0.4	0.3	0.3
4.0	0.2	0.2	0.2	0.2	0.2	0.1	0.1
5.0	1.0	1.0	1.0	0.9	0.9	0.8	0.8
6.0	0.1	0.1	0.1	0.1	0.1	0.1	0.1
7.0	0.2	0.2	0.3	0.3	0.3	0.3	0.3
8.0	0.1	0.1	0.1	0.1	0.1	0.1	0.1
9.0	0.0	0.0	0.0	0.0	0.0	0.0	0.0
10.0	0.2	0.2	0.2	0.2	0.2	0.2	0.2
11.0	0.0	0.0	0.0	0.0	0.0	0.0	0.0
12.0	0.0	0.1	0.1	0.1	0.1	0.1	0.1
13.0	0.1	0.1	0.1	0.1	0.0	0.0	0.0
14.0	0.0	0.1	0.1	0.1	0.1	0.0	0.0
15.0	0.0	0.0	0.0	0.0	0.0	0.0	0.0
16.0	0.0	0.1	0.1	0.1	0.1	0.0	0.0

The Decay Portion

Within the decay portion, the sound spectrum of all the sections consists only of harmonic partials. There are no occurrences of inharmonic partials. The sections in this portion have some differences when compared with the sections in the attack portion. In this portion, each occurrence of the fundamental harmonic always has the highest intensity (also called the power spectrum density or perceived loudness) level compared with other partials, which also occur in the sound spectrum. This is unlike the attack portion, in which there are some occurrences of the fundamental harmonic with an intensity level lower than other harmonic partial values, even though the perceived tone is still the A4 note. In the decay portion, all the peak relative amplitude values focus on the fundamental harmonic only.

A shift in the frequency is also found to occur within this portion. Table 5 displays the shift frequency of each section within the decay portion. In this portion, although there is a shift in frequency, most of the fundamental

TABLE 4
Difference in the fundamental frequency of the sections within the attack portion

Fundamental Frequency (Hz)	Section
442.77640	A1
	A2
442.10358	A3
441.43066	A4

TABLE 5
Difference in the fundamental frequency of all sections within the decay portion

Fundamental Frequency (Hz)	Section
442.10358	D1
	D2
	D3
	D4
441.43066	D5
	D6
	D7
	D8

frequency focuses on 441.43066 Hz. There is only one fundamental frequency that focuses on another frequency (442.10358 Hz). This occurs in the first section within the decay portion (also called D1).

Table 6 displays the changes over time in the relative amplitudes of the sound spectrum within the decay portion. This table clearly displays the consistency of the relative amplitudes of the eighth, tenth, twelfth and fourteenth harmonics. Throughout the decay portion, there is no change in their relative amplitudes, which remain at 0.1.

The Sustain Portion

As in the previous two portions, all the sections in the sustain portion consist of only harmonic partials. In this portion, every section records each occurrence of the fundamental frequency at the highest intensity compared with other partials. This is very similar to the decay portion. Table 7 shows the shift in frequency which occurs in each section within the sustain portion. These results indicate that most sections within the sustain portion focus on the frequency of 441.43066 Hz. There are only two sections with a fundamental frequency that focuses on another frequency: section S4 and S13. In these two sections, the fundamental frequency focuses on 442.10358 Hz.

The results within the sustain portion show that most partials begin to evolve throughout this portion. This is especially marked at section S13 where only the first nine partials occur. Table 8, which shows changes in the relative amplitude of the sound spectrum over time, clearly show the intensity of high frequencies (beginning at the seventeenth harmonic) becoming so low that their relative amplitudes become insignificant. In this portion, as all partials in the sound spectrum start to evolve, there are no partials with consistent relative amplitudes other than the high frequencies (beginning at the seventeenth harmonic) whose relative amplitudes need no longer remain under consideration.

The Release Portion

In this portion, the partials that appear in the spectrum consist of both harmonic and inharmonic partials. Most of the inharmonic partials occur after

TABLE 6
Changes in the relative amplitudes of the sound spectrum over time within the decay portion

n f	D1	D1+D2	D1+D2 +D3	D1+D2 +D3+D4	D1+D2 +D3+D4 +D5	D2+D3 +D4+D5 +D6	D3+D4 +D5+D6 +D7	D4+D5 +D6+D7 +D8	D5+D6 +D7+D8	D6+D7 +D8	D7+D8	D8
1.0	1.0	1.0	1.0	1.0	1.0	1.0	1.0	1.0	1.0	1.0	1.0	1.0
2.0	0.5	0.5	0.5	0.5	0.6	0.6	0.6	0.6	0.6	0.6	0.6	0.6
3.0	0.2	0.2	0.2	0.2	0.2	0.2	0.2	0.2	0.2	0.2	0.2	0.2
4.0	0.1	0.1	0.1	0.1	0.1	0.1	0.1	0.1	0.2	0.2	0.2	0.2
5.0	0.7	0.7	0.7	0.7	0.7	0.7	0.8	0.8	0.8	0.8	0.8	0.8
6.0	0.1	0.1	0.1	0.1	0.2	0.2	0.2	0.2	0.2	0.2	0.2	0.2
7.0	0.2	0.2	0.2	0.3	0.3	0.3	0.3	0.3	0.3	0.3	0.3	0.3
8.0	0.1	0.1	0.1	0.1	0.1	0.1	0.1	0.1	0.1	0.1	0.1	0.1
9.0	-	-	-	-	-	-	-	-	-	-	-	-
10.0	0.1	0.1	0.1	0.1	0.1	0.1	0.1	0.1	0.1	0.1	0.1	0.1
11.0	-	-	-	-	-	0.1	-	-	-	-	-	-
12.0	0.1	0.1	0.1	0.1	0.1	0.1	0.1	0.1	0.1	0.1	0.1	0.1
13.0	-	-	0.1	-	-	-	-	-	-	-	-	-
14.0	0.1	0.1	0.1	0.1	0.1	0.1	0.1	0.1	0.1	0.1	0.1	0.1
15.0	-	-	-	-	-	-	-	0.1	0.1	0.1	0.1	0.1
16.0	0.1	0.1	0.1	0.1	0.1	0.1	-	-	-	-	-	0.1
17.0	-	-	0.1	0.1	0.1	0.1	0.1	0.1	0.1	0.1	0.1	0.1

TABLE 7
Difference in the fundamental frequency of each section in the sustain portion

Fundamental Frequency (Hz)	Section
	S1
441.43066	S2
	S3
442.10358	S4
	S5
	S6
	S7
441.43066	S8
	S9
	S10
	S11
	S12
442.10358	S13

the fourth harmonic. Table 9 shows the changes in the relative amplitude of the sound spectrum over time within the release portion. After the first section, the peak amplitude displaces to the second harmonic. In the release portion, all the partials are evolving, and in the final two sections (R7 and R8), there are only three partials remaining. Table 10 shows the shift in frequency that occurs within the release portion. These results indicate that all sections within the release portion do not focus on a specific frequency. The fundamental frequencies shift very frequently among the frequencies 442.10358 Hz, 441.43066 Hz, 440.75775 Hz, 438.0661 Hz, 437.39319 Hz and 435.37445 Hz.

Resynthesis Process Results

In the process of resynthesis, each of the relative amplitude values obtained from the spectrum analysis are inserted into the Equation (1), according to their correlated time values and harmonic values. Finally, all series of arrays y1, y2, y3, are concatenated into a double arrayed matrix and generated to produce a resynthesis sound.

DISCUSSION

There are five major findings obtained from this study. Firstly, the micro variations in the power spectrum of each of the partials are discussed. This is followed by a discussion on the shifting of the fundamental frequency, which was observed throughout the sections. The weak fundamental in the attack portion is discussed next, followed by the presence of inharmonicity in the release portion. Finally, data bandwidth in the generation of sound is considered.

TABLE 8
Changes in the relative amplitudes of the sound spectrum over time within the sustain portion

nf	S1	S1+S2	S2+S3	S3+S4	S4+S5	S5	S6	S7	S8	S9	S10	S10+ S11	S10+S11 +S12	S11+S12	S11+S12 +S13	S12+S13	S13
1.0	1.0	1.0	1.0	1.0	1.0	1.0	1.0	1.0	1.0	1.0	1.0	1.0	1.0	1.0	1.0	1.0	1.0
2.0	0.6	0.6	0.6	0.6	0.6	0.6	0.5	0.5	0.5	0.4	0.4	0.4	0.4	0.4	0.4	0.4	0.4
3.0	0.2	0.2	0.2	0.2	0.3	0.3	0.2	0.2	0.2	0.3	0.2	0.2	0.2	0.2	0.2	0.3	0.3
4.0	0.2	0.1	0.1	0.1	0.1	0.1	0.2	0.1	0.1	0.1	0.1	0.1	0.1	0.1	0.1		
5.0	0.9	0.8	0.8	0.7	0.7	0.7	0.8	0.7	0.6	0.5	0.5	0.5	0.5	0.5	0.4	0.4	0.3
6.0	0.1	0.1	0.2	0.3	0.3	0.3	0.2	0.2	0.2	0.3	0.3	0.3	0.3	0.3	0.3	0.3	0.4
7.0	0.3	0.3	0.3	0.2	0.2	0.2	0.3	0.2	0.2	0.2	0.2	0.2	0.2	0.2	0.2	0.1	0.1
8.0	0.1	0.1	0.1	0.1	0.1	0.1	-	-	-	-	-	-	-	-	-	-	-
9.0	-	-	-	-	0.1	0.1	-	-	-	0.1	0.1	0.1	0.1	0.1	0.1	0.1	0.1
10.0	0.2	0.2	0.2	0.1	0.1	0.1	0.1	0.1	0.1	0.1	0.1	0.1	0.1	0.1	0.1	0.1	-
11.0	0.1	0.1	0.1	0.1	0.1	0.1	0.1	0.1	0.1	0.1	0.1	0.1	0.1	0.1	0.1	0.1	-
12.0	0.1	0.1	0.1	0.1	0.1	0.1	0.1	0.1	0.1	0.1	0.1	0.1	0.1	0.1	0.1	0.1	-
13.0	-	-	-	-	-	-	-	-	-	-	0.1	0.1	0.1	0.1	0.1	0.1	-
14.0	0.1	0.1	0.1	0.1	-	-	0.1	-	0.1	-	0.1	0.1	0.1	0.1	-	-	-
15.0	0.1	-	-	-	-	-	-	-	-	-	-	-	-	-	-	-	-
16.0	0.1	0.1	0.1	0.1	0.1	0.1	0.1	0.1	-	-	0.1	0.1	-	-	-	-	-
17.0	-	-	-	-	0.1	-	-	-	-	-	-	-	-	-	-	-	-

TABLE 9
Changes in the relative amplitudes of the sound spectrum over time within the release portion

nf	R1	R1+R2	R2	R2+R3	R3	R3+R4	R4	R4+R5	R5	R5+R6	R6	R7	R7+R8	R8
1.0	1.0	1.0	0.8	0.8	0.9	0.6	0.4	0.3	0.2	0.3	0.3	0.3	0.4	0.4
2.0	0.4	0.7	1.0	1.0	1.0	1.0	1.0	1.0	1.0	1.0	1.0	1.0	1.0	1.0
3.0	0.2	0.4	0.4	0.5	0.6	0.6	0.6	0.5	0.5	0.5	0.5	0.5	0.4	0.3
4.0	0.1	0.1	-	0.2	0.2	0.1	0.1	0.1	-	-	-	-	-	-
4.1	-	0.2	0.2	0.2	-	-	-	-	-	-	-	-	-	-
5.0	0.1	0.1	-	0.1	0.1	0.1	-	-	-	0.1	0.1	-	-	-
5.1	-	0.3	0.3	0.3	-	-	-	0.1	0.1	0.1	-	-	-	-
6.0	0.3	0.3	-	-	-	-	-	-	-	-	-	-	-	-
6.1	-	0.5	0.5	0.4	0.4	0.2	0.1	0.1	0.1	0.1	-	-	-	-
7.0	0.1	0.1	-	-	-	-	-	-	-	-	-	-	-	-
7.1	-	0.1	0.1	0.1	0.1	0.1	-	-	-	-	-	-	-	-

TABLE 10
Difference in the fundamental frequency of each section within the release portion

Fundamental Frequency (Hz)	Section
440.75775	R1
435.37445	R2
438.06610	R3
	R4
437.39319	R5
441.43066	R6
442.10358	R7
441.43066	R8

Micro Variations in the Sound Spectrum with Respect to Time

The results show that the power spectrum of each of the partials varies with respect to time. These significant results indicate that spectrum changes over time are a very important feature in the synthesis of high quality or authentic sound. These changes in the loudness of each partial over time contribute to the timbre of the violin tone. These results are quite similar to findings by Mellody and Wakefield (1999), whose research focuses on the time-frequency characteristics of violin vibrato.

Shifting Fundamental Frequency

The shifting fundamental frequency that occurred in the sound spectrum of the recorded violin signal occurs in the sound spectrum of all the sections of the waveform (Table 11). The fundamental frequency does not focus on one

TABLE 11
The shifting fundamental frequency that occurs in all sections

Fundamental Frequency (Hz)	Window (which contains this fundamental frequency)
442.77640	Attack portion – A1, A2
442.10358	Attack portion – A3
	Decay portion – D1
	Sustain portion – S4, S13
	Release portion – R7
441.43066	Attack portion – A4
	Decay portion – D2, D3, D4, D5, D6, D7, D8
	Sustain portion – S1, S2, S3, S5, S6, S7, S8, S9, S10, S11, S12
	Release portion – R6, R8
440.75775	Release portion – R1
438.06610	Release portion – R3, R4
437.39319	Release portion – R5
435.37445	Release portion – R2

specific value of frequency. It is most prominent in the attack portion and the release portion of the waveform.

During the recording process, the violin player was requested to play single notes, without the use of vibrato. It may be concluded therefore that the shifting frequency observed is not caused by the playing technique. As a further point to note, playing techniques such as vibrato, which consist of changing the frequency throughout the playing of a note, cause larger frequency fluctuations than the shifts obtained from this study. A possible cause of the frequency shifts observed in this research may be due to the inertia of the violin string. The greatest amount of shifting occurs in the attack and release portions of the waveform, when the string changes from a rest state to a vibrating state (attack portion) and again from a vibrating state back to a rest state (release portion). The slight shifts in the decay and sustain portions are natural results of the uncertainty principle, which does not expect absolute and perfectly matching measurements in any observation but rather allow for a small margin of error.

These results indicate that the most frequent fundamental frequency is 441.43066 Hz, which is the focus point of most of the sections in the decay and sustain portions. Fundamental frequencies such as 440.75775 Hz, 438.0661 Hz, 437.39319 Hz, and 435.37445 Hz are only held by sections within the release portion. These frequencies are found to be inaccurate, especially during the resynthesis process. If such frequencies are selected for insertion into the resynthesis equations, the sound generated becomes artificial and the pitch of the synthesis is changed.

Weak Fundamental Harmonics

A weaker strength or intensity of the fundamental harmonic, especially within the initial attack portion, was discovered. Table 3 indicates that within the first three windows, which occur from the starting point (0.00 seconds) to 0.06 seconds, the highest spectrum energy does not focus on the fundamental frequency, but is concentrated on the second harmonic. These results indicate that the intensities of the fundamental harmonic only dominate when the timbre of the tone becomes much stronger and more stable.

Inharmonicity

Within the release portion, several inharmonic overtones are obtained. The inharmonic overtones only occur in the upper partials of the sound spectrum. This may be due to the mechanical stiffness as explained by Martin (1998). According to his explanation, freely vibrating strings may produce inharmonic partials. Further study is needed to explain the occurrence of the inharmonic partials.

Data Reduction

The amount of hard disk space required to store the originally recorded violin sample is 221 kilobytes. The hard disk capacity required to store the control file

that controls the resynthesised sound, is only 13.7 kilobytes. Although this work only considers the spectrum of the original sound signal, the sound resynthesised from these parameters is found to be quite close to the original.

This is indicated through the sound discrimination experiment that was carried out in this research. In this sound discrimination experiment, the resynthesised sound, the original recorded violin sound and four other synthesised violin tones produced by commercially available synthesis techniques were loaded as soundfonts (a data format that defines the information required by a computer to create musical notes or sound effects through wavetable synthesis). The release portion of the experimentally produced resynthesised sound (with its transient noise) was not included in the model due to the reasons explained in the earlier paragraphs. All the various violin tones were played back through a Creative Sound Blaster Live card. The other synthesised violin sounds were XWave PCI Audio OPL2/OPL3 Device, Yamaha SXG 50 Driver, Creative S/W Synth and the original chipset of the Creative Sound Blaster Live card. 20 listeners were then asked to discriminate between the six versions of the sound, which were played back twice in a set order. The listeners were asked to rate the realism of the played back sound on a five-point scale ranging from 0-20%, 20-40%, 40-60%, 60-80% and 80-100%. Results from this experiment indicated that about 90% of the listeners claimed that the synthesised sound from this research (which was obtained through time-varying spectral modelling technique) sounded similar to the original recorded violin sound (which was used for sound analysis in this research). However, the resynthesis process reduced the required hard disk capacity by about 93.8%. By reducing the usage of the hard disk capacity, the execution time of the sound resynthesis process may be increased. In addition, it may also enable a computer to store a whole range of a violin sound incorporating different techniques of playing.

CONCLUSION

It has been shown that for the single violin tone, the micro variations in the sound spectrum contribute significantly towards the timbre of the tone. When these parameters are used for resynthesis purposes, a significant file size saving is obtained, with minimal concessions to the sound quality. Further study needs to be done to complete the model for the violin for all notes within its range and for all techniques of performance. A detailed study needs to be done on further data simplification that may be undertaken without sacrificing the sound quality

REFERENCES

BEAUCHAMP, J. W. 1982. Synthesis by spectral amplitude and 'brightness' matching of analyzed musical instrument tones. *Journal of the Audio Engineering Society* **30(6)**: 396-406.

BENADE, H. 1990. *Fundamentals of Musical Acoustics.* Second edition. New York: Dover.

BERG, R. E. and D. G. STORK. 1995. *The Physics of Sound.* Englewood Cliffs, New Jersey: Prentice Hall.

BRIGHAM, E. O. 1988. *The Fast Fourier Transform and Its Applications.* Englewood Cliffs, NJ: Prentice-Hall, Inc.

DODGE, C. and T. A. JERSE. 1997. *Computer Music: Synthesis, Composition, and Performance.* New York: Schirmer Books.

HANDEL, S. 1995. Timbre perception and auditory object identification. In *Hearing,* ed. B. C. J. Moore. New York: Academic.

MARTIN, K. D. 1998. Toward automatic sound source recognition: identifying musical instruments. Paper presented at the *NATO Computational Hearing Advanced Study Institute,* Il Ciocco IT.

MCADAM, S., J. W. BEAUCHAMP and S. MENEGUZZI. 1999. Discrimination of musical instrument sounds resynthesized with simplified spectrotemporal parameter. *Journal of the Acoustical Society of America* **105(2)**: 882-897.

MELLODY, M. and G. H. WAKEFIELD. 2000. The time-frequency characteristics of violin vibrato:Modal distribution analysis and synthesis. *Journal of the Acoustical Society of America* **107(1)**: 598-611.

MIRANDA, E. R. 1998. *Computer Sound Synthesis for the Electronic Musician.* Oxford: Focal Press.

SERRA, X. and J. SMITH. 1990. Spectral modeling synthesis: A sound analysis/synthesis system based on a deterministic plus stochastic decomposition. *Computer Music Journal.* **14(4)**: 12-24.

VAGGIONE, H. 1996. Articulating microtime. *Computer Music Journal* **20(2)**: 33-38.

ISSN: 0128-7680
Pertanika J. Sci. & Technol. 11(2): 191 - 203 (2003)

A Comparison of JPEG and Wavelet Compression Applied to CT Images

Amhamed Saffor, Abdul Rahman Ramli & Kwan-Hoong Ng[1]
Multimedia and Imaging Systems Research Group,
Department of Computer and Communication System Engineering,
Universiti Putra Malaysia, 43400 UPM, Selangor, Malaysia
[1]Department of Radiology, Universiti of Malaya Medical Center,
59100 Kuala Lumpur, Malaysia
E-mail: saffor@hotmail.com

Received: 18 September 2001

ABSTRAK

Satu kajian mampatan imej menjadi lebih penting kerana satu imej yang tidak boleh mampat memerlukan satu jumlah ruang storan/simpanan yang besar dan lebar jalur transmisi yang tinggi. Makalah ini memfokuskan kepada perbandingan kuantitatif kaedah kehilangan mampatan yang digunakan ke atas pelbagai jenis imej 8-bit Computed Tomography (CT). Algoritma mampatan Joint Photographic Experts Group (JPEG) dan Wavelet telah digunakan ke atas satu set imej CT, iaitu otak, dada, dan abdomen. Semua algoritma tersebut digunakan ke atas setiap imej untuk mencapai nisbah mampatan maksimum (CR). Setiap imej yang dimampatkan kemudiannya telah dinyah mampat dan analisis kuantitatif dilakukan untuk membandingkan setiap imej mampatan-dinyah mampat dengan kesesuaian imej asal. Enjin Mampatan Wavelet (edisi piawaian 2.5), dan Bestari JPEG (Versi 1.1.7) telah digunakan dalam kajian ini. Indeks statistik terkira adalah min ralat kuasa dua (MSE), nisbah isyarat-hingar (SNR) dan nisbah isyarat-hingar puncak (PSNR). Keputusan menunjukkan bahawa mampatan Wavelet menghasilkan kualiti mampatan yang lebih baik berbanding JPEG untuk mampatan tinggi. Daripada nilai-nilai berangka yang diperoleh kami perhatikan bahawa PSNR untuk imej dada dan abdomen adalah bersamaan dengan 24 dB untuk nisbah mampatan sehingga 31:1 dengan menggunakan JPEG dan 18 dB untuk nisbah mampatan sehingga 33:1 dengan menggunakan Wavelet. Untuk imej otak, PSNR adalah bersamaan dengan 26 hingga 30 dB untuk nisbah mampatan di antara 40 hingga 125:1 dengan menggunakan JPEG, manakala dengan menggunakan Wavelet, PSNR adalah bersamaan dengan 22 hingga 34 dB untuk nisbah mampatan di antara 52 hingga 240:1. Darjah mampatan juga didapati bergantung pada struktur anatomi dan kerumitan imej-imej CT.

ABSTRACT

A study of image compression is becoming more important since an uncompressed image requires a large amount of storage space and high transmission bandwidth. This paper focuses on the quantitative comparison of lossy compression methods applied to a variety of 8-bit Computed Tomography (CT) images. Joint Photographic Experts Group (JPEG) and Wavelet compression algorithms were used on a set of CT images, namely brain, chest, and abdomen. These algorithms were applied to each image to achieve maximum compression ratio (CR). Each compressed image was then

decompressed and quantitative analysis was performed to compare each compressed-then-decompressed image with its corresponding original image. The Wavelet Compression Engine (standard edition 2.5), and JPEG Wizard (Version 1.1.7) were used in this study. The statistical indices computed were mean square error (MSE), signal-to-noise ratio (SNR) and peak signal-to-noise ratio (PSNR). Our results show that Wavelet compression yields better compression quality compared with JPEG for higher compression. From the numerical values obtained we observe that the PSNR for chest and abdomen images is equal to 24 dB for compression ratio up to 31:1 by using JPEG and 18 dB for compression ratio up to 33:1 by using wavelet. For brain image the PSNR is equal to 26 to 30 dB for compression ratio between 40 to 125:1 by using JPEG, whereas by using wavelet the PSNR is equal to 22 to 34 dB for compression ratio between 52 to 240:1. The degree of compression was also found dependent on the anatomic structure and the complexity of the CT images.

Keywords: Image compression, Computed Tomography (CT), wavelet compression, JPEG, medical images

INTRODUCTION

Image compression is fundamental to the efficient and cost-effective use of digital medical imaging technology and applications. There are two methods of image compression: lossless compression enables an exact reproduction of the original image from the compressed file. However, this scheme achieves relatively low compression rates of about 3:1. The second, lossy compression eliminates the redundant and high frequency data from an image, which is usually outside the range of human visual perception. This results in much higher compression ratios, typically 20:1 or greater, but with some data loss (Saffor *et al.* 2001). There are a number of techniques or compression algorithms for producing lossy or lossless images (Slone *et al.* 2000). It is quite important that the method used is based on an adopted medical imaging standard. Standards ensure simplified and long-term interoperability with other imaging devices; they also minimize the risk of diagnostic data being rendered obsolete over time (Erickson *et al.* 1998). Digital Imaging and Communications in Medicine (DICOM) is a medical imaging standard for all imaging modalities. The DICOM standard supports RLE (Run Length Encoding) lossless compression, and JPEG lossy compression for both static and dynamic clips. RLE lossless compression is good for static images, typically achieving ratios of 3:1 for grayscale images (Iyriboz *et al.* 1999). A variety of lossy compression techniques are available, with some of them standardized e.g. JPEG, which has the advantage of being available as commercial products, but also has the disadvantage of creating block artifacts at respectable compression ratios, i.e., over 10:1. This is a consequence of its 8 x 8 discrete cosine transform (DCT) coding scheme (Persons *et al.* 2000). Most current research efforts in lossy compression that appear promising involve the discrete wavelet transform (DWT), after the pioneering work by Daubechies (1988). The reasons for this are that the DWT

operates on the whole image as a single block thereby avoiding blocking artifacts typical in JPEG, while dynamically adjusting its spatial/frequency resolution to the appropriate level in various regions of the image (Savcenko *et al.* 2000). Wavelet compression methods appear to perform better than JPEG, particularly for large-matrix images such as radiographs using the dual pathology approach, compression ratios as high as 80:1 (Bradley and Erickson 2000). The goal of this paper is to compare Wavelet and JPEG lossy compression methods applied to a set of CT images by using Wavelet Compression Engine (standard edition 2.5) available at Wavelet Compression Engine, 2000, and JPEG wizard version (1.1.7) available at Pegasus Imaging Corporation. The size of each image before compression is 512 x 512 x 8 bit.

IMPLEMENTATION

Techniques commonly employed for image data compression result in some degradation of the reconstructed image. A widely used measure of reconstructed image fidelity for an N x M size image is the mean square error (MSE) as given by Stephen *et al.*(2000).

$$MSE = \frac{1}{N.M}\sum_{i=0}^{N-1}\sum_{j=0}^{M-1}\left(\left|f(i,j)-f'(i,j)\right|^2\right) \qquad (1)$$

Where $f(i,j)$ is the original image data and $f'(i, j)$ is the compressed image value. Signal-to-Noise Ratio (SNR) is widely used in the signal processing literature (since it is related to the signal power and noise power), and is perhaps more meaningful because it gives 0 dB for equal signal and noise power. SNR is used more commonly in the image-coding field. So, the SNR that is used corresponding to the above error is defined as

$$SNR = 10\log\left\{\frac{\sum_{i=0}^{N-1}\sum_{j=0}^{M-1}f(i,j)^2}{\sum_{i=0}^{N-1}\sum_{j=0}^{M-1}\left(f(i,j)-f'(i,j)\right)^2}\right\} \qquad (2)$$

Another quantitative measure is the peak signal-to-noise ratio (PSNR), based on the root mean square error of the reconstructed image. The formula for PSNR is given by

$$PSNR = 10\log\left(\frac{(255)^2}{MSE}\right) \qquad (3)$$

where RMSE, is calculated as

$$RMSE = \sqrt{MSE} \tag{4}$$

Values for these quantities were obtained using LuraWave Smart Compression software (version 1.7.1) available at Lura Tech Gmblt, 2000.

METHOD

By using the formulas in the previous section, some parameters were calculated for JPEG and Wavelet respectively. Signal-to-Noise-Ratio (SNR) measures are estimates of the quality of a reconstructed image compared with the original image. Mean Square Error (MSE) is the cumulative squared error between original and compressed image. Lower value of MSE means lesser error, and these values give higher Peak Signal-to-Noise Ratio (PSNR). PSNR is another qualitative measure based on the root-mean-square-error of the reconstructed image. In our study we calculate the compression ratio, MSE, SNR and PSNR for various sets of CT images: - 18,20 and 17 image sequence for brain, chest and abdomen respectively.

RESULTS AND DISCUSSION

Fig. 1 shows three different CT images, which are for brain, chest and abdomen. Tables 1 and 2 represent the results for compression ratio (CR), MSE, SNR and PSNR for CT-brain by using JPEG and Wavelet compression respectively. These results were also plotted in *Figs. 2, 3* and *4*. The results for chest and abdomen images are given in Tables 3 - 6 respectively. These results were also plotted in *Figs. 5 - 10*. The images in *Fig. 11* provide a subjective comparison between JPEG and Wavelet for compressed different CT images in terms of PSNR. The comparisons between the results are given in Table 7.

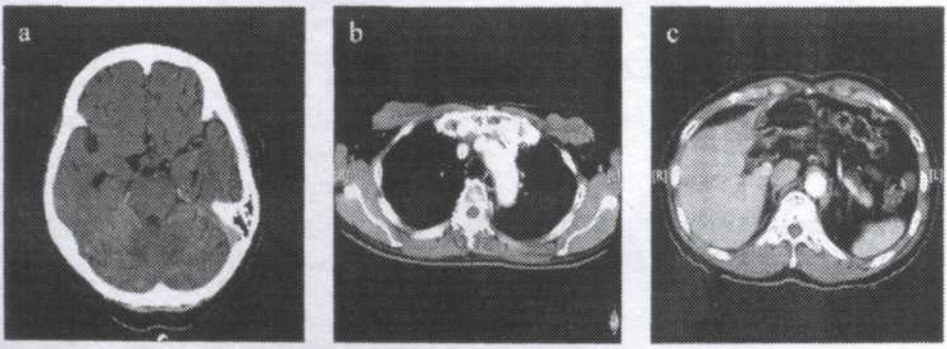

Fig. 1: (a) CT-brain image, (b) CT- chest image, and (c) CT-abdomen image

TABLE 1
Analysis of CT-brain images by using JPEG

JPEG					
Image No	Anatomical Structure	Maximum Compression ratio	MSE	SNR dB	PSNR dB
Image01	Orbit +Sinus air cells +brain +skull bone	40	147.0	18.82	26.45
Image02	Orbit +Sinus air cells +brain +skull bone	41	151.44	18.19	26.32
Image03	Orbit +Sinus air cells +brain +skull bone	41	143.78	18.50	26.55
Image04	Air cells +brain +skull bone	45	128.94	19.45	27.02
Image05	Brain +skull bone	52	112.55	18.42	27.61
Image06	Air cells +brain +skull bone	55	107.52	19.18	27.81
Image07	Brain +skull bone + ventricle	56	106.73	19.08	27.84
Image08	Brain +skull bone + ventricle	56	105.69	19.27	27.89
Image09	Brain +skull bone + ventricle	55	107.96	19.17	27.79
Image10	Brain +skull bone + ventricle	74	66.31	22.52	29.91
Image11	Brain +skull bone + ventricle	78	63.7	22.52	30.08
Image12	Brain +skull bone + ventricle	79	63.21	22.56	30.12
Image13	Brain +skull bone + ventricle	73	65.72	22.53	29.95
Image14	Brain +skull bone	77	62.19	22.77	30.19
Image15	Brain +skull bone	81	60.72	22.73	30.29
Image16	Brain +skull bone	88	59.38	22.57	30.39
Image17	Brain +skull bone	104	57.9	22.17	30.50
Image18	Skull bone	125	55.64	18.34	30.67

TABLE 2
Analysis of CT-brain images by using Wavelet compression

Wavelet compression					
Image No	Anatomical Structure	Maximum Compression ratio	MSE	SNR dB	PSNR dB
Image01	Orbit +Sinus air cells +brain +skull bone	52	383.82	14.66	22.29
Image02	Orbit +Sinus air cells +brain +skull bone	55	381.52	14.18	22.32
Image03	Orbit +Sinus air cells +brain +skull bone	57	394.50	14.12	22.17
Image04	Air cells +brain +skull bone	63	327.37	15.40	22.98
Image05	Brain +skull bone	76	254.27	15.89	24.08
Image06	Air cells +brain +skull bone	83	219.97	16.08	24.71
Image07	Brain +skull bone + Ventricle	83	211.05	16.12	24.89
Image08	Brain +skull bone + Ventricle	83	211.05	16.27	24.89
Image09	Brain +skull bone + Ventricle	82	232.85	15.84	24.46
Image10	Brain +skull bone + Ventricle	125	114.76	20.14	27.53
Image11	Brain +skull bone + Ventricle	136	97.47	20.68	28.24
Image12	Brain +skull bone + Ventricle	136	96.09	20.74	28.31
Image13	Brain +skull bone + Ventricle	114	107.97	20.38	27.80
Image14	Brain +skull bone	120	95.27	20.92	28.34
Image15	Brain +skull bone	129	83.25	21.36	28.93
Image16	Brain +skull bone	142	68.46	21.95	29.77
Image17	Brain +skull bone	185	42.04	23.56	31.89
Image18	Skull bone	240	26.04	21.64	33.97

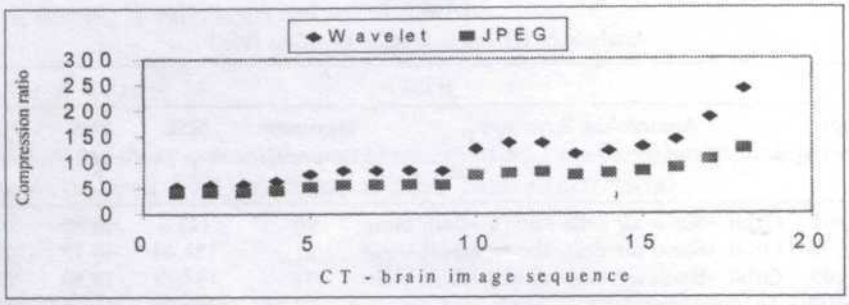

Fig. 2: Compression ratio against CT-brain image sequence for JPEG and Wavelet compression

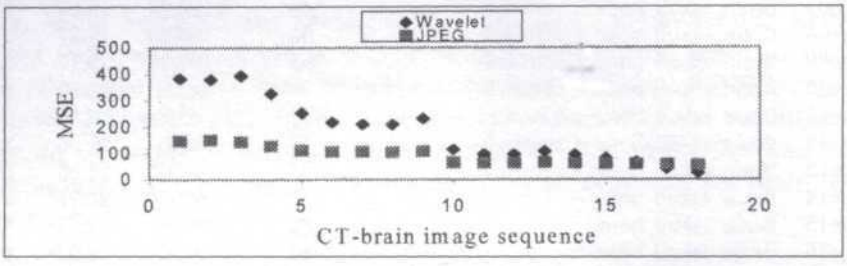

Fig. 3: MSE against CT-brain image sequence for JPEG and Wavelet compression

TABLE 3
Analysis of CT-chest images by using JPEG

		JPEG			
Image No	Anatomical Structure	Maximum Compression ratio	MSE	SNR dB	PSNR dB
Image01	Small vessels + esophagus + more tissues	27	271.68	15.11	23.79
Image02	The same + lungs	27	264.02	15.52	23.91
Image03	The same + lungs	28	258.07	15.48	24.01
Image04	The same + lungs is bigger	28	253.12	15.44	24.09
Image05	The same + superior vena cave + bigger lungs	29	248.50	15.35	24.18
Image06	Less tissues +bigger lungs	28	250.76	15.03	24.19
Image07	The same as above + aortic arch	29	248.48	14.98	24.18
Image08	The same + less tissues	28	253.56	15.18	24.09
Image09	The same + division of aorta	26	198.23	15.61	25.16
Image10	Lungs bigger + pulmonary vessel	28	253.12	14.89	24.09
Image11	Less tissues + more pulmonary vessel	29	249.78	15.03	24.16
Image12	Heart (upper border) + lungs bigger	28	253.29	14.64	24.09
Image13	The same as above	28	256.37	14.78	24.04
Image14	The same + more heart	28	250.53	14.60	24.14
Image15	Much less tissues + more heart	28	255.48	14.68	24.06
Image16	No aorta + bigger lungs + less tissues	28	253.70	15.08	24.08
Image17	Inferior vena cave	29	248.25	15.04	24.18
Image18	The same as above	28	252.42	15.29	24.11
Image19	The same as above + liver	28	252.95	15.34	24.10
Image20	Bigger liver + less heart +spleen bowels	27	251.34	15.54	24.13

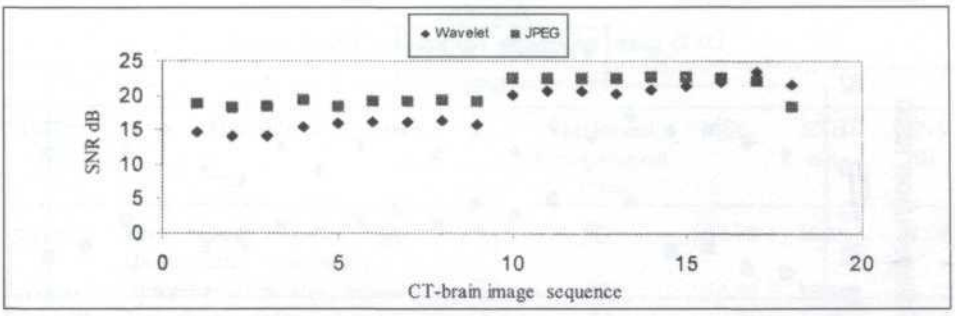

Fig. 4: SNR against CT-brain image sequence for JPEG and Wavelet compression

TABLE 4
Analysis of CT-chest images by using Wavelet compression

		Wavelet compression			
Image No	Anatomical Structure	Maximum Compression ratio	MSE	SNR dB	PSNR dB
Image01	Small vessels + esophagus + more tissues + bones	30	1099.00	9.25	17.72
Image02	The same + lungs	30	1075.08	9.62	17.82
Image03	The same + lungs	31	1060.19	9.55	17.88
Image04	The same + lungs is bigger	31	1058.02	9.45	17.88
Image05	The same + Superior vena cave + bigger lungs	31	1040.56	9.32	17.96
Image06	Less tissues +bigger lungs	30	1048.37	9.01	17.93
Image07	The same as above + aortic arch	31	1039.98	8.95	17.96
Image08	The same + less tissues	30	1067.82	9.13	17.85
Image09	The same + division of aorta	30	1033.06	8.64	17.99
Image10	Lungs bigger + pulmonary vessel	30	1071.52	8.83	17.83
Image11	Less tissues + more pulmonary vessel	30	1048.68	8.98	17.92
Image12	Heart (upper border) + lungs bigger	30	1057.48	8.63	17.88
Image13	The same as above	30	1094.81	8.67	17.74
Image14	The same + more heart	30	1070.48	8.50	17.84
Image15	Much less tissues + more heart	29	1078.03	8.64	17.80
Image16	No aorta + bigger lungs + less tissues	30	1082.35	8.97	17.78
Image17	Inferior vena cave	31	1058.16	8.91	17.88
Image18	The same as above	30	1066.75	9.13	17.85
Image19	The same as above +liver	30	1077.87	9.22	17.80
Image20	Bigger liver+ less heart +spleen bowels	30	1080.32	9.38	17.79

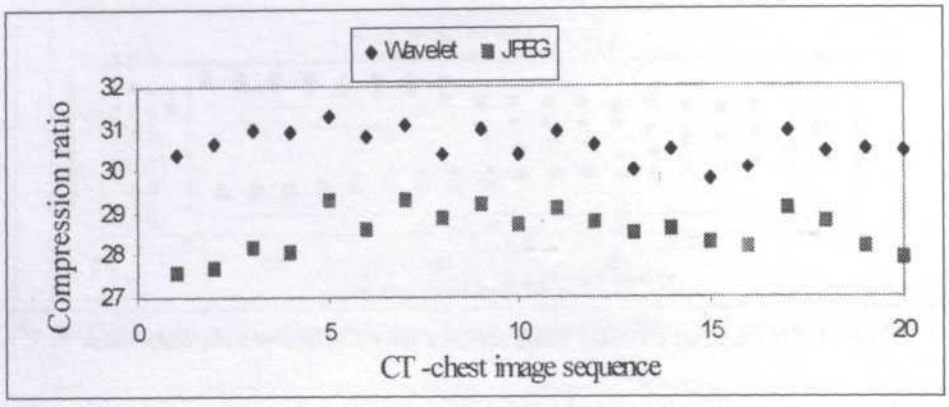

Fig. 5: Compression ratio against CT-chest image sequence for JPEG and Wavelet compression

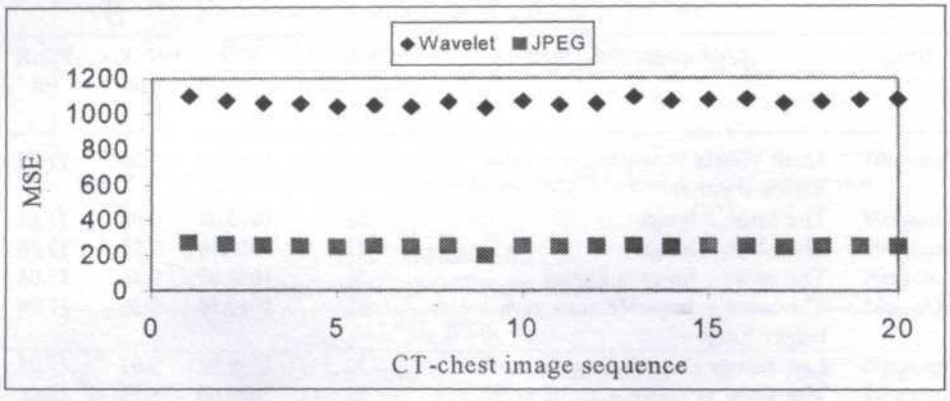

Fig. 6: MSE against CT-chest image sequence for JPEG and Wavelet compression

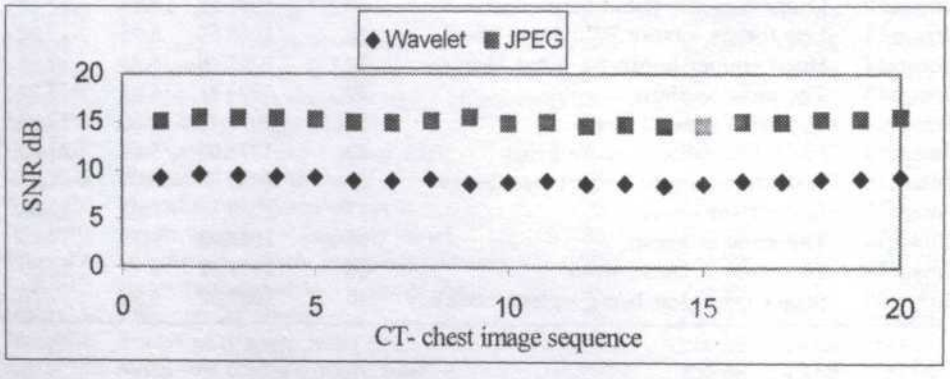

Fig. 7: SNR against CT-chest image sequence for JPEG and Wavelet compression

TABLE 5
Analysis of CT-abdomen images by using JPEG

		JPEG			
Image No	Anatomical Structure	Maximum Compression ratio	MSE	SNR dB	PSNR dB
Image01	Liver bigger + spleen bigger + lung diminishing + no heart	27	257.78	15.89	24.02
Image02	Spleen smaller +less tissue + more bowel	27	254.34	15.89	24.07
Image03	Less liver + spleen vessels + bigger stomach	28	249.21	15.80	24.16
Image04	Liver less + spleen vessels more stomach + more bowels	27	253.07	15.56	24.08
Image05	Less liver + stomach + less bowels diminishing + + spleen diminishing	27	255.20	15.28	24.06
Image06	Less liver + no stomach + kidney appears + much more bowels	26	254.73	14.96	24.07
Image07	Spaces between the organs become wider + less bone + kidney appears + less liver	26	255.39	14.89	24.06
Image08	Vessels for right kidney + less liver + less bones + more bowels	27	250.40	14.59	24.14
Image09	More vessels of both kidneys + very small liver	27	247.94	14.45	24.18
Image10	The same as above	27	248.63	14.21	24.17
Image11	Liver diminishing	29	243.73	14.14	24.26
Image12	No liver + more space between the organs + less bone	29	240.83	14.49	24.31
Image13	No kidney vessels + kidney diminishing	29	241.48	13.73	24.30
Image14	Soft tissues of the abdomen seen + less bowel + image become smaller	31	234.56	13.98	24.43
Image15	Less bowel	30	236.13	14.18	24.40
Image16	The same as above	30	236.40	14.99	24.39
Image17	The same as above	31	236.06	13.84	24.40

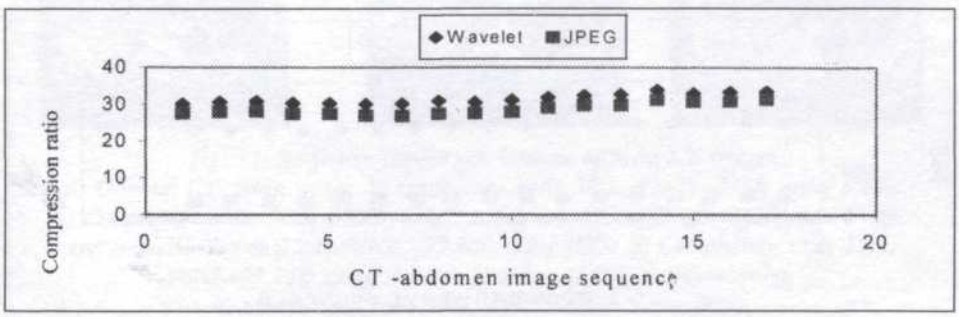

Fig. 8: Compression ratio against CT-abdomen image sequence for JPEG and Wavelet compression

TABLE 6
Analysis of CT-abdomen images by using Wavelet compression

Image No	Anatomical Structure	Wavelet compression: Maximum Compression ratio	MSE	SNR dB	PSNR dB
Image01	Liver bigger + spleen bigger + lung diminishing + no heart	30	1077.81	9.84	17.81
Image02	Spleen smaller +less tissue + more bowel	30	1064.08	9.84	17.86
Image03	Less liver + spleen vessels + bigger stomach	30	1051.14	9.73	17.91
Image04	Liver less + spleen vessels more stomach + more bowels	30	1056.65	9.52	17.81
Image05	Less liver + stomach + less bowels diminishing + spleen diminishing	30	1065.35	9.07	17.85
Image06	Less liver + no stomach + kidney appears + much more bowels	30	1059.17	8.96	17.81
Image07	Spaces between the organs become wider + less bone + kidney appears + less liver	30	1065.00	8.86	17.86
Image08	Vessels for right kidney + less liver + less bones + more bowels	30	1044.38	8.57	17.94
Image09	More vessels of both kidneys + very small liver	30	1048.07	8.38	17.93
Image10	The same as above	31	1047.92	8.15	17.93
Image11	Liver diminishing	31	1018.98	8.13	18.05
Image12	No liver + more space between the organs + less bone	32	1010.61	8.26	18.05
Image13	No kidney vessels + kidney diminishing	32	1015.28	7.70	18.06
Image14	Soft tissues of the abdomen seen + less bowel + image become smaller	33	990.33	7.73	18.17
Image15	Less bowel	32	1003.72	7.89	18.11
Image16	The same as above	33	991.96	7.77	18.15
Image17	The same as above	33	994.13	7.59	18.15

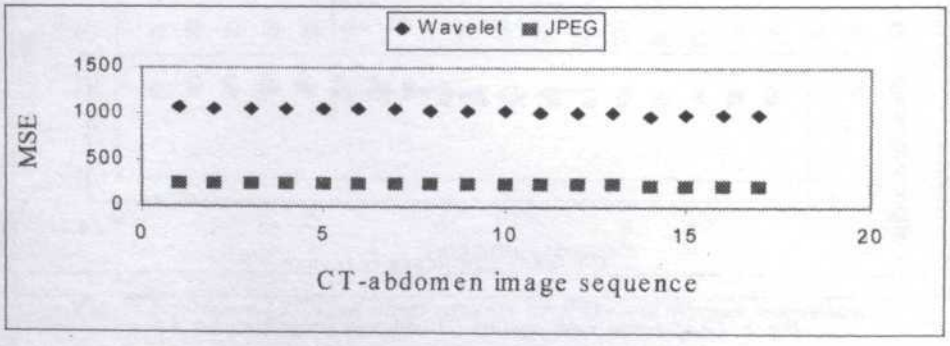

Fig. 9: MSE against CT-abdomen image sequence for JPEG and Wavelet compression

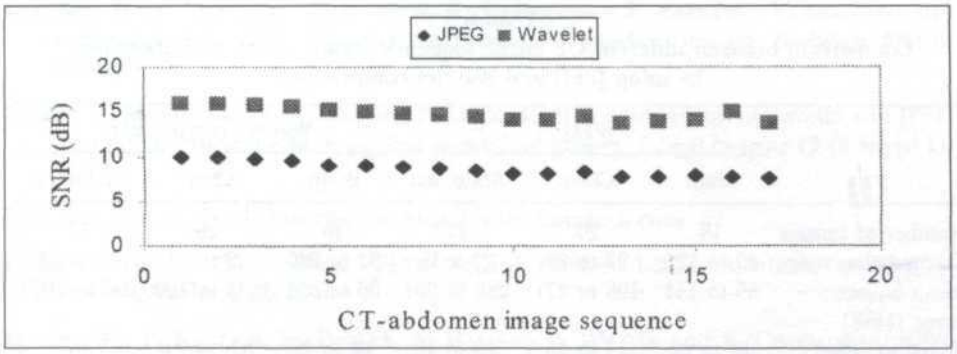

Fig. 10: SNR against CT-abdomen image sequence for JPEG and Wavelet compression

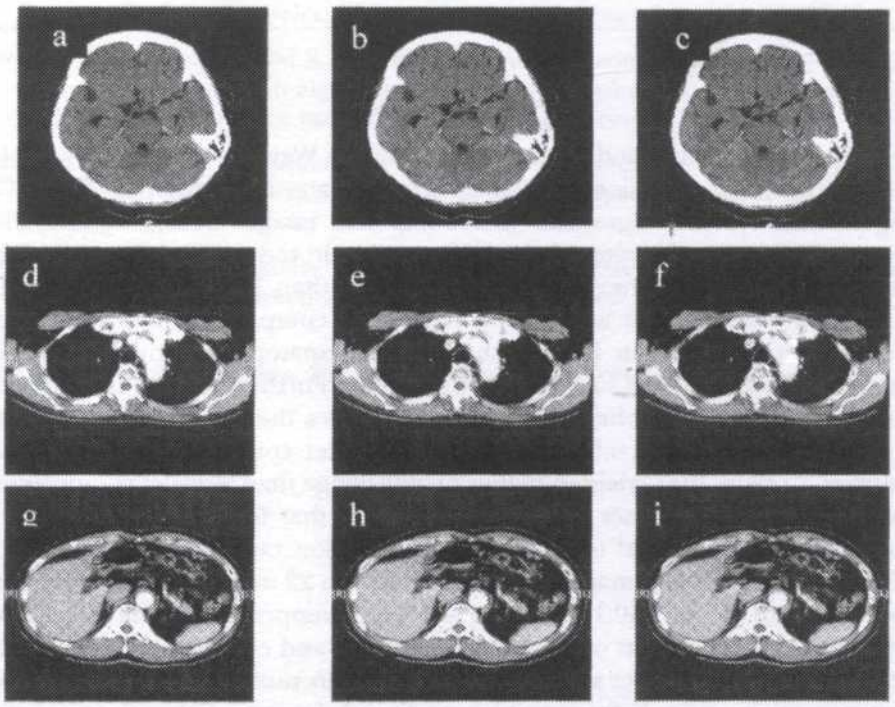

Fig. 11: Subjective comparison between different CT images
a) Original CT- brain image, b) compression ratio 30:1, PSNR =31dB using JPEG,
c) Compression ratio 30:1, PSNR =31dB using wavelet, d) Original CT- chest image,
e) Compression ratio 15:1, PSNR =25.2dB using JPEG, f) Compression ratio 15:1,
PSNR=25.7dB using wavelet, g) Original CT- abdomen image,
h) Compression ratio 15:1, PSNR =33dB using JPEG,
i) Compression ratio 15:1, PSNR =26dB using wavelet

TABLE 7
Comparison between different CT image sequence (brain, chest, and abdomen) by using JPEG and Wavelet compression

	JPEG			Wavelet compression		
	Brain	Chest	Abdomen	Brain	Chest	Abdomen
Number of Images	18	20	17	18	20	17
Compression ratio	40 to 125	27 to 29	27 to31	52 to 240	29 to 31	30 to 33
Mean Square Error (MSE)	55 to 151	198 to 271	236 to 257	26 to 394	1033 to 1099	990 to 1077
Signal to Noise Ratio (SNR) dB	18 to 22	14 to 15	13 to 15	14 to 23	8.5 to 9.6	7 to 9
Peak Signal to Noise Ratio (PSNR) dB	26 to 30	23 to 24	24 to 24	22 to 34	17 to 18	17 to 18

CONCLUSION

From the results of this study we conclude that the Wavelet compression can be used at higher compression ratios before information loss than JPEG for CT images. The Wavelet algorithm introduces less image errors, which yields higher PSNR for low bit rate. We have shown that in terms of image quality, the Wavelet algorithm is either equivalent or better than JPEG for these images. Our results illustrate that we can achieve higher compression ratios for brain than chest and abdomen images and that the anatomical structure and its complexity have an effect on image compression. Furthermore we also observe that by using JPEG, for chest and abdomen images the PSNR values obtained were higher than those achieved by using Wavelet compression. For a lower compression ratio, JPEG yielded higher quality image than Wavelet compression. From the numerical values obtained we observe that for chest and abdomen images the PSNR is equal to 24 dB for compression ratio up to 31:1 by using JPEG, whereas for brain image the PSNR is equal to 22 to 34 dB for compression ratio between 52 to 240:1 by using Wavelet compression. The degree of compression is dependent on anatomic structures and complexity of diagnostic information in the image; so careful consideration must be given to the level of compression ratio before archiving clinical images. Otherwise essential information will be lost.

REFERENCES

BRADLEY, J. and M. D. ERICKSON. 2000. Irreversible compression of medical images Department of Radiology Mayo Foundation, Rochester, M. Accessed on November 2000. http://www.scarnet.org/pdf/SCAR%20White%20Paper.pdf

DAUBECHIES, I. 1988. Orthonormal bases of compactly supported wavelets. *Comm. Pure Appl. Math.* **41:** 909-96.

ERICKSON, B, A. MANDUCA, P. PALISSON, K. R. PERSONS, F. EARNEST, V. SAVCENKO and l. HANGIANDREOU. 1998. Wavelet compression of medical images. *Radiology* **206(3):** 599-607.

IYRIBOZ, T., M. ZUKOSKI, K. HOPPER and P. STAGG. 1999. A comparison of wavelet and JPEG lossy compression methods applied to medical images. *J. Digit Imaging* **12** (2 Suppl 1): 14-17.

LURA TECH GMBL. 2000. Available at http://www.Luratech.com

Pegasus Imaging Corporation (JPEG wizard version 1.3.7). Available at http://www.pegasusimaging.com

PERSONS, K., P. PALLISON, M. PATRICE, A. MANDUCA, J. WILLIAN and E. CHARBONEAU. 2000. Ultrasound grayscale image compression with JPEG and Wavelet techniques. *J. Digit Imaging* **13(1):** 25-32.

SAFFOR, A., R. RAMLI and NG. KWAN. 2001. A comparative study of image compression between JPEG and Wavelet. *Malaysia Journal of Computer Science* **14 (1)**: 39-45.

SAVCENKO, V., B. ERICKSON and K. PERSONS. 2000. An evaluation of JPEG and JPEG 2000 irreversible compression algorithms applied to neurologic computed tomography and magnetic resonance images. *J. Digit Imaging* **13** (suppl 1): 183-185.

SLONE, R. *et al.* 2000. Assessment of visually lossless irreversible image compression: Comparison of three methods by using an image-comparison workstation. *Radiology* **215:** 543-553.

STEPHEN, K. and J. D. THOMPSON. 2000. Performance analysis of a new semi orthogonal spline wavelet compression algorithm for tonal medical images. *Med. Phys.* **27:** 276-288.

Wavelet Compression Engine. 2000. Available at http://www.cengines.com.

Pertanika J. Sci. & Technol. 11(2): 205 - 217 (2003)
ISSN: 0128-7680

Heat Treated Hydrotalcite as Support for Lipase Immobilization

Siti Salhah Othman[1], Mahiran Basri[1*], Mohd. Zobir Hussein[2], Taufiq Yap Yun Hin[2], Mohd. Basyaruddin Abd. Rahman[1], Raja Noor Zaliha Abd. Rahman[1] & Abu Bakar Salleh[1]

[1]Centre for Research in Enzyme & Microbial Technology, Fakulti Sains & Pengajian Alam Sekitar, Universiti Putra Malaysia, 43400 UPM, Serdang, Selangor, Malaysia

[2]Jabatan Kimia, Fakulti Sains & Pengajian Alam Sekitar, Universiti Putra Malaysia, 43400 UPM, Serdang, Selangor, Malaysia

E-mail: mahiran@ fsas. upm. edu.

Received: 6 December 2001

ABSTRAK

Hidrotalsit (HT) dan hidrotalsit terawat haba (HTHT) dengan Mg^{2+}: Al^{3+} pada nisbah 4 telah disediakan melalui kaedah pemendakan bersama melalui penggoncangan secara berterusan dan pemanasan pada 200°C. Dari corak belauan sinar-X bahan-bahan ini, didapati bahawa hidrotalsit telah berjaya disintesis dan struktur berlapis gandanya tidak terurai oleh pemanasan kepada 200°C. Lipase daripada *Candida rugosa* kemudiannya disekat gerak kepada bahan ini melalui kaedah penjerapan fizikal. Didapati bahawa peratus kandungan protein meningkat daripada HT (20%) kepada HTHT (40%). Keaktifan lipase yang tersekat gerak diuji melalui tindak balas esterifikasi di antara asid oleik dan butanol di dalam heksana. Enzim tersekat gerak ini kemudiannya dicirikan dari segi kestabilan terhadap suhu, pelarut (heksana) dan penyimpanan. Kestabilan lipase tersekat gerak didapati lebih tinggi jika dibandingkan dengan lipase asli (NL).

ABSTRACT

Hydrotalcite (HT) and heat treated hydrotalcite (HTHT) with Mg^{2+}:Al^{3+} of ratio 4 were prepared by co-precipitating through continuous agitation and heating to 200 °C, respectively. From the X-ray diffraction patterns of these materials, it was found that hydrotalcite had been successfully synthesized and the layered structure was not collapsed by the heat treatment up to 200°C. Lipase from *Candida rugosa* was then immobilized onto these materials, through the physical adsorption method. It was found that percentage of protein loading increases from HT (20%) to HTHT (40%). Their activities were tested by the esterification reaction of oleic acid and butanol in hexane. The immobilized enzymes were then characterized in terms of their thermal, solvent (hexane) and storage stability. Their various stabilities were comparatively higher than native lipase (NL).

Keywords: Lipase, immobilization, hydrotalcite, heat treatment, esterification, stability

INTRODUCTION

Knowledge on lipase has increased especially in the areas of molecular structure and mechanism of action. Their wide applications are often centered on its ability to catalyze hydrolytic reactions in an aqueous medium and the reverse esterification reaction in organic solvents where ester bonds are formed (Kirchner *et al.* 1985). Lipases have been isolated from a wide variety of mammalian and microbial sources and are commercially available in quantity. In mammals, pancreatic lipase are involved in the digestion of dietary fat (Lin *et al.* 1982). *Candida rugosa* is an example of a microbial lipase, which hydrolyses all ester bonds of natural or synthetic triacylglycerols and have been widely used in the complete hydrolysis of fats as well as in the esterification reactions. Besides that, it is also known as a highly stereoselective enzyme which catalyses stereoselective esterification as well as transesterification reaction in organic medium (Triantafyllou *et al.* 1993).

However, soluble forms of lipase were reported to have low operational range and stability (Basri *et al.* 1995). In order to ease these problems, methods of immobilization of enzymes onto insoluble materials were introduced and this has formed the basis of many biotechnological processes and analytical devices. Immobilization not only eases enzyme-product separation, but also allows enzyme recyclability and persistency of its functional activities that help to bring about the increased stability of an enzyme (Fagain 1997). This has been proven, as most immobilized enzymes of various sources have been found, applicable in the pharmaceutical, cosmetic, fragrance and flavour industries (Basri *et al.* 1996).

Hydrotalcite or layered double hydroxides (LDH) is the most common member of the group of minerals known as the LDH or the so called anionic clays. It consists of layers of M^{II} and M^{III} cations with a similar layered structure to that of brucite, $Mg(OH)_2$ with Mg octahedrally surrounded by six oxygens in the form of hydroxides with the octahedral units forming infinite sheets. These sheets are then stacked together through hydrogen bonding forming layers of hydroxides (Carlino and Hudson 1995).

Hydrotalcite has long attracted interest in the variety of areas of physics, chemistry, biology and material sciences. They possess many properties comparable to clay but also add new and interesting applications (Mitchell 1990). Its heat treated and intercalated derivatives are new materials known to have extensive use and applications in areas of gas separations, pharmaceutical science, catalysis (Miyata and Hirose 1978; Miyata and Kumura 1973), anion exchanger and adsorbents (Meyn *et al.* 1990; Miyata 1983). In this study, hydrotalcite and heat treated hydrotalcite were synthesized. It was then used as support for lipase immobilization. They were then characterized and their activities were investigated.

MATERIALS AND METHODS

Lipase from *Candida rugosa* (Type VII) was purchased from Sigma Chemicals, Germany. $Al(SO_4)_3.17H_2O$, $MgSO_4.8H_2O$ were purchased from Hamburg, Germany, while $NaCO_3$ and NaOH were supplied by Fluka, Switzerland and Mallickrodt, Mexico. Substrates, oleic acid and butanol were from BDH Laboratory, England and J. T. Baker, U.S.A. All reagents and solvents used were of highest analytical grade.

Synthesis of Hydrotalcite

Mg-Al-CO_3 hydrotalcite were prepared following an aqueous precipitation and thermal crystallization method described by Reichle (1985). In this synthesis, 100 mL of a solution containing 0.25 M of $MgSO_4.8H_2O$ and 0.06 M of $Al_2(SO_4)_3.17H_2O$ was added dropwise over a vigorously stirred 100 mL solution containing NaOH (3.5 M) and Na_2CO_3 (1.0 M). The slurry obtained was aged at 65 °C for 18 h in a water bath (Memmert GmbH, Germany). After it was cooled, it was then filtered and washed with a copious amount of distilled water until the pH of the washing was neutral. The resulting white solid was dried at 120 °C for 24 h before being ground in a pestle and mortar. Powder of the refined solid (HT) was characterized using X-ray diffractometer (Siemens D-5000, Germany) with Ni filtered, CuKa radiation at 40 KV and 20 mA. The samples were mounted on glass slides and scanned at 2°-65° with 2θ/min at 0.003°. General features that are typical of all hydrotalcite are the sharp and intense lines at the low values of the 2θ angles at about 7-8 Å.

Surface characterization of the materials was carried out by nitrogen gas adsorption-desorption at 77 K using a Micromeretics ASAP 2000. Prior to the adsorption of nitrogen gas, the samples were out-gassed to at least 5×10^{-3} mm Hg in an evacuation-heated chamber at 120 °C, overnight.

The surface area and pore size distribution were calculated using Brunauer, Emmett and Teller (BET), and Brunauer, Johner and Halenda (BJH) equation, respectively. The specific total pore volumes were estimated from the nitrogen uptake at $P/P_o = 0.99$ (Gill and Montes 1994).

Preparation of Heat Treated Hydrotalcite

The powder (HT) was heated in a quartz furnace (Carbolite, Sheffield, England) for 5 h at 200 °C. Powder of HTHT was characterized as stated above.

Partial Purification of Lipase

Partial purification by water extraction was carried out by dissolving 1.5 g of crude commercial lipase from *Candida rugosa* (Type VII) in 15.0 mL of distilled water. The mixture was stirred for 30 min and centrifuged at 10000 rpm for 15 min. The undissolved solid suspension was discarded after centrifugation while the supernatant was used as partially purified lipase and stored at -20°C prior to use.

Immobilization of Lipase

The supernatant (15.0 mL) was added to 2.0 g of hydrotalcite. The mixture was incubated at room temperature for 1 h in a horizontal waterbath shaker with continuous shaking at 100 rpm. The lipase-immobilized hydrotalcite was separated from the supernatant by filtering through Whatman no. 1 filter paper. The immobilized enzymes were then lyophilized in a freeze drier (Labconco 195, Kansas City, England). Percentage of protein immobilized is calculated based on the total protein used (100%) in the immobilization reaction.

Protein Assay

The amount of protein was determined by Bradford method (Bradford 1976), with Coomassie brilliant blue assay, using bovine serum albumin as standard. In a typical protein assay, lipase solution (100 µL; 0.1 g/mL) was mixed with Bradford reagent (5.0 mL). The protein concentration was determined spectrophotometrically at a wavelength of 595 nm using the calibration curve of bovine serum albumin.

Activity Assay

The reaction system consisted of 2.0 mL hexane, 4.0 mmole 1-butanol, 2.0 mmole oleic acid and 0.3 g immobilized lipase or 50 mg of native lipase. The mixture was incubated at 30°C for 5 h with continuous shaking at 150 rpm. Reaction was terminated by dilution with 3.5 mL ethanol:acetone (1:1 v/v) and the remaining free fatty acid in the reaction mixture was determined by titration with 0.15 M NaOH using an automatic titrator (ABU90, Radiometer, Copenhagen) to an end point of pH 10.0. The activities were expressed as mmol/min/mg protein using the Equation (1) below:

$$\text{Esterification Activity} = \left[\frac{(V_c - V_s)M] \div t}{W}\right] \quad (1)$$

Whereby, V_c – titration volume of the control (mL)
V_s – titration volume of the sample (mL)
M – molarity of NaOH
t – time (min)
W – amount of protein

Effect of Temperature on the Esterification Activity

To investigate the most suitable temperature for the esterification reaction, the reaction mixtures were incubated at different temperatures (30, 40, 50, 60, 70°C) for 5 h with continuous shaking at 150 rpm. The residual esterification activities were determined. The relative activities were expressed as percentages of the activities at different temperatures as compared to the activity at optimum temperature (40°C).

Thermal Stability

Enzymes were incubated at various temperatures (30, 40, 50, 60, 70°C) in sealed vials for 1 h. The enzymes were left to cool at room temperature before determination of esterification activity was carried out. The activities were expressed as percentages of the relative activities at different temperatures compared to the activity of the untreated enzyme.

Leaching Study

To investigate the effect of washing on the immobilized lipase, 0.3 g of immobilized lipase were carefully washed with increasing amount of hexane (4.0, 8.0, 12.0, 16.0, 20.0 mL) with 4.0 mL at each wash. The activities of the immobilized lipase at each volume of hexanes were determined by esterification reaction. The activities of the lipases were expressed as percentages of the relative activities at different wash cycle compared to the activity of the unwashed enzyme.

Stability in Organic Solvent

To investigate the stability of the immobilized enzyme in organic solvent, they were incubated in hexane at room temperature from day one to day ten. After the incubation, their residual activities were determined at 30 °C. The residual activities were expressed as percentages of their activity at the different time intervals compared to the activity at day one.

Storage Stability

This study was conducted to investigate the stability of native lipase compared to immobilized lipases at different storage temperature. The enzymes were kept for 60 days. The residual activities were determined and expressed as percentages of the residual activities at 60 days compared to the initial activity at day one.

RESULTS AND DISCUSSION

Analysis of Hydrotalcite

Powder XRD patterns of HT and HTHT, are shown in *Figs. 1(a)* and *1(b)*, respectively. The patterns show that pure hydrotalcite phase was obtained. The basal spacing of HT and HTHT are similar, indicating that the layered structure of the material is still maintained and non-collapsed even after heat treatment at 200°C for 5 h. However, further heating at higher temperature leads to intensity decay of hydrotalcite and collapse of the layered structure.

Figs. 2 and *3* show the pore size distribution of HT and HTHT. A sharp pore size distribution peaks were observed for both. This sharp maximum is associated with a dip in the desorption isotherm which is not reflected in the adsorption isotherm. Such a feature is a characteristic of the laminar clay-like structure as expected from the known structure of hydrotalcite. As heat treatment proceeds this peak decreases in intensity together with gradual changing of shape to a wider one (Hussein *et al.* 1995).

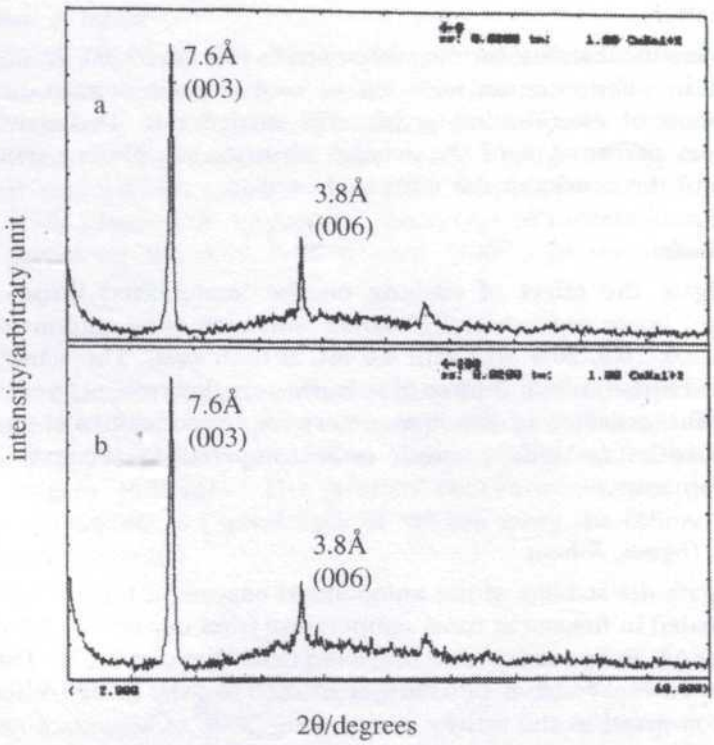

Fig. 1: (a) XRD pattern of Hydrotalcite (HT) prepared at ratio (Mg^{2+}:Al^{3+}) 4, (b) XRD pattern of Heat Treated Hydrotalcite (HTHT) prepared at ratio (Mg^{2+}:Al^{3+})4

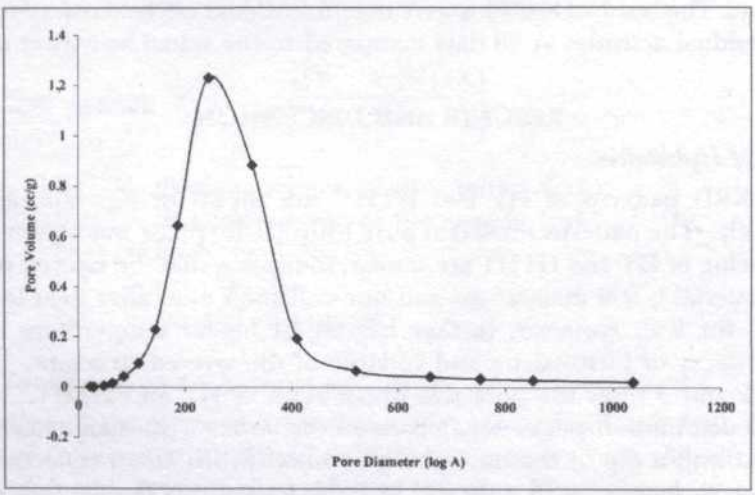

Fig. 2: Pore size distribution of Hydrotalcite (HT) of Mg^{2+}:Al^{3+} prepared at ratio 4

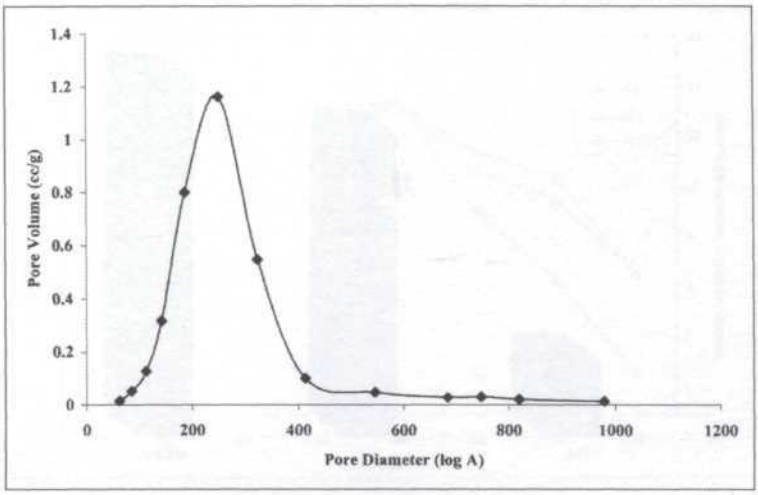

Fig. 3: Pore size distribution of Heat Treated Hydrotalcite (HTHT) of Mg^{2+}:Al^{3+} prepared at ratio 4

TABLE 1
BET surface area, micropore volume and BJH desorption pore size distribution of HT and HTHT of Mg^{2+}:Al^{3+} prepared ratio 4

LDH	BET Surface Area (m^2/g)	Micropore Volume (cc/g)	BJH Desorption (Å)
HT	53.8	0.0007	228
HTHT	62.0	0.0025	139

Summary of the BET surface area, micropore volume and BJH desorption pore size distribution of these materials are shown in Table 1.

Immobilization of Lipase

In a typical immobilization of lipase on HT and HTHT, the percentages of protein immobilized were 20% and 40%, respectively. The increase in protein immobilized on HTHT as compared to on HT is in accordance with the surface area and porosity of the materials. When the surface area of the materials increases, more protein can be adsorbed. Similarly, as heat treatment eliminates water molecules from the interlayers of the materials, larger space is obtained between the brucite sheets of the materials. This then allows more enzyme molecules to enter the interlayers.

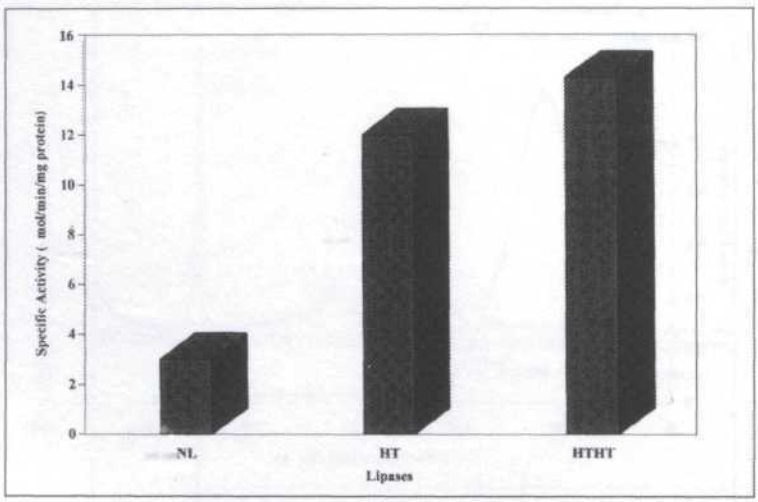

Fig. 4: Specific of immobilized (HT and HTHT) and Native (NL) lipases in the effect of heat treatment

Specific Activities of Immobilized Lipase and Native Lipase

From the plot in *Fig. 4*, HTHT seemed to have the higher specific activity compared to HT. Their specific activities are significantly higher than native lipase (NL). This shows that immobilization increases the specific activity of lipases and immobilization on the heat-treated hydrotalcite further increase lipase specific activity. In this study, the amount of the protein used was kept constant for all the enzymes. Thus, the higher activity in the immobilized lipases as compared to the native lipase may be due to the immobilized lipases being more active and stable in organic solvents. The higher activity in HTHT as compared in HT could be due to the large amount of enzymes being trapped in HTHT, with better porosity.

Effect of Temperature on the Esterification Activity

In *Fig. 5*, activities of the immobilized and native lipase were increased at temperatures between 30°C and 40°C. However, drastic decrease in activity occurred after 50°C especially for native lipase. Activities of lipase were low at 30°C which may be due to the diffusion limitation of reactant caused by increase in reactant viscosity at low temperature. The optimum temperature was at 40°C for both native and immobilized lipases. This shows that immobilization did not alter the general character of the lipase. Among these enzymes, lipase immobilized onto HTHT seemed to protect the enzyme best against denaturation by heat.

According to Fagain (1997), lipases suffer denaturation at higher temperatures. This is due to the reactivation of the peptide bonds and amino acid side chains, which causes them to participate in deleterious reactions at

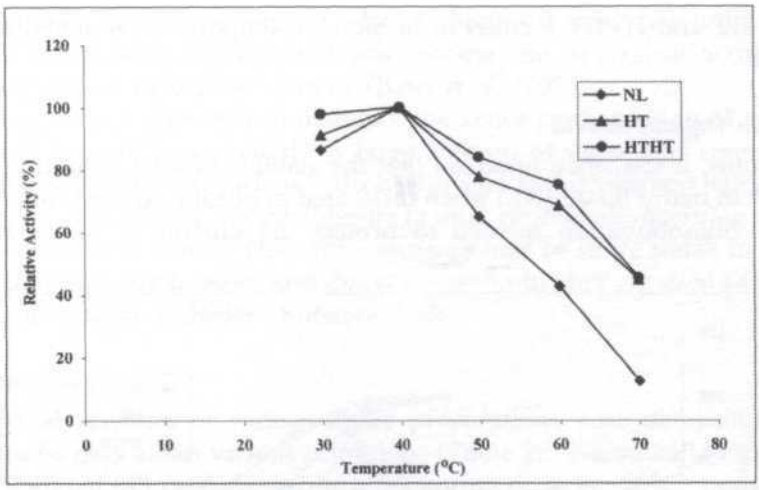

Fig. 5: Effect of temperature on esterification activity of native (NL) and immobilized (HT, HTHT) lipases

higher temperatures. This then causes the weak stabilizing interactions and a built-up conformational stability in an enzyme to be destroyed. In order to overcome this problem, lipase requires ample conformational mobility that it can achieve through immobilization or attachment on flexible solid support.

Thermal Stability

Stability of lipases immobilized onto HT and HTHT, is shown in *Fig. 6.* The derivatised lipase preparations were significantly more thermostable than native lipase even after 1 h of incubation at temperatures between 30°C to 70°C. Among these, lipase immobilized onto HTHT show highest thermal stability.

At temperatures above 30°C, enzyme resistance to adverse heat influences and persistency of its molecular integrity to face denaturants were weakened. This denaturation happens when a fully functional monomeric enzyme looses its biological activity in vitro by the unfolding of its tertiary structure to a disordered polypeptide. At this point, the key residues are no longer aligned closely enough for continued participation in functional or structure stabilizing interactions.

Immobilization had however increased thermal stability of lipase. Although heat considerably reduce conformational flexibility of native and immobilized lipase, immobilized lipase is still capable of performing its vibrational and more complex movement required for efficient catalytic activity.

Leaching Study

The immobilized lipase preparations retained their catalytic activities at 100% even after 5 washing cycles. This indicated that lipase from *C. rugosa* remained immobilized to HT and HTHT even after careful washing with 20 mL of

hexane. HT and HTHT seemed to be suitable supports for immobilization of enzymes.

Stability in Organic Solvent

In this study, it was again observed that the stability of immobilized lipase was higher than native lipase (NL) when incubated in hexane, at room temperature (*Fig. 7*). Immobilization seemed to protect the enzyme from denaturation

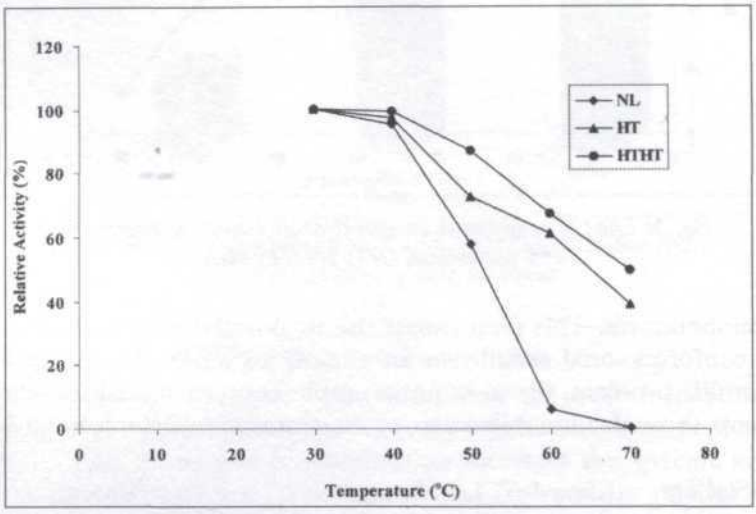

Fig. 6: Thermal stability of native (NL) and immobilized (HT, HTHT) lipases

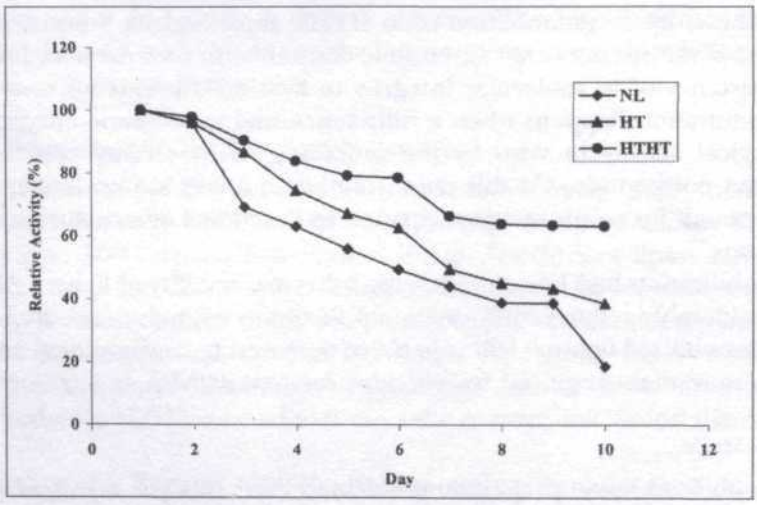

Fig. 7: Solvent stability of native (NL) and immobilized (HT, HTHT) lipases incubated in hexane at room temperature (26.5°C)

caused by the presence of organic solvent. Supports used may induce water molecules surrounding lipase, which was necessary for its catalytic activity from being stripped off by organic solvent (Basri *et al.* 1997).

Although water is needed to maintain the active conformation of enzymes, only a thin layer of it is needed. A large amount of water may result in the undesirable side reactions such as hydrolysis of acid anhydrides and halogenates. Furthermore, thermodynamic equilibrium of most processes concerning enzymes are unfavourable in water. Therefore, enzymes may be more stable in organic solvents than they are in water and this is a reason why they are used as reaction medium in catalytic activities (Klibanov 1986).

Storage Stability

The residual activities of various lipase preparations were determined after storing for 60 days under various conditions (Table 2). Native and immobilized lipases exhibited full catalytic activity after storing them at –20°C. Immobilized lipases retained their full catalytic activity when stored at 0°C. At very low temperatures, the lipase is probably locked in its native, catalytically active conformation. When stored at higher temperatures, immobilized lipases showed increase storage stability compared to native lipase. At these temperatures, the stabilization may be owing to multipoint attachment of the enzymes to the supports, creating a more rigid enzyme molecule. Hence, disruption of the active center becomes less likely to occur (Basri *et al.* 1994).

TABLE 2
Storage stability of native (NL) and immoblized (HT, HTHT) lipases after being incubated for 60 days at different storage conditions

Lipases	Residual Activity (%)			
	RT	4°C	0°C	-20°C
NL	26	36	70	100
HT	72	78	100	100
HTHT	75	82	100	100

- 100% is based on the initial synthetic activity of lipases using butanol and oleic acid.

CONCLUSION

The immobilization of lipase was successfully carried out, referring to the increase in activity and stabilities of the native lipase (NL) after immobilization. HTHT used seemed to meet the requirements of a suitable support and had satisfied a number of criteria as it allows easy lipase immobilization without having to loose its catalytic activity due to the large pore size and most importantly, it can be obtained through simple and inexpensive methods.

ACKNOWLEDGMENT

This project was financed by Universiti Putra Malaysia.

REFERENCES

Basri, M., K. Ampon, W. M. Z. W. Yunus, C. N. A. Razak and A. B. Salleh. 1994. Stability of hydrophobic lipase derivatives immobilized on organic polymer beads. *Appl. Biochem. Biotechnol.* **48**: 173-183.

Basri, M., K. Ampon, W. M. Z. W. Yunus, C. N. A. Razak and A. B. Salleh. 1995. Enzymic synthesis of fatty esters by hydrophobic lipase derivatives immobilized on to organic polymer beads *J. Am. Oil. Chem. Soc.* **72**: 407-411.

Basri, M., W. M. Z. W. Yunus, S. Y. Wong, K. Ampon, C. N. A. Razak and A. B. Salleh. 1996. Immobilization of lipase from *Candida rugosa* on synthetic polymer beads for use in the synthesis of fatty esters. *J. Chem. Technol. Biotechnol.* **66:** 169-173.

Basri, M., K. Ampon, W. M. Z. W. Yunus, C. N. A. Razak and A. B. Salleh. 1997. Enzymatic synthesis of fatty esters by alkylated lipase. *J. Molec. Catal. B : Enzymatic* **3**: 171-176.

Bradford, M. M. 1976. A rapid and sensitive method for the quantification of microgram quantities of protein utilizing the principle of protein dye binding. *Anal. Biochem.* **72**: 581-590.

Carlino, S. and M. J. Hudson. 1995. Thermal intercalation of layered double hydroxides: Capric acid into an Mg-Al LDH. *J. Mater. Chem.* **5(9)**: 1433-1442.

Fagain, C. O. 1997. Manipulating protein stability. In *Stabilizing Protein Functions.* p. 67-191. Berlin, Heidelberg, New York: Springer.

Gill, A. and M. Montes. 1994. Effect of thermal treatment on microporous accessibility in aluminium pillared clays. *J. Mater. Sci. Lett.* **4(9)**: 1494-1496.

Hussein, M. Z., Z. Zainal and H. H. Swee. 1995. Scanning electron microscopy and surface area studies of calcined ZnCrCl layered double hydroxides. *J. Mater. Sci. Lett.* **14**: 1747-1750.

Kirchner, G., M. Scollar and A. M. Klibanov. 1985. Resolution of racemic mixture via lipase catalysis in organic solvents. *J. Am. Chem.* **107**: 7072-7076.

Klibanov, A. M. 1986. Enzymes that work in organic solvents. *Chemtech* June: 354-359.

Lin, Y. H., R. A. Moreau and A. C. Huang. 1982. Involvement of glyoxysomal lipase in the hydrolysis of storage triacylglycerol in the cotyledons of soy bean seedlings. *Plant Physiol.* **70**: 108-112.

Meyn, M., K. Beneke and G. Lagaly. 1990. Anion-exchange reactions of layered double hydroxides. *Inorg. Chem.* **29:** 5201-5207.

Mitchell, V. I. 1990. *Pillared Layered Structures, Current Trends and Applications.* p. 151-201. Amsterdam: Elsevier Applied Science.

Miyata, S. and T. Hirose. 1978. Adsorption of N_2, O_2, CO_2 and H_2 on hydrotalcite-like system: Mg^{2+}-Al^{3+}-$Fe(CN)_6^{4-}$. *Clays and Clay Minerals* **26**: 441-447.

MIYATA, S. and T. KUMURA. 1973. Synthesis of new hydrotalcite-like compounds and their physico-chemical properties. *Chem. Lett.* :843-848.

MIYATA, S. 1983. Anion-exchange properties of hydrotalcite-like compounds. *Clays and Clay Minerals* **31**: 305-311.

REICHLE, W. T. 1985. Catalytic reactions by thermally activated, synthetic, anionic clay minerals. *J. Catal.* **94** : 547-557.

TRIANTAFYLLOU, A. O., P. ADLERCREUTZ and B. MATTIASSON. 1993. Influence of the reaction medium on enzyme activity in bio-organic synthesis: Behaviour of lipase from *Candida rugosa* in the presence of polar additives. *Biotechnol. Appl. Biochem.* **17:** 167-179.

ISSN: 0128-7680
Pertanika J. Sci. & Technol. 11(2): 219 - 228 (2003)

Effect of Particle Size and Compression Pressure on Thermal Diffusivity of Polyaniline (Emeraldine Base and Emeraldine Salt) Measured by a Photoflash Method

L. Y. C. Josephine, W. Mahmood Mat Yunus & Teh Chze Ling
Department of Physics
Faculty of Science and Environmental Studies
Universiti Putra Malaysia
43400 UPM, Serdang, Selangor, Malaysia

Received: 15 January 2002

ABSTRAK

Polyaniline merupakan salah satu polimer pengkonduksi yang baik telah menarik perhatian ramai selama beberapa tahun kebelakangan ini disebabkan kestabilan alam sekitar, kekonduksian yang baik pada suhu bilik dan penggunaannya yang berpotensi dalam bidang industri elektronik dan mikroelektronik. Dalam kajian ini, kami melaporkan kesan saiz zarah dan tekanan pemampatan terhadap nilai peresapan terma bagi sampel emeraldine base dan emeraldine salt (polyaniline). Sampel kajian telah disediakan dengan menggunakan saiz zarah yang berbeza dan ditekan kepada bentuk kepingan bulat pada tekanan yang berbeza. Pengukuran peresapan terma dilakukan pada suhu bilik (25°C) dengan menggunakan teknik sinaran lampu kilat. Nilai peresapan terma bagi sampel emeraldine base dan emeraldine salt yang diukur adalah masing-masing dalam ranj (1.52 hingga 1.79) × 10^{-3}cm^2/s dan (1.37 ke 1.56) × 10^{-3}cm^2/s. Kami mendapati bahawa peresapan terma bagi emeraldine base dan emeraldine salt meningkat secara linear terhadap tekanan yang dikenakan. Untuk kedua-dua kes, nilai peresapan terma juga meningkat apabila saiz zarah menjadi semakin kecil. Morfologi dan struktur sampel polyaniline (emeraldine base dan emeraldine salt) telah dianalisis dengan menggunakan Pengimbas Elektron Mikroskop (SEM), Belauan Sinar X (XRD) dan Pengukuran Transformasi Fourier Inframerah (FTIR).

ABSTRACT

Polyaniline as one of the most promising conducting polymers has attracted much attention for many years due to its excellent environmental stability, good conductivity at room temperature and other potential applications in electronic and microelectronic industries. In this paper we report the effect of particle size and compression pressure on thermal diffusivity of emeraldine base and emeraldine salt polyaniline samples. The samples were prepared using different particle size and pressed to a pallet form at different pressure. The measurement was carried out at room temperature (25°C) using a photoflash technique. The measured thermal diffusivity of emeraldine base and emeraldine salt were in the ranges (1.52 to 1.79) × 10^{-3}cm^2/s and (1.37 to 1.56) × 10^{-3}cm^2/s respectively. We found that the thermal diffusivity of the emeraldine base and emeraldine salt increases linearly with the applied pressure. For both, the thermal diffusivity value increases when the particle size became smaller. The morphology and structure of polyaniline samples (emeraldine

base and emeraldine salt) were analyzed from Scanning Electron Microscope (SEM), X-Ray Diffraction (XRD) and Fourier Transform Infrared (FTIR) measurements.

Keywords: Thermal diffusivity, photoflash, emeraldine base, emeraldine salt, particle size

INTRODUCTION

Polyaniline has emerged as a potential conductive material due to its comparatively good environmental stability, easy preparation and wide areas for its applications such as rechargeable batteries, electromagnetic interference shielding, light emitting diodes, display devices and biosensors (Campos *et al.* 1999).

The electronic properties of polyaniline can reversibly be controlled by protonation as well as by redox doping. Therefore, polyaniline could be visualized as a combination of reduced {–NH–B–NH–} and oxidized {–N=Q=N–} repeat units where –B– denotes a benzenoid and =Q= denotes a quinoid unit respectively. Depending upon the oxidation state of nitrogen atoms which exist as amine or imines configuration, polyaniline can adopt various structures such as leucoemeraldine (fully reduced form), emeraldine base (50% oxidized form), pernigraniline (fully oxidized form) and protonated form which is the conducting emeraldine salt (Toyoda and Nakamura 1995).

The emeraldine base (*Fig. 1*) form of Polyaniline can be converted from an insulating to a "metallic" state if protons are added to the –N= sites while the number of electrons in the chain is held constant.

Exposure of the emeraldine base (EB) polymer to a protonic acid such as HCl causes a transformation to the emeraldine salts (ES) form of polyaniline as shown in *Fig. 2*. The salt polymer exhibits metallic properties including Pauli susceptibility, a metallic thermopower, and free-carrier absorption typical of a

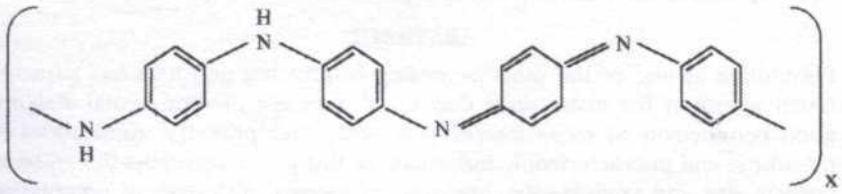

Fig. 1: Schematic illustration of emeraldeine base polymer (unprotonated)

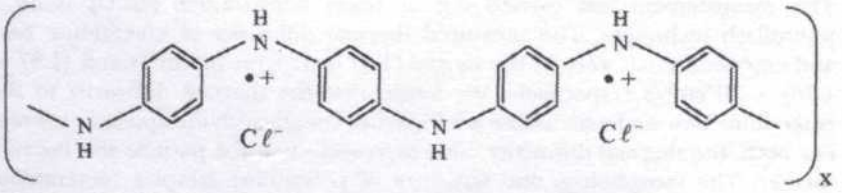

Fig. 2: Schematic illustration of emeraldine salt (fully protonated, x = 0.5)

metal (Zuo *et al.* 1989). After protonation, the conductivity increased about 10 orders of magnitude to a maximum value (10^1–10^2Scm^{-1}).

The thermal diffusivity, α, of a medium is the thermophysical property that determines the speed of the heat propagation by conduction during changes of temperature with time. The photoflash method is one of the most common ways to measure thermal diffusivity of a solid sample. It is based on depositing a very short energy pulse on the front face of a small disc shaped sample, and calculating its thermal diffusivity from the characteristic curve (thermogram) of the temperature excursion of its rear surface (Parker *et al.* 1961).

In this paper, we report the effect of particle size and applied pressure on the thermal diffusivity values of polyaniline samples (emeraldine base and emeraldine salt). Characterization of the emeraldine base and emeraldine salt have also been carried out using Scanning Electron Microscope (SEM), X-Ray Diffraction (XRD) and Fourier Transform InfraRed (FTIR) measurements.

EXPERIMENT

The emeraldine base and emeraldine salt powders were supplied by Zipperling Kessler & Co (Germany) with quoted particle size ranges from 3 to 100 μm. A sieve was used to separate the emeraldine powder into different particle size ranges (3–25 μm, 3–45 μm, and 3–100 μm). Emeraldine base and emeraldine salt powders in different particle sizes were placed into the 8.2 mm diameter mould to form a pallet shape sample by using a 12 HP pressing machine (Shi Chyan Electric Industrial & Co. Ltd). The compression pressure applied onto the mould was 250 psi, 450 psi, 650 psi, 850 psi and 1050 psi. The samples were then polished using abrasive silicone carbide to the desired thickness.

Thermal diffusivity analysis was carried out by a photoflash technique. Photoflash technique is a well–established method for measuring the thermal diffusivity, with very simple procedures in a wide temperature range. The photoflash technique setup used in the present experiment is schematically shown in *Fig. 3(a)*. *Fig. 3b* shows the ideal characteristic curve of the temperature measured at the rear surface of the sample.

Camera flash (Maxxum flash 5400HS) was used as energy pulse source in the photoflash technique to determine the thermal diffusivity of the sample. It was located 2 cm in front of the sample as shown in *Fig. 3(a)*. The photodiode was used to detect the pulse from the camera flash and subsequently triggered the digital oscilloscope. In this setup, a K-type thermocouple is used to monitor the temperature at the rear surface of the sample. The signal was then amplified by preamplifier (SR560) and was transferred to the oscilloscope. The signal was then analyzed for the thermal diffusivity using a personal computer. Every measurement was made at an interval of 10 min to allow the sample to be thermally.equilibrated with room temperature. All the measurements were carried out at room temperature (25°C).

For an opaque material, the temperature at the rear surface can be expressed as (Parker *et al.* 1961).

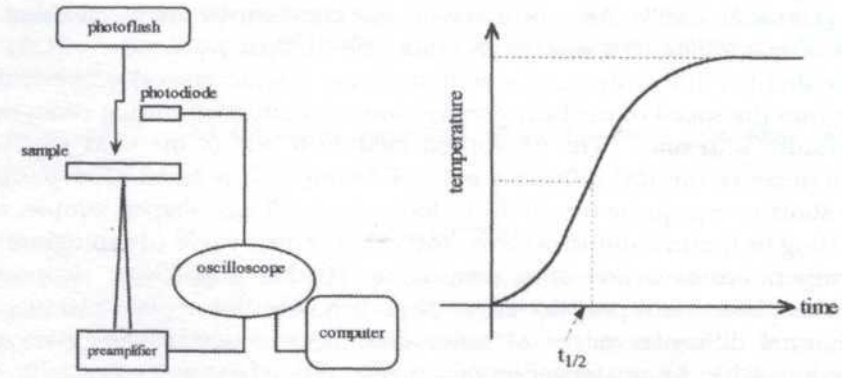

Fig. 3: a) Experimental set up b) Thermogram for ideal condition

$$T(L,t)=\frac{Q}{\rho C_p L}\left[1+2\sum_{n=1}^{\infty}(-1)^n \exp\left(-\frac{n^2\pi^2 at}{L^2}\right)\right] \quad (1)$$

where Q is the energy of the light pulse. L is the thickness of a sample, and t is the transient response time. C_p, ρ, and n are the specific heat, sample density and a positive integer. The term in a square bracket can be expressed as

$$V=\left[1+2\sum_{n=1}^{\infty}(-1)^n \exp\left(-\frac{n^2\pi^2 at}{L^2}\right)\right] \quad (2)$$

which represents a function of maximum temperature rise at the rear surface and varies from 0 to 1. The maximum temperature of the rear surface can be written as

$$T(L,t)_{max}=\frac{Q}{\rho C_p L} \quad (3)$$

Parker *et al.* (1961), who was the first, derived the basic and analytical solution, found out for ideal conditions, the thermal diffusivity of the material can be calculated as

$$\alpha=\frac{0.1388L^2}{t_{1/2}} \quad (4)$$

where $t_{1/2}$ is a characteristic time on the thermogram when the rear surface reaches one half of its final temperature. Numerous corrections have been introduced to account for radiative heat losses during the process, the finite width of the energy pulse, and other factors interfering with the experiment.

The effect of radiation heat loss at the rear surface can be calculated from the transient response curve by employing the ratio technique. Heat loss corrections should be based on Clark and Taylor rise-curve data or Cowan cooling-curve effect (Maglic and Taylor 1992).

The emeraldine base and emeraldine salt were also characterized by a computer–controlled x–ray diffractometer, XRD (Siemens D–5000) using CuK α radiation with a scanning speed of $2°min^{-1}$. The diffraction patterns of emeraldine base and emeraldine salt powders were obtained by scanning the samples with an interval of scanning angle (2θ) from 5° to 60°. The FTIR experiments were conducted by using fully computerized FTIR spectrometer (Perkin Elmer 1650). The surface morphology of the emeraldine base and emeraldine salt were investigated by using a scanning electron microscope, SEM (JEOL model 6400). The SEM samples were gold(sputtered prior to observation.

RESULTS AND DISCUSSION

In this experiment, the heat loss correction was calculated using the Clark and Taylor rise–curve (Maglic and Taylor 1992). The ratio $t_{0.75}/t_{0.25}$ is determined from the experimental data where $t_{0.75}$ and $t_{0.25}$ are the times to reach 75% and 25% of the maximum respectively. Then the correction factor, K can be calculated as:

$$K_R = -0.3461467 + 0.361578\left(\frac{t_{0.75}}{t_{0.25}}\right) - 0.06520543\left(\frac{t_{0.75}}{t_{0.25}}\right) \quad (5)$$

The corrected value of thermal diffusivity at the half(time will be

$$\alpha_{cor} = \frac{\alpha_{0.5} K_R}{0.13885} \quad (6)$$

Another situation which should be considered in this experiment is the finite pulse–effect. The pulse duration, τ for the camera flash (Maxxum flash) is 9 ms. According to Cape and Lehman (1963), when the width of the heat pulse $\tau \ll t_c$, where $t_c = \pi^2 L^2/\alpha$, finite pulse-time effect is negligible. In this experiment, the calculated ratio, τ / t_c for the emeraldine base and emeraldine salt are much smaller than 1 ($\tau/t_c \ll 1$), therefore the finite pulse time-effect in the present case is negligible.

Fig. 4 shows the thermal diffusivity as a function of pressure for different particle sizes of emeraldine base and emeraldine salt respectively. It was noted that the thermal diffusivity value for the emeraldine base and emeraldine salt

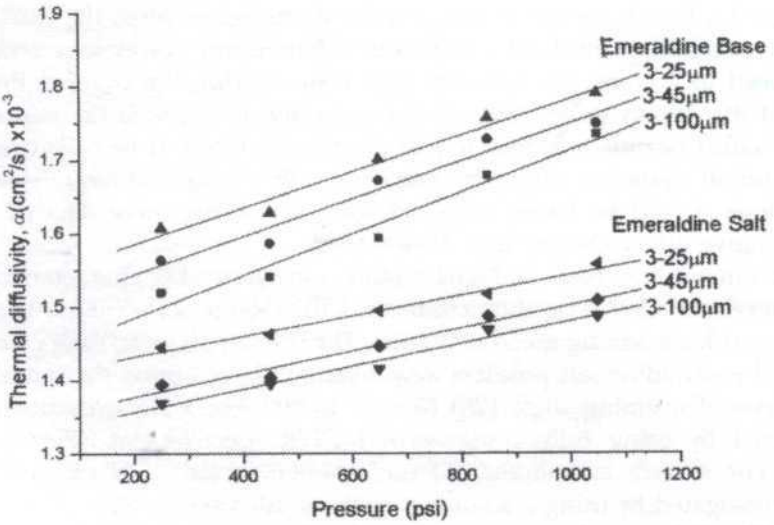

Fig. 4: Comparison between thermal diffusivity of emeraldine base and emeraldine salt at different pressure and different particle size

increased with the increasing of applied pressure. We also observed that the thermal diffusivity values increased when the particle size of the sample becomes smaller. This may be due to the fact that when the pressure increases, the inter-particle bonding becomes stronger and makes the molecules transferring heat better. Furthermore, when the particle size become smaller, the samples will have less porosity. It is also observed that the thermal diffusivity values of the emeraldine base are always higher than the thermal diffusivity of the emeraldine salt although emeraldine salt has a higher electrical conductivity value (Zipperling Kessler & Co Germany). That the electronic contribution to the total thermal conductivity can be considered small because the bulk material has a disordered structure and may contain an amount of impurities (Albuquerquey *et al.* 2000). The thermal diffusivity values obtained in the present measurement for both emeraldine base and emeraldine salt are listed in Table 1.

The XRD spectrum of the emeraldine base is shown in *Fig. 5*, where small peaks were observed, at $2\theta = 15°$, $20°$ and $25°$. Similar peaks were also observed for emeraldine salt. This shows that the degree of crystallinity of the sample is relatively low (Zilberman *et al.* 1977). Since the emeraldine base and emeraldine salt exhibit the same amorphous pattern, a comparison of the areas under the curves indicates that the emeraldine base is more crystalline than the emeraldine salt.

The FTIR spectra of polyanilines (emeraldine base and emeraldine salt) as a function of wavenumber (400 – 4000 cm^{-1}) were analysed and the peaks are listed in Table 2. It can be seen that the peaks shift towards the lower wavenumbers in the case of doped samples (emeraldine salt). This can be

TABLE 1
The corrected value of thermal diffusivity for emeraldine base and emeraldine salt

Pressure (psi)	Corrected Thermal diffusivity of Emeraldine base (3–25 μm) x 10^{-3} (cm^2/s)	Corrected Thermal diffusivity of Emeraldine base (3–45 μm) x 10^{-3} (cm^2/s)	Corrected Thermal diffusivity of Emeraldine base (3–100 μm) x 10^{-3} (cm^2/s)
250	1.61	1.56	1.52
450	1.63	1.59	1.54
650	1.70	1.67	1.59
850	1.75	1.73	1.68
1050	1.79	1.75	1.73
Pressure (psi)	Corrected Thermal diffusivity of Emeraldine salt (3(25μm) x 10^{-3} (cm/s)	Corrected Thermal diffusivity of Emeraldine salt (3(45μm) x 10^{-3} (cm/s)	Corrected Thermal diffusivity of Emeraldine salt (3(100μm) x 10^{-3} (cm/s)
250	1.44	1.39	1.37
450	1.46	1.40	1.39
650	1.49	1.45	1.41
850	1.52	1.49	1.47
1050	1.56	1.51	1.49

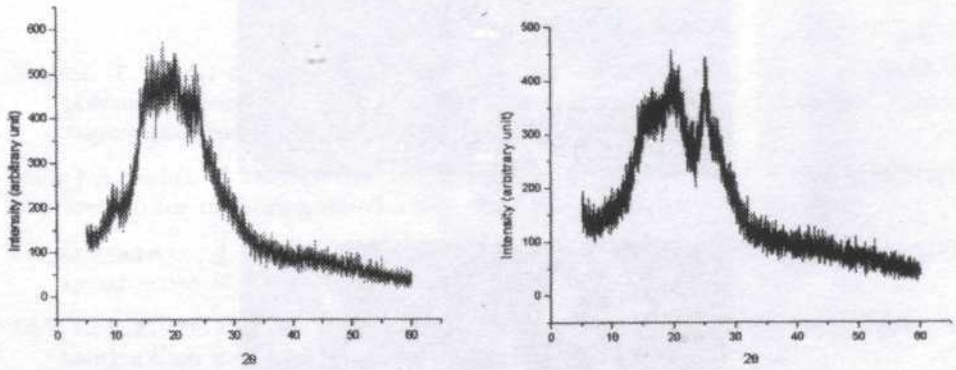

(a) (b)

Fig. 5: X-ray diffraction patterns, (a) emeraldine base (b) emeraldine salt

attributed to the protonation of imines nitrogen, resulting in the conversion of the quinoid ring into a benzenoid ring (Trchova *et al.* 1999, Mathur *et al.* 2001). For example, the absorption peak of the benzoid units in the emeraldine salt shifted from 1499 cm^{-1} to 1465 cm^{-1}. It might be one of the major reasons for the higher electrical conductivity of the doped polyaniline.

TABLE 2
Assignments of the main peaks in the FTIR spectra of PAni (EB) and PAni (ES)

Peak assignment	PAni(EB)	PAni (ES)
Bending of C–C on Q	–	510 cm^{-1}
Bending of C–C on B	–	589 cm^{-1}
Bending of C–C on B, Q	–	688 cm^{-1}
Bending of C–H (out(of(plane) of B (*para*–disubstituted)	832 cm^{-1}	799 cm^{-1}
Bending of C–H (in plane), mode of N=Q=N, Q=N^+H–B, B–N+H–B	1148 cm^{-1}	1121 cm^{-1}
Stretching of C–N^+	–	1229 cm^{-1}
Stretching of C_{ar}–N	1310 cm^{-1}	1298 cm^{-1}
Stretching of Q=N–B	1378 cm^{-1}	–
Stretching of N–B–N ring	1499 cm^{-1}	1465 cm^{-1}
Stretching of N=Q=N ring	1588 cm^{-1}	1559 cm^{-1}

B = benzenoid ring, Q = quinoid ring

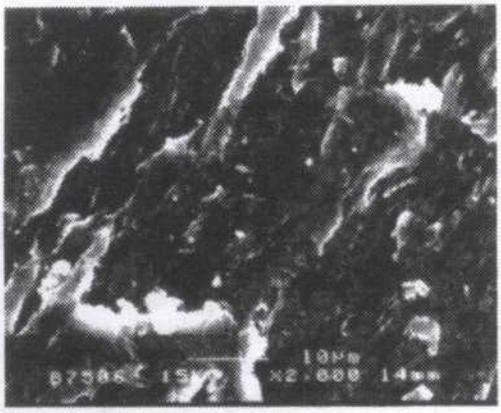

(a)

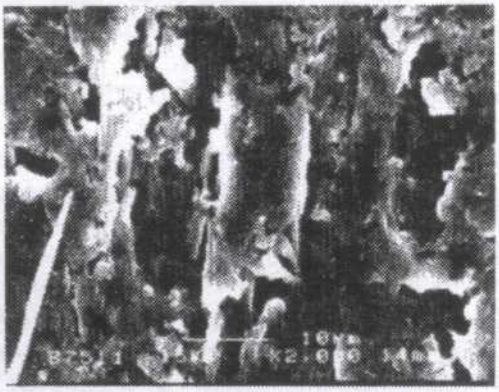

(b)

Fig. 6: (a) Micrograph of emeraldine base, (b) Micrograph of emeraldine salt

The morphologies of the sample surface at magnification of 2000X are shown in *Fig. 6.* Emeraldine salt (*Fig. 6a*) showed an irregular structure, with both large and small grains. Emeraldine salt also shows larger particles than those of emeraldine base (*Fig. 6b*). The larger particles in emeraldine salt may due to an excess of dopant that did not react with emeraldine base (Compas *et al.* 1999).

CONCLUSION

The thermal diffusivity of emeraldine base and emeraldine salt have been measured using a simple and inexpensive photoflash method at room temperature. The measured thermal diffusivity of emeraldine base and emeraldine salt were in the ranges (1.52 to 1.79)cm/s and (1.37 to 1.56)cm/s respectively. We found that the thermal diffusivity of the emeraldine base and emeraldine salt increases linearly with the applied pressure. It was observed that the sample with the smaller particle size gives the higher thermal diffusivity value.

ACKOWLEDGEMENT

The authors would like to thank MOSTE for financial support through IRPA grant (02-04-09-0065). We also like to thank Mr. Lim Chee Siog and Mr Lim Kean Pah for their helpful discussion particularly for the FTIR and XRD analysis.

REFERENCES

CAMPOS, T. L. A., D. F. KERSTING and C. A. FERREIRA. 1999. Chemical synthesis of polyaniline using sulphanilic acid as dopant agent into the reactional medium. *Surface and Coatings Technology* **122:** 3–5.

CAPE, J. A. and G. W. LEHMAN. 1963. Temperature and finite pulse(time effect in the flash method for measuring thermal diffusivity. *J. Appl. Phys.* **34**: 1909–1913.

DE ALBUQUERQUE, J. E., W. L. B. MELO and R. M. FARIA. 2000. Photopyroelectric spectroscopy of polyaniline films. *J. Poly. Sci.* **B 38**: 1294–1300.

FU Y. P., E. P. TEH, Z. A. WAHAB and W. M. M. YUNUS. 2000. Thermal diffusivity of polymer using a flash method. *J. Solid St. Sci. and Technol. Letter* **7**: 160–164.

L. DING, X. WANG and R. V. GREGORY. 1999. Thermal properties of chemically synthesized polyaniline (EB) powder. *Synthetic Metals* **104**: 73–78.

MAGLIC, K. D. and R. E. TAYLOR. 1992. The Apparatus for Thermal Diffusivity Measurement by the Laser Pulse Method. In *Compendium of Thermophysical Property Measurement Methods* **2:** 281–314. New York, London: Plenum Press.

MATHUR, R., D. R. SHARMA, S. R. VADERA and N. KUMAR. 2001. Doping of emeraldine base with the monovalent bridging iron oxalate ions and their transformation into nanostructured conducting polymer composites. *Acta Mater.* **49**: 181–187.

PARKER, W. J., R. J. JENKINS, C. P. BUTLER and G. L. ABBOT. 1961. Flash method of determining thermal diffusivity, heat capacity and thermal conductivity. *J. Appl. Phys.* **32**: 1679–1684.

TOYOTA, T. and H. NAKAMURA. 1995. Photoacoustic spectroscopy of polyaniline films. *Jpn. J. Appl. Phys.* **34**: 2907–2910.

TRCHOVA, M., J. STEJSKAL and J. PROKES. 1999. Infrared spectroscopic study of solid(state protonation and oxidation of polyaniline. *Synthetic Metals* **101**: 840–841.

ZILBERMAN, M., G. I. TITELMAN, A. SIEGMANN, Y. HABA, M. NARKIS and D. ALPERSTEIN. 1977. Conductive blends of thermally dodecylbenzene sulfonic acid–doped polyaniline with thermoplastic polymers. *J. Appl. Poly. Sci.* **60**: 243–253.

ZIPERLING KESSLER & Co Germany-ORMECON GmbH, Ferdinand-Harten-Str 7, D-22949 Ammersbek, Germany.

ZUO, F., M. ANGELOPOULOS, A. G. MACDARMID and A. J. EPSTEIN. 1989. A conductivity of Emeraldine polymer. *Phys. Rev.* **B 39**: 3570–3578.

ISSN: 0128-7680
Pertanika J. Sci. & Technol. 11(2): 229 - 236 (2003)

Evaluation of Some Proposed Methods for Protecting Bridge Substructure Using Physical Models

Thamer Ahmed Mohammed, Mohd. Saleh Jafaar, Waleed Abdul Malik Thanoon, Abdul Halim Ghazali, Megat Johari M. Mohd. Noor, Badronnisa Yusuf & Mohammed Salem

Civil Engineering Department, Faculty of Engineering, Universiti Putra Malaysia, 43400 UPM Serdang, Selangor, Malaysia

Received: 30 January 2002

ABSTRAK

Jambatan yang dibina di atas tanah yang mudah terhakis menyeberangi aliran sungai adalah terdedah kepada bahaya banjir terutama di kawasan pelabuhan dan landasan. Akibatnya, lubang aliran air akan terbentuk pada substruktur jambatan. Lubang aliran air itu boleh ditafsirkan dengan kedalaman lubang air yang dipanggil kedalaman lubang aliran air tempatan dan saiz kawasan aliran. Pengalaman lepas telah menunjukkan kadar kedalaman lubang air yang meningkat di kawasan substruktur jambatan, menyebabkan kelemahan pada asas struktur dan menjelaskan jambatan. Pencegahan mengelakkan aliran air pada asas substruktur jambatan perlu bagi mengurangkan risiko keruntuhan. Formasi lubang aliran air pada substruktur jambatan dianggap kompleks dan fenomena ini melibatkan proses pengiraan kedalaman lubang air yang kurang tepat. Model fizikal mengekalkan perkakas utama sebagai pengukur saiz aliran lubang air pada substruktur jambatan. Dalam kajian ini, keberkesanan lima jenis kaedah yang dicadangkan, diuji dengan menggunakan sebuah model fizikal. Kaedah-kaedahnya adalah kaedah tumpang kolar, tumpang pelbagai kolar, tumpang berslot, cerucuk depan tumpang dan penggunaan 'riprap'. Model fizikal terdiri daripada saluran menyerong (5 m panjang, 76 mm lebar dan 250 mm tinggi) dengan pasir di atas tapak semaian (bersaiz nominal: 35 mm) dan sebuah tumpang berbentuk silinder yang diperbuat daripada kayu jati yang keras (berdiameter 16 mm). Sebuah kolar yang diperbuat daripada besi berdiameter 40 mm dilekatkan pada model tersebut. Dimensi sebuah slot 7 mm × 20 mm (lebar × dalam) dibuka di bahagian atas tumpang. Beberapa batang paku berdiameter 3 mm digunakan bagi menyerupai cerucuk. Pasir kasar yang digred, digunakan sebagai 'riprap'. Data yang diambil daripada model fizikal menunjukkan penggunaan tumpang pelbagai kolar memberikan 88% pengurangan pada kawasan aliran manakala pengurangan maksimum kawasan aliran berjarak dari 73% kepada 64%, bergantung kepada kadar aliran pada saluran. Pencegahan 'riprap' pada substruktur jambatan juga efektif dalam mengurangkan kawasan aliran maksimum dan pengurangan jarak dari 100% kepada 68%. Walau bagaimanapun, pengurangan kawasan aliran berjarak dari 100% kepada 83%. Pengurangan tersebut bergantung kepada kadar aliran.

ABSTRACT

Bridges constructed across streams with erodable beds are normally subjected to serious scouring during the flood at piers and abutment sites. As a result, scour holes will be formed at the bridge substructure. The scour hole can be described by its maximum vertical scour depth which is called local scour depth

and by the size of its projected scour area. Experience has shown that progressive depth of scour holes at the site of bridge substructures could undermine the foundation and result in bridge failure. Protection against scouring for constructed bridges is necessary to minimize the risk of failure. The formation of the scour hole at the bridge substructure is considered as very complex and this phenomenon is so involved that only very limited success has been made to predict the size of the scour hole computationally. Physical model remains the principal tool employed for estimating the size of scour hole at the site of bridge substructure. In this study, the efficiency of five different proposed methods of protecting the bridge substructure were tested using a physical model. These methods are piers with collar, pier with multiple collars, pier with slot, piles in front of piers, and using riprap. The physical model comprises a tilted flume (5 m long, 76 mm wide and 250 mm high) with sand on its bed (nominal size = 0.35 mm) and a single circular cylindrical pier model which was made of hard teak wood (diameter =16 mm). A collar form steel with a diameter of 40 mm was attached to the pier model. A slot of a dimension 7 mm x 20 mm (width x depth) was opened in the upper side of the pier. Steel nails 3 mm in diameter each were used to simulate the piles. Coarse graded gravel was used as a riprap. Data collected from the physical model showed that using multiple collars around the pier can give 88% reduction in the scour area while the reduction in the maximum scour depth ranges from 73% to 64%, depending on the flow rate in the flume. It was observed that the riprap protection at the bridge substructure is also effective in reducing the maximum scour depth and reduction ranges from 100% to 68%. However, the reduction in the scour area ranges from 100% to 83%. The reduction was also dependent on the flow rate.

Keywords: Bridge substructure, scour hole, pier, protection, physical model

INTRODUCTION

Bridges constructed across streams with erodable beds are normally subjected to serious scouring at piers and abutment sites during floods. As a result, scour holes will form at the bridge substructure. The scour hole is a result of the interference of the bridge substructure with flowing water. This interference will result in a considerable increase in mean velocity of the flowing water in the stream section at the bridge site. Scouring vortex will be developed when the fast moving flow near the water surface (at the location of the maximum velocity in the channel section) strikes the blunt nose of the pier and is deflected towards the bed where the flow velocity is low. Portion of the deflected surface flow will dive downwards and outwards. *Fig. 1* shows this mechanism. This will act as a vacuum cleaner and suck the soil particles from area around the pier site. The scoured hole formed at the site of bridge substructure has a random geometrical shape. Normally, one simple or compound scour hole will form around one pier. Qadar (1981) proved through experimental work that the local scour at the pier site occurred due to the effect of vortices. The scour hole can be described by its maximum vertical scour depth which is called local scour depth and by the size of its projected scour area. The pattern of scour at the bridge substructure will depend on river

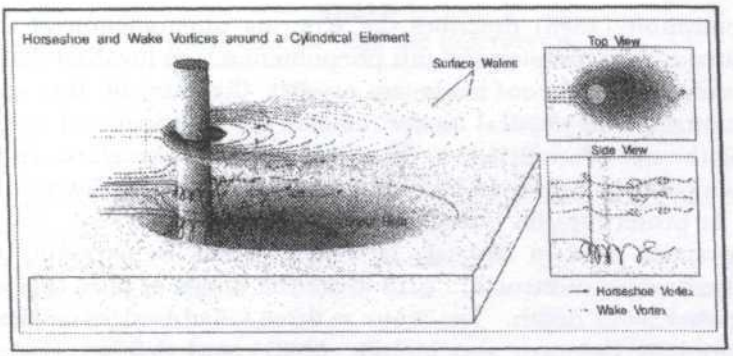

Fig.1: Three-dimensional schematic drawing showing the mechanism of scour hole forming at a site of bridge pier

discharge, bed slope, bed material, direction of flow, alignment of pier, pier's shape, pier's size and the number of piers used. Protection against scouring for constructed bridge is necessary to minimize the risk of failure.

Experience has shown that progressive depth of scour hole at the site of bridge substructure could undermine the foundation and result in bridge failure. Many bridges failed around the world because of extreme scour around pier and abutment, for example during the spring floods of 1987, 17 bridges in New York and New England, USA were damaged or destroyed by scour. In 1985, floods in Pennsylvania, Virginia, USA destroyed 73 bridges. A total number of 383 bridges failed in the USA, caused by catastrophic floods and 25% of these bridges failed due to the damage to the pier's foundation, while 72% failed due to damage to the abutment's foundation (Federal Highway 1991). Another extensive study conducted in 1978 indicated that the number of failed bridges due to the damage to the pier's foundation was almost equal to the number of failed bridges due to the damage to the abutment's foundation. Chiew (1992) studied the effect of making a slot with different dimensions in the pier body on the reduction in scour depth. A reduction of 20% was obtained when he used a pier with a slot having a width equal to a quarter of the pier diameter and a height greater than twice the pier diameter.

Many researchers proposed to use a collar with a pier as a method of protection against scour. However, the earliest proposal was made by Thomas (1967). In general, the use of collar with a bridge pier appears to be effective in reducing the scour depth at the pier site. However, when the bed material at the pier site which is protected by the collar is removed and transported by the flowing water, the pier beneath the collar will be exposed and under such a condition, it losses its effectiveness (Chiew 1992).

Chiew (1996) proposed a semiempirical method to size the stones for riprap protection. Chiew and Lim (2001) proposed a semiempirical equation to compute the maximum depth of the riprap degradation. Lauchlan and Melville (2001) proposed an empirical equation to estimate the size of riprap protection for a given size of the pier substructure.

Cheremisinoff (1988) describes the scouring phenomenon at the bridge substructure as very complex and this phenomenon is so involved that only very limited success has been made to predict the size of the scour hole computationally, and physical model remains the principal tool employed for estimating the size of scour hole at the site of bridge substructure. In this paper a physical model was employed to investigate the efficiency of different proposed methods in protecting the bridge substructure from scouring.

The practice used in Malaysia by Public Works Department (PWD), to protect the bridges substructure is to make the depth of piles cap more than the computed scour depth. The scour at three failed bridges in New Zealand was analyzed by Coleman and Melville (2001) and defined as degradation scour, bend scour and local scour. Finally, the foundation geometry also affects the dimension of the scour hole as mentioned by Melville and Raudkivi (1996).

MATERIAL AND METHODS

A tilted glass-sided flume (5 m long, 76 mm wide and 250 mm high) with erodable material was put in its bed. Sand with an average particle size of 0.35 mm was used in the flume bed as an erodable material. A hard teak wood pier model (16 mm diameter) was fixed firmly at the center of the flume cross section. The protection methods which were tested in this study included a collar around the pier, multiple collar, pier with slot, piles in front of the pier, and riprap around the pier. A 40 mm diameter circular steel plate with a thickness of 5 mm was used as collar with the pier model. A slot with a dimension 7 mm x 20 mm (width x height) was made in the pier below the water surface. Long nails of 3 mm diameter were used to simulate the piles and were located in front of the location pier model. Course graded gravel was used as a riprap. For a measured flow rate, the size of the scour hole was measured with and without protection. The data collected is shown in Table 1 while *Fig. 2* shows the profiles of various protection methods used in the experiments.

RESULTS AND DISCUSSION

The simulation of scouring at bridge substructure was conducted by using a single circular cylindrical pier model (diameter =16 mm) which was fixed in a glass sided flume (5 m long, 76 mm bed width, and 250 mm total depth) with a sand bed (d_{50}= 0.35 mm). The range of the flow rate which was used to run the experiments was between 0.5 to 1.5 L/s. Five different methods of protecting the bridge substructure were tested in the present study. These methods are collars around the pier, multiple collars around the pier, piers with slots, piles in front of piers, and using riprap. *Fig. 2* shows various protection methods used in the experiments. The scour hole dimension was recorded with time and it was observed that after 1 h there was no appreciable change to this dimension. Based on the collected data, a comparison is made between the various studied methods of protection (Table 2, *Fig. 3* and *Fig. 4*).

TABLE 1
Data collected from the experiments

Description	Flow Rate (L/S)	Projected Area of Scour (Cm^2)	Maximum Depth of local Scour (mm)	Remarks
Pier model without protection	0.5	39.6	26	
Protection with collar	0.5	30	18	
Protection with multiple collars	0.5	4.9	7	The measurements
Protection with slot	0.5	33	20	were taken one hour
Protection using piles in front of pier	0.5	35	24	from the commencement of each run.
Protection using riprap	0.5	0	0	
Pier model without protection	1.0	40.7	28	
Protection with collar	1.0	34	20	
Protection with multiple collars	1.0	4.90	10	
Protection with slot	1.0	36	22	
Protection using piles in front of pier	1.0	37	26	
Protection using riprap	1.0	3.8	3	
Pier model without protection	1.5	40.7	28	
Protection with collar	1.5	34	22	
Protection with multiple collars	1.5	4.90	10	
Protection with slot	1.5	36	23	
Protection using piles in front of pier	1.5	37	26	
Protection using riprap	1.5	7.06	9	

The results showed that the method of riprap protection and the method of protection using multiple collars are the best among the other studied methods of protecting bridge substructure. Using riprap method, a reduction of 100%, 90% and 83% were recorded in the scour area for flow rates of 0.5 L/s, 1 L/s and 1.5 L/s respectively. However, the reductions in the scour depth were 100%, 89% and 68% for the flow rates of 0.5 L/s, 1 L/s, and 1.5 L/s respectively. A constant reduction of 88% was observed in the scour area and for all values of flow rates when a multiple collar protection method was used. However, reductions in the scour depth were 73% and 64% for flow rates of 0.5 L/s and 1 L/s respectively. A reduction of 64% in scour depth was observed when the flow rate was increased to 1.5 L/s.

In the study, with a slot of dimensions of 0.44D X 1.25D (width x depth) located at the top part of the pier model and 10 mm below the flowing water surface, the recorded reduction in the maximum scour depth using this type of protection ranges from 23% to 18% for different values of flow rates. In the present study a collar with a diameter equal 2.5 times the pier diameter (2.5D) was used and an average reduction of 20% was recorded.

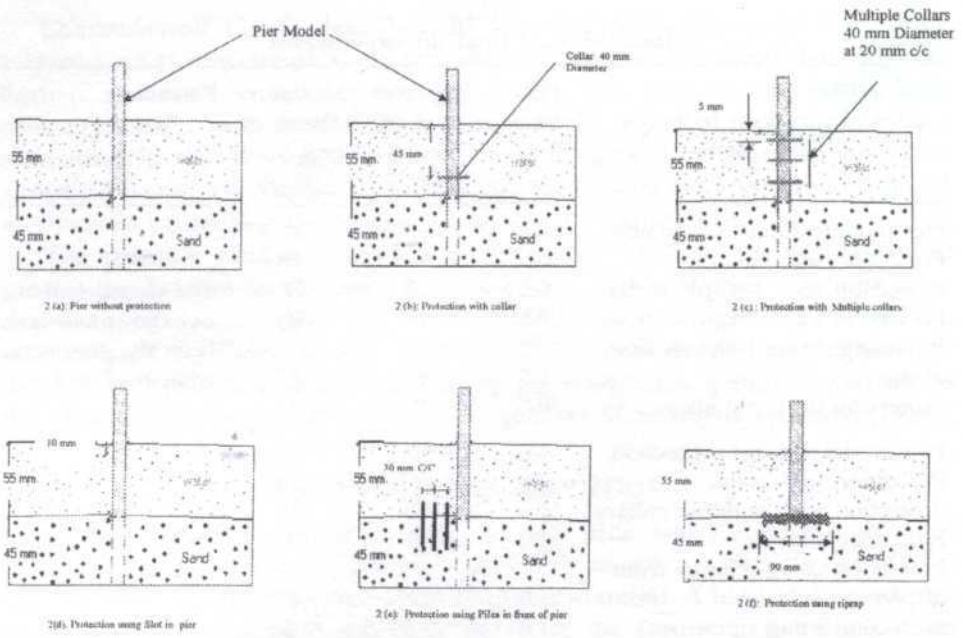

Fig. 2: Various methods of protecting bridge substructure from local scouring

TABLE 2
Reduction in maximum scour depth and area of scour at the pier model

Method of Protection	Flow Rate (L/s)	Reduction in Scour Depth (%)	Reduction in Scour Area (%)
Collar around the pier		30	24
Multiple collars around the pier		73	88
Slot at the top of the pier	0.5	23	17
Piles in front of the pier		8	12
Riprap around the pier		100	100
Collar around the pier		29	16
Multiple collars around the pier		64	88
Slot at the top of the pier	1	21	12
Piles in front of the pier		7	9
Riprap around the pier		89	90
Collar around the pier		21	16
Multiple collars around the pier		64	88
Slot at the top of the pier	1.5	18	12
Piles in front of the pier		7	9
Riprap around the pier		68	83

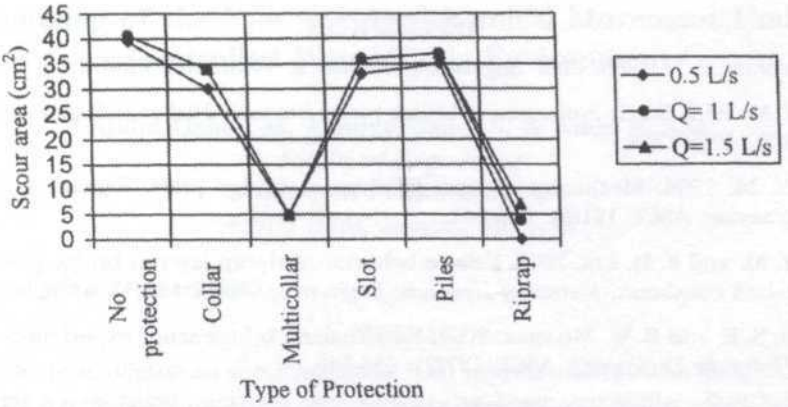

Fig. 3: Scour area around the pier model

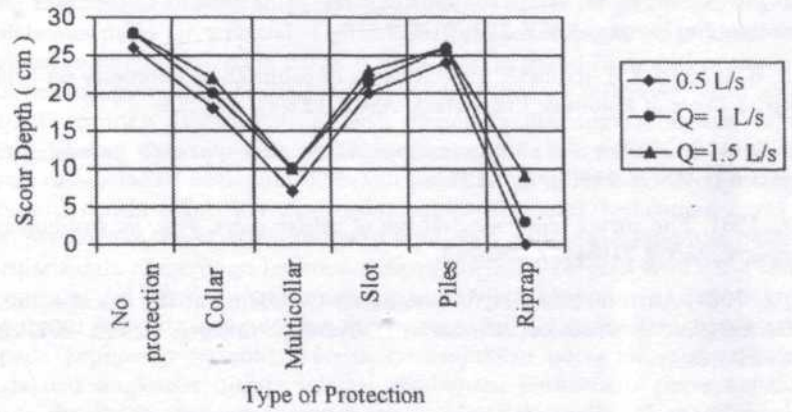

Fig. 4: Maximum scour depth at the site of pier model

CONCLUSIONS

Among the five methods tested to protect the pier model, it was found that using multiple collars around the pier can give 88% reduction in the scour area recorded before this protection. The reduction in the maximum scour depth ranges from 73% to 64% depending on the flow rate of the flume. It was observed that the riprap protection at the bridge substructure was also effective in reducing the maximum scour depth, a reduction from 100% to 68% was observed depending on the flow rate. The reduction in the scour area ranged from 100% to 83% depending also on the flow rate.

The collected data from the physical model showed that the method of riprap gives best protection against scour at flow rates of 0.5 L/s and 1 L/s while at the flow rate of 1.5 L/s, the method of multiple collar and method of riprap both have almost the same effectiveness in scour protection.

REFERENCES

CHEREMISINOFF, P. N. 1988. *Civil Engineering Practice.* **2**: Tchnomics Publishing Company.

CHIEW, Y. M. 1992. Scour protection at bridge piers. *Journal of Hydraulic Engineering,* ASCE **118(9)**: 1260-1268.

CHIEW, Y. M. 1996. Mechanics of riprap failure at bridge piers. *Journal of Hydraulic Engineering,* ASCE **121(9)**: 635-641.

CHIEW, Y. M. and F. H. LIM. 2001. Failure behavior of riprap layer at bridge piers under live–bed condition. *Journal of Hydraulic Engineering,* ASCE **126(1)**: 43-55.

COLEMAN, S. E. and B. W. MELVILLE. 2001. New Zealand bridge scour experiences. *Journal of Hydraulic Engineering,* ASCE **127(7)**: 535-546.

FEDERAL HIGHWAY ADMINISTRATION. 1991. Evaluating scour at bridges. U. S. Department of Transportation, Publication no. FHW-IP-90-017.

LAUCHLAN, C. S. and B. W. MELVILLE. 2001. Riprap protection at bridge pier. *Journal of Hydraulic Engineering,* ASCE **127(5)**: 412-418.

MELVILLE, B. W. and A. J. RAUDKIVI. 1996. Effects of foundation geometry on bridge pier scour. *Journal of Hydraulic Engineering,* ASCE **122(4)**: 203-209.

MELVILLE, B. W. 1997. Pier and abutment scour: Integrated approach. *Journal of Hydraulic Engineering,* ASCE **123(2)**: 125-136.

QADAR, A. 1981. The vortex scour mechanism at bridge piers. *Proc. the Institutions of Civil Engineers,* Part 2 **71(8443):** 739-757.

THOMAS, Z. 1967. An Interesting Hydraulic Effect Occurring at the Local Scour. In *12th IAHR Congress, International Association of Hydraulic Research,* p. 194 -201. Delft, the Netherlands.

Pertanika J. Sci. & Technol. 11(2): 237 - 247 (2003)
ISSN: 0128-7680

Modeling of the Fate and Agrochemical Movement Under Controlled Water Table Environment

Abdul Hakim M. Almdny, Salim S. & Amin M.S.M
Faculty of Engineering
Universiti Putra Malaysia,
43400 UPM, Serdang Malaysia

Received: 4 February 2002

ABSTRAK

Kajian telah dijalankan untuk mengenal pasti keberkesanan amalan pengurusan paras air terhadap angkutan persekitaran dan kesan agrokimia. Satu kajian makmal dijalankan menggunakan tanah pasir berkolum yang terganggu bagi mengenal pasti angkutan dan kesan nitrat (NO_3), sejenis bahan kimia pertanian yang biasa diguna terhadap persekitaran bawah tanah yang dipengaruhi oleh kedalaman paras air terkawal. Tiga sampel kedalaman paras air terkawal yang digunakan ditetapkan, pada paras 0.25 m, 0.50 m dan 0.75 m dari permukaan dan rawatan penyaliran bebas (tiada kedalaman aras air terkawal). Satu model statistik mudah berasaskan analisis kepelbagaian regresi linear dibina menggunakan data eksperimen bagi menyerupai penurunan dan angkutan nitrat dalam tanah berkolum di bawah paras air yang berbeza. Model regresi dibina daripada pemboleh ubah yang terpilih termasuk kedalaman paras air dari permukaan, masa dan kedalaman tepu. Satu persamaan yang luas didapati daripada data eksperimen bersama dengan koefisien korelasi R^2=0.83. Prestasi persamaan ini diuji dengan menggunakan data eksperimen dan didapati keputusan daripada ujian tersebut memuaskan dan boleh diterima. Berdasarkan kepada keputusan tersebut, jelas ia menunjukkan paras air mempengaruhi perlakuan angkutan nitrat. Sebagai tambahan, penurunan paras kelikatan nitrat diperoleh daripada rawatan paras air. Keputusan ini mengesyorkan bahawa tidak mustahil melakukan degradasi pada bahan kimia dan biologi bagi menurunkan angkutan nitrat dengan mengawal kedalaman paras air.

ABSTRACT

The study was undertaken to investigate the effect of water table management practices on the environmental transport and fate of agrochemicals. A laboratory based study using disturbed sand soil columns was conducted to investigate the transport and fate of nitrate (NO_3), a commonly used agricultural chemical, to the underground environment as effected by controlled water table depths. Three controlled water table depths set as 0.25m, 0.50m, and 0.75m from the surface and free drainage treatment (no controlled water table depth) were used. A simple statistical model based on multiple linear regression analysis was developed using experimental data to simulate reduction and transport of nitrate in soil columns under different water table depths. The regression model was developed from selected physical variables including water table depth from the surface, time, and saturated depth. An imperial equation was obtained from the experimental data with a correlation coefficient of R^2 = 0.83. The performance of this equation was tested using experimental data and it was found that the output from this equation is acceptable and satisfactory.

According to the simulated and observed results, it was clearly shown that the water table depth affects the characteristics of transport nitrate. In addition significant reduction in nitrate concentration was achieved through different water table treatments. The results suggest it is possible to promote biological and chemical degradation to reduce nitrate transport by controlling water table depths.

Keywords: Water table depths, statistical model, nitrate concentration

INTRODUCTION

Ground water quality degradation in rural areas is frequently attributed to agricultural production practices involving the use of fertilizers and pesticides for sustaining productivity. A fraction of farm chemicals moves to surface and ground water reservoirs by mass flow and diffusion processes .The accrual of soluble agricultural chemicals, particularly nitrate NO_3 to ground water is a natural process and source of potential degradation of ground water (Prunty and Montgomery 1991). At present, ground water contamination from agricultural non-point sources has become a major environmental concern and awareness, which is needed to protect ground water quality. A variety of interacting physical, chemical, and biological processes determined how far agrochemicals will move in the soil, how long it will persist in the environment, and at what concentration it will appear in water resources system. Recently researchers have been investigating the possibility of developing best management practices to protect water resources from agrochemical pollution. A few studies have been reported in evaluating the ability of water table management practices to reduce negative impact on water quality (Evans *et al.* 1989; Belcher 1989). Because of high costs and heterogeneities in soil properties caused by spatial and temporal variations in field experiments, most research has been performed in laboratories, usually in repacked soil columns or large field lysimeters.

To assess the impact of agrochemicals on water quality, predicting the transport and the fate of agricultural chemicals released into the environment it is necessary to minimize adverse impacts and optimize positive impacts. The complexity of agricultural chemical transport and the fate processes encourage the development and use of computer and statistical models for assessing the movement of chemicals in different pathways and under different climatological, geological, and management scenarios. Due to the complexity and costs of field experimental procedures, the use of statistical and computer modeling as an alternative is essential in conducting research in this area. In recent years, substantial progress has been made in the use of modeling as a tool to integrate processes for predicting agricultural chemical behavior in the environment.

Various contaminate transport models have been developed under different management practices for monitoring agrochemical behavior in an environmental system (Wagenet 1990). Regression models are examples of empirical models used as a tool for predicting the concentration of agrochemicals

in water system (Druliner *et al.* 1996) . Based on laboratory experiment studies, the specific objectives of this study was to investigate the effect of various water table depths on the transport and fate of nitrate to subsurface environment and to create a statistical model to simulate the nitrate reduction under these conditions. Also the model validation was done by comparing the predicted outputs from the model with the observed data to study the effect of water table depths on the predicted outputs.

MATERIALS AND METHODS

Soil Preparation

This research was undertaken to investigate the effect of water table levels on agricultural chemical transport to underground environment, specifically nitrate transport and transformation, and to identify water table management strategies that can help to reduce the potential of agricultural chemical (nitrate) pollution to both surface and ground water. The main factor considered in this research is the effect of water table levels on nitrate movement. To achieve the overall objectives, this study consists primarily of laboratory work and then a statistical model to simulate the studied problem. The laboratory experiments were conducted on a column system. The columns were constructed from PVC pipes with a 30 cm diameter and 1-meter high welded with thin iron sheet at one end. The columns were equipped by two holes at the bottom of each column for collecting water samples and to maintain water table levels at the desired depths in each column. A water supply system was attached to the side of columns to monitor water table depth (*Fig. 1*). The soil used in the column experiments

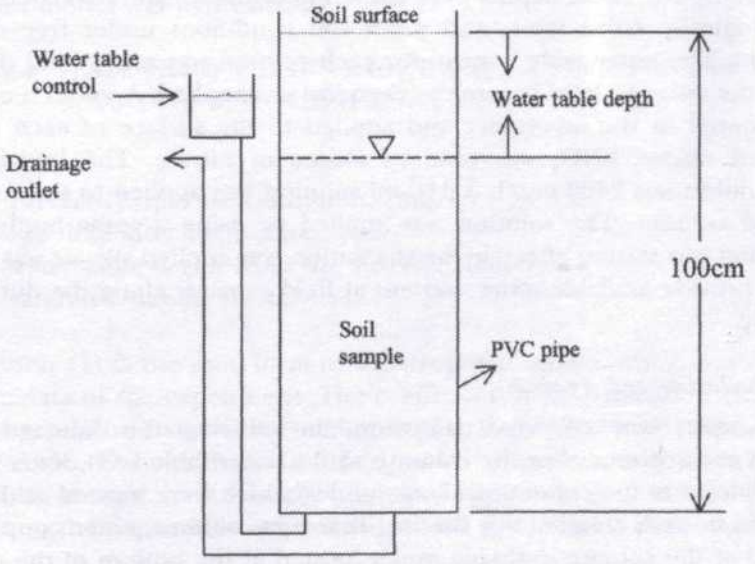

Fig. 1: Experimental column

was disturbed sandy soil collected from the field. The soil samples were air-dried and sieved through 2 mm sieves before being placed in the columns. Selected physical properties of the soil used in this study are listed in Table 1. A total of four columns were used in this study. To approximate the bulk density of the original soil 1.35 g/cm^3, an equivalent weight of soil was used to make the soil volume to each column.

TABLE 1
Summary of soil physical properties used in the study

Soil property	Measured values
Silt (%)	3.98 %
Clay (%)	1.02 %
Sand (%)	95 %
Coarse sand (%)	30.70 %
Medium sand (%)	27.73 %
Fine sand (%)	25.20 %
Very fine sand (%)	11.8 %
Bulk density (g/cm3)	1.35 g/cm3
Hydr. Conduct (cm/sec)	0.0855 cm/sec

Water Table Experiment

Three control water table depths set as 0.25m, 0.50m, 0.75m from the surface and free drainage treatment (no control water table) were conducted in the column experiments to evaluate the effect of different water table depths on nitrate transport. These depths were chosen to simulate saturated conditions in the biologically active layer, and moist soil conditions under free drainage treatment. The water table control for each column was set to hold the water table at the assigned level before the chemical was applied. A solution of nitrate was prepared in the laboratory and applied to the surface of each column. Potassium nitrate KNO_3 was used as source of nitrate. The initial nitrate concentration was 2400 mg/l. A 150 ml solution was applied to the surface of each soil column. The solution was applied by using a spray bottle. Water application was started after chemical solution was applied. Water was applied daily to provide available water content at field capacity along the duration of the study.

Sample Collection and Analysis

Water samples were collected daily from the outlet at the drainage control point on each column. For the columns with a water table level, water samples were collected at the column drainage outlet, which were located at the water table level in each column. For the free drainage columns, water samples were collected at the column drainage outlet located at the bottom of the column. The volume of the samples collected was enough for nitrate analysis. The

collected water samples from each column drainage outlet were analyzed to develop nitrate concentration curves for each water table depth. All water samples were analyzed immediately for nitrate concentration using a distillation method.

Statistical Evaluation Methods

In this study a simple statistical model based on multiple linear regression analysis as described by SPSS statistical package Version 10.0.5 and data collected from the experiments were used to evaluate reduction and transport of nitrate in soil columns with different water table depths. An empirical regression model was developed from selected variables including the depth of water table from the surface, time, and saturated depth (range of saturated conditions). In developing the regression model, the interactions between the variables were considered. Several statistical evaluation procedures were used to test the performance of the model (Addiscott and Whitmore 1987). These methods included mean error ME, root mean square error RMSE, correlation coefficient r, Thiel's coefficient U, and coefficient of determination R^2.

RESULTS AND DISCUSSION

Model Development

An imperial regression model was developed to simulate the reduction in nitrate concentration under different water table depths. The effective variables governing the studied phenomenon were considered in the model building. The model independent variables were selected based on the higher correlation coefficient with the dependent variable (r = 0.91). The general form of the regression model was expressed as:

$$\text{Log } y = -1.424 - 1.406\ T\ D\ D^2 - 1.469\ T\ S\ T^2 + 2.870\ S\ T^2 - 7.864\ D\ S\ S^2 - 9.503\ T^2\ D^2\ S^2 + 0.630\ D\ T^2 + 2.096\ D + 1.095\ T \quad (1)$$

where:

y = predict Nitrate concentration, (mg/l).
T = log time after application, (day)
D = water table depth from the surface, (meter)
S = saturated depth, (meter)

Equation (1) is the final form of the proposed model, which was obtained from the data of the experiment. The coefficient of determination (R^2) of the proposal model was significant and relatively high (R^2 =0.83) with standard error of 0.156. The coefficients of the regression model are given in Table 2. The results of t-test indicated the statistical significance of the independent variables on the dependent variable (t_{crit} =1.64 at 0.05level) as shown in Table 2.

TABLE 2
Parameter estimates for the final regression model

Predictor	Coefficient	Standard error	t-ratio	$t_{crit,0.95}$	R^2
Constant	-1.424	0.251	-5.67	1.64	0.83
TDD2	-1.406	0.273	-5.14		
TST2	-1.469	0.165	-8.90		
ST2	2.87	0.428	6.70		
DSS2	-7.864	2.118	-3.71		
T2D2S2	-9.503	0.923	-10.2		
DT2	0.630	0.091	6.89		
D	2.096	0.275	7.63		
T	1.095	0.222	4.93		

The high value of R^2 indicated that the regression model was appropriate to explain the relationship between these variables. The value of R^2 0.83 indicates that 83% of the variation in the dependent variable is explained by the regression variables in the model. This information is quite useful in assessing the overall accuracy of the model.

Model Verification

The verification process involves comparison between model predicted and observed data, preferably those not used in the model building process to achieve the best possible match of simulated outputs with observed data (Donigian 1983). For the proposed model, the verification process was conducted by comparing the regression model output with the data collected based on laboratory experiments. Comparison between simulated and measured results is shown graphically in *Fig. 2*. The results show satisfactory agreement between simulated and measured data. For the verification of this model, a best-fit regression model with R^2 = 0.81 was obtained for the relationship between simulated nitrate concentration and measured data. It is noticed that there is no significant difference in R^2 between the verification and the developed model. Careful visual observation of the best-fit line for the pooled data (*Fig. 2*) revealed that few points at the end of the best-fit line dominate the slope of the best-fit line. Otherwise, the best-fit line passing through rest of the data (excluding few points on the extreme left) provided a slope much closer to the 1:1 line (t-ratio = 0.46 compared to t-crit =1.67 at 0.05 significance level). The scatter of measured and simulated data on the developed model gives a good simulation to observed under study conditions. This statistically reasonable agreement between the measured and modeled results suggests that the model performed well.

Comparison with Experimental Results

The results of the experiments indicated that nitrate had different concentration curves depending upon the water table depths. Therefore the verification of

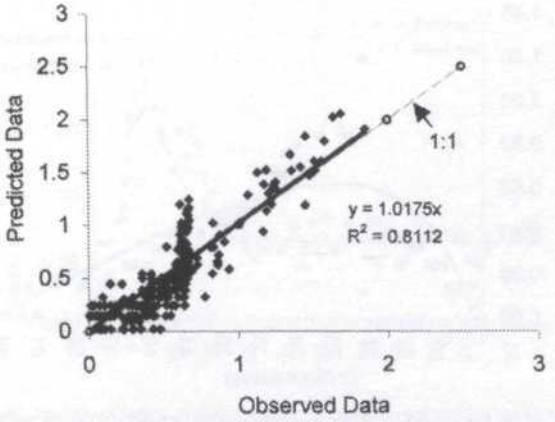

Fig. 2: Compassion between predicted and observed NO_3 concentration

the model was implemented upon all water table depths. A comparison of observed and model simulated nitrate concentration under 0.25 m, 0.50 m, 0.75 m and free drainage water table treatments are shown in *Figs. 3* to *6*. It is apparent from these figures that there is relatively good agreement between simulated and measured data. The nitrate concentration for 0.25 m, and 0.50 m, 0.75 m water table depths were lower compared to that under free drainage water table treatment. A similar trend was found in the simulated results from the model. These results suggest that more nitrates have been denitrified, especially in 0.25 m and 0.50 m water table depths. The saturated conditions in 0.25 m, and 0.50 m water table depths and anaerobic conditions, which are usually associated with high water content, may create the potential for more nitrate denitrification compared to the free drainage water table depth. In the column with free drainage water table depth, nitrate had to travel longer through the unsaturated zone where less denitrification would occur because of the lower degree of saturation. In the column with 0.75 m water table depth the saturated and anaerobic conditions may not have been sufficient to produce similar results for 0.25 m and 0.50 m water table depths. As a result, denitrification in the 0.75 m water table depth and free drainage columns would be lower compared to that in 0.25 m and 0.50 m water table columns. It appears that the different water table depths provide different degrees of saturation condition associated with different degree of anaerobic conditions, which is resulting in different degradation rates for nitrate. These observations agree with that reported by Jebelle and Prasher (1995) who found that shallow water tables would cause a faster degradation of nitrate. They assumed that the soil water content may affect soil chemical, physical and microbiological activity which would influence soil biodegradability. In addition, under saturated conditions, degradation capacity could be significantly increased. Several statistical parameters of the observed and simulated concentration curves were calculated. These statistical measures are used as indicators of the extent at which the

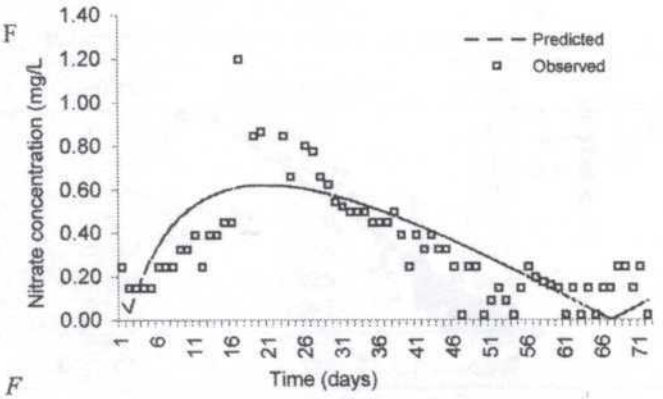

Fig. 3: Observed and predictive nitrate concentration under 0.25 m water table treatment

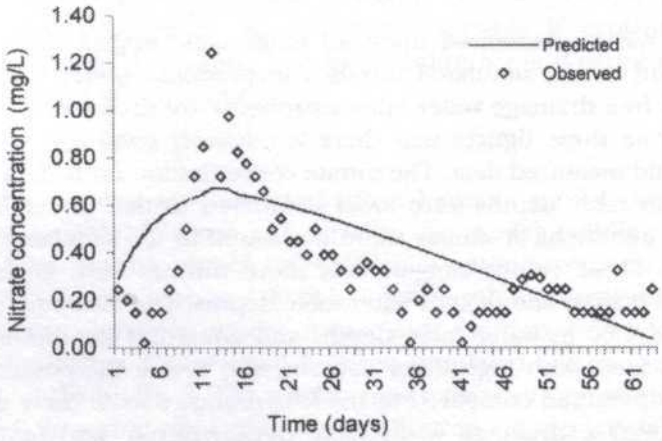

Fig. 4: Observed and predictive nitrate concentration under 0.50 m water table treatment

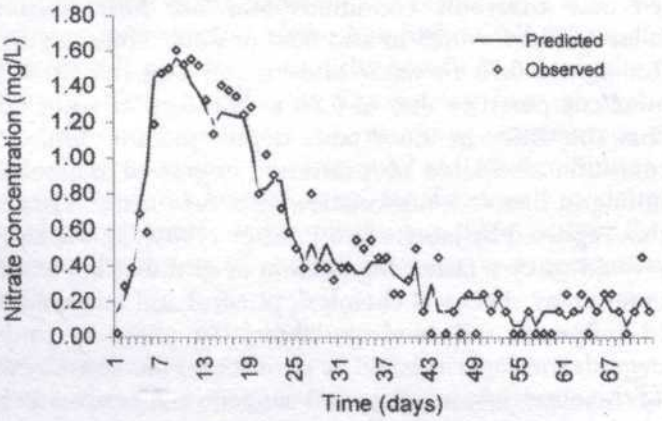

Fig. 5: Observed and predictive nitrate concentration under 0.75 m water table treatment

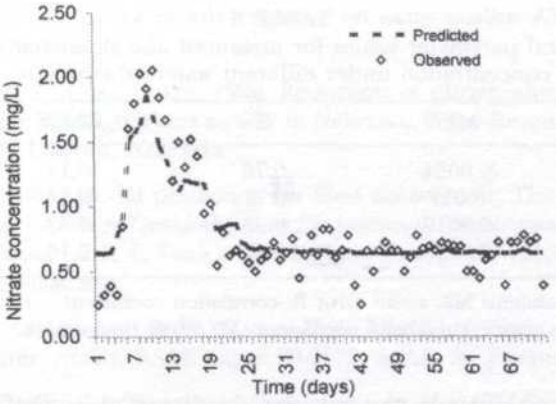

Fig. 6: Observed and predictive nitrate concentration under free water table treatment

model prediction match the observed data. Statistical methods suggested by Voltz and Webster (1990) was used to evaluate the simulation capability of the model. The statistical parameters used in this study are: the mean error (ME). This quantity measures the bias of the prediction and should be close to zero for unbiased methods. The second parameter is the root mean square error (RMSE) that measures the absolute size of the error. This measure is similar to the mean absolute error except that the squaring function is used instead of the absolute value function. It is more sensitive to large errors than the mean absolute error. Furthermore, the regression model was also tested using Theil's coefficient U that is given by Naylor (1970). The mathematical expressions of these statistical parameters are as described below.

$$ME = 1/n \quad (P_i - A_i) \tag{2}$$

$$RMSE = \quad 1/n \quad (P_i - A_i)^2 \tag{3}$$

$$U = \frac{\sqrt{\frac{1}{n} \quad (P_i - A_i)^2}}{\sqrt{\frac{1}{n} \quad P_i^2} + \sqrt{\frac{1}{n} \quad A_i^2}} \tag{4}$$

where n is the number of samples, P_i is the observed value and A_i the simulated one.

The values obtained for each statistical parameter under different water table depths are listed in Table 3. The calculated mean error values between measured and simulated in all water table depths was close to zero. Also low values of root mean square error were observed in all water table depths. A high value of correlation coefficient between measured and simulated data was observed for all water table depths. Beside these, the values of Thiel's coefficient was calculated in all water table depths According to the limits of the numerical

TABLE 3
Statistical parameter values for measured and simulated nitrate concentration under different water table depths

WT	ME	R	RMSE	U
0.25m	-0.0034	0.78	0.17	0.20
0.50m	-0.017	0.71	0.24	0.23
0.75m	-0.0019	0.96	0.12	0.86
FD	-0.0098	0.92	0.18	0.019

W T: water table treatments ME: mean error R: correlation coefficient
R: Root-mean-square error U : Theil's coefficient FD : Free water table.

values of Thiel's coefficient, the calculated value of this coefficient was found close to zero, which indicates perfect agreement between the model predictions and observed data in all water table depths. These statistics demonstrate good agreement between simulated and measured data under different water table depths.

CONCLUSIONS

Several conclusions can be drawn from this study. The water table depth is an important factor affecting nitrate transport. The degree and extent of saturation in the soil profile as a result of different water table depths may enhance the biological and chemical degradation of the contaminants such as fertilizer and herbicides. Under water-saturated conditions, denitrification capacity could be significantly increased and low concentrations of nitrate were observed. A suitable soil water condition may maintain a soil-water microenvironment at a favorable level, which would enhance some soil chemical, physical and microbiological activities. These activities can breakdown the contaminants and cause less risk of pollution to the water systems. Based on the experimental results, a simple statistical model was developed to simulate the reduction in nitrate transport under different water table depths. For all water table treatments, the model simulations are not significantly different from the observed data. The statistical parameters that included mean error, root mean square error, correlation coefficient, determinations coefficient R^2 and Theil's coefficient were used to test the simulation capability of the proposal model under different water table treatments. The parameters demonstrate good agreement between model simulation and measured data under different water table depths.

REFERENCES

ADDISCOTT, T. M. and WHITMORE. 1978. Computer simulation of changes in soil mineral nitrogen and crop nitrogen during autumn, winter and spring. *J. Agric. Sci. Camb.* **109**: 141-157.

BELCHER, H. W. 1989. Influence of sub irrigation on water quality. ASAE Paper No. 89 - 2577, ASAE, St. Joseph, Mi.

DRULINER, A. D. and T. S. MC GRATH. 1996. Reduction of nitrate nitrogen and atrazine contamination in the high plains aquifer in Nebraska. Water-Resources Investigations Report 95-4202 Lincoln, Nebraska.

DONIGIAN JR, A. S. 1983. Model predictions vs filed observation: The model validation testing process. In *Fate of Chemicals in the Environment, Compartmental and Multimedia Model for Predictions*, ed. R. L. Swan and A. Eschenroder, p. 151-171.Washington, D .C.: American Chemical Soc.

EVANS, R. O., J .W. GILLIAM and R. W. SKAGGS. 1989. Managing water table management systems for water quality. ASAE paper 89-2179. ASAE, St. Joseph. MI.

NAYLOR, T. H. 1970. *Computer Simulation Experiment with Models of Economic System.* John Wiley Company.

JEBELLIE, S. J. and S. O. PRASHER. 1995. Environmental benefits of water table management. ASAE Paper No 957211. ASAE, Joseph, MI.

PRUNTY, L. and B. R. MONTGOMERY. 1991 Lysimeter study of nitrogen fertilizer and irrigation rates on quality of recharge and corn yield. *Journal of Environment Quality* **20**: 373 - 380.

VOLTZ, M. and R. WEBSTER. 1990. A comparison of kriging, cubic spines and classification for predicting soil properties from sample information. *J. Soil Sci.* **41**: 473-490

WAGENET, R. J. and P. S. C. 1990. Modeling pesticide fate in soils. In *Pesticides in the Soil Environment: Processes, Impacts, and Modeling* ed. H. H. Cheng. SSSA Book Series: 2.

ISSN: 0128-7680
Pertanika J. Sci. & Technol. 11(2): 249 - 259 (2003)

Determination of Organochlorine Pesticides in Vegetables by Solid-Phase Extraction Cleanup and Gas Chromatography

Alvin Chai Lian Kuet[1] & Lau Seng[2]
[1]Agricultural Research Centre, Semongok, P.O. Box 977, 93720 Kuching, Sarawak, Malaysia
[2]Universiti Malaysia Sarawak, 94300 Kota Samarahan, Sarawak, Malaysia

Received: 19 March 2002

ABSTRAK

Satu kaedah pembersihan yang ringkas dan cepat telah dihasilkan untuk menentukan racun perosak organoklorin pada sayur-sayuran. Sisa baki racun perosak diekstrak dengan aseton dan diklorometana. Ekstrak dibersihkan dengan turus ekstraksi fasa pepejal amina kuaterner dan aminopropil. Racun perosak ditentukan dengan kromatografi gas yang dilengkapkan dengan pengesan tangkapan elektron. Perolehan semula untuk enam jenis racun perosak pada tiga jenis sayur-sayuran iaitu lobak merah, timun dan sawi hijau pada aras 0.5 mg/kg adalah di antara 68% dan 109.3%. Keputusan ini adalah setanding dengan yang diperoleh daripada kaedah pembersihan melalui gel silika.

ABSTRACT

A simple and rapid cleanup procedure has been developed for simultaneous determination of organochlorine pesticides in vegetables. Residues were extracted with acetone and dichloromethane. Extracts were cleaned up by a mixed-mode solid-phase extraction column, quaternary amine and aminopropyl. The pesticides were determined by gas chromatography with electron capture detector. The recoveries of 6 pesticides in three crops, namely carrot, cucumber and green mustard, fortified at 0.5 mg/kg were in the range of 68% to 109.3%. The results obtained were comparable to those obtained by silica gel cleanup method.

Keywords: Solid phase extraction, organochlorine, chlorophenyl, conazole pesticides, gas chromatography

INTRODUCTION

Organochlorine (OC) pesticides were used extensively worldwide in the early 1950s due to their effectiveness, low cost and acute toxicity. The highly lipophilic properties of these pesticides have led to contamination of the environment and the food chain. This has resulted in their restriction or banning in most industrialized countries. But, they remain as important pesticides in agriculture and public health in developing countries, where their use is still permitted. In Malaysia, most of the OC pesticides were no longer registered. The only two OC pesticides currently in use are lindane and endosulfan.

Several multi-residue methods have been developed for the analysis of OC pesticides. Luke *et al.* (1975) developed a rapid multiresidue procedure utilizing florisil cleanup prior to gas chromatography (GC) analysis. The samples were extracted with acetone and partitioned with methylene chloride-petroleum ether. Recoveries for 31 pesticides varied with the polarities of pesticides studied. However, the method was simple and fast with great potential for the analysis of many more compounds. Luke *et al.* (1981) further simplified this method by eliminating the florisil cleanup step by injecting the extract directly into GC with a Hall electrolytic conductivity detector. Good recoveries were obtained for 82 pesticides studied. A rapid multiresidue procedure for fruits, based on methanol extraction was developed by Holland and Mcghie (1983). Water and highly water-soluble co-extractives were removed by partitioning the pesticides into toluene. Further cleaning up was performed by carbon-cellulose-florisil before GC determination. High recoveries were obtained for 30 pesticides studied.

Numerous methods have been developed for the analysis of OC pesticides using solid-phase extraction (SPE) cleanup. Hsu *et al.* (1991) investigated C18 and florisil SPE as replacement for Attagel cleanup procedures for halogenated organic pesticides in broccoli, carrot, celery and orange. The recoveries obtained were comparable to the later method. Lee *et al.* (1991) evaluated the analysis of 7 chlorinated hydrocarbons using reverse phase SPE cleanup for potato, tomato, orange, carrot, broccoli and melon. The method was able to detect at 0.01 ppm level. Holstege *et al.* (1994) reported a multiresidue method, which was able to detect 17 OC pesticides in plant and animal tissue samples. Samples were cleaned up either by automated gel permeation chromatography, silica gel mini column or C18 SPE. Cook *et al.* (1999) investigated the gravity-fed SPE cleanup method for halogenated, phosphorus, sulfur, nitrogen and carbamate pesticides. Results showed that recoveries of 75 - 130 % were possible for GC and LC methods. Odanaka *et al.* (1991) examined SPE C18, C8, C2, CH and pH sorbents for cleanup of melon, apple, cabbage, eggplant and green pepper. The results of these investigations suggested that a significant reduction on the amount of solvents used, less sample matrixes interference, an improvement in accuracy and precision were encountered. A method for the determination of 251 pesticide residues in fruit and vegetable samples using GC-MS and LC was described by Fillion *et al.* (2000). Co-extractives are removed by passing the acetronitrile extract through octadecyl (C18), carbon and aminopropyl cartridge SPE cleanup. Limit of detection ranged from 0.02 and 1.0 mg/kg for most compounds studied. Sheridan and Meola (1999) reported a method for detection, quantitation and confirmation of more than 100 pesticides in fruits, vegetables and milk by gas chromatography (GC) with ion trap mass spectrometry (MS/MS) using quaternary amine (SAX) and PSA for cleanup. The sensitivity of this method for many analytes was equal to or lower than those of selective GC detectors such as flame photometric detectors and electrolytic conductivity detectors.

This paper reports the extraction of six pesticides in vegetables using acetone and dichloromethane, cleanup on SPE SAX/NH_2 and determine on GC-ECD. The results were compared to the silica gel cleanup method.

EXPERIMENT

Chemicals and Reagents

All the chemicals and reagents were of analytical grade. Pesticide standards were obtained from Dr. Ehrenstorter, Germany. SPE tubes, Isolute SAX/NH_2, 1 gm, 6 mL, were purchased from International Sorbent Technology.

Instrumentation

A Hewlett-Packard 6890 Gas Chromatograph equipped with Electron Capture Detector was used for the determination of pesticides. GC conditions were set at : Injector temperature, 260°C; detector 280°C; carrier flow (nitrogen) 1.2 mL/min; oven temperature, 100°C (0.2 min), rate 20°C/min to 180°C, rate 2°C/min to 250°C, rate 50°C/min to 300°C (5 min). Pesticides were analysed on an Ultra 1, 25 m × 0.32 mm × 0.5 mm column.

Procedures

The method was validated using four OC pesticides; gamma-BHC, beta-endosulphan, alpha-endosulphan and dieldrin; one chlorophenyl fungicide; chlorothalonil, and one conazole fungicide; hexaconazole. These pesticides were fortified in carrot (*Daucus carota*), cucumber (*Cucumis sativa*), and green mustard (*Brassica chinensis*). Each sample was fortified with 0.5 ppm of each pesticide. Three replicate fortifications for each matrix type were prepared.

Extraction was carried out using a procedure described by Steinwandter (1985). 50 g of sample was homogenised in a blender containing 100 mL acetone, 75 mL dichloromethane and 15 g sodium chloride for three min. The homogenised mixture was allowed to separate into its organic and aqueous layers. The organic layer was transferred to a beaker containing 3 g of sodium sulphate.

For the silica gel method (Steinwandter 1985), which is currently used in our laboratory, 2 mL of extract was transferred to a chromatographic column packed with 10 g of silica gel. The column was eluted with 60 mL of hexane-methylene chloride mixture (4:1 v/v). The eluate was analysed on GC-ECD.

For SPE method, SAX/NH_2 sorbent was used for cleanup. Prior to use, the SAX/NH_2 was conditioned with 10 mL of acetone : petroleum ether (1:2 v/v). 2 mL of extract was transferred to the SPE tube. The SPE tube was eluted with 10 mL of acetone : petroleum ether (1:2 v/v) at flow rate of 1 mL/min. The eluate collected was analysed on GC-ECD.

Statistical Analysis

A t-test was used to determine the significance of difference between the recoveries of the silica gel method and SPE method. They were considered

significantly different when the values of t (calculated) > t (critical) at 95% confidence level.

RESULTS AND DISCUSSION

Development of SPE Conditions

Development of the SPE solvent system was based on several criteria. Solvents, which were hazardous or expensive to dispose of, were not evaluated. A volatile solvent system must be used, as rapid evaporation of a large volume would be required in sample preparation without causing loss of volatile pesticides. The solvent system must be sufficiently polar to extract most polar pesticides. The final extract should have only minimum of matrix co-extractives.

The studies showed that a flow rate of 1 mL/min was sufficient to recover all the pesticides except hexaconazole. It was noted that the SPE should not be left dry after conditioning. This could result in a significant loss of pesticides. The optimum solvent systems for SAX/NH_2 was acetone : petroleum ether (1:2). Increasing the polarity of the solvent would cause lower recoveries for most of the pesticides studied. This is because most of the OC pesticides are non-polar and using solvent with higher polarity will not elute out the pesticides completely.

Recovery Studies

Six pesticides were selected for this study. They were hexaconazole, γ-BHC, chlorothalonil, alpha-endosulphan, dieldrin and beta-endosulphan. Hexaconazole, a conazole fungicide and chlorothalonil, a chlorphenyl fungicide was included in this study because they are detectable by GC-ECD and also commonly used by vegetable farmers. The results of the recovery study are given in Table 1. The recoveries for five pesticides, namely g-BHC, chlorothalonil, alpha-endosulphan, dieldrin and beta-endosulphan ranged from 70 - 107.7% with coefficient of variation (CV) of 1.5% to 8.3%. Lower recoveries of 44.3% were obtained for hexaconazole.

TABLE 1
Recovery of organochlorine pesticides

Pesticide	Recovery[(a)] %	CV %
Hexaconazole	44.3	8.3
Gamma-BHC	70.0	6.1
Chlorothalonil	107.7	7.6
Alpha-endosulphan	90.0	3.6
Dieldrin	95.7	1.5
Beta-endosulphan	93.7	2.1

CV = coefficient of variation
(a) n = 3

Method Validation

Three types of vegetables, namely carrot, cucumber and green mustard, which represent root, cucurbit and brassica families, were selected for this study. As each group contains different chemical compounds, they may co-elute with the pesticides and hence may cause interferences during the GC analysis.

Carrot

Recovery results from spiked carrot samples using SPE SAX/NH_2 and silica gel column chromatography cleanup are shown in Table 2. For the later method, the recoveries ranged from 79.7% to 104% with CV of 3.0% to 5.8%. Comparable results were obtained from SPE SAX/NH_2 cleanup method with recoveries ranging from 68% to 117.7%. When comparing these two methods, the t-value showed that the calculated value was lower than the critical value. Hence, there is no significant difference between these two methods. Chromatograms for the carrot samples using SAX/NH_2 and silica gel cleanup are shown in *Figs. 1* and *2*. Both chromatograms showed no interference peaks, which co-eluted with the pesticides. However, the chromatogram for SPE cleanup contained more unknown peaks especially after the b-endosulphan peak than the silica gel method. This may be due to smaller amounts of sorbent use in SPE cleanup (1 g) than those in silica gel cleanup (10 g). However, the colour of both extracts was yellow. As no interference compound was encountered, no further cleanup was necessary.

TABLE 2
Recovery of organochlorine pesticides from spiked carrot samples using SAX/NH_2 and silica gel cleanup

Pesticide	SAX/NH_2		Silica gel	
	Recovery [(a)] %	CV %	Recovery[(a)] %	CV %
Hexaconazole	93.3	2.1	79.7	4.7
Gamma-BHC	109.3	4.6	81.7	5.8
Chlorothalonil	76.3	5.5	95.3	4.0
Alpha-endosulphan	107.3	3.8	102.0	3.6
Dieldrin	68.0	6.2	103.3	4.0
Beta-endosulphan	117.7	3.5	104.0	3.0
AV	95.3		94.3	
SD	19.8		11.0	

AV= average mean
SD = standard deviation
CV = coefficient of variation
(a) n = 3

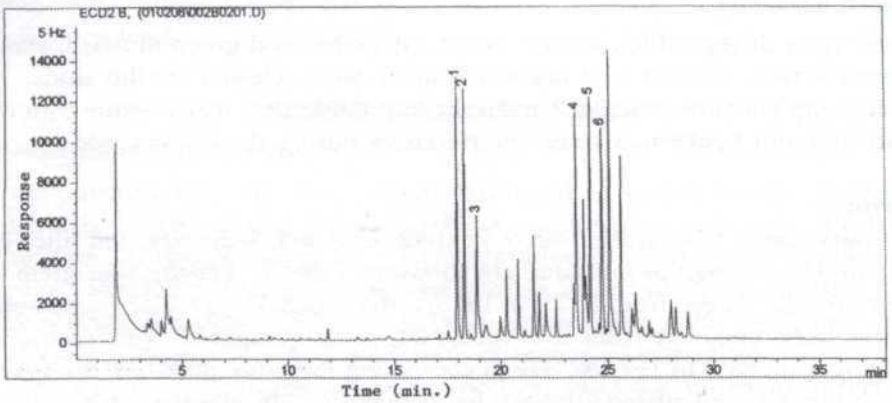

Fig. 1: GC chromatogram of carrot extract after SPE clean-up. Peaks: 1, hexaconazole; 2, gamma-BHC; 3, chlorothalonil; 4, alpha-endosulfan; 5, dieldrin; 6, beta-endosulfan

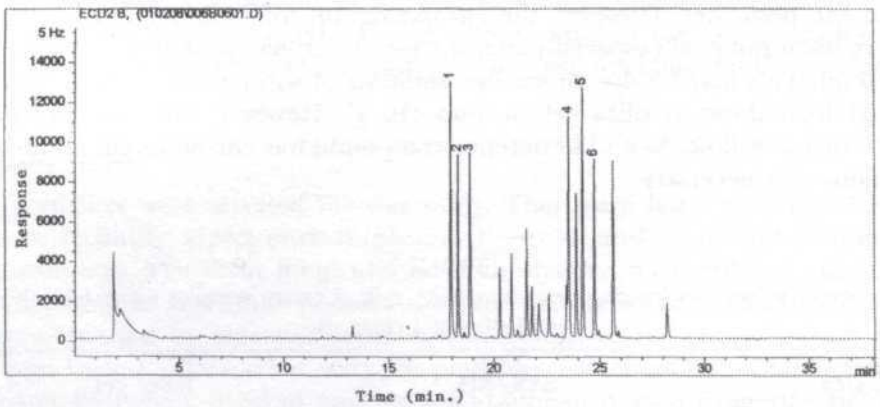

Fig. 2: GC chromatogram of carrot extract after silica gel clean-up. Peaks: 1, hexaconazole; 2, gamma-BHC; 3, chlorothalonil; 4, alpha-endosulfan; 5, dieldrin; 6, beta-endosulfan

Cucumber

Recovery results of pesticides from fortified cucumber samples using SAX/NH_2 and silica gel cleanup methods are given in Table 3. Except for hexaconazole, which showed lower recovery of 48%, the recoveries of other pesticides using silica gel method were in the range of 71.0% to 121.3% with CV of 7.0% to 8.5%.

In this study, higher recoveries were obtained for hexaconazole using SPE cleanup method. The recoveries for all the six pesticides evaluated were in the range of 74.0% to 109.7% with CV of 1.0% to 4.0%. Statistical analysis showed that the calculated t-value was lower than the critical t-value. Therefore, there is no significant difference between these two methods.

The chromatograms for silica gel and SPE cleanup methods are shown in *Figs. 3* and *4*. The extract of cucumber was colourless after the SPE and silica

TABLE 3
Recovery of organochlorine pesticides from spiked cucumber samples using SAX/NH_2 and silica gel cleanup

Pesticide	SAX/NH_2		Silica gel	
	Recovery[(a)] %	CV %	Recovery[(a)] %	CV %
Hexaconazole	74.0	1.0	48.0	6.1
Gamma-BHC	95.0	2.0	71.0	7.0
Chlorothalonil	77.7	1.5	109.7	8.5
Alpha-endosulphan	97.3	3.1	115.7	7.6
Dieldrin	105.0	3.0	121.3	7.1
Beta-endosulphan	109.7	4.0	116.7	7.4
AV	93.1		97.1	
SD	14.4		30.2	

AV = average mean
CV = coefficient of variation
SD = standard deviation
(a) n = 3

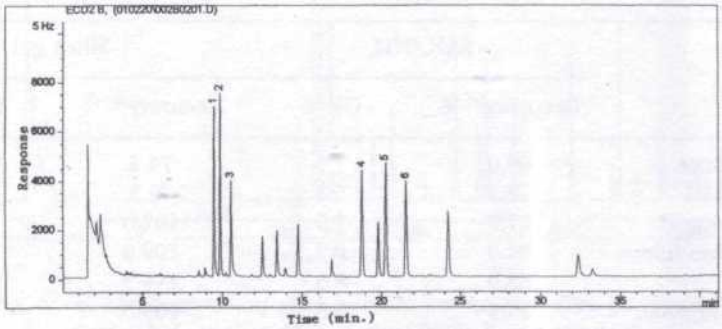

Fig. 3: GC chromatogram of cucumber extract after SPE clean-up. Peaks: 1, hexaconazole; 2, gamma-BHC; 3, chlorothalonil; 4, alpha-endosulfan; 5, dieldrin; 6, beta-endosulfan

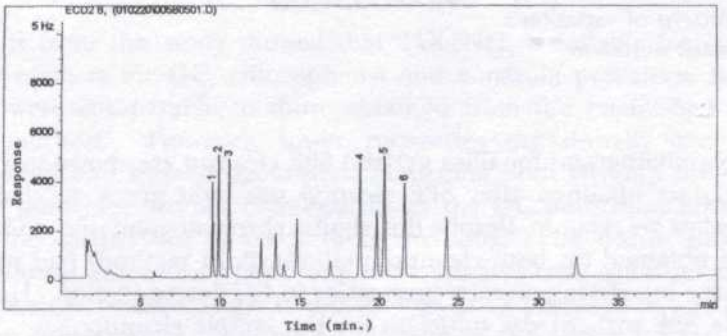

Fig. 4: GC chromatogram of cucumber extract after silica gel clean-up. Peaks: 1, hexaconazole; 2, gamma-BHC; 3, chlorothalonil; 4, alpha-endosulfan; 5, dieldrin; 6, beta-endosulfan

gel cleanups. Similar chromatograms with no interfering peaks were obtained for both cleanup methods. The chromatograms were cleaner as compared to the carrot sample. This was due to fewer compounds present in the cucumber samples which give response to the ECD. It was concluded that a single SPE SAX/NH_2 was sufficient for the cleanup of cucumber sample.

Green Mustard

The results obtained from spiked green mustard samples using SAX/NH_2 and silica gel cleanup are given in Table 4. The recoveries obtained for silica gel cleanup were in the range of 74.3% to 109.3% with CV of 5.0% to 15.0%. Except for chlorothalonil, which showed lower recoveries of 27.3%, the recoveries for other pesticides obtained by SPE SAX/NH_2 were comparable to the silica gel cleanup method. Their recoveries were in the range of 69% to 98.3% with CV of 5.5% to 8.5%. Statistical analysis showed that the calculated t-value was lower than the critical t-value (excluding chlorothalonil). Therefore, there is no significant difference between these two methods.

TABLE 4
Recovery of organochlorine pesticides from spiked green mustard samples using SAX/NH_2 and silica gel cleanup

Pesticide	SAX/NH_2		Silica gel	
	Recovery[(a)] %	CV %	Recovery[(a)] %	CV %
Hexaconazole	69.0	7.6	74.3	5.5
Gamma-BHC	77.7	5.7	72.3	5.0
Chlorothalonil*	27.3	1.5	102.0	7.6
Alpha-endosulphan	84.0	8.2	109.0	7.6
Dieldrin	88.0	8.5	111.3	8.0
Beta-endosulphan	98.3	5.5	109.3	15.0
AV	83.4		95.2	
SD	11.0		20.1	

AV= average mean excluding*
CV = coefficient of variation
SD = standard deviation
(a) n = 3

The chromatograms for silica gel and SPE cleanup are shown in *Figs. 5* and *6*. The extract obtained after SPE cleanup was light green as compared to yellow in silica gel cleanup. Despite this, similar chromatogram with no interfering peaks was obtained for both cleanup methods. Both methods had successfully removed the interfering co-extractives prior to GC determination. Hence, only one single SPE sorbent was sufficient for the sample cleanup.

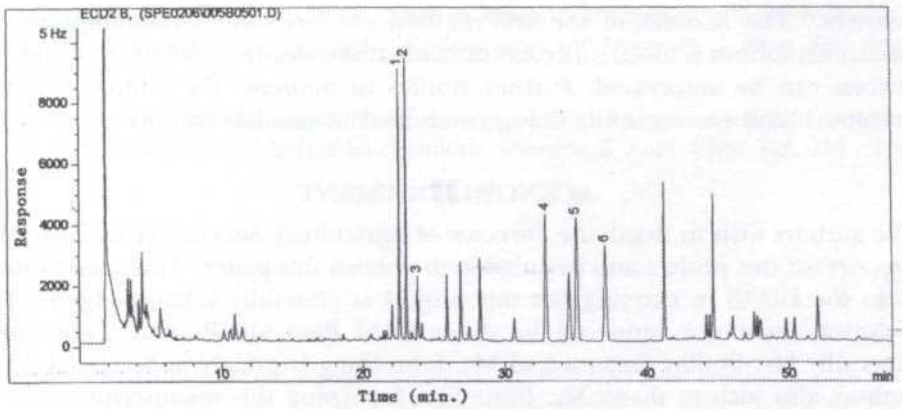

Fig. 5: GC chromatogram of green mustard extract after SPE clean-up. Peaks: 1, hexaconazole; 2, gamma-BHC; 3, chlorothalonil; 4, alpha-endosulfan; 5, dieldrin; 6, beta-endosulfan

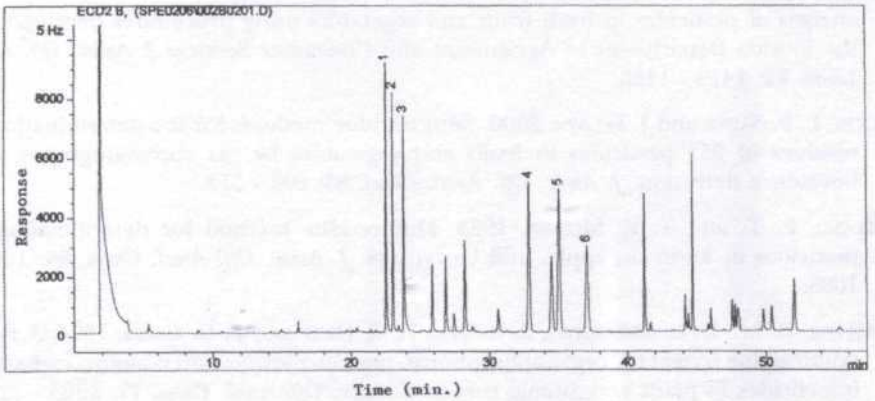

Fig. 6: GC chromatogram of green mustard extract after silica gel clean-up. Peaks: 1, hexaconazole; 2, gamma-BHC; 3, chlorothalonil; 4, alpha-endosulfan; 5, dieldrin; 6, beta-endosulfan

CONCLUSION

The results from this study showed that SAX/NH_2 is suitable for cleanup of vegetable extracts for OC, chlorophenyl and conazole pesticides. Recoveries obtained were comparable to those obtained from the established silica gel cleanup method. However, lower recoveries occasionally occurred for chlorothalonil and hexaconazole pesticides using both cleanup methods. As these two pesticides are not classified under the OC pesticides, further study needs to be carried out to verify these methods. The results showed that sample cleanup with SPE sorbent were more efficient than silica gel method as less chemicals were used (1 g). It also showed great potential as an alternative method to conventional silica gel for cleanup of vegetables extracts and it is possible to extend the application for the analysis of other pesticides and

matrices. The benefits of the SPE method are less solvent consumption, no hazardous solvent is used, no cross-contamination, shorter analysis time and the process can be automated. Further studies to optimise the sample size and detection limit are currently being conducted in our laboratories.

ACKNOWLEDGEMENT

The authors wish to thank the Director of Agriculture Sarawak (DOAS) for his support for this project and permission to publish this paper. Financial support from the DOAS in carrying out this project is gratefully acknowledged. The technical assistance rendered by the staff of Pesticide Residue Laboratory, especially Mr. Phillip Gudom and Mr. John Yong is greatly appreciated. The authors also wish to thank Ms. Irene Sim for typing this manuscript.

REFERENCES

Cook, J., M. P. Beckett, B. Reliford, W. Hammock and M. Engel. 1999. Multiresidue analysis of pesticides in fresh fruits and vegetables using procedures developed by the Florida Department of Agriculture and Consumer Services *J. Assoc. Off. Anal. Chem.* **82**: 1419 - 1435.

Fillion, J., F. Sauve and J. Selwyn. 2000. Multiresidue methods for the determination of residues of 251 pesticides in fruits and vegetables by gas chromatography with floresence detection. *J. Assoc. Off. Anal. Chem.* **83**: 698 - 713.

Holland, P. T. and T. K. Mcghie. 1983. Multiresidue method for determination of pesticides in kiwifruit, apple, and berryfruits. *J. Assoc. Off. Anal. Chem.* **66**: 1003 - 1008.

Holstege, D. M., D. L. Scharberg, E. R. Tor, L. C. Hart and F. D. Galey. 1994. A rapid multiresidue screen for organophosphorus, organochlorine, and n-methyl carbamate insecticides in plant and animal tissues. *J. Assoc. Off. Anal. Chem.* **77**: 1263 - 1274.

Hsu, R. C., I. Biggs and N. K. Saini. 1991. Solid-phase extraction cleanup of halogenated organic pesticides. *J. Agric. and Food Chem.* **39:** 1658 - 1666.

Lee, S. M., M. L. Papathekis, H. M. C. Feng, G. F. Hunter and J. E. Carr. 1991. Multipesticide residue method for fruits and vegetables. *Fresenius Z. Anal. Chem.* **339**: 376 - 383.

Luke, M. A., J. E. Froberg and H. T. Masumoto. 1975. Extraction and cleanup of organochlorine, organophosphate, organonitrogen, and hydrocarbon pesticides in produce for determination by gas-liquid chromatography. *J. Assoc. Off. Anal. Chem.* **58**: 1020 - 1026.

Luke, M. A., J. E. Froberg, G. M. Doose and H. T. Masumoto. 1981. Improved multiresidue gas chromatographic determination of organophosphorus, organonitrogen, and organohalogen pesticides in produce using flame photometric and electrolytic conductctivity detector. *J. Assoc. Off. Anal. Chem.* **64**: 1187 - 1195.

Odanaka, Y., O. Matano and S. Goto. 1991. The use of solid bonded-phase extraction as alternative to liquid-liquid partitioning for pesticide residue analysis of crops. *Fresenius J. Anal. Chem.* **339**: 368 - 373.

SHERIDAN, R. S. and J. R. MEOLA. 1999. Analysis of pesticide residues in fruits, vegetables, and milk by gas chromatography/tandem mass spectrometry. *J. Assoc. Off. Anal. Chem.* **82**: 982 - 990.

STEINWANDTER, H. 1985. Universal 5-min on-line method for extracting and isolating pesticide residues and industrial chemicals. *Fresenius Z. Anal. Chem.* **322**: 752 - 754.

ISSN: 0128-7680
Pertanika J. Sci. & Technol. 11(2): 261 - 272 (2003)

Isolation and Characterization of a Molybdenum Reducing Enzyme in *Enterobacter cloacae* Strain 48

Shukor M. Y. A., C. H. Lee, I. Omar, M. I. A. Karim[1], M. A. Syed & N. A. Shamaan
Department of Biochemistry and Microbiology,
[1]Department of Biotechnology,
Universiti Putra Malaysia,
43400 UPM, Serdang, Selangor, Malaysia

Received: 16 April 2002

ABSTRAK

Enzim yang menurunkan molybdenum telah diasingkan daripada *Enterobacter cloacae* Strain 48 dengan menggunakan pemecahan amonium sulfat, kromatografi pertukaran ion DE-selulosa dan penurasan gel Sephacryl S-200. Elutan daripada penurasan gel Sephacryl S-200 yang telah dipekatkan menunjukkan kehadiran 3 subunit protein masing-masing mempunyai berat molekul 80, 90 dan 100 kDa apabila dilakukan SDS-PAGE. Pencirian aktiviti menurunkan molybdenum oleh fraksi dari elutan Sephacryl S-200 yang dipekatkan dilakukan dengan menggunakan 12-molybdofosfat (12-MoP) sebagai substrat. pH dan suhu optimum bagi tindak balas penurunan molybdenum ialah 5.0 dan 28-33°C. NADH didapati lebih baik daripada NADPH sebagai agen penurun bagi tindak balas tersebut; plot resiprokal berganda aktiviti menurunkan molybdenum melawan NADH dan NADPH masing-masing menghasilkan nilai K_m dan V_{max} 1.65 mM, 6.28 nmol molybdenum biru terhasil/min/mg dan 2.13 mM and 4.10 nmol molybdenum biru terhasil/min/mg. Plot resiprokal berganda aktiviti menurunkan molybdenum melawan 12-MoP dan 20-molybdodifosfat pula menghasilkan nilai K_m 0.3 mM dan 0.4 mM. Nilai V_{max} pula adalah sama bagi kedua-dua substrat iaitu 6 nmole molybdenum biru terhasil/min. Kaedah pengasaian aktiviti menurunkan molybdenum dengan menggunakan 12-MoP didapati lebih mudah dan cepat jika dibandingkan dengan kaedah masa kini yang menggunakan molybdat sebagai substrat.

ABSTRACT

Molybdenum reducing enzyme was isolated from *Enterobacter cloacae* Strain 48 by ammonium sulphate fractionation, DE-cellulose ion-exchange chromatography and Sephacryl S-200 gel filtration. SDS-PAGE of the concentrated Sephacryl S-200 gel filtration eluates revealed the presence of 3 protein subunits of molecular weight 80, 90 and 100 kDa. The active concentrated fraction from the Sephacryl S-200 gel filtration step was then characterized for molybdenum reducing activity with 12-molybdophosphate (12-MoP) as a substrate. The optimum pH and temperature of the reaction was 5.0 and 28-33°C, respectively. NADH was a better reducing agent in the reaction than NADPH; the double reciprocal plot of activity against NADH and NADPH revealed apparent K_m and V_{max} values of 1.65 mM, 6.28 nmole molybdenum blue produced/min/mg and 2.13 mM and 4.10 nmole molybdenum blue produced/min/mg, respectively. The double reciprocal plot of activity against 12-MoP and 20-molybdodiphosphate revealed apparent K_m

values of 0.3 mM and 0.4 mM, respectively. The apparent V_{max} values are similar for both substrates at 6 nmole molybdenum blue produced/min. The assay method for molybdenum reducing activity using 12-MoP was found to be easier and more rapid than the present method of using molybdate as a substrate.

Keywords: Molybdenum reducing enzyme, 12-molybdophosphate, *Enterobacter cloacae* Strain 48

INTRODUCTION

Several heavy metals may be detoxified in bacteria by the action of the metal reductases as shown in the reduction of Fe^{3+} in *Spirillum itersonii, Escherichia coli* and *Paracoccus denitrificans* by ferric reductases (Dailey Jr and Rascelles 1977). The ferric reductase found in *Spirillum itersonii* reduced Fe^{3+} with NADH or succinate as the electron donor and is located in the respiratory chain before cytochrome *c* while in *Azotobacter vinelandii* and *Pseudomonas aeroginosa*, the ferric reductases used NADH as an electron donor and are located in the cytoplasm (Lascelles and Burke 1978; Cox 1980; Huyer and Page 1989).

Molybdenum has been reported to be reduced to molybdenum blue by several bacteria such as *Thiobacillus ferroxidans, Escherichia coli* K12 and *Enterobacter cloacae* Strain 48 with NADH as the electron donor (Campbell *et al.* 1985; Ghani *et al.* 1993; Sugio *et al.* 1988). The molybdenum reducing enzyme in *E. cloacae* Strain 48 has been proposed to be a membrane-bound oxidoreductase, and the reduction reaction carried out anaerobically (Ariff *et al.* 1997).

The reduction of molybdenum to molybdenum blue in *E. cloacae* Strain 48 has been reported to be inhibited by high phosphate concentration (100 mM) in the culture media (6). However, the bacteria was able to reduce the metal when grown in media containing low phosphate concentration (2.9 mM). It has been suggested that high phosphate concentration prevented the formation of molybdophosphates but did not affect the reduction of molybdenum.

Molybdenum reducing activity in bacteria has been assayed using molybdate and NADH, phosphate and other salts at pH 7.0, under anaerobic conditions (Ghani *et al.* 1993). The formation of molybdophosphate complexes (Lee 1977; Sims 1961), which gives the characteristic blue colour of molybdenum blue was determined at 710 nm after the addition of a strong reducing agent such as stannous chloride (Killefer and Linz 1952). The absorption spectrum of molybdenum blue formed by the bacteria is different from that formed chemically (Glenn and Crane 1956). While most of the earlier studies used bacteria culture or crude extracts of the bacteria to demonstrate molybdenum reduction, no work has been carried out to isolate and characterize the protein that catalyses molybdenum reduction.

We report the initial isolation, partial purification and characterization of a molybdenum reducing enzyme in *E. cloacae* Strain 48 to provide evidence that molybdenum reduction in *E. cloacae* strain 48 is catalysed by an enzyme.

MATERIALS AND METHODS

Enterobacter cloacae Strain 48 was grown in 1L minimal salts media, pH 7.0, containing glucose (1.0%), $(NH_4)_2SO_4$ (0.3%), $MgSO_4.7H_2O$ (0.05%), NaCl (0.5%), yeast extract (0.1%), $Na_2MoO_4.2H_2O$ (0.24%) and Na_2HPO_4 (1.72%) at 30°C for 24 h with gentle shaking (100 rpm), following the method of Ghani *et al.* (1993).

Isolation of Molybdenum Reducing Activity

The purification procedure for molybdenum reducing enzyme was carried out at 4°C unless stated otherwise.

Bacterial cells were harvested from 5L minimal salts media, pH 7.0 by centrifugation at 10,000 g for 20 min and the pellet obtained was rinsed three times with distilled water before being resuspended and recentrifuged. The resulting pellet was resuspended in 10 mL 50 mM Tris buffer pH 7.5 and the bacterial cells were lysed by sonication using four cycles of 1 min with 4 min cooling intervals.

The lysed fraction was then centrifuged at 10,000 g for 40 min and the resulting supernatant subjected to 0-80% ammonium sulphate fractionation. Highest molybdenum reducing activity was detected in the pellet of 40-50% ammonium sulphate fractions. The pellet obtained from the 40-50% ammonium sulphate fraction was centrifuged at 10,000 g for 40 min and resuspended in 10 mL 50 mM Tris buffer pH 7.5 containing 5 mM 2-mercaptoethanol. The suspension was then dialysed against 5L of the same buffer for 5 h.

The dialysate (3 mL) was loaded onto a DE-cellulose column (1.6 cm x 35 cm) equilibrated with 50 mM Tris buffer pH 7.5 containing 5 mM β-mercaptoethanol. Five mL fractions were collected at a flow rate of 0.5 mL per min. A linear gradient of 200 mL 0-300 mM NaCl was applied. Proteins were monitored at 280 nm and molybdenum reducing activity assayed in the collected fractions. Fractions that contained molybdenum reducing activity were pooled and concentrated to a minimal volume by ultra-filtration before being applied to a Sephacryl S-200 column (1.6 cm x 60 cm) equilibrated with the same buffer. The fraction volume and flow rate were similar to that used in the ion exchange chromatography procedure. The fractions containing high molybdenum reducing activity were pooled and concentrated by ultra-filtration.

Protein concentration was determined by the method of Bradford (1976) and SDS-PAGE carried out according to the method of Laemlli (1974).

Assay of Molybdenum Reducing Activity Using 12-MoP as the Substrate

This assay was based on the formation of MoP (as 12-MoP) from molybdate and phosphate (Campbell *et al.* 1985). The 12-MoP formed is assumed to accept the electrons from NADH in the reaction catalysed by molybdenum reducing enzyme. The electrons were then trapped in the lattice structure since MoP is known to accept electrons from reducing agents such as dithionite resulting in

the formation of molybdenum blue (Tosi *et al.* 1998). The hypothetical reaction between 12-MoP and NADH is depicted as;

$$\text{12-MoP} + \text{NADH} + H^+ \rightarrow \text{Molybdenum blue} + NAD^+$$

12-MoP was prepared as a 20mM stock solution in distilled water adjusted to pH 5.0 with HCl. To 0.8 mL of reaction mixture consisting of $(NH_4)_2SO_4$ (0.3%), $MgSO_4.7H_2O$ (0.05%) and NaCl (0.5%) at pH 5.0, 0.12 mL 20mM 12-MoP and 20 mL 150mM NADH were added in succession. The reaction was started by the addition of 50 mL partially purified enzyme preparation containing approximately 1 mg protein, and the absorbance monitored after every min at 865 nm.

The reducing activity was calculated based on the extinction coefficient of molybdenum blue of 16.7 $mM^{-1}cm^{-1}$ at 865 nm. One unit of molybdenum reducing activity is defined as the amount of enzyme that is required to catalyse the production of 1 nmole molybdenum blue from 12-MoP per min under the conditions specified.

Molybdenum Reducing Assay Using Molybdate as the Substrate

Molybdenum reducing activity with molybdate as the substrate was determined according to the method described by Ghani *et al.* (1993). Briefly, the reaction mixture consisted of 1 mL solution containing $(NH_4)_2SO_4$ (0.3%), $MgSO_4.7H_2O$ (0.05%) and NaCl (0.5%) at pH 7.0, 0.4 mL 0.5M molybdate, 0.5 mL 20mM Na_2HPO_4 and 0.1 mL 80mM NADH. To start the reaction, 20 mL of partially purified enzyme preparation containing approx. 20 mg protein was added to the reaction mixture. Nitrogen gas was pumped into the cuvette for approx. 30 s. The mixture was incubated for 1 h at 28°C after which the absorbance at 710 nm was measured. The amount of molybdenum blue was calculated from a standard curve of molybdenum reduced by stannous chloride in the presence of phosphate.

Effect of pH and Temperature on Molybdenum Reducing Enzyme

To study the effect of pH on molybdenum reducing activity, 50 uL of partially purified enzyme preparation (approx. 0.1 mg) was added to a total volume of 2.0 mL reaction mixture of various pHs containing 4.8 umol 12-MoP, 8 umol NADH and 0.4 mmol potassium antimonyl tartarate. The reaction mixture was incubated at 28°C and absorbance at 865 nm measured at 1 min intervals.

The effect of temperature on molybdenum reducing activity was tested under conditions similar to that used in the study of the effect of pH on molybdenum reducing activity. However, potassium antimonyl tartarate was added to act as a catalyst for the reduction of 12-MoP at temperatures lower than 30°C (Tosi *et al.* 1998; Clesceri *et al.* 1989). The reaction mixture was incubated at various temperatures for 20 min in a temperature-controlled water bath and the reaction started by adding 0.1 mg partially purified enzyme. The

reaction mixture was then incubated for another 10 min after which the absorbance at 865 nm was read.

Effect of NADH and NADPH on Molybdenum Reducing Activity

To 1.60 mL reaction mixture pH 5.0 containing 3 mM 12-MoP and 0.2 mM potassium antimonyl tartarate, 0.1 mL of NADH and NADPH were added. Distilled water was added to make up the total volume to 2 mL. To start the reaction, 50 uL of partially purified enzyme preparation containing approx. 0.1 mg protein, was added and after 1 min the absorbance at 865 nm was read.

Effect of 12-MoP and 20-Molybdodiphosphate on Molybdenum Reducing Activity

12-MoP($H_3Mo_{12}O_{40}P$, Mo:P ratio 12:1) and 20-molybdodiphosphate ($20MoO_4 2H_3PO_4.2H_2O$, Mo:P ratio 20:2) were prepared as 20 mM solutions in 50 mM citrate phosphate buffer pH 5.0. The cloudy solution became clear when left stirring overnight.

40 µL of 150 mM NADH was added to 1.60 mL of reaction mixture pH 5.0 containing 3 mM 12-MoP or 20-molybdodiphosphate and 0.2 mM potassium antimonyl tartarate. When 20-molybdodiphosphate was used, the potassium antimonyl tartarate was excluded. Distilled water was added so that the total volume was 2 mL. The reaction was started by the addition of 50 uL partially purified enzyme preparation containing approx. 0.1 mg protein. The absorbance at 865 nm was read after one min intervals.

RESULTS

Isolation of Molybdenum Reducing Enzyme

Molybdenum reducing enzyme in *E. cloacae* Strain 48 had been isolated by 40-50% ammonium sulphate fractionation followed by ion exchange on DE-cellulose and gel filtration on Sephacryl S-200. The results of the purification procedure are summarised in Table 1. Ammonium sulphate fraction was an excellent method for isolating the enzyme with a 6.5 fold purification while the recovery was kept high at 97% of the initial value. Ion exchange chromatography on DE-cellulose of the salt fraction yielded a single peak (*Fig. 1*). Although the purification was impressive with a high purification fold, a large reduction in activity was recorded for the ion exchange and gel filtration steps (*Fig. 2*). The final yield was 1.6% of the initial value and the final specific activity was 240 unit/mg protein realizing a purification of 40-fold over the initial value.

For both the ion exchange and gel filtration chromatographic steps, the volume of the active fractions were large and molybdenum reducing activity was low, making it necessary to concentrate the eluates. The concentrated eluates from the Sephacryl S-200 gel filtration step was subsequently used in characterization of the enzyme. SDS-PAGE of the concentrated eluates from the Sephacryl S-200 gel filtration step showed 3 protein subunits of estimated molecular weights of 80, 90 and 100 kDa (*Fig. 3*).

TABLE 1
A summary of the purification of molybdenum reducing enzyme in *Enterobacter cloacae* Strain 48

Fraction	Total Protein (mg)	Total Activity (Units)	Specific Activity (Unit/mg protein)	Fold Purification	Yield %
Crude homogenate	5000	30,000	6.0	1	100
40-50% saturated ammonium sulphate	750	29,000	39.0	6.5	97.0
DE-cellulose	40	4,500	113.0	18.8	15.0
Sephacryl S-200	2	480	240	40.0	1.6

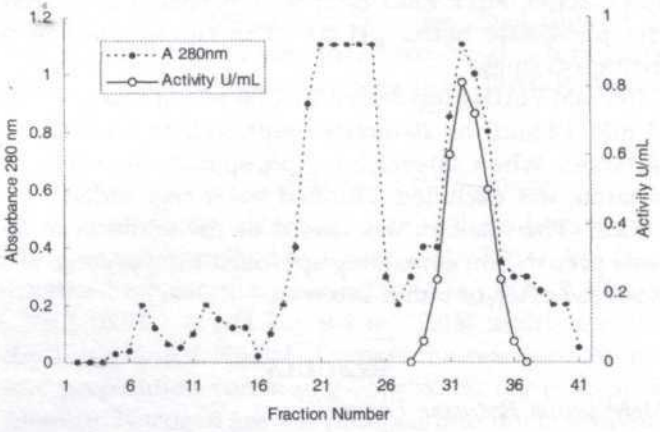

Fig. 1: DE-cellulose ion exchange chromatography profile of molybdenum reducing enzyme in E. cloacae Strain 48. A 0-0.3M NaCl gradient was applied between fractions 5 - 40

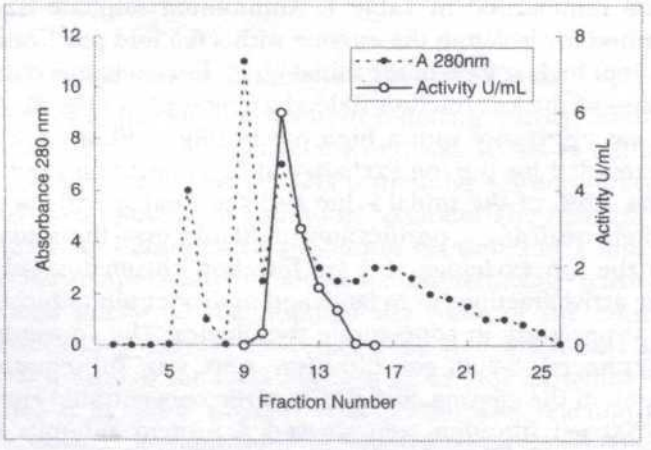

Fig. 2: Sephacryl S-200 gel filtration profile as a purification step molybdenum reducing enzyme in E. cloacae Strain 48

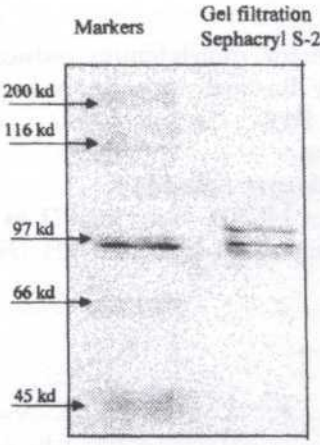

Fig. 3: SDS-PAGE of the molybdenum reducing enzyme purified in E. cloacae Strain 48. The concentrated eluate of Sephacryl S-200 gel filtration step was applied to SDS-PAGE. Staining of the electrophoresed sample with Coomassie brilliant blue yield 3 subunits of estimated molecular weight of 80, 90 and 100 kDa

Characterisation of Molybdenum Reducing Enzyme

Optimum pH

Fig. 4 shows the optimum pH for molybdenum reducing enzyme to be pH 5.0. There was almost no activity at pH 7.0 and above. The activities detected were between the range of pH 3.5 – 6.0. Molybdenum reducing activity mainly occurs in acidic pH.

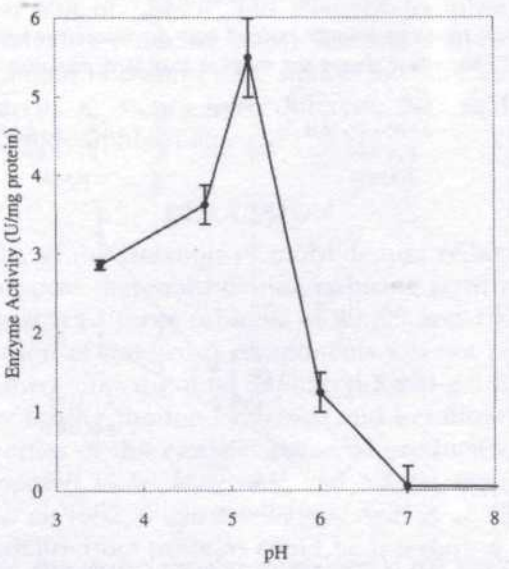

Fig. 4: Molybdenum reducing activity over pH range of 3.0 to 8.5. The values shown are mean ± standard deviation

Optimum Temperature

The optimum temperature for molybdenum reducing activity was between 28-33°C (*Fig. 5*). The activity drastically dropped at higher temperatures and no activity was detected below 20°C.

NADH and NADPH as Reducing Agents

A double reciprocal plot of NADH and NADPH as substrates revealed that NADH was a better reducing agent than NADPH (*Fig. 6*). The apparent V_{max}

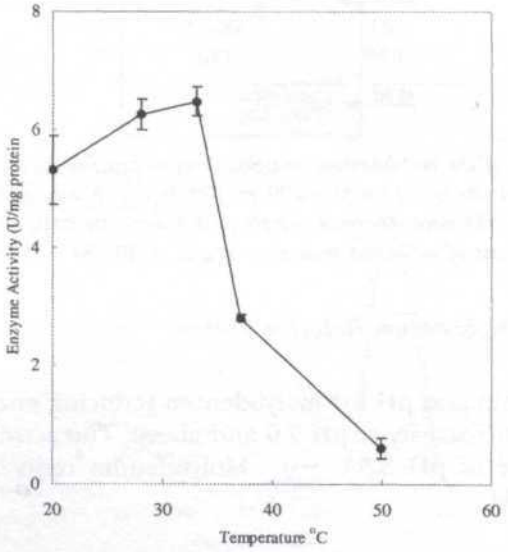

Fig. 5: Molybdenum reducing activity assayed over a temperature range of 20 – 50°C. The values shown are mean ± standard deviation

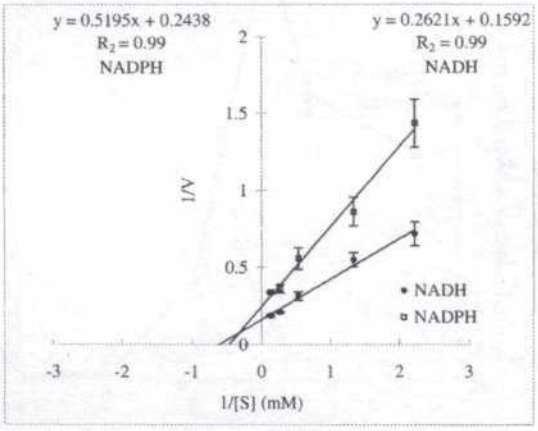

Fig. 6: Double reciprocal plot of molybdenum reducing activity with NADPH and NADH as reducing agents. The values shown are mean ± standard deviation. V, nmol molybdenum blue produced/min/mg protein under the conditions specified; (S), mM NADH or NADPH

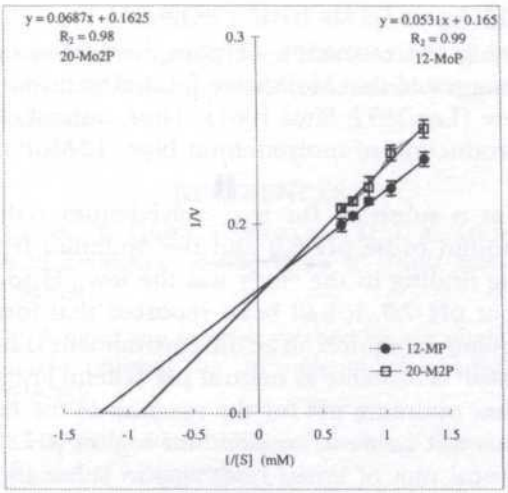

Fig 7: Double reciprocal plots of two different substrates in molybdenum reducing activity. The values shown are mean ± standard deviation. V, nmol molybdenum blue produced/ min/mg protein under the conditions specified; (S), mM 12-molybdophosphate (12-MP) or 20-molybdodiphosphate (20-M2P)

and K_m values for NADH were 6.28 nmole molybdenum blue produced/min and 1.65 mM, while for NADPH, the values were 4.10 nmole molybdenum blue produced /min and 2.13 mM, respectively.

12-MoP and 20-Molybdodiphosphate as Oxidants

A double reciprocal plot of 12-MoP and 20-molybdodiphosphate as electron acceptors for molybdenum reducing activity showed that the apparent V_{max} of 6.10 nmole molybdenum blue/min were similar for both compounds (*Fig. 7*). However, the apparent K_m values were different; 0.32 mM for 12-MoP and 0.42 mM for 20-molybdodiphosphate.

DISCUSSION

Based on the results of the isolation of molybdenum reducing activity in the present study, we propose that molybdenum reducing activity is catalysed by an enzyme comprising at least three subunits of 80, 90 and 100 kDa in size.

Further purification of the active components was not possible due to the very low yield obtained after the final Sephacryl S-200 gel filtration step. The large loss in activity during the ion exchange and gel filtration step could be linked to the properties of the enzyme. Bacterial production of molybdenum blue had been proposed to be anaerobic and NADH dependent (Campbell *et al.* 1985; Ghani *et al.* 1993; Sugio *et al.* 1988; Ariff *et al.* 1997). Possibly, the cofactors(s) that stabilized the proteins could be lost during the ion exchange step and being continuously exposed to oxygen could further contribute to the loss of activity.

Molybdate could be reduced to molybdenum blue in the presence of phosphates, indicating the formation of phosphomolybdate (Campbell *et al.* 1985). It has been suggested that MoPs were formed transiently from molybdate to molybdenum blue (Lee 1977; Sims 1961). Thus, instead of molybdate as the substrate for the production of molybdenum blue, 12-MoP may be used as an alternative.

Using 12-MoP as a substrate for the molybdenum reducing activity, the optimum pH was found to be pH 5.0 and the optimum temperature around 30°C. An interesting finding in the study was the low pH for the reaction and the lack of activity at pH 7.0. It had been reported that formation of 12-MoP and molybdates in general, requires an acidic environment (Lee 1977; Braithwaite 1981) and that 12-MoP is unstable at neutral pH (Glenn and Crane 1956). This could explain the low optimum pH for the reaction of the enzyme on 12-MoP, since the substrate is not stable at neutral and higher pH.

A double reciprocal plot of initial rates against substrate concentrations at 2.4 mM 12-MoP registered a higher apparent V_{max} for NADH than NADPH (6.28 and 4.10 nmole/min, respectively), but the apparent K_m for NADH was lower than NADPH (1.65 and 2.13 mM, respectively). It seemed that NADH is the prefered reducing agent of molybdenum reducing activity over NADPH.

At 3mM NADH, the double reciprocal plots against 12-MoP and 20-molybdodiphosphate yielded a similar apparent V_{max} value of 6.10 nmole/min but different apparent K_m values of 0.32 and 0.42 mM, respectively. It is obvious that 12-MoP is preferred over 20-molybdodiphosphate.

The concentration of 12-MoP was found to be critical for the reaction. A significant reduction in activity was observed above 3mM 12-MoP concentrations. Also, low molybdenum reducing activity was observed at low 12-MoP concentration. It seemed that molybdenum reducing activity is at an optimum between 1 - 3 mM 12-MoP. The possibility of molybdenum reducing enzyme being allosteric could not be discounted since the preparation used comprised at least 3 subunits by SDS-PAGE.

Potassium antimonyl tartarate seemed to assist in the formation of molybdenum blue from 12-MoP. It was reported that 12-MoP is unstable in very dilute solution and potassium antimonyl tartarate functioned as a stabilising agent in the phosphate determination method (Clesceri *et al.* 1989).

We have found that the assay for molybdenum reducing activity using 12-MoP as the substrate to be advantageous over the use of molybdate; it is rapid, can be completed in a few min and did not require nitrogen as the gas phase. The assay method of using molybdate as the substrate required a much longer time to complete the reaction, phosphate to be added as a reactant and nitrogen as the gas phase. It was also found that V_{max} for 12-MoP was several folds higher than molybdate, making it a more rapid assay to perform.

In conclusion, evidence has been provided to support the suggestion that molybdenum reduction in *E. cloacae* strain 48 is catalysed by an enzyme consisting of three subunits and is dependent on NADH. An assay for molybdenum reducing activity using 12-MoP as a substrate has been proposed.

ACKNOWLEDGEMENTS

This project was supported by funds from The Ministry of Science, Technology and the Environment, Malaysia, Japan International Cooperation Agency and Universiti Putra Malaysia.

REFERENCES

ARIFF, A. B., M. ROSFARIZAN, B. GHANI, T. SUGIO and M. I. A. KARIM. 1997. Molybdenum reducing activity in *Enterobacter cloacae* Strain 48. *World Journal of Microbiology and Biotechnology* **13**: 643-647.

BRADFORD, M. M. 1976. A rapid and sensitive method for the quantitation of microgram quantities of protein utilizing the principle of protein-dye binding. *Analytical Biochemistry* **72**: 248-252.

BRAITHWAITE, E.R. 1981. Molybdenum. In *Specialty Inorganic Chemicals,* ed. R. Thompson. London: Royal Society of Chemistry.

CAMPBELL, A. M., A. D. CAMPBELL and D. B. VILLARET. 1985. Molybdate reduction by *Escherichia coli* K12 and its *chl* mutants. *Proceedings of the National Academy of Sciences, USA* **82**: 227-231.

CLESCERI, L. S., A. E. GREENBERG and R. R. TRUSSEL. 1989. *Standard Methods for the Examination of Wastewater.* p. 4-166 – 4-178. 17th ed. Baltimore, Md: American Public Health Association, Port City Press, Baltimore, Maryland.

COX, C. D. 1980. Iron reductases from *Pseudomonas aeruginosa. Journal of Bacteriology* **141**: 199-204.

DAILEY JR. H. and J. RASCELLES. 1977. Reduction of iron and synthesis of protoheme by *Spirillum itersonii* and other organisms. *Journal of Bacteriology* **129:** 815-820.

GHANI, B., M. TAKAI, N. ZUL HISHAM, N. KISHIMITO, MOHAMED A. K. ISMAIL, T. TANO and T. SUGIO. 1993. Isolation and characterization of a Mo^{6+} - reducing bacterium. *Applied and Environmental Microbiology* **59**: 1176-1180.

GLENN, J. L. and F. L. CRANE. 1956. Studies of metalloflavoproteins V. The action of silicomolybdate in the reduction of cytochrome C by aldehyde oxidase. *Biochimica et Biophysica Acta* **22**: 111-115.

HUYER, M. and W. G. PAGE. 1989. Ferric reductase activity in *Azotobacter vinelandii* and its inhibition by Zn^{2+}. *Journal of Bacteriology* **171**: 4031-4037.

KILLEFER, D. H. and A. LINZ. 1952. *Molybdenum Compounds, Their Chemistry and Technology.* New York: Interscience Publisher.

LAEMLLI, U. K. 1974. Cleavage of structural proteins during the assembly of the head of bacteriophage T_4. *Nature* **227**: 680 – 685.

LASCELLES, J. and K. A. BURKE. 1978. Reduction of ferric iron by L-lactate and DL-glycerol-3-phosphate in membrane preparations from *Staphylococcus aureus* and interactions with nitrate reductase system. *Journal of Bacteriology* **134**: 585-589.

LEE, J. D. 1977. *Concise Inorganic Chemistry.* 3rd edition. New York: Van Reinhold Co.

Sims, R.P.A. 1961. Formation of heteropoly blue by some reduction procedures used in the microdetermination of phosphorus. *Analyst* **86**: 584-590.

Sugio, T., Y. Tsujita, T. Katagiri, K. Inagaki and T. Tano. 1988. Reduction of Mo^{6+} with elemental sulfur by *Thiobacillus ferreoxidans*. *Journal of Bacteriology* **181**: 5956-5959.

Tosi, E. A., A. F. Cazzoli and L. M. Tapiz. 1998. Phosphorus in oil. Production of molybdenum blue derivative at ambient temperature using noncarcinogenic reagents. *Journal of American Official Chemical Societies* (Abstr.) **75**: 41-44.

ISSN: 0128-7680
Pertanika J. Sci. & Technol. 11(2): 273 - 282 (2003)

Bahan Transduser Gas CO_2 Menggunakan Timol Biru Terdop dalam Membran Kitosan

Musa Ahmad & Nur Mazidah Shahidan
Pusat Pengajian Sains Kimia dan Teknologi Makanan
Fakulti Sains dan Teknologi
Universiti Kebangsaan Malaysia
43600 Bangi, Selangor, Malaysia

Diterima: 23 Mei 2002

ABSTRAK

Bahan transduser untuk pengesanan gas CO_2 telah disediakan dalam kajian ini dengan mendopkan penunjuk pH, timol biru dalam membran kitosan. Hasil kajian menunjukkan timol biru berjaya dipegunkan dalam membran kitosan dan masih dapat mengekalkan rangsangan terhadap kehadiran gas CO_2 seperti dalam larutan. Kelakuan penunjuk ini dalam larutan bebas dan larutan kitosan terhadap gas ini turut dikaji sebagai perbandingan. Dua parameter yang dikaji adalah kesan kepekatan gas CO_2 dan kebolehulangan penunjuk.

ABSTRACT

A transducer material for CO_2 gas detection was prepared in this study by doping pH indicator, thymol blue in chitosan membrane. The results showed that thymol blue was successfully immobilised in chitosan membrane and still maintains its response to the presence of this gas as in solution. The behavior of the indicator in free solution, and chitosan solution towards CO_2 gas was also studied for comparison. The two parameters studied were the effect of CO_2 gas concentration and the reproducibility of the indicator.

Kata kunci: Bahan transduser, gas CO_2, timol biru, membran kitosan

PENGENALAN

Kitosan merupakan suatu poliamina (poli-D-glukosamina) linear dan terdiri daripada kumpulan amina dan hidroksi yang reaktif. Polimer semula jadi ini terbiodegradasi dan selamat digunakan. Sifat-sifat ini membolehkan kitosan digunakan dalam bidang perubatan sebagai antitumor, antikolesterol, meningkatkan pembentukan tulang dan mengurangkan tekanan sistem pusat.

Dalam kajian ini, penunjuk timol biru dipegunkan dalam membran kitosan untuk menghasilkan suatu bahan transduser yang dapat mengesan kehadiran gas CO_2. Seperti diketahui umum, gas CO_2 merupakan hasil sampingan daripada kebanyakan proses perindustrian, pembakaran bahan api dan juga pemusnahan kawasan perhutanan. Pengesanan gas CO_2 adalah penting kepada alam sekitar, analisis bioperubatan dan kimia analisis. Kehadiran gas ini akan menyebabkan penunjuk bertindak balas dan seterusnya menghasilkan isyarat kolorimetrik yang boleh dikesan oleh pengesan. Penunjuk timol biru dipilih kerana murah,

mudah didapati, stabil secara kimia, mempunyai ketoksikan yang rendah, tidak membentuk mendakan dengan analit dan mempunyai kepekaan yang tinggi. Membran kitosan pula dipilih sebagai penyokong dalam kajian ini kerana proses pemegunan reagen dapat dilakukan dengan mudah. Selain daripada itu, kitosan bersifat lengai kimia, stabil di udara dan tidak toksik. Sifat membran kitosan yang lutsinar dan mempunyai bentuk yang sekata membolehkan bahan transduser CO_2 yang dihasilkan dicirikan dengan kaedah spektroskopi serapan menggunakan Spektrofotometer UL-Nampak. Kajian kami sebelum ini banyak ditumpukan kepada pemegunan penunjuk pH dalam filem sol-gel sama ada sebagai transduser untuk pengesanan gas CO_2 (Ahmad dan Quah 1997; Ahmad dan Liew 1996; Ahmad dan Azizan 2001) atau untuk digunakan dalam titratan asid-bes (Ahmad dan Tan 2001).

EKSPERIMEN

Penyediaan Larutan

Larutan timol biru disediakan dengan menambahkan 0.2032 g serbuk timol biru ke dalam 30 mL NaOH 0.1 M. Larutan dicairkan ke isi padu 250 mL di dalam kelalang isi padu 250 mL. Larutan bes NaOH 0.1M disediakan dengan melarutkan 1.0328 g ketulan pepejal NaOH di dalam air suling dan larutan dicairkan hingga ke paras senggatan kelalang isi padu 250 mL. Larutan asid asetik 1% disediakan dengan memasukkan sebanyak 5 mL asid asetik glasial ke dalam kelalang isi padu 500 mL yang mengandungi sedikit air dan campuran dicairkan ke paras senggatan dengan pelarut yang sama. Larutan kitosan 1% disediakan dengan melarutkan 5.005 g kitosan ke dalam asid asetik glasial yang dicairkan dengan 500 mL air suling (asid asetik 1%). Larutan dikacau dengan menggunakan pengacau magnet selama 24 jam bagi menghasilkan larutan yang homogen.

Peralatan

Semua pengukuran serapan dalam kajian ini telah dilakukan menggunakan alat Spektrofotometer UL- Nampak jenama Varian, model Cary 100. Pengukuran pH dilakukan menggunakan Meter pH model Cyberscan manakala alat Trace Gas Mixer digunakan untuk mengawal kadar percampuran gas CO_2 dan N_2 untuk mendapatkan peratusan komposisi gas CO_2 yang berbeza.

Pemegunan Reagen dalam Membran Kitosan

Membran kitosan yang terpegun dengan larutan reagen timol biru disediakan dengan menambahkan 10 mL larutan timol biru ke dalam 50 ml larutan kitosan. Larutan kemudiannya dituangkan ke dalam piring petri dan dikeringkan di dalam oven pada suhu 30°C selama 5 hari. Membran kitosan terpegun yang telah dikeringkan dipotong mengikut ukuran 50 mm × 25 mm.

Pencirian Penunjuk

Spektrum serapan timol biru direkodkan pada julat panjang gelombang 350-700 nm. Gas CO_2 dialirkan pada kadar 5 mL $minit^{-1}$ untuk melihat rangsangan kehadiran gas ini terhadap timol biru dalam keadaan larutan dan terpegun dalam membran kitosan.

Analisis kebolehulangan yang merujuk kepada pengukuran yang dilakukan beberapa kali menggunakan sampel yang sama (Alabbas *et al.* 1989) dilakukan dalam kajian ini sebanyak 7 kali. Spektrum serapan timol biru direkodkan sebelum dan selepas gas CO_2 dialirkan. Dalam kajian ini gas CO_2 dialirkan pada kadar 5 mL min-1 selama 1 min. Kesan kepekatan gas CO_2 berbeza terhadap rangsangan timol biru dikaji dengan mengalirkan gas CO_2 dan gas N_2 ke dalam alat pencampur gas untuk mendapatkan gas CO_2 dengan kepekatan yang berbeza. Kepekatan CO_2 yang digunakan adalah 0%, 25%, 50%, 75% dan 100%.

HASIL DAN PERBINCANGAN

Membran kitosan yang mikroporos dihasilkan dalam kajian ini melalui kaedah tuangan dengan mengeringkan larutan kitosan pada suhu 30°C selama 5 hari. Sifat membran kitosan yang mikroporos ini membolehkan molekul penunjuk pH terperangkap di antara rantaian polimer glukosamina. Molekul-molekul kitosan bersifat hidrofilik kerana mengandungi kumpulan-kumpulan reaktif (-OH dan $-NH_2$) yang banyak dan ini membolehkan pemerangkapan penunjuk berlaku dengan mudah (Xianfang dan Eli 1996).

Pencirian Timol Biru dalam Larutan Bebas

Timol biru yang digunakan dalam kajian ini merupakan ahli kumpulan sulfonaftalein (Fluka 1985), mempunyai julat pH 8.0-9.6 dan memberikan perubahan warna dari kuning dalam keadaan asid ke warna biru dalam keadaan bes (Kolthoff dan Bruckenstein 1959). Secara kimia, perubahan yang berlaku boleh diwakilkan oleh tindak balas kimia seperti yang digambarkan dalam *Rajah 1.*

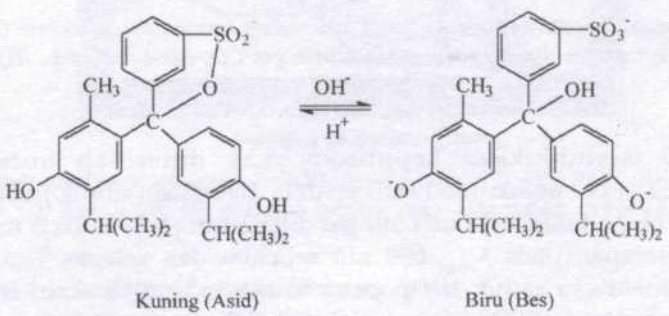

Rajah 1: Keseimbangan reagen pH dalam larutan asid dan bes bagi penunjuk timol biru

Rajah 2 menunjukkan spektrum serapan penunjuk timol biru dalam larutan bebas apabila gas CO_2 dialirkan pada sela masa 0.5 min selama 2 min. Seperti diperhatikan, semakin lama didedahkan kepada gas CO_2, keamatan serapan reagen timol biru pada panjang gelombang 600 nm semakin berkurangan. Warna larutan juga didapati berubah dari warna biru ke kuning. Ini adalah disebabkan oleh sifat kebesan larutan timol biru yang menjadi semakin berkurang apabila gas CO_2 dialirkan. Peningkatan sifat asid larutan penunjuk timol biru ditunjukkan oleh peningkatan serapan pada panjang gelombang sekitar 450 nm. Penurunan serapan ini berlaku hingga ke satu tahap di mana semua larutan timol biru telah bertukar kepada asid. Pemerhatian ini memungkinkan penunjuk timol biru digunakan untuk pengesanan gas CO_2 sekiranya tidak terdapat gas-gas berasid lain yang hadir semasa penentuan dilakukan. Potensi reagen fenolftalein (Ahmad dan Quah 1997), timol biru (Ahmad dan Azizan 2002) dan bromotimol biru (Ahmad dan Azizan 2001) yang terdop dalam filem sol-gel untuk pengesanan gas CO_2 telah dibincangkan sebelum ini. Mekanisme pengesanan gas CO_2 menggunakan penunjuk pH telah dibincangkan oleh Mills dan Qing (1994).

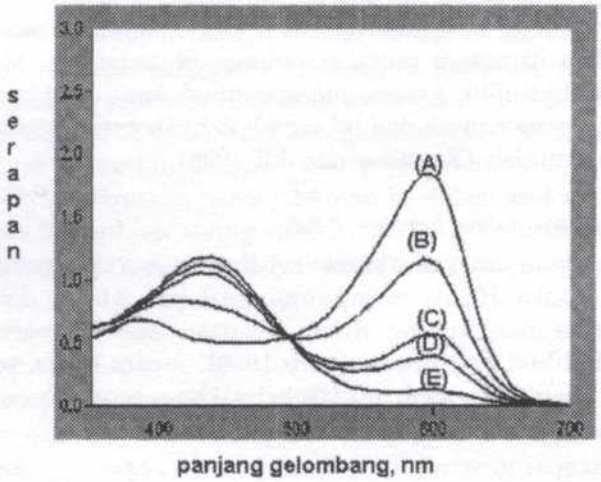

Rajah 2: Spektrum serapan timol biru dalam larutan bebas sebelum (A) dan selepas didedahkan kepada aliran gas CO_2 selama 0.5 min (B), 1.0 min (C), 1.5 min (D) dan 2.0 min (E)

Rajah 3 menunjukkan keputusan yang diperoleh untuk analisis kebolehulangan penunjuk timol biru apabila digunakan untuk pengesanan gas CO_2. Dalam eksperimen ini, kadar alir gas ditetapkan pada kadar 5 mL min^{-1} dan perubahan serapan pada λ_{maks} 600 nm sebelum dan selepas 1 min gas CO_2 dialirkan direkodkan untuk setiap pengukuran yang dilakukan. Nilai peratus sisihan piawai relatif (RSD) bagi analisis kebolehulangan dalam larutan bebas timol biru ialah 13.6%.

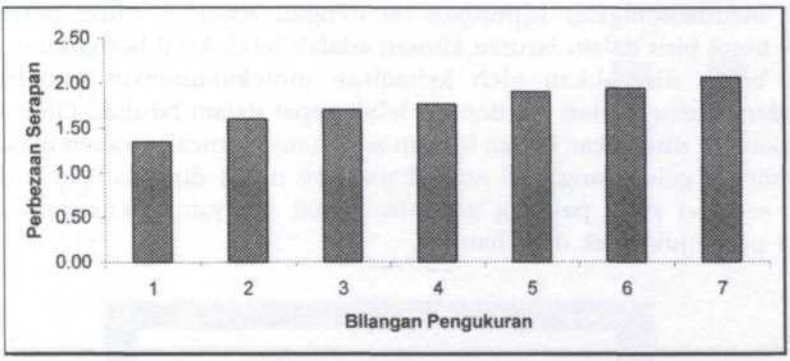

Rajah 3: Graf nilai perubahan serapan pada λ_{maks} 596 nm melawan bilangan pengukuran untuk analisis kebolehulangan reagen timol biru terhadap gas CO_2 dalam larutan bebas

Rajah 4 menunjukkan rangsangan reagen timol biru apabila didedahkan kepada gas CO_2 pada kepekatan yang berbeza. Daripada keputusan ini, semakin tinggi kepekatan gas CO_2 yang dialirkan masuk ke dalam larutan timol biru, semakin banyak penurunan yang berlaku pada nilai serapan pada λ_{maks} 600 nm. Ini berlaku kerana kuantiti CO_2 yang banyak akan menyebabkan molekul timol biru menghasilkan spesies asid yang berwarna kuning dan sifat kebesan timol biru berkurangan.

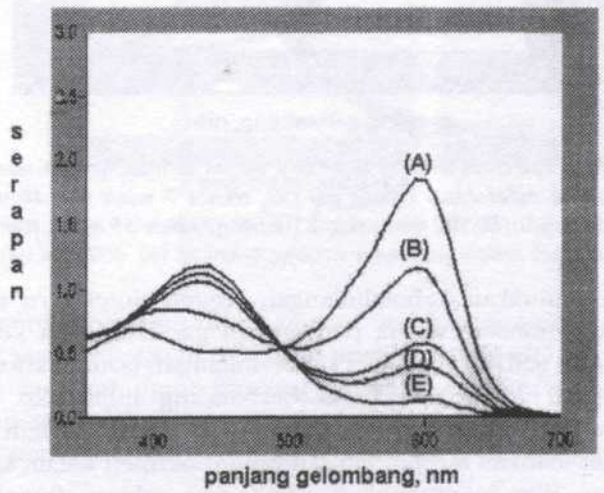

Rajah 4: Spektrum kesan kepekatan gas CO_2 berbeza iaitu 0% (A), 25% (B), 50% (C), 75% (D) dan 100% (E) terhadap serapan timol biru dalam larutan bebas

Pencirian Timol Biru dalam Larutan Kitosan

Rajah 5 menunjukkan spektrum serapan timol biru dalam larutan kitosan apabila gas CO_2 dialirkan secara berterusan untuk tempoh selama 30 min.

Apabila membandingkan keputusan ini dengan *Rajah 2*, kadar penurunan serapan timol biru dalam larutan kitosan adalah lebih kecil berbanding dalam larutan bebas disebabkan oleh kehadiran molekul-molekul kitosan yang menghalang pemelarutan gas dengan lebih cepat dalam larutan. Oleh kerana larutan kitosan disediakan dalam larutan asid, hanya puncak serapan maksimum pada panjang gelombang 436 nm sahaja yang dapat diperhatikan manakala puncak serapan pada panjang gelombang 600 nm yang menunjukkan sifat kebesan penunjuk tidak diperhatikan.

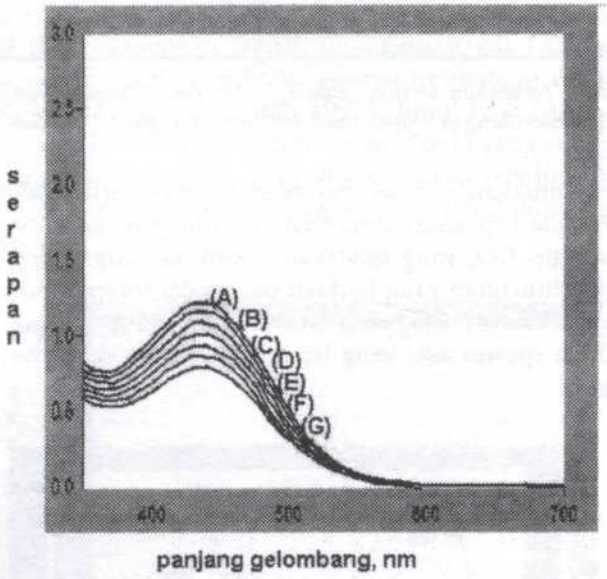

Rajah 5: Spektrum serapan timol biru dalam larutan kitosan sebelum (A) dan selepas didedahkan kepada gas CO_2 selama 5 minit (B), 10 minit (C), 15 minit (D), 20 minit (E), 25 minit (F) dan 30 minit (G)

Rajah 6 menunjukkan kebolehulangan reagen timol biru dalam larutan kitosan apabila digunakan untuk pengesanan gas CO_2 pada kepekatan yang sama. Nilai peratus RSD bagi analisis kebolehulangan larutan kitosan timol biru ialah 47.8%. Nilai ini adalah besar berbanding nilai RSD untuk kajian kebolehulangan yang dilakukan untuk penunjuk dalam larutan bebas (*Rajah 3*). Ini adalah disebabkan larutan kitosan yang diperoleh dalam kajian ini tidak begitu homogen dan menyebabkan sebahagian cahaya dipantulkan keluar semasa pengukuran serapan dilakukan. Kehilangan isyarat ini menyebabkan keamatan serapan yang berbeza diperoleh walaupun kepekatan penunjuk timol biru dalam larutan kitosan berkenaan adalah sama.

Rajah 7 menunjukkan spektrum serapan timol biru dalam larutan kitosan apabila kepekatan gas CO_2 yang berbeza dialirkan kepadanya pada suatu tempoh masa yang tetap. Hasil kajian menunjukkan penunjuk timol biru dalam larutan kitosan memberikan respons berbeza terhadap kepekatan gas CO_2 yang

Rajah 6: Graf nilai perubahan serapan pada λmaks 436 nm melawan bilangan pengukuran untuk analisis kebolehulangan reagen timol biru terhadap gas CO_2 dalam larutan kitosan

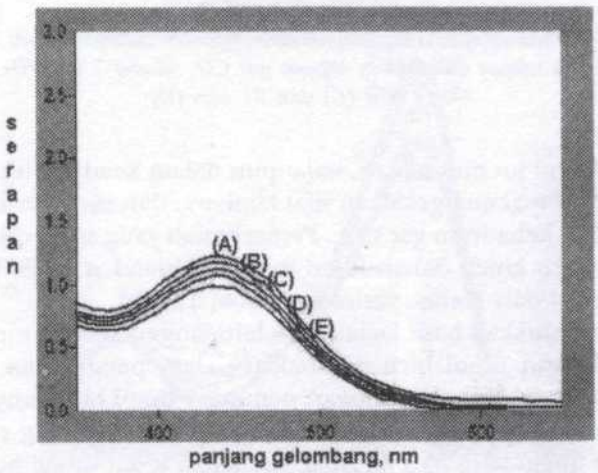

Rajah 7: Spektrum kesan kepekatan gas CO_2 berbeza iaitu 100% (A), 75% (B), 50% (C), 25% (D) dan 0% (E) terhadap serapan timol biru dalam larutan kitosan

berlainan. Seperti yang telah dibincangkan untuk penunjuk timol biru dalam larutan bebas, pada kepekatan CO_2 yang tinggi, kuantiti CO_2 yang banyak akan menyebabkan molekul timol biru menghasilkan spesies asid. Oleh kerana larutan kitosan sendiri bersifat asid, pengaliran gas CO_2 akan menambahkan sifat keasidan penunjuk berkenaan pada kadar yang perlahan.

Pencirian Timol Biru Terdop dalam Membran Kitosan

Rajah 8 menunjukkan spektrum serapan penunjuk timol biru yang terpegun dalam membran kitosan apabila gas CO_2 dialirkan secara berterusan pada sela masa 7 min selama 21 min. Perubahan keamatan serapan setelah pengaliran gas CO_2 menunjukkan reagen timol biru terdop dalam membran kitosan dapat memberikan rangsangan yang baik apabila gas CO_2 dialirkan. Bentuk spektrum yang diperoleh adalah menyamai dengan spektrum serapan dalam larutan

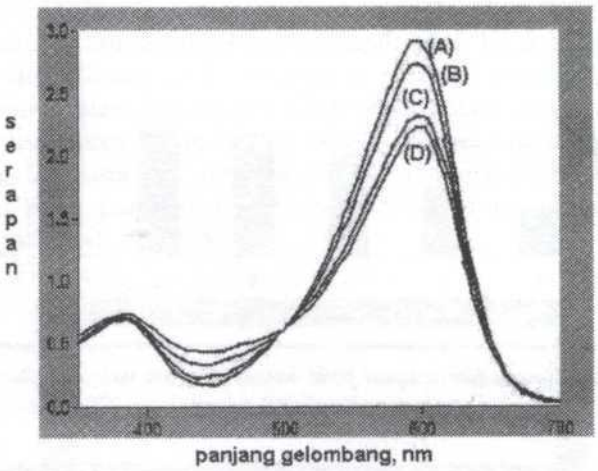

Rajah 8: Spektrum serapan reagen timol biru dalam membran kitosan sebelum (A) dan selepas didedahkan kepada gas CO_2 selama 7 min (B), 14 min (C) dan 21 min (D)

bebas (*Rajah 2*). Ini menunjukkan, walaupun dalam keadaan terdop, penunjuk timol biru masih dapat mengekalkan sifat kimianya dan memberikan rangsangan yang baik dengan kehadiran gas CO_2. Pemerhatian yang sama dilaporkan untuk pemegunan reagen kimia dalam filem sol-gel (Ahmad *et al.* 2001; Ahmad dan Tan 2001; Ahmad dan Narayanaswamy 1995a, 1995b).

Rajah 9 menunjukkan hasil kajian kebolehulangan apabila membran kitosan yang terdop dengan timol biru digunakan dalam pengesanan gas CO_2 pada kepekatan yang sama. Kebolehulangan penunjuk timol biru yang terdop dalam membran kitosan didapati memberikan kebolehulangan yang rendah dengan nilai RSD yang tinggi iaitu 54.7%. Nilai ini adalah lebih tinggi berbanding nilai kebolehulangan penunjuk yang sama dalam larutan kitosan (*Rajah 6*). Ini berlaku kerana taburan penunjuk timol biru dalam membran kitosan didapati tidak sekata. Oleh itu pengukuran serapan yang dilakukan pada titik yang berlainan di atas membran yang sama didapati memberikan bacaan serapan yang berbeza. Kebolehulangan membran kitosan terdop dengan timol biru untuk pengesanan gas CO_2 dapat diperbaiki sekiranya membran kitosan dengan taburan penunjuk yang sekata dapat dihasilkan.

Rajah 10 pula menunjukkan spektrum serapan penunjuk timol biru yang terpegun dalam membran kitosan apabila kepekatan gas CO_2 yang berbeza dialirkan kepadanya. Bentuk spektrum serapan yang diperoleh adalah sama seperti bentuk spektrum serapan dalam larutan bebas. Serapan reagen timol biru pada panjang gelombang 600 nm didapati semakin menurun apabila gas CO_2 pada kepekatan yang lebih tinggi dialirkan.

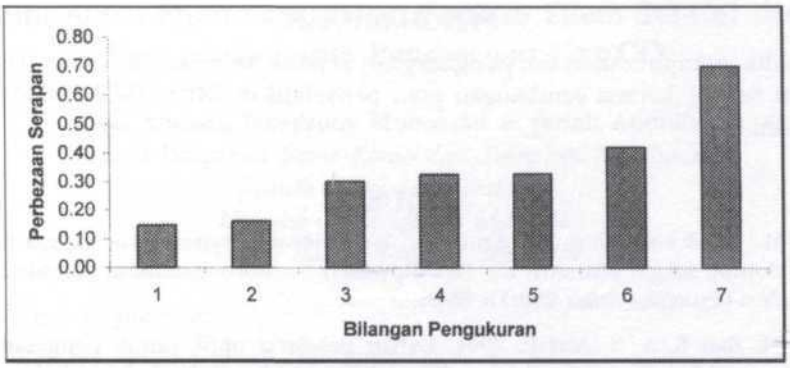

Rajah 9: Graf nilai perubahan serapan pada λ_{maks} 598 nm melawan bilangan pengukuran untuk analisis kebolehulangan reagen timol biru terhadap gas CO_2 dalam membran kitosan

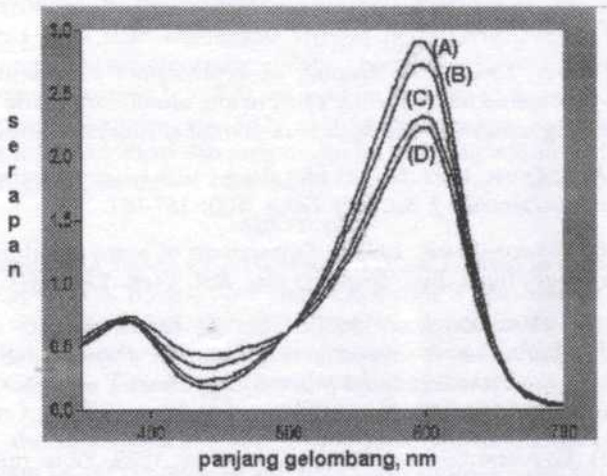

Rajah 10: Spektrum kesan kepekatan gas CO_2 berbeza iaitu 0% (A), 25% (B), 50% (C), 75% (D) dan 100% (E) terhadap serapan reagen timol biru dalam membran kitosan

KESIMPULAN

Hasil kajian menunjukkan kitosan boleh digunakan sebagai matrik dalam penyediaan bahan transduser untuk pengesanan gas CO_2. Membran kitosan telah berfungsi dengan baik untuk memerangkap molekul penunjuk timol biru tanpa mengubah sifat kimia reagen tersebut. Membran kitosan terdop mampu memberikan gerak balas yang positif terhadap kepekatan gas CO_2 yang berbeza. Kebolehulangan penunjuk dalam larutan bebas, larutan kitosan dan membran kitosan masih perlu dipertingkatkan lagi kerana nilai peratus RSD yang diperoleh adalah tinggi iaitu 13.6% dan 47.8%, serta 54.7% masing-masingnya.

PENGHARGAAN

Penyelidik ingin merakamkan penghargaan kepada Kementerian Sains, Teknologi & Alam Sekitar kerana sumbangan gran penyelidikan IRPA 03-02-02-0044 untuk kajian ini.

RUJUKAN

AHMAD M., N. MOHAMMAD dan J. ABDULLAH. 2001. Sensing material for O_2 gas prepared by doping sol-gel film with tris (2,2-Bipyridyl) dichlororuthenium complex. *Journal of. Non-Crystalline Solids* **290(1)**: 86-91.

AHMAD M. dan S. A. S. AZIZAN. 2001. Bahan penderia optik untuk pengesanan CO_2 menggunakan bromotimol biru terpegun dalam filem sol-gel. *Journal of the Institute of Materials Malaysia* **2(1)**: 47-58.

AHMAD M. dan T. W. TAN. 2001. Optical pH sensing material prepared from doped sol-gel film for use in acid-base titration. *ASEAN Journal on Science and Technology for Development* **18(2)**: 37-43.

AHMAD M. dan M. S. LIEW. 1997. Doping of bromotymol blue onto glass matrices prepared by sol-gel technique using silica oxide, aluminium oxide and magnesium oxide as starting materials. *The Malaysian Journal of Analytical Science* **3(2)**: 281-288.

AHMAD M. dan A. L. QUAH. 1997. Sol-gel film doped with phenolpthalien: Potential use for CO_2 sensor. *Pertanika J. Sci. and Techn.* **5(2)**: 157-167.

AHMAD M. dan R. NARAYANASWAMY. 1995a. Entrapment of some aluminium(III)-sensitive reagents in sol-gel films. *Bull. Singapore Nat. Inst. Chem.* **23**: 55-60.

AHMAD M. dan R. NARAYANASWAMY. 1995b. The use of sol-gel film as a matrix for immobilisation of some fluorimetric reagents. In *Polymers and Other Advanced Materials: Emerging Technologies and Business Opportunities,* ed. P.N. Prasad, E. Mark and T.J. Fai, p. 727-737. New York: Plenum Press.

ALABBAS S. H., D. C. ASHWORTH dan R. NARAYANASWAMY. 1989. Fibre optic for chemical sensing. *Anal. Proc.* 26: 373-378.

FLUKA CATALOGUE. 1984/85. Chemicals and Biochemicals, Switzerland, Fluka AG, Buchs.

KOLTHOFF, I. M. dan S. BRUCKENSTEIN. 1959. *Acid-Bases in Analytical Chemistry.* New York: Interscience Publishers.

MILLS, A. dan C. QIN. 1994. Tuning colorimetric and fluorimetric gas sensor for CO_2. *Anal. Chim. Acta.* **285:** 113-123.

WARF J. C. 1982. *Pathways in Analytical Chemistry.* 2nd ed. Los Angeles: James C. Warf Publication.

XIANFANG, Z. dan R. ELI. 1996. Supported chitosan-dye affinity membranes and their protein adsorption. *J. of Membrane Science* **117**: 271-278.

Pertanika J. Sci. & Technol. 11(2): 283 - 291 (2003)
ISSN: 0128-7680

Pemegunan Fluoresein dalam Lapisan Filem Sol-Gel dan Potensinya untuk Pengesanan Gas CO_2

Musa Ahmad, Norezuny Mohamad & Jariah Abdullah
Pusat Pengajian Sains Kimia dan Teknologi Makanan
Fakulti Sains dan Teknologi
Universiti Kebangsaan Malaysia
43600 Bangi, Selangor, Malaysia

Diterima: 12 Jun 2002

ABSTRAK

Penghasilan lapisan filem sol-gel terdop yang boleh digunakan sebagai fasa reagen dalam pembinaan penderia kimia gentian optik dibincangkan dalam kertas kerja ini. Reagen fluoresein yang sensitif terhadap gas CO_2 didopkan di dalam larutan sol-gel dan lapisan filem sol-gel disediakan menggunakan kaedah celup dengan kaca slaid digunakan sebagai penyokong. Filem sol-gel yang didopkan dengan reagen fluoresein didapati membebaskan cahaya pendarfluor pada panjang gelombang λ_{em}= 520 nm apabila diuja pada panjang gelombang λ_{ex} = 490 nm. Kehadiran gas CO_2 akan merendahkan keamatan cahaya pendarfluor yang dihasilkan dan rangsangan ini dapat dijanakan semula dengan mengalirkan gas N_2 ke dalam bilik sampel.

ABSTRACT

The preparation of a doped sol-gel film which could be used as a reagent phase in the development of optical fibre chemical sensor is discussed in this paper. Fluorescein which is sensitive towards CO_2 gas was doped in the sol-gel solution and the sol-gel film was prepared by using a dip-coating method with slide glass used as a support. The sol-gel film doped with fluorescein was found to fluoresces at λ_{em}= 520 nm when excited at λ_{ex} = 490 nm. The presence of CO_2 will reduce the fluorescence intensity of the entrapped fluorescein and the response could be regenerated by flowing N_2 gas to the sample compartment.

Kata kunci: Reagen fluoresein, penderia kimia gentian optik, filem sol-gel, cahaya pendarflour

PENGENALAN

Proses sol-gel merupakan satu fenomena kimia dan melibatkan larutan oksida logam satu komponen atau pelbagai komponen yang mengalami pengelan untuk membentuk rangkaian koheren yang tegar. Perubahan larutan kepada gel menghasilkan istilah 'sol-gel'. Proses sol-gel bermula apabila Ebelmen buat pertama kalinya mensintesis $Si(OEt)_4$ pada tahun 1846 dan ia menjadi gel apabila terdedah kepada lembapan udara (Dislich 1971). Proses ini mula menjadi terkenal pada 1942 setelah Geffcken dan Berger berjaya menyediakan lapisan oksida tunggal (Brinker dan Scherer 1990).

Dalam kajian ini, proses sol-gel digunakan untuk menyediakan suatu lapisan filem lutsinar yang didopkan dengan reagen kimia. Pada amnya, pendopan

kimia ialah pemegunan bahan terubahsuai organik ke dalam polimer organik semasa proses pempolimeran sedang berlaku. Pelbagai reagen fotometrik yang boleh digunakan untuk mengesan kation, anion, spesies redoks dan zarahan terampai udara telah berjaya dipegunkan dalam kumpulan sol-gel iaitu silika, titanium dan xerogel yang lain (Lev *et al.* 1995). Avnir *et al.* (1992) pula telah berjaya memegunkan beberapa bahan bioaktif seperti enzim di dalam filem sol-gel. Dalam kajian ini, reagen fluoresein yang sensitif terhadap kehadiran gas CO_2 akan didopkan di dalam filem sol-gel. Dalam kajian kami terdahulu, penunjuk fenolftalein telah berjaya dipegunkan dalam filem sol-gel dan potensinya untuk pengesanan gas CO_2 telah dibincangkan (Musa dan Ling 1997).

EKSPERIMEN

Bahan-bahan Kimia

Bahan-bahan kimia yang digunakan ialah tetraetilortosilikat, TEOS (Aldrich, 99.0 %); triton X-100 (BDH); etanol (BDH, 99.7%); ammonia (Aldrich, 25.0%); asid hidroklorik, HCl (BDH); N,N-dimetilformamida, DMF (BDH, 99.0%); tetrabutilammonium hidroksida dalam metanol, TBuAOH (Sigma, 12.5%); kalium hidroksida, KOH (Aldrich); fluoresein, FL (Sigma) dan karbon dioksida, CO_2.

Peralatan

Spektrum pendarfluor untuk larutan reagen dan larutan sol-gel diperoleh menggunakan alat Spektrometer SLM Aminco Luminesen Siri II. Spektrum pendarfluor untuk filem sol-gel terdop diperoleh daripada alat yang sama dengan menggunakan aksesori permukaan pepejal.

Cara Kerja

(i) Reagen – Larutan stok FL disediakan dengan melarutkan 200 mg FL ke dalam 1L 0.1 M KOH. Larutan 10.6mM FL disediakan dengan mencampurkan 8.33 mL larutan stok FL dengan 0.21 mL larutan TBuAOH ke dalam kelalang isi padu dan menjadikannya ke isi padu 50.00 mL dengan pelarut DMF. Larutan sol-gel disediakan dengan mencampurkan 2 mL TEOS dan 1 mL 0.1M HCl dalam suatu bikar kecil. Sebanyak 4 mL etanol kemudiannya dimasukkan ke dalam bikar ini dengan perlahan-lahan, diikuti dengan 7 titis triton-X 100 dan campuran larutan dikacau selama 5 jam. Pemegunan reagen dilakukan dengan mencampurkan 2 mL larutan stok sol-gel dengan 2 mL larutan FL dan campuran dikacau selama 1 jam. Semua cara kerja ini dilakukan pada suhu bilik.

(ii) Penyediaan lapisan filem nipis – Kaedah penyalutan celup digunakan dalam kajian ini untuk penyediaan filem sol-gel dan kaca slaid digunakan sebagai penyokong. Penyokong dibersihkan terlebih dahulu dengan etanol dan dipastikan dalam keadaan kering sebelum digunakan. Penyalutan celup

dilakukan dengan mencelup penyokong kaca slaid ke dalam larutan sol-gel dan ditarik dengan perlahan bagi memperoleh lapisan yang nipis. Penyokong ini kemudiannya dibiarkan kering dalam desikator dalam keadaan menegak.

KEPUTUSAN DAN PERBINCANGAN

Reagen FL yang digunakan dalam kajian ini sensitif terhadap kehadiran gas CO_2 dan warnanya akan berubah apabila terdedah kepada gas tersebut (Richard dan James 1972). Gerak balas FL terhadap gas CO_2 adalah berdasarkan kepada persamaan berikut:

$$CO_2 + H_2O \leftrightharpoons H_2CO_3$$

$$H_2CO_3H_2O \leftrightharpoons HCO_3^- + H_3O^+$$

$$2H_3O^+ + \underset{\text{(berpendar)}}{FL^{2-}} \leftrightharpoons 2H_2O + H_2O + \underset{\text{(tidak berpendar)}}{H_2FL}$$

Bagi reagen FL, ion FL^{2-} merupakan spesies yang berpendarfluor dan ion ini dominan dalam pelarut yang beralkali tinggi. Dengan kehadiran gas CO_2, perubahan warna anion FL^{2-} akan dicerap iaitu dari oren kepada tidak berwarna. Bahan yang tidak berwarna ini merupakan laktonik neutral, H_2FL yang tidak berpendar.

Spektrum pendarfluor bagi FL dalam DMF apabila didedahkan kepada gas CO_2 secara berterusan ditunjukkan dalam *Rajah 1.* Cahaya pendarfluor dicerap pada panjang gelombang λ_{em} = 520 nm apabila pengujaan dilakukan pada panjang gelombang λ_{em} = 490 nm. Seperti dijangkakan keamatan spektrum pendarfluor didapati semakin berkurangan apabila didedahkan kepada gas CO_2 kerana pembentukan laktonik neutral, H_2FL yang tidak bersifat pendarfluor.

Rajah 2 menunjukkan spektrum pendarfluor FL dalam larutan sol-gel apabila didedahkan kepada CO_2 secara berterusan. Bentuk spektrum pendarfluor yang diperoleh kelihatan sama seperti spektrum pendarfluor FL dalam larutan bebas. Ini menunjukkan bahawa larutan sol-gel bersifat lengai dan tidak mengubah sifat optik dan kimia bagi reagen FL semasa proses pendopan. Seperti yang diperhatikan dalam larutan bebas, keamatan cahaya pendarfluor didapati semakin berkurangan dengan pendedahan secara berterusan gas CO_2.

Rajah 3 menunjukkan spektrum pendarfluor bagi reagen FL dalam lapisan filem sol-gel apabila didedahkan kepada gas CO_2 secara berterusan. Bentuk spektrum pendarfluor yang diperoleh adalah sama seperti yang diperoleh apabila FL berada dalam larutan bebas dan larutan sol-gel. Panjang gelombang pengujaan dan pancaran juga didapati masih kekal pada 490 nm dan 520 nm, masing-masingnya. Namun, jika spektrum pendarfluor FL dalam larutan bebas, larutan sol-gel dan filem sol-gel dibandingkan, dapat dilihat bahawa pengurangan keamatan pendarfluor adalah paling kecil dalam lapisan sol-gel diikuti dengan larutan sol-gel dan larutan bebas apabila didedahkan kepada gas CO_2 secara berterusan. Keadaan ini dijangkakan disebabkan pembentukan rangkaian antara

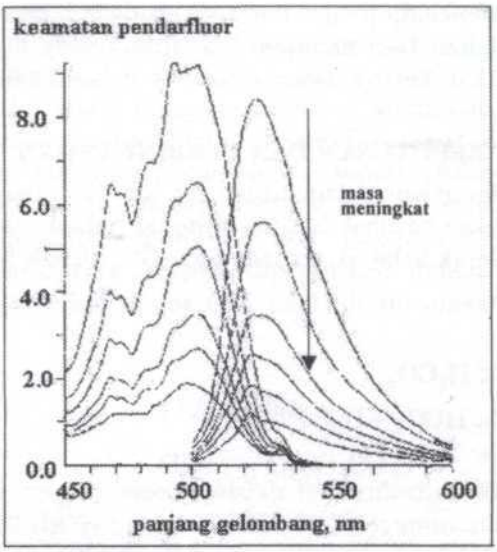

Rajah 1: Spektrum pendarflour bagi FL dalam larutan bebas dengan kehadiran gas CO_2 apabila λ_{ex} = 490 nm dan λ_{em} = 520 nm

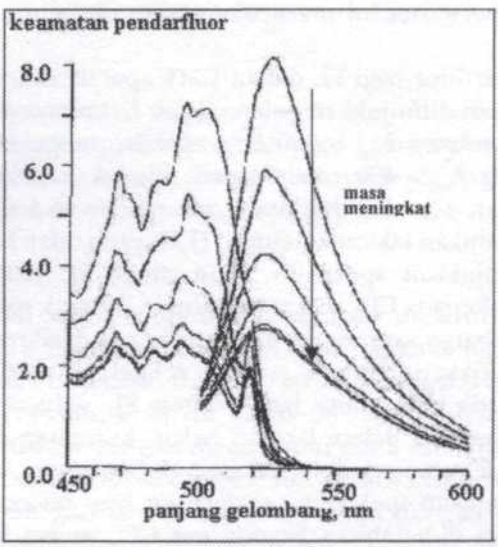

Rajah 2: Spektrum pendarflour bagi FL dalam larutan sol-gel dengan kehadiran gas CO_2 apabila λ_{ex} = 490 nm dan λ_{em} = 520 nm

molekul sol-gel yang terbentuk semasa proses sol-gel yang menghalang pergerakan molekul gas CO_2 dan oleh itu mengehadkan tindak balas antara gas ini dengan ion FL^{2-}.

Rajah 4 menunjukkan spektrum pendarfluor untuk FL dalam larutan bebas, larutan sol-gel dan filem sol-gel. Seperti yang telah dibincangkan, pemegunan

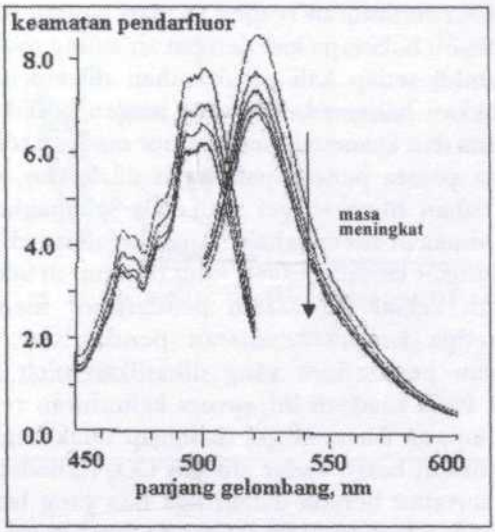

Rajah 3: Spektrum pendarflour bagi FL dalam filem nipis sol-gel dengan kehadiran gas CO_2 apabila λ_{ex} = 490 nm dan λ_{em} = 520 nm

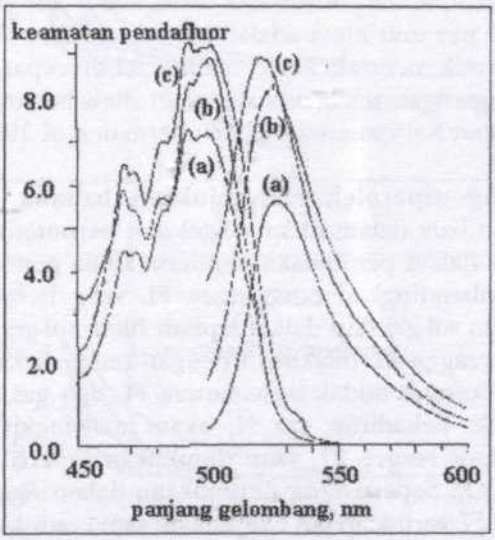

Rajah 4: Bandingan spektrum pendarflour bagi FL dalam larutan bebas (c), Larutan sol-gel (b) dan filem nipis sol-gel (a), (λ_{ex} = 490 nm dan λ_{em} = 520 nm).

FL dalam larutan dan filem sol-gel masih mengekalkan sifat kimia dan sifat optik bagi reagen kerana sol-gel yang bersifat lengai. Keamatan pendarfluor untuk FL dalam filem sol-gel walau bagaimanapun memberikan bacaan terendah kerana kuantiti reagen FL yang dapat dipegunkan dalam filem sol-gel semasa penyediaan filem menggunakan kaedah celup adalah lebih rendah berbanding kepekatan FL dalam larutan bebas dan larutan sol-gel.

Bagi menguji kesan kelunturan reagen FL dari lapisan filem sol-gel, lapisan filem berkenaan dibasuh beberapa kali dengan air suling nyahion dan spektrum pendarfluornya diambil setiap kali pembasuhan dilakukan. Keputusan yang diperoleh menunjukkan bahawa kelunturan reagen berlaku hanya pada dua basuhan yang pertama dan keamatan pendarfluor menjadi tetap selepas basuhan yang ketiga. Semasa proses pencelupan filem dilakukan, sebahagian reagen akan terpegun di dalam filem sol-gel manakala sebahagian yang lain hanya terjerap di atas permukaan filem sahaja. Apabila cucian dilakukan, keamatan pendarfluor berkurangan kerana reagen yang terjerap di atas permukaan filem sol-gel akan dibasuh keluar. Keamatan pendarfluor menjadi tetap selepas proses basuhan ketiga kerana keamatan pendarfluor yang ditunjukkan merupakan keamatan pendarfluor yang dihasilkan oleh FL yang terpegun dalam filem sol-gel. Pada keadaan ini, proses kelunturan reagen yang terjerap di atas permukaan lapisan filem sol-gel dianggap tidak begitu penting.

Rajah 5 menunjukkan kesan kadar alir gas CO_2 terhadap masa rangsangan FL apabila reagen tersebut berada dalam tiga fasa yang berbeza iaitu larutan bebas, larutan sol-gel dan lapisan filem sol-gel. Secara umum dapat diperhatikan bahawa kadar alir mempengaruhi masa yang diambil untuk rangsangan keadaan mantap dicapai. Kadar alir yang tinggi akan mempercepat masa rangsangan keadaan mantap tercapai dan sebaliknya. Pada kadar alir yang tinggi, kuantiti gas CO_2 yang hadir per unit masa adalah juga tinggi dan oleh itu tindak balas pembentukan laktonik neutral, H_2FL adalah lebih cepat. Kesan kadar alir terhadap masa rangsangan telah dibincangkan oleh beberapa penyelidik lain sebelum ini (Musa dan Narayanaswamy 1997; Berman *et al.* 1990; Narayanaswamy dan Sevilla 1988).

Keputusan yang diperoleh menunjukkan bahawa reagen FL dapat dipegunkan dengan baik dalam filem sol-gel dan berpotensi untuk digunakan sebagai fasa reagen dalam pembinaan penderia kimia gentian optik untuk gas CO_2. *Rajah 6* membandingkan rangsangan FL yang berada dalam keadaan bebas, dalam larutan sol-gel dan dalam lapisan filem sol-gel terhadap gas CO_2. Penjanaan semula reagen FL dilakukan dengan mengalirkan gas N_2 ke dalam bilik sampel. Oleh kerana tindak balas antara FL dan gas CO_2 adalah tindak balas jenis berbalik, kehadiran gas N_2 akan menyingkirkan gas CO_2 dan keamatan pendarfluor reagen FL akan dipulihkan seperti sebelum bertindak balas dengan gas CO_2. Seperti yang ditunjukkan dalam *Rajah 6*, secara umum bentuk rangsangan FL terhadap gas CO_2 adalah sama untuk ketiga-tiga keadaan FL iaitu sama ada dalam larutan bebas, larutan sol-gel atau dalam filem nipis sol-gel. Perbezaan keamatan pendarfluor yang diperoleh untuk FL yang terdop dalam filem sol-gel walau bagaimanapun adalah jauh lebih rendah berbanding dalam larutan bebas dan larutan sol-gel. Ini adalah disebabkan kuantiti FL yang terdop dalam filem sol-gel adalah jauh lebih rendah daripada kuantiti FL dalam larutan bebas dan larutan sol-gel. Seperti yang telah dibincangkan sebelum ini, perubahan keamatan yang kecil ini adalah juga disebabkan oleh kewujudan rangkaian dalam filem sol-gel yang menyukarkan pergerakan molekul CO_2 untuk bertindak balas dengan FL. Dalam larutan bebas dan larutan sol-gel,

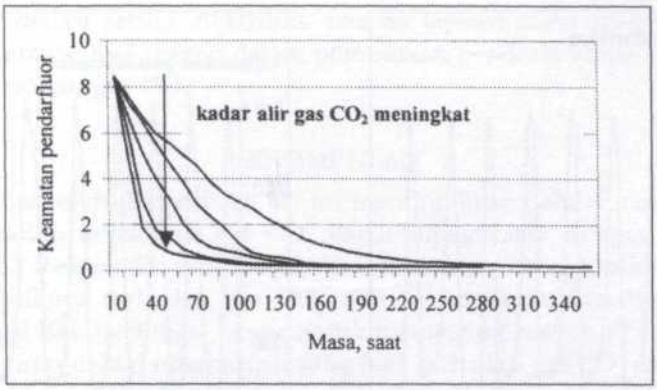

(A)

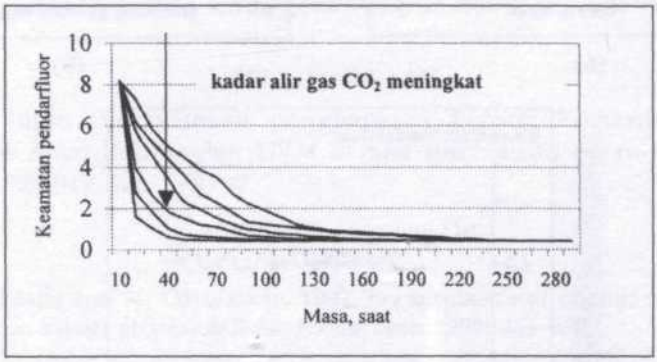

(B)

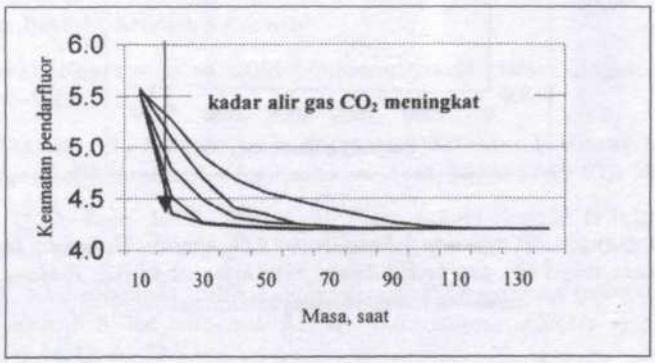

(C)

Rajah 5: Kesan kadar alir terhadap masa rangsangan FL terhadap kehadiran gas CO_2 apabila FL berada dalam larutan bebas (A), larutan sol-gel (B) dan terdop dalam filem nipis sol-gel (C). Keamatan pendarflour diukur pada panjang gelombang λ_{em} = 520 nm apabila pengujian dilakukan pada panjang λ_{ex} = 490 nm.

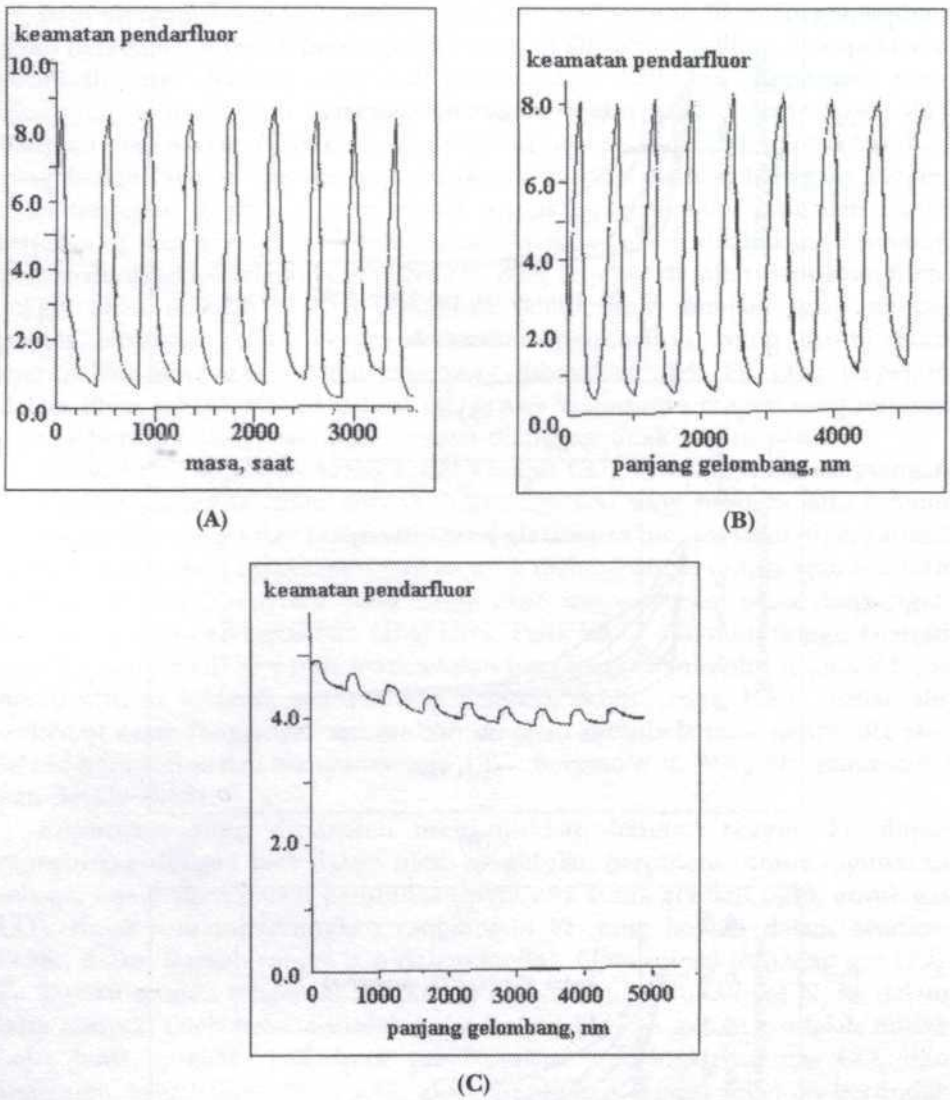

Rajah 6: Rangsangan FL terhadap kehadiran gas CO_2 apabila FL berada dalam larutan bebas (A), larutan sol-gel (B) dan terdop dalam filem nipis sol-gel (C). Penjanaan semula FL dilakukan dengan mengalirkan gas N_2

kedua-dua molekul CO_2 dan FL bebas bergerak dan tindak balas dapat berlaku dengan lebih sempurna. Daripada *Rajah 6* (C), dapat diperhatikan bahawa rangsangan garis dasar tidak diperoleh untuk FL yang terdop dalam lapisan filem sol-gel. Setiap kali penjanaan dilakukan dengan gas N_2, keamatan pendarfluor tidak dapat dipulihkan sepenuhnya. Perbezaan keamatan yang dihasilkan apabila FL didedahkan kepada gas CO_2 walau bagaimanapun sama. Perbezaan keamatan pendarfluor yang kecil dan masalah rangsangan garis

dasar dapat diatasi secara elektronik apabila lapisan filem sol-gel terdop ini digunakan sebagai fasa reagen dalam pembinaan penderia kimia gentian optik untuk pengesanan gas CO_2.

KESIMPULAN

Hasil yang diperoleh daripada kajian ini menunjukkan bahawa reagen FL yang sensitif terhadap kehadiran gas CO_2 dapat dipegunkan dengan baik dalam filem sol-gel. Reagen FL yang terpegun masih dapat mengekalkan sifat kimia dan sifat optiknya terhadap gas CO_2 dan ini menunjukkan bahawa sol-gel bersifat lengai dan berfungsi hanya untuk memegang reagen FL. Reagen yang terpegun menunjukkan rangsangan yang baik terhadap gas CO_2 dan reagen FL dapat dijanakan semula dengan mengalirkan gas N_2. Kajian ini akan diteruskan dengan menggunakan filem sol-gel terdop dengan FL ini sebagai fasa reagen dalam pembinaan penderia kimia gentian optik untuk pengesanan gas CO_2.

PENGHARGAAN

Penyelidik ingin merakamkan penghargaan kepada Kementerian Sains, Teknologi & Alam Sekitar dan UKM kerana sumbangan geran penyelidikan IRPA 09-02-02-0012 dan S/9/97.

RUJUKAN

AVNIR D., S. BRAUN and M. OTTOLENGHI. 1992. Encapsulation of organic molecules and enzymes in sol-gel glasses. *ACS Symposium Series* **4999:** 384-404.

BERMAN C. J, G. D.CHRISTIAN and L. W. BURGES. 1990. *Anal. Chem.* **62**: 2006.

BRINKLER C. J. and G. W. SCHERER. 1990. *Sol-Gel Science: The Physics and Chemistry of Sol-Gel Processing.* Boston: Academis Press Inc.

DISLICH, H. 1971. New routes to multicomponent oxide glasses. *Angew. Chem. Int. Ed.* **10(6)**: 363-434.

LEV, O., M. TRIONSKY, L. RABINOVICH, V. GLEZER, S. SAMPATH, 1. PANKRATOV dan J. GUN. 1995. Organically modified sol-gel sensors. *Anal. Chem.* **67(1)**: 22A-30A.

MUSA A. dan Q. A. LING. 1997. Pendopan filem sol-gel dengan fenolftalien: Potensi penggunaan sebagai penderia CO_2. *Pertanika J. Sci. & Technol.* **5(2)**: 155-167.

MUSA A. and R. NARAYANASWAMY. 1997. A flow-cell optical fibre sensor based on immobilised chrome azurol S for aqueous Al(III) monitoring. *ASEAN J. Sci. Technology Development* **14(1)**: 61-73.

NARAYANASWAMY R. and F. SEVILLA III. 1988. Optosensing of hydrogen sulphide through paper impregnated with lead acetate. *Fresenius Z. Anal. Chem.* 329, 789.

RICHARD, M. G. and C. G. W. JAMES. 1972. *Atmospheres.* p. 126-141. Prentice Hall, Inc.

Pertanika J. Sci. & Technol. 11(2): 293 - 300 (2003)
ISSN: 0128-7680

Synthesis and Physico-Chemical Investigation of Vanadium Phosphorus Oxide Catalysts Derived from $VO(H_2PO_4)_2$

Y. H. Taufiq-Yap & C. K. Goh
Department of Chemistry,
Faculty of Science and Environmental Studies,
Universiti Putra Malaysia, 43400 UPM, Serdang,
Selangor, Malaysia

Received: 13 June 2002

ABSTRAK

Mangkin vanadium fosforus oksida telah disediakan melalui $VO(H_2PO_4)_2$ dengan menggunakan dua kaedah: i) tindak balas V_2O_4 dengan α-H_3PO_4 dan ii) penurunan $VOPO_4.2H_2O$ dengan menggunakan oktan-3-ol. Prekursor ini dikalsinkan dalam campuran *n*-butana/udara pada 673 K selama 75 jam. Mangkin ini dicirikan dengan menggunakan pelbagai teknik, seperti luas permukaan BET, XRD, FTIR dan SEM.

ABSTRACT

Vanadium phosphorus oxide catalysts were prepared via $VO(H_2PO_4)_2$ by using two methods: i) reaction of V_2O_4 with α-H_3PO_4 and ii) reduction of $VOPO_4.2H_2O$ with octan-3-ol. The precursors were calcined in *n*-butane/air mixture at 673 K for 75 h. These catalysts were characterised by using various techniques, such as BET surface area, XRD, FTIR and SEM.

Keywords: Vanadium phosphorus oxide, *n*-butane, maleic anhydride, vanadyl dihydrogen phosphate, partial oxidation

INTRODUCTION

Vanadium phosphorus oxide catalysts have been widely accepted to contain selective and active phase for heterogeneous oxidation of *n*-butane to maleic anhydride (Centi 1993). Vanadyl pyrophosphate, $(VO)_2P_2O_7$ (V^{4+} phase with a P/V ratio of 1) was claimed to be the main crystalline phase for industrial catalysts. This phase is mostly generated from the precursor phase, $VOHPO_4.0.5H_2O$ via a topotactic transformation during the catalyst activation (Centi 1993; Johnson *et al.* 1984). Initially, $VOHPO_4.0.5H_2O$ precursor can be prepared by: i) using aqueous HCl as the reducing agent for V_2O_5 and ii) using isobutanol as the reducing agent and solvent for V_2O_5. Sananes *et al.* (1994; 1995a; 1995b; 1996) have investigated the preparation of VPO catalysts derived from $VO(H_2PO_4)_2$. They claimed that this catalyst displays ultraselective formation of maleic anhydride and no CO or CO_2 formation at low *n*-butane conversion. However, Hannour *et al.* (1998) found that the activity and selectivity of the amorphous and partly crystalline $VO(PO_3)_2$ catalysts were not exceeding 40% with formation of CO and CO_2. A small amount of furan, acrylic acid, acetic acid and acrolein were also observed. These findings are in agreement with

Wang *et al.* (2000) where maleic anhydride selectivity observed was typically 50% with CO and CO_2 formation. Later, Bartley *et al.* (2000a; 2000b) introduced the synthesis of catalyst derived from $VO(H_2PO_4)_2$ precursor by using aldehydes and ketones as reducing agents. They reported that the selectivity to maleic anhydride is typically 20-30% due to impurity of $VO(H_2PO_4)_2$. Even with these controversies in the literatures, continual efforts are still being made to investigate the physico-chemical properties of $VO(H_2PO_4)_2$ catalyst. In this study, vanadium phosphorus oxide catalysts derived from $VO(H_2PO_4)_2$ precursor were prepared using two methods: i) reaction between V_2O_4 with phosphoric acid and ii) reduction of $VOPO_4.2H_2O$ by using 3-octanol. Their physico-chemical characteristics were compared to the catalyst prepared by the normal organic method via $VOHPO_4.0.5H_2O$ precursor.

EXPERIMENT

Catalyst Preparation

Preparation of $VOHPO_4.0.5H_2O$

15 g of V_2O_5 (from Fluka) was suspended by rapid stirring into a mixture of isobutyl alcohol (90 mL) and benzyl alcohol (60 mL). The mixture was refluxed for 3 h at 393 K with continuous stirring. The mixture was then cooled to room temperature and left stirring at this temperature overnight. The *o*-H_3PO_4 (85% from Merck) was added and further refluxed for 2 h. The blue slurry was then filtered, washed and dried at 373 K for 24 h. The resulting precursor is referred to as VPOpreA.

Preparation of $VO(H_2PO_4)_2$ from V_2O_4

10 g of V_2O_4 (from RdH) was refluxed with 82 mL of *o*-H_3PO_4 (85% from Merck) at 453 K for 1 h. The suspension was centrifuged and the solid was redispersed with diethyl ether. Finally, the product was dried at 373 K for 24 h. The resulting precursor is referred to as VPHpreA.

Preparation of $VO(H_2PO_4)_2$ from Reduction of $VOPO_4.2H_2O$ by Using 3-octanol

$VOPO_4.2H_2O$ was prepared by reacting V_2O_5 (12 g from Fluka) with *o*-H_3PO_4 (115.5 g, 85% from Merck) in water (24 mL H_2O/g solid) under reflux for 24 h. The yellow solid was recovered by filtration, washed with water and then acetone and dried at 383 K for 24 h. $VOPO_4.2H_2O$ recovered was refluxed with 3-octanol (50 ml alcohol/ mol $VOPO_4.2H_2O$) for 21 h. Then, the blue solid product was obtained by filtration and was dried at 373 K for 24 h. The resulting precursor is referred to as VPHpreB.

All the precursors were calcined in *n*-butane/air mixture (0.75% *n*-butane in air) for 75 h at 673 K and the resulting catalysts were denoted as VPO, VPH-A and VPH-B, respectively.

Catalysts Characterisation

X-ray diffraction (XRD) analyses were carried out by using a Shimadzu diffractometer model XRD-6000 Diffractometer employing CuK_{α} radiation generated by a Phillips glass diffraction x-ray tube broad focus 2.7 kW type on the catalysts at ambient temperature.

Fourier transform infrared (FTIR) spectra were obtained by using a Perkin Elmer 1725X Spectrometer. The instrument was equipped with an infrared source element, a KBr beam splitter and a detector.

B.E.T. (Brunauer-Emmer-Teller) surface area measurements were carried out by using nitrogen adsorption-desorption at 77 K using a Micromeritics ASAP 2000 instrument.

SEM was done using a JOEL JSM-6400 electron microscope. The samples were coated with gold by using a Sputter Coater. The photographs were captured using a Mamiya camera with Kodak Verichrome Pan 100 black and white negatives.

RESULTS AND DISCUSSION

B.E.T. Surface Area Measurements

B.E.T. surface area of the two catalysts derived from $VO(H_2PO_4)_2$ precursor were significantly low, *i.e.* 1.1 m^2g^{-1} for VPH-A and 2.3 m^2g^{-1} for VPH-B compared to 18.2 m^2g^{-1} for VPO catalyst. This result is in agreement with those reported earlier by Sananes *et al.* (1995a; 1996), Hannour *et al.* (1998) and Bartley *et al.* (2000a; 2000b). The adsorption-desorption isotherms of nitrogen at 77 K for all the catalysts were shown in *Fig. 1.* These catalysts gave isotherms of Type II with the presence of hysteresis loop (Sing *et al.* 1985), indicating the presence of a mixture of porosity and mesopores. The hysteresis loop is a type E, indicating the presence of pore with ink-bottle shape or by pores having varying widths.

X-ray Diffraction

Fig. 2 shows the XRD patterns of all the precursors. VPOpre gave the characteristic peaks of $VOHPO_4.0.5H_2O$ (JCPDS File No. 37-0269) at 2θ= 15.0°, 27.0° and 30.5° correspond to (001), (121) and (220) planes, respectively. VPHpreA showed only sharp diffraction peaks for $VO(H_2PO_4)_2$ (JCPDS File No. 40-0038) at 2θ= 14.0°, 28.2° and 31.6° correspond to (110), (220) and (130) planes, respectively. However, VPHpreB gave diffraction peaks of a mixture of $VOHPO_4.0.5H_2O$ and $VO(H_2PO_4)_2$. The peaks' relative intensities for VPHpreB are lower compared to VPOpre and VPHpreA.

The XRD patterns of VPO, VPH-A and VPH-B catalysts are shown in *Fig. 3.* VPO shows characteristic peaks of $(VO)_2P_2O_7$ (JCPDS File No. 34-1381) with main peaks at 2θ= 23.0°, 28.5° and 30.0°, which correspond to the reflections from (020), (204) and (221) planes, respectively. The diffractogram of VPH-A catalyst gave a poor crystalline of $VO(PO_3)_2$ in agreement with the finding by Hannour *et al.* (1998) with a very broad peak spanning 2θ= 10.0°- 60.0°,

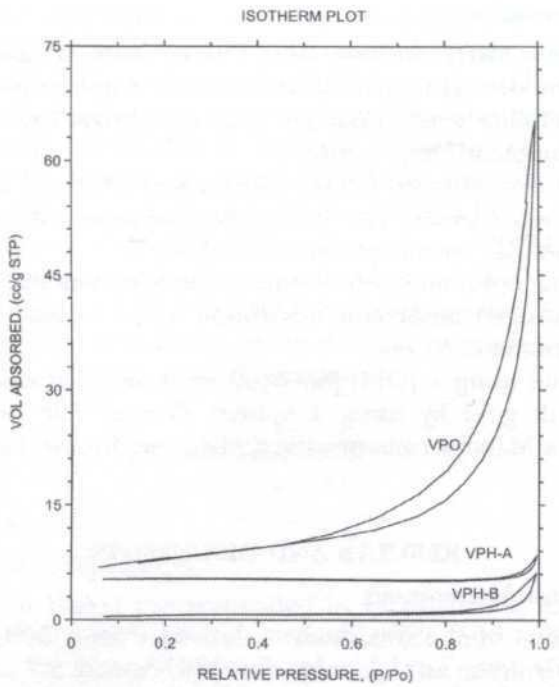

Fig. 1: The adsorption-desorption isotherms of nitrogen at 77 K for VPO, VPH-A and VPH-B catalysts

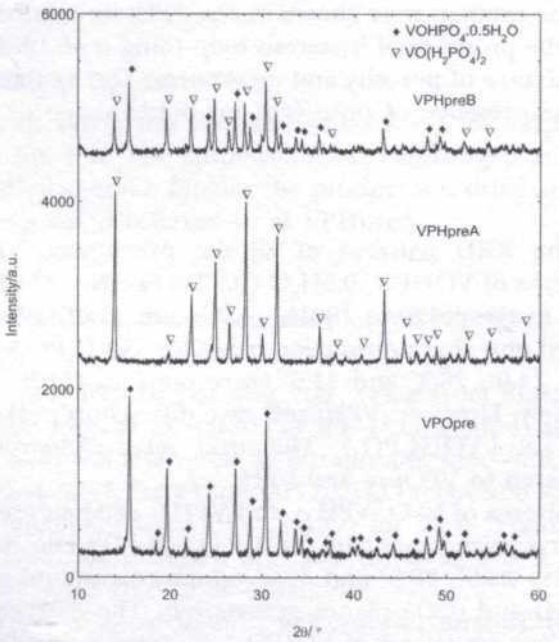

Fig. 2: XRD patterns of VPOpre, VPHpreA and VPHpreB

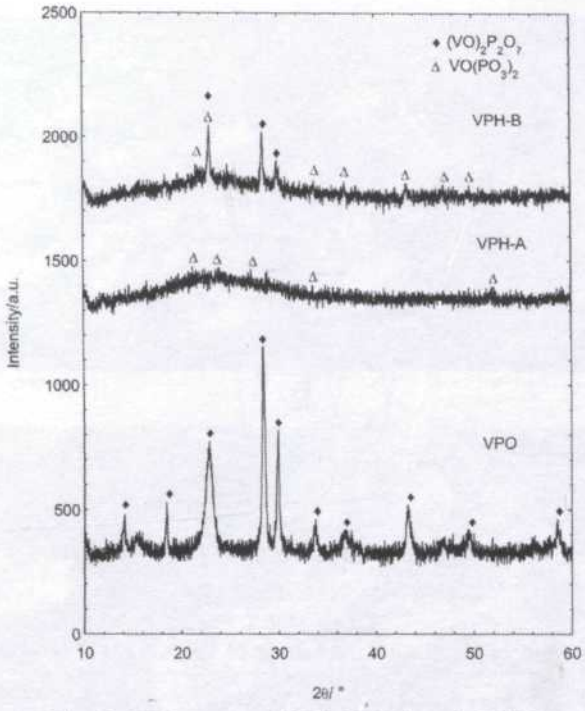

Fig. 3: XRD pattern of VPO, VPH-A and VPH-B

indicating the presence of an amorphous phase. However, small peaks at 2θ= 22.3°, 24.0°, 27.0°, 32.8° and 53.0° were observed which correspond to (001), (220), (211), (040) and (260) planes, respectively and assigned to $VO(PO_3)_2$ (JCPDS File No. 34-1433). The XRD patterns of VPH-B catalyst gave $(VO)_2P_2O_7$ as the main phase at 2_= 22.9°, 29.0° and 30.0°. Additional smaller peaks which were also observed could all be assigned to $VO(PO_3)_2$.

Fourier Transform Infrared (FTIR)

FTIR spectra for VPO, VPH-A and VPH-B catalysts were shown in *Fig. 4*. VPO shows the absorption bands at 1248, 1148, 1100, 1030, 970, 930, 740 cm^{-1} and a series of bands in the region below 700 cm^{-1}. However, VPH-A and VPH-B revealed a broad band in the region 1230-900 cm^{-1}. The bands with wave numbers above 700 cm^{-1} can be assigned to valence vibrations of P-O bonds in various anions of phosphorus with oxygen and the bands from the region below 700 cm^{-1} can be assigned to deformation vibration of these groupings (Brutovsky *et al.* 1982). The absorption bands at 1248, 1148, 1100 and 1030 cm^{-1} of VPO are assigned to vibration of two PO_3 groups, which differ by the type of symmetry, and the bands at 970, 930 and 740 cm^{-1} can be assigned to the vibrations V=O, ν_{as}(POP) and ν_s(POP), respectively. The band at 1230 cm^{-1} for VPH-A and VPH-B can be assigned to $\nu_{as}(PO_3)$. Detailed assignment of the observed bands is shown in Table 1.

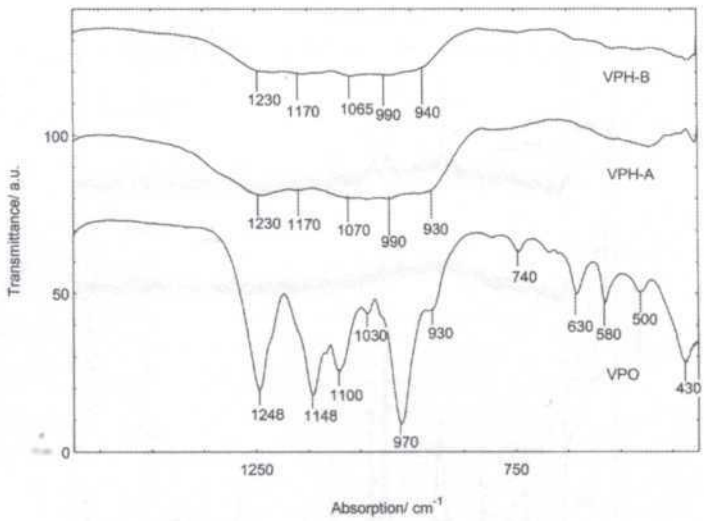

Fig. 4: FTIR spectrum of VPO, VPH-A and VPH-B

TABLE 1
Assignment of IR absorption bands of VPO, VPH-A and VPH-B

Wave number (cm^{-1})			Vibration
VPO	VPH-A	VPH-B	
1248	1230	1230	$\nu_{as}(PO_3)$
1148, 1100, 1030	1170, 1050, 1036	1140, 1065	$\nu_s(PO_3)$
970	990	990	V=O
930	940	-	$\nu_{as}(POP)$
740	-	-	$\nu_s(POP)$

Scanning Microscopy Electron

The SEM micrographs for VPO, VPH-A and VPH-B catalysts shown in *Fig. 5* gave distinctly different morphologies. VPO catalyst appeared to be rosette-shape agglomerate, consisting of plate-like crystals which was similar to the reported morphology for $(VO)_2P_2O_7$ catalyst (Kiely *et al.* 1995). The dominant morphology observed for VPH-A was blocky-shape with regular sided oblong crystallites with the ratio of the sides being 1:1:4 regardless of the dimensions of the crystal. This result is in agreement with the findings reported for $VO(PO_3)_2$ obtained by Sananes *et al.* (1996). The VPH-B consists of a mixture of smaller oblong blocky-shape and plate-like crystallites with the size of 1-3 μm in length and less than 100 nm in thickness. This result is consistent with the XRD result where the particle thickness at (040) for VPH-B and VPH-A catalysts are 921.6 and 2072.0 Å, respectively.

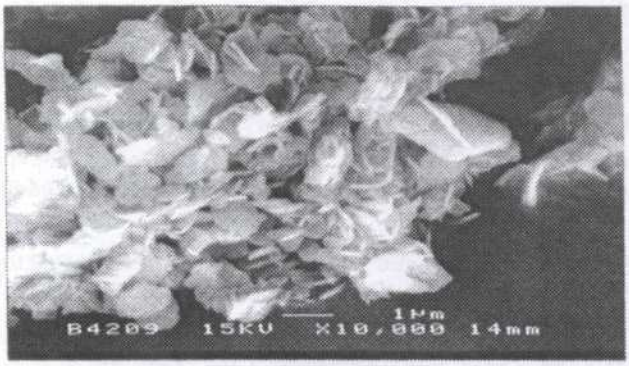

(a)

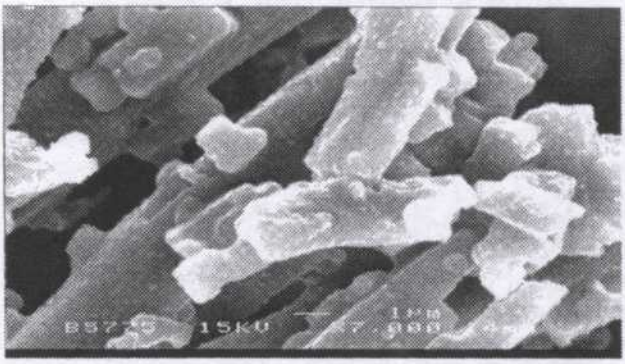

(b)

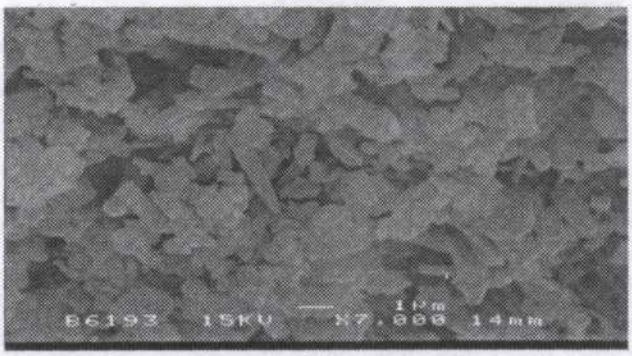

(c)

Fig. 5: SEM micrographs of (a) VPO, (b) VPH-A and (c) VPH-B

ACKNOWLEDGEMENT

Financial assistance from the Malaysian Ministry of Science, Technology and Environment is gratefully acknowledged.

REFERENCES

BARTLEY, J. K., C. RHODES, C. J. KIELY, A. F. CARLEY and G. J. HUTCHINGS. 2000. *n*-Butane oxidation using $VO(H_2PO_4)_2$ as catalyst derived from an aldehyde/ketone based preparation method. *Phys. Chem. Chem. Phys.* **2**: 4999-5006.

BARTLEY, J. K., R. P. K. WELLS and G. J. HUTCHINGS. 2000. The unexpected role of aldehydes and ketones in the standard preparation method for vanadium phosphate catalysts. *J. Catal.* **195**: 423-427.

BRUTOVSKY, M., S. GEREJ, F. VASILCO and J. GEREJOVA. 1982. X- ray diffractograms and IR spectra of modified vanadium-phosphate catalysts. *Col. Chec. Chem. Commun.* **47**: 1290-1300.

CENTI, G. 1993. Vanadyl pyrophosphate catalysts. *Catal. Today* **16**: 5.

HANNOUR, F. K., A. MARTIN, B. KUBIAS, B. LUCKE, E. BORDES and P. COURTINE. 1998. Vanadium phosphorus oxides with P/V=2 used as oxidation and ammoxidation catalysts. *Catal. Today* **40**: 263-272.

JOHNSON, J. W., D. C. JOHNSTON, A. J. JACOBSON and J. F. BRODY. 1984. Preparation and characterization of $VO(HPO_4),0.5H_2O$ and its topotactic transformation to $(VO)_2P_2O_7$. *J. Am. Chem. Soc.* **106**: 8123- 8128.

KIELY, C. J., S. SAJIP, I. J. ELLISON, M. T. SANANES, G. J. HUTCHINGS and J. C. VOLTA. 1995. Electron microscopy studies of vanadium phosphorus oxide catalysts derived from $VOPO_4.2H_2O$. *Catal. Lett.* **33**: 357-368.

SANANES, M. T., I. J. ELLISON, T. MARIA, J. C. VOLTA and G. J. HUTCHINGS. 1994. Control of the composition and morphology of vanadium phosphate catalyst precursors from alcohol treatment of $VOPO_4.2H_2O$. *J. Chem. Soc. Chem. Commun.* **1**: 1039-1094.

SANANES, M. T., G. J. HUTCHINGS and J. C. VOLTA. 1995. On the role of the $VO(H_2PO_4)_2$ precursor for *n*-Butane oxidation into maleic anhydride. *J. Catal.* **154**: 253-260.

SANANES, M. T., G. J. HUTCHINGS and J. C. VOLTA. 1995. *n*-Butane to maleic anhydride and furan with no carbon oxide formation using a catalysts from $VO(H_2PO_4)_2$. *J. Chem. Soc. Chem. Commun.* **1**: 243-244.

SANANES, M. T., I. J. ELLISON S. SAJIP, A. BURROWS, C. J. KIELY, J. C. VOLTA and G. J. HUTCHINGS. 1996. *n*-Butane oxidation using catalysts prepared by treatment of $VOPO_4.2H_2O$ with octanol. *J. Chem. Soc. Faraday Trans.* **92**: 137-142.

SING, K. S. W., D. H. EVERETT, R. A. W. HAUL, L. MOSCOU, R. A. PIEROTTI, J. ROUQUEROL and T. SIEMIENIEWSKA. 1985. Reporting physisorption data for gas/solid systems with special reference to the determination of surface area and porosity. *Pure & Appl. Chem.* **57**: 603.

WANG D., M. C. KUNG and H. H. KUNG. 2000. Oxidation of butane over vanadium-phosphorus oxides of P/V≥2. *Catal. Lett.* **65**: 9-17.

Pertanika J. Sci. & Technol. 11(2): 301 - 309 (2003)
ISSN: 0128-7680

Thermal Diffusivity Measurement of Abrasive Paper Using Photoacoustic Technique

Wan Yusmawati Wan Yusoff & W. Mahmood Mat Yunus
Department of Physics
Faculty of Science and Environmental Studies
Universiti Putra Malaysia
43400 UPM, Serdang, Selangor, Malaysia

Received: 26 June 2002

ABSTRAK

Pengukuran nilai resapan terma untuk dua jenis kertas pasir dilaporkan. Untuk tujuan ini dua jenis kertas pasir, silikon karbaid dan aluminium oksida dipilih sebagai sampel kajian. Nilai resapan terma kertas pasir silikon karbaid dengan saiz grit 320, 360, 400, 600, 800, 1000, 1200 dan 1500 telah diukur. Sebaliknya, untuk sampel kertas pasir aluminium oksida hanya dua sampel (saiz grit 120 dan 240) sahaja dipilih dalam kajian ini. Semua pengukuran dilakukan pada suhu bilik dengan permukaan berpasir menghadap kepada sinar laser. Nilai resapan terma efektif yang diperoleh untuk silikon karbaid adalah dalam julat (5.1 - 8.9) x 10^{-2} cm^2/s iaitu lebih kecil berbanding nilai resapan terma untuk seramik silikon karbaid yang disediakan daripada serbuk silikon karbaid. Sebaliknya untuk kertas pasir aluminium oksida, nilai resapan terma efektif (0.18 cm^2/s dan 0.35 cm^2/s) adalah lebih tinggi daripada nilai resapan terma seramik aluminium oksida yang pernah dilaporkan. Struktur permukaan sampel dikaji dengan menggunakan SEM pada pembesaran 100X.

ABSTRACT

Measurements of thermal diffusivity of two types of abrasive papers are reported. We have chosen silicon carbide and aluminium oxide abrasive papers as our samples. Thermal diffusivity of silicon carbide abrasive paper with the grit size of 320, 360, 400, 600, 800, 1000, 1200, and 1500 were measured. On the other hand, only two grit size (120 and 240) of aluminium oxide abrasive papers were chosen in the present experiments. All the measurements were carried out at room temperature with the abrasive surface facing the laser beam. The effective thermal diffusivity values obtained for silicon carbide are in the range of (5.1 - 8.9) x 10^{-2} cm^2/s, which is lower than the value of thermal diffusivity of pellet ceramic silicon carbide prepared from silicon carbide powder. For aluminium oxide abrasive papers the effective value of thermal diffusivity (0.18 cm^2/s dan 0.35 cm^2/s) is higher than the value reported for aluminium oxide ceramic. The surface structure of the sample was investigated using SEM with the magnification of 100X.

Keywords: Abrasive paper, thermal diffusivity, photoacoustic technique, silicon carbide, aluminium oxide

INTRODUCTION

Abrasive paper is a tough paper coated with an abrasive material such as a silica, garnet, silicon carbide, or aluminium oxide. It is mainly used for grinding, polishing metals, machine tools, car bodywork and furniture. Before the 1950s, silicon carbide was available only through the industrial Acheron process for making abrasive material. Silicon carbide is a high performance material selectively used throughout diverse industries for severe applications, including condition of high abrasive wear, high corrosion, high power and high temperature electronic. In this paper, we report the photoacoustic measurement of the effective thermal diffusivity of abrasive papers (i.e. silicon carbide and aluminium oxide abrasive papers). Generally a grit number is used to specify the particle size of abrasive material, i.e. the higher grit number, the smaller the particle size.

The thermal diffusivity, α is of direct importance in the heat-flow studies, as it determines the rate of periodic or transient heat propagation through a medium. Abrasive papers are used occasionally for polishing purposes. Therefore, its thermal diffusivity is important so as to maintain the physical surface of samples. Bigger particle size (higher thermal diffusivity) will destroy the physical surface of the samples.

The thermal diffusivity value of ceramic aluminium oxide has been determined by using flash method (Yano *et al.* 2000) and photothermal deflection technique (Chung *et al.* 1997). During the past two decades, the use of photoacoustic (PA) measurements has gradually diffused into a wide range of branches of science, from agricultural and medical sciences to environmental sciences in general (Lima *et al.* 2000). This encouraging process can be connected to the sensitivity of the PA signal to changes in the sample's physical characteristics due to modifications in processing conditions.

EXPERIMENT SETUP

The open photoacoustic cell (OPC) for measuring thermal diffusivity has been proposed by Perondi *et al.* (1987). The OPC technique is simple and the easiest method for measuring thermal diffusivity, α of solid sample such as metals, ceramics, polymers and composites. The OPC experiment set-up used for the PA measurement of thermal diffusivity at room temperature is shown in *Fig.1.* The mechanically modulated beam from He-Ne laser (Model Melles Griot, 05-LHR-828) with output power 30 mW is focused onto the sample. When the modulated laser beam was illuminated onto the front surface of the sample, the heat generated in the sample diffuses to the air in the small photoacoustic chamber. Hence, the pressure in the air chamber oscillates at the chopping frequency, which can be detected by the sensitive microphone (electret microphone-Cirkit U.K.). This microphone has a 2.5 mm diameter of circular opening hole, a metallized electret diaphragm, 45 μm long air gap separating the diaphragm and a metal back-plate. This typical microphone design is schematically shown in *Fig. 2.* The resulting signals depend not only on the

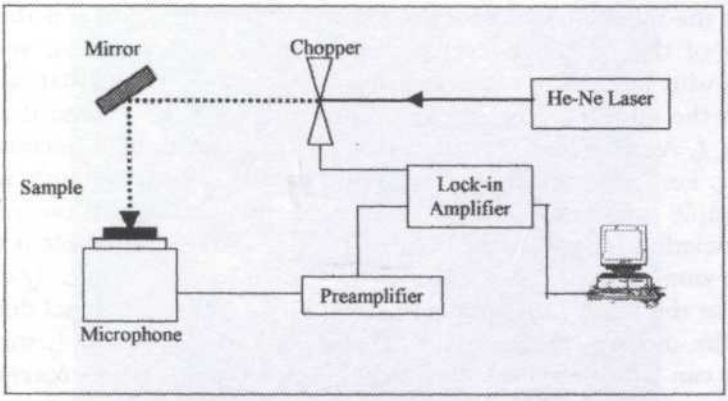

Fig. 1: Experiment setup of the open photoacoustic cell technique

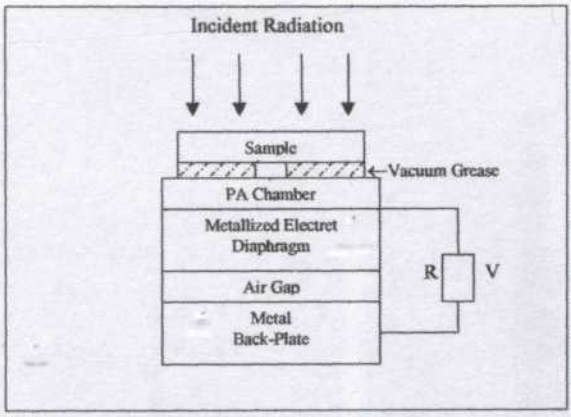

Fig. 2: Schematic view of the eletret microphone used as the open photoacoustic cell detection in the thermal diffusivity measurements

amount of heat generated in sample (i.e. on the optical-absorption coefficient and the light-into-heat conversion efficiency of the sample) but also on how heat diffuses through the sample. The photoacoustic signal being generated was amplified by a preamplifier (SR 560) and then processed by a lock-in amplifier (SR 530). The amplitude and phase of the PA signals were recorded and analyzed for thermal diffusivity value.

The theory of the PA effect in solid sample has been described by R-G theory in 1976 (Rosencwaig and Grasho 1976). According to this theory, the heat generated in the sample is transferred to the gas immediately upon contact. An important parameter involved is the thermal diffusion length of the sample, μ_s which can be defined in terms of thermal diffusivity, α by simple relation as

$$\mu_s = \sqrt{\alpha / \pi f} \qquad (1)$$

where f is the modulation frequency of the incident light and α is the thermal diffusivity of the sample materials. From Equation (1), we can see that μs decreases with increasing of modulation frequency. It means that, at very low frequency the diffusion length is very large, and it can be greater than sample thickness, l_s. As the frequency increases, μ_s decreases until it becomes of the order of l_s. For a characteristic frequency, $f = f_c$ the diffusion length, μ_s is equal to the sample thickness, l_s ($\mu_s = l_s$). Thus, we may distinguish two regimes; at high modulation frequencies ($f > f_c$) or ($\mu_s < l_s$) where the sample is thermally thick, the amplitude of PA signal varies as $f^{-1.5}$. In contrast, when ($f < f_c$) or ($\mu_s > l_s$) for the thermally thin sample, the amplitude of the PA signal decreases as f^{-1} with the modulation frequency. Hence by knowing f_c and l_s, the thermal diffusivity can be determined by applying Equation (1), which corresponds to the situation ($l_s = \mu_s$), i.e.

$$\alpha_s = \pi f_c l_s^2 \tag{2}$$

The quantity that measures the rate of diffusion of heat in the sample is the thermal diffusivity, α in which can be related to thermal conductivity, k as

$$\alpha = k/\rho c \tag{3}$$

where ρ is the density of sample and c is the specific heat at constant pressure. In the present work, a scanning electron microscope (SEM) was used to analyze the roughness of the abrasive paper surface. *Figs. 3, 4* and *5* show examples of SEM micrographs of aluminium oxide and silicon carbide abrasive papers surface taken at different grit sizes (1500, 600 and 120 grit size).

RESULTS AND DISCUSSION

Photoacoustic signals of aluminium oxide and silicon carbide abrasive papers with grit size of 120 and 1500 are respectively shown in *Fig. 6*. In order to determine the characteristic frequency, where the sample changes its behavior from thermally thick to thermally thin, a method proposed by Da Costa and Siquire (1996) was employed. Therefore the graph of ln (PA signal) versus ln (chopping frequency) has been plotted. Typical examples of ln (PA) signal as a function of ln (f) of aluminium oxide (5.08×10^{-2} cm thickness) and silicon oxide (1.83×10^{-2} cm thickness) abrasive papers are respectively shown in *Fig. 7*. The two regimes can be distinguished by two different inclinations of straight lines. The characteristic frequency, f_c is the frequency at which the sample changes its behavior from thermally thick to thermally thin. In these two cases, the f_c was determined to be 40.64 Hz and 52.48 Hz that correspond to the thermal diffusivity values of 0.350 cm^2s^{-1} and 0.0551 cm^2s^{-1} respectively. The same procedure was conducted for the other abrasive paper samples. All the thermal diffusivity values of abrasive paper samples obtained in this work are listed in Table 1.

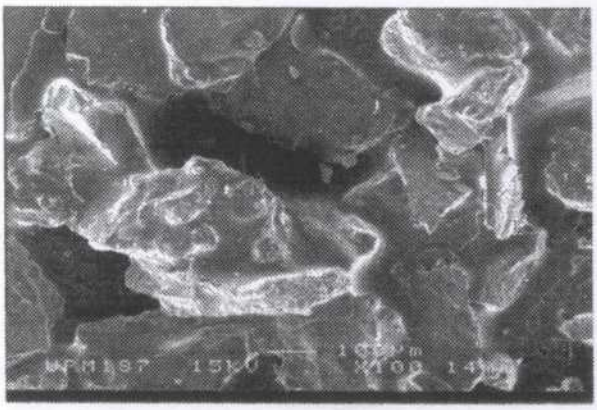

Fig. 3: SEM micrograph of aluminium oxide abrasive paper with grit size 120

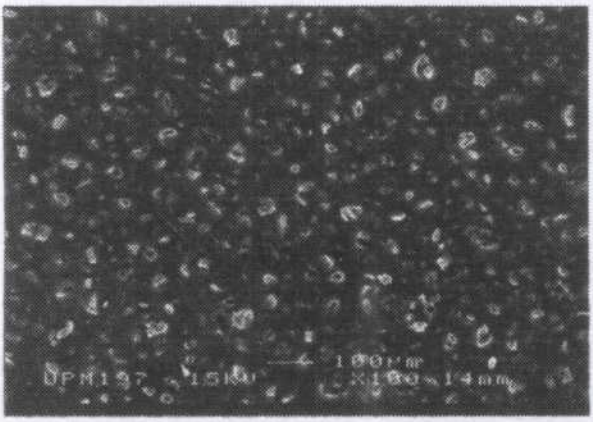

Fig. 4: SEM micrograph of silicon carbide abrasive paper with grit size 120

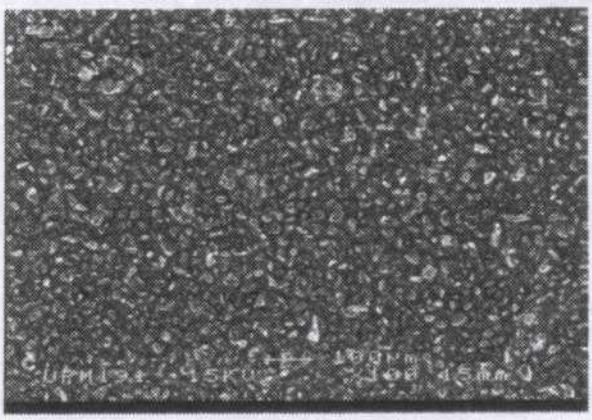

Fig. 5: SEM micrograph of silicon carbide abrasive paper with grit size 1500

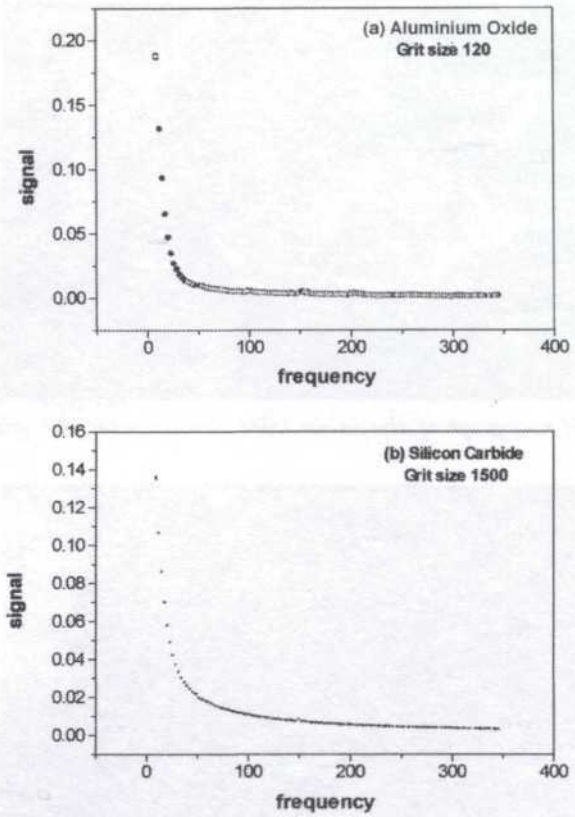

Fig. 6: Plot PA signal amplitude as a function of the modulation frequency for (a) Aluminium oxide abrasive paper (b) Silicon carbide abrasive paper

TABLE 1
Thermal diffusivity of aluminium oxide and silicon carbide abrasive papers measured by photoacoustic technique

Grit Size	Thermal diffusivity, α (cm^2s^{-1})	
	Aluminium Oxide (Abrasive paper) AlO_3	Silicon Carbide (Abrasive paper) SiC
120	0.3500	-
240	0.1800	-
320	-	0.0798
360	-	0.0886
400	-	0.0727
600	-	0.0552
800	-	0.0511
1000	-	0.0651
1200	-	0.0620
1500	-	0.0551

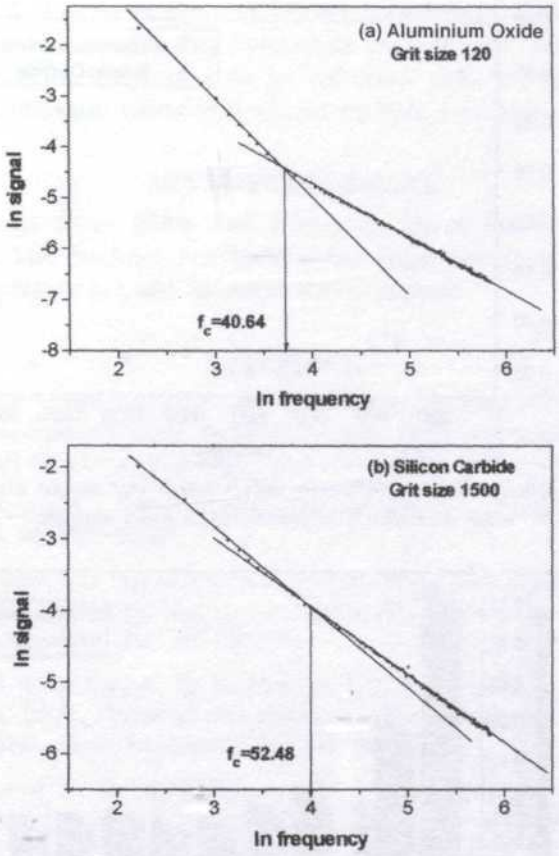

Fig. 7: Plot of ln (PA signal) versus ln (chopping frequency) for (a) Aluminium oxide abrasive paper with grit size of 120 (b) Silicon carbide abrasive paper with grit size of 1500

The results for all abrasive paper samples measured in this study are summarized in *Fig. 8* and *Fig. 9*. The highest effective thermal diffusivity (α = 0.350 cm^2s^{-1}) was obtained from aluminium oxide abrasive paper which corresponds to the grit size of 120. The lowest effective thermal diffusivity (α = 0.0511 cm^2s^{-1}) was obtained from silicon carbide abrasive paper that corresponds to the grit size of 800. In general, the effective thermal diffusivity values of silicon carbide abrasive paper are lower than the aluminium oxide abrasive paper.

We observed that the thermal diffusivity values of aluminium oxide abrasive paper (grit size 120 and 240) obtained in the present measurements are higher than the values reported by Hazelton *et al.* 1998 (i.e. (0.100 cm^2s^{-1}). On the other hand, for silicon carbide abrasive paper, our thermal diffusivity values are lower than the values of thermal diffusivity of silicon carbide ceramic (0.21 - 0.69 cm^2s^{-1}) as reported by Sánchez-Lavega *et al.* 1997. The differences among

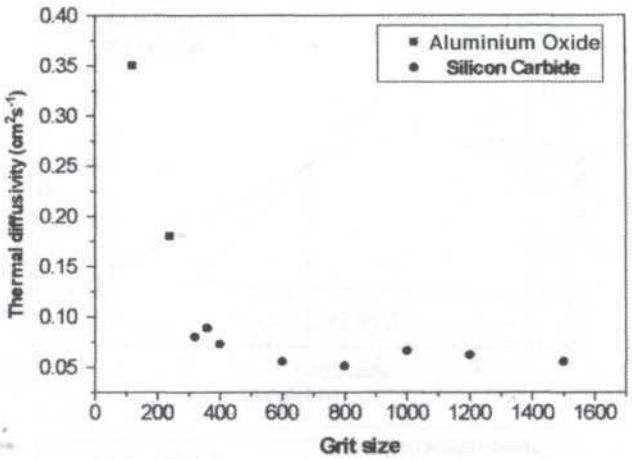

Fig. 8: Effective thermal diffusivity values versus grit size for aluminium oxide and silicon carbide abrasive paper samples

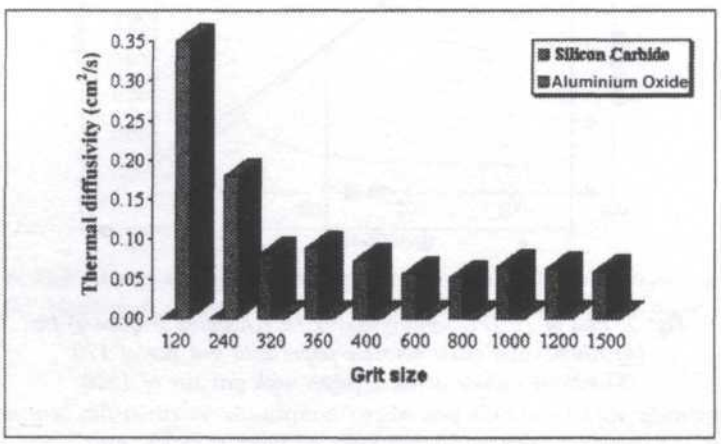

Fig. 9: Histrogram shows the relative effective thermal diffusivity of aluminium oxide and silicon carbide abrasive papers as presented in Fig. 8

the results for thermal diffusivity obtained in the present measurements are due to the different sizes of the abrasive materials used in processing. In addition to that, it may also be affected by the different processing condition and surface porosity of the abrasive papers, and the paper material of the abrasive paper itself.

CONCLUSION

The effective thermal diffusivity of silicon carbide and aluminium oxide abrasive papers has been determined using the open photoacoustic cell detection. The values of effective thermal diffusivity measured at room temperature of 10

different sizes of abrasive paper samples are varied from 0.050 to 0.350 cm^2s^{-1}. Since the physical and processing conditions are different, the results obtained in the present work are found to be different with the values of thermal diffusivity of aluminium oxide and silicon carbide ceramics.

ACKNOWLEDGEMENT

Financial support from IRPA and Universiti Putra Malaysia are gratefully acknowledged. The facilities provided by the Department of Physics, UPM to carry out this project are also grateful acknowledged.

REFERENCES

CHUNG, Y. D., A. P. CHOJNACKA, C. T. AVEDISIAN and R. RAJ. 1997. Thermal diffusivity of particulate composites made from aluminium oxide and nickel aluminide by a photothermal deflection technique. *Acta Material* **45**: 2983-2993.

DA COSTA, A. C. R. and A. F. SIQUEIRA. 1996. Thermal diffusivity of conducting polypyrrole. *J. Appl. Phys.* **80**: 5579-5582.

HAZELTON, C., J. RICE, L. L. SNEAD and S. J. ZINKLE. 1998. Effect of neutron radiation on the dielectric, mechanical and thermal properties of ceramics for rf transmission windows. *J. Nuc. Mat.* **253**: 190-195.

LIMA, C. A. S., M. B. S. LIMA, L. C. M. MIRANDI, J. BAEZA, J. FREER, N. REYES, J. RUIZ and M. D. SILVA. 2000. Photoacoustic characterization of blenched wood pulp and finished papers. *Meas. Sci. Technol.* **11:** 504-508.

PERONDI, L. F. and L. C. M. MIRANDA. 1987. Minimal-volume photoacoustic cell measurement of thermal diffusivity: Effect of the thermoelastic sample bending. Theory of the photoacoustic effect with solid. *J. Appl. Phys.* **47**: 64-69.

ROSENCWAIG, A. and A. GERSHO. 1976. Theory of the photoacoustic effect with solid. *J. Appl. Phys.* **47**: 64-69.

SÁNCHEZ-LAVEGA, A., A. SALAZAR, A. OCARIZ, L. POTTIER, E. GOMEZ, L. M. VILLAR and E. MACHO. 1997. Thermal diffusivity measurements in porous ceramics by photothermal methods. *J. Appl. Phys. A* **65**: 15-22.

YANO, T., K. ICHIKAWA, M. AKIYOSHI and Y. TACHI. 2000. Neutron irradiation damage in aluminium oxide and nitride ceramics up to a fluence of 4.2x1026 n/m2. *Journal of Nuc. Mat.* **283-287**: 947-951.

Pertanika J. Sci. & Technol. 11(2): 311 - 324 (2003)
ISSN: 0128-7680

Design, Development and Calibration of a Drive Wheel Torque Transducer for an Agricultural Tractor

A. F. Kheiralla, Azmi Yahya, M. Zohadie & W. Ishak
Department of Biological and Agricultural Engineering
Faculty of Engineering, Universiti Putra Malaysia
43400 UPM Serdang, Selangor, Malaysia
E-mail: azmiy@eng.upm.edu.my

Received: 14 August 2002

ABSTRAK

Satu unit penderia sepadan untuk mengukur daya kilas pada roda pacuan sebuah traktor telah direka bentuk, dibangunkan serta ditentukur. Unit tersebut mempunyai reka bentuk satu aci penyambung yang dipasang di antara bebibir gandar roda belakang dan rim gandar roda belakang traktor. Tolok tarikan jenis rintangan dilekatkan pada permukaan lilitan aci serta dijambat dalam litar Wheatstone mengikut konfigurasi piawai bagi pengukuran magnitud daya kilas. Litar jambatan pada setiap sisi aci pemacu belakang disambungkan ke sistem perolehan data dalam traktor melalui gelang terbelah pada hujung aci pemacu. Setiap unit penderia telah direka bentuk untuk julat daya kilas bersamaan 0 hingga 32 kNm dengan kepekaan bersamaan 14.492 (tarikan/kNm. Ujian penentukuran statik ke atas unit penderia menunjukkan kelelurusan dan kejituan pengukuran yang sangat baik dengan masing-masing mempunyai pekali sekaitan bersamaan 0.9994 dan 0.9994. Histerisis unit penderia bagi pengukuran statik didapati tidak bererti. Ralat pengukuran unit penderia tidak melebihi 0.20% daripada magnitud daya kilas untuk pengukuran statik dan 0.1% untuk pengukuran dinamik rangsangan. Ujian demonstrasi di ladang menunjukkan pengukuran bagi magnitud daya kilas pada roda pacuan belakang traktor adalah pada tahap yang sangat memuaskan. Sistem perolehan data berjaya mengimbas serta merekod isyarat yang diterimanya daripada kedua-dua unit penderia. Unit penderia ini merupakan sebahagian daripada sistem peralatan yang lengkap dalam traktor Massey Ferguson 3060 yang akan digunakan untuk pembentukan satu pangkalan data yang lengkap tentang keperluan kuasa dan tenaga bagi traktor-peralatan yang bekerja di ladang.

ABSTRACT

An appropriate transducer unit for measuring the drive wheel torque of a tractor was designed, developed and calibrated. The unit adopts a design having an extension shaft mounted in between the rear wheel axle flange and rear wheel rim of a tractor. Resistance type strain gauges were bonded on the shaft circumferential surfaces into a Wheatstone bridge circuitry for a standard torque measurement configuration. The bridge circuitry on each side of the rear drive axle was interfaced to a data acquisition system on board a tractor via a slip ring at the drive shaft end. Each transducer unit has been designed for a torque range of 0 to 32 kNm with a sensitivity of 14.492 μStrain/kNm. Static calibration tests on the transducer revealed excellent measurement linearity and measurement accuracy with coefficients of correlation or R^2 equal to 0.9994 and 0.9994, respectively. The transducer hysteresis for static

measurement was not significant. The transducer measurement errors were not more than 0.20% and 1% of the measured torque magnitudes under static and simulated dynamic measurements, respectively. Field demonstration test showed that the measurement for the torque magnitude at the rear wheel of the tractor was satisfactory. The data acquisition system had successfully scanned and recorded the signals from both transducers. These transducer units are part of the complete instrumentation system in the Massey Ferguson 3060 tractor to be used in the generation of comprehensive database on the power and energy requirements of the tractor-implement working in the field.

Keywords: Tractor, instrumentation, transducer, wheel torque

INTRODUCTION

Increasing populations demand more and more power and energy in agriculture to produce food and fibres. Inefficient tractor operations increase the cost of agricultural production. The need to maintain their profitability have emphasized requirements to maximize the field operation efficiency. Selection and matching of tractors to implement any specific field operation have been largely based on prior experience rather than the understanding of the involved performance factors. Therefore, information on tractor-implement field performance is required for their efficient and effective use.

Information on tractor-implement field performance in ASAE standard and published literature is based on cropping practices that differ greatly from those in Malaysia. A regional agricultural machinery management database is badly needed to help planners, managers and engineers in making decisions concerning the management of the agricultural field machinery. It is therefore necessary to have detailed information on power demand and energy requirements of any machinery utilized in the locality area.

Measurements of wheel torque have received considerable attention in tractive performance studies. Instrumentation that measures the wheel torque and angular velocity would enable the tractive of the drive wheel to be investigated. The common method for wheel torque measurements is strain gauges with a slip ring mounted at the outer end of the axle to stationary recording equipment (Tompkin and Wilhelm 1982; McLaughlin *et al.* 1993; El-Janobi *et al.* 1997). The other method, telemetry is that of actually transmitting the strain gauge signal through the use of radio-frequency transmitters mounted on shaft and picking up the signal by means of a receiver placed nearby (Palmer 1985; Watts and Longstaff 1989; Synder and Buck 1990).

The Department of Biological and Agricultural Engineering, Universiti Putra Malaysia has initiated a research work to develop an instrumentation and data acquisition system on-board a Massey Ferguson 3060 tractor for comprehensive information on the performance of the tractor and its working implement in the field. The intended system would have the capacity of measuring and monitoring engine speed, PTO speed, forward speed, drive wheel slippage, acres worked, fuel consumption per hour, fuel consumption per hectare, acres worked, cost factor, fuel consumed, fuel remaining, and

distance, also at the same time have the capacity of measuring and recording horizontal pull at the tractor drawbar, wheel torque at both tractor rear wheels, PTO torque at the tractor PTO output, and both horizontal and vertical forces at the point hitches (Kheiralla and Azmi 2001). Extensive field testing will be conducted with this instrumented tractor on the aspects of power demand and energy requirements of various agricultural field operations in Malaysia. Ultimately, the obtained data would be processed, analyzed, and transformed into agricultural machinery management data for Malaysia.

This paper describes the design, development, calibration and demonstration of one of the available transducers, namely driver wheel torque transducer.

MATERIALS AND METHODS

General Description

The design of wheel torque transducer is based on an extension shaft that is mounted between wheel axle flange and tire rim of a tractor (*Fig. 1*). A RBE-4A Kyowa slip ring and a special made adapter are fitted to one end of the extension shaft. Two sets of KFG-5-120-D16-11-L1M-2S Kyowa, 90° rossette, 120 Ohm, 2.1 gauge factor strain gauges are bonded at 45° shear planes into a into full bridge configuration on opposite sides of the extension shaft. A 2.5 mA constant current excitation source is supplied from the data acquisition system to each wheel torque transducer via their slip rings. Two L shaped steel conduits are mounted on each side of the tractor mudguards to carry the cables from slip rings to the data acquisition system inside the tractor cab. *Fig. 2* shows the arrangement of wheel torque transducers on the drive axle shaft. The block diagram shown in *Fig. 3* illustrates the complete system.

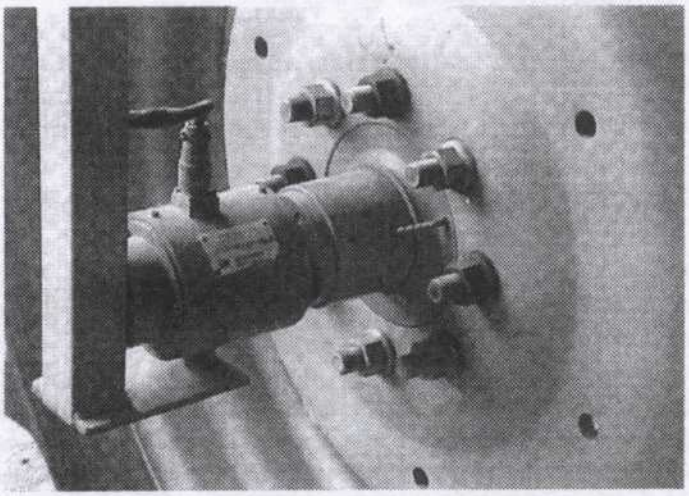

Fig. 1: Wheel torque transducer

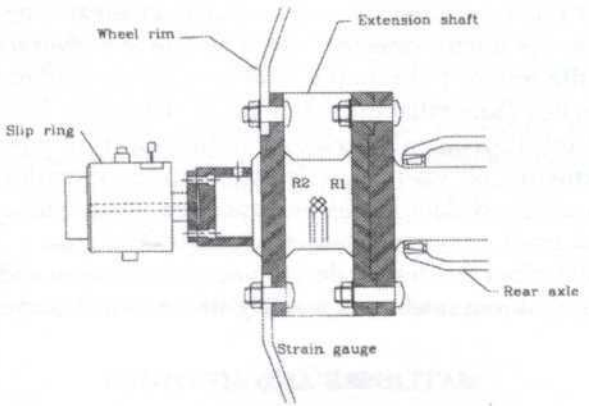

Fig. 2: The arrangement of wheel torque transducer on drive axle shaft

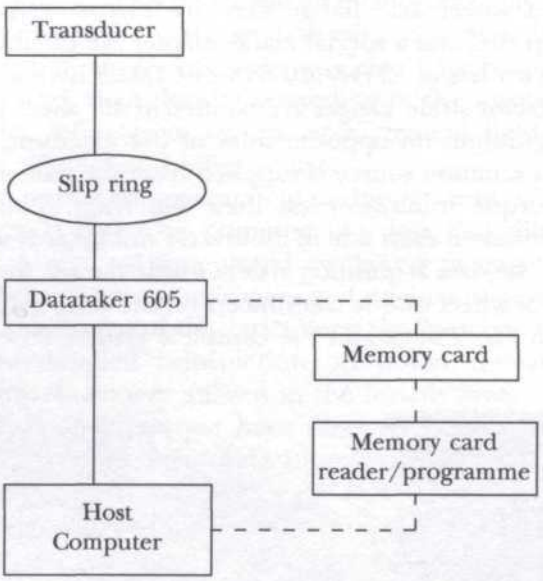

Fig. 3: Block diagram of wheel torque transducer measurement

Extension Shaft Design

The difficulties faced in mounting strain gauges on the rear drive axle to measure the direct torque led to the adoption of an extension shaft. The installed extension shaft on the drive axle should be able to support the tractor drive wheel torque, dynamic loading and bending moment at the same time sensitive to shear strain.

The expected wheel torque, which the transducer was designed to measure, was estimated from tractor rated engine power. A Massey Ferguson 3060 tractor having an engine power of 64 kW and a rated engine speed of 2200 rpm would produce flywheel torque of 277.8 Nm. There would be only a slight lost of

transmitted power from the engine to drive wheels for the mechanical rotating system. The torque magnitudes at drive wheels are equal for a tractor traveling straight on uniform surfaces. Therefore, the torque magnitude at each drive wheel is given as (Goering 1990):

$$T_w = \frac{\eta}{2}\left(\frac{N_e}{N_w}\right)T_e \tag{1}$$

where T_w is the drive wheel torque in Nm, T_e is the flywheel torque in Nm, N_w is the drive wheel speed in rpm, Ne is the engine speed in rpm and η is transmission efficiency in percentage. The wheel torque magnitude for a tractor traveling at lowest gear (i.e. 2.3 km/hr and running at rated engine speed of 2200 rpm) is equal to 32.26 kNm.

The significance of bending is an important criteria in the design of the extension shaft. The dynamic load at the drive wheel is made up of the static load and the weight transfer to the wheel as a result of mounted implement on the tractor. The weight transfer on the tractor is given as (Liljedal *et al.* 1989):

$$\Delta R_r = \frac{P.h}{L_1} \tag{2}$$

where P is the maximum drawbar pull in kN, h the drawbar height in m and L_1 the tractor wheelbase in m. The weight transfer magnitude is 8.63 kN at a maximum drawbar pull of 50 kN for the specified tractor having a drawbar height of 0.41 m and wheelbase of 2.38 m. Knowing the weight transfer magnitude of 8.63 and the rear wheel static load of 23.343 kN, gives each wheel a dynamic load of 15.987 kN for a simple moment calculation. Thus, computed maximum bending moment on the extension shaft is 14.228 kNm for a load of 15.987 kN at a span of 1.78 m.

The shaft diameter design equation for applied torque and bending moment of under static loading condition is described as (Hindhede 1987):

$$D = \left(\frac{32 f_s}{\pi S_{yt}}\sqrt{\left(\frac{S_{yt}}{S_e}M\right)^2 + \frac{3}{4}T^2}\right)^{\frac{1}{3}} \tag{3}$$

where D is the shaft diameter in mm, T is the applied torque in kNm, M is the bending moment in kNm, S_{yt} is the yield tensile strength in MN/m^2 and S_e is the endurance strength in MN/m^2 and f_s is the dimensionless factor of safety.

The material used for the shaft is mild steel SAE 1020 having a yield strength of 300 MN/m^2. Based on shaft material strength, practical constraints and tractor requirements, an extension shaft having 100 mm diameter and 120

mm length with two flanges at both ends was designed as a compromise between transducer strength and sensitivity. A special adapter having 88 mm external diameter and 60 mm length was made and fitted at one end of the extension shaft to hold the slip ring. The final extension shaft design is shown in *Fig. 4.*

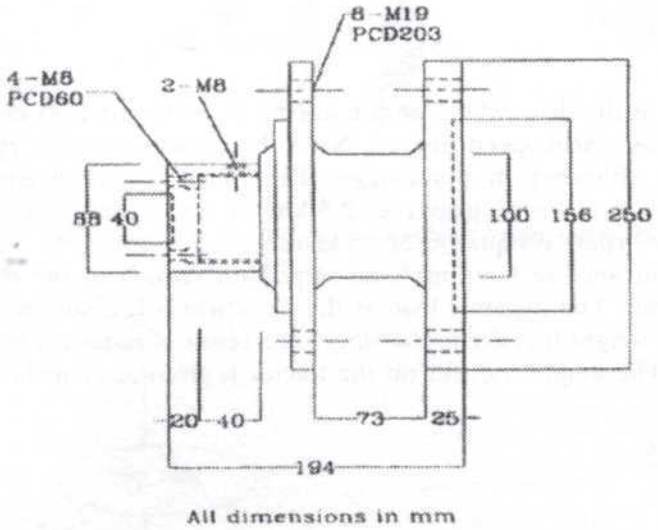

Fig. 4: Dimensions of the extension shaft and adapter

The strain due to torque loading at 45° location to the shaft axis is given as (Timoshenko and Gere 1990):

$$\varepsilon_{45^\circ} = \frac{8T}{\pi D^3 G} \tag{4}$$

where ε_{45° is the output strain in μStrain, T is the applied torque in Nm, D is the shaft diameter in mm and G the modulus of rigidity in GPa. Knowing the shaft diameter of 100 mm, torque magnitude of 32260 Nm and shaft modulus of rigidity of 80 GPa, the maximum strain ε_{45° was calculated to be 981μStrain.

Strain Gauges Configuration

The wheel torque sensing element design had 2 sets of Kyowa KFG-5-120-D16-11-L1M-2S, 90° rossette strain gauges installed on opposite sides of the extension axle shaft and positioned at 45° to axle axis to give the maximum sensitivity to torsional strains. The selected gauges have α gauge resistance of 120 Ohm, α gauge factor of 2.1, and one-meter length lead wires. The available 4 gauges are wired to a constant current full Wheatstone bridge configuration. A full bridge 2.5 mA constant current supply from data acquisition system is used to excite the strain gauges bridge on the wheel torque transducer.

The gauge installation was carried out after smoothing the extension shaft surface by fine silicon carbide abrasive paper. Accurate markings for the gauge locations on the shaft were made possible with the aid of a Digimetic Height gauge. The strain gauges were positioned at 180° apart on the predetermined surface of the shaft and glued permanently using an epoxy adhesive. Finally, SG280 protective coating was applied to the installed gauges to provide protection against water, humidity and mechanical abrasion.

The sensitivity of the transducer is expressed in terms of bridge output strain per unit torque applied. The predicted output strain for the wheel torque transducer circuit under design torque is calculated to be 981μStrain. Since the output of constant current for the data acquisition system is measured in μStrain, the predicted channel sensitivity is calculated to be 30.41 μ Strain/ kNm.

Natural Frequency and Dynamic Response

The designed transducer should be able to measure dynamic mode response of the tractor wheel torque. The dynamic response of wheel torque transducer and tractor drive shaft can be modeled as torsional vibration of two mass-shaft. The model used to simulate a tractor and wheel torque transducer is shown in *Fig. 5.* The applied torque at the shaft end causes the axle and transducer to vibrate and the complete transducer unit to respond to torsional oscillatory motion (Timoshenko *et al.* 1990). In order for the recorded torque to be influenced by any vibration motion, its natural frequency should be larger than the frequency of exciting vibrations. The natural frequency of transducer and drive axle shaft can be expressed as (Liljedal *et al.* 1989):

$$f = \frac{1}{2\pi}\sqrt{\left(k_t \frac{J_1 + J_2}{J_1 J_2}\right)} \qquad (5)$$

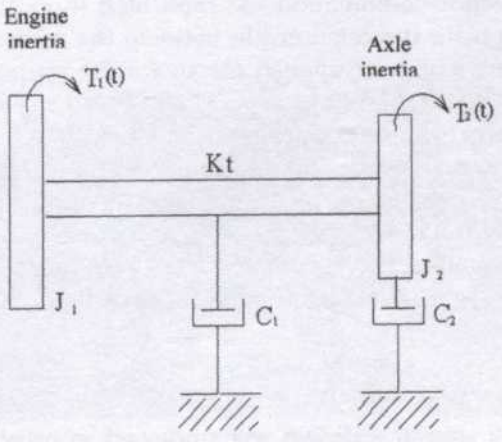

Fig. 5: Transducer drive shaft modeled as torsional vibration of two mass shafts

where f is the natural frequency in Hz, J_i is the effective torsional inertia at engine in kgm^2, J^2 is equivalent torsional inertia at the axle shaft converted from vehicle mass and rolling resistance and is given as $J_2 = mr^2$ in kgm^2, and k_t the stiffness of the drive shaft given as $k_t=\pi GD^4/32L$ in Nm/rad.

A medium-sized tractor based from Crolla, (1978) could develop an effective torsional inetria of 2 kgm^2 at its engine. Knowing the tractor mass of 3898 kg, rolling radius of 0.79 m, axle shaft diameter of 82 mm, shaft length of 0.70 m and shaft modulus of rigidity of 80 GPa, the calculated axle inertia and stiffness were respectively 2495 kgm^2 and 507279 Nm/rad. Then, the natural frequency of the transducer and tractor drive shaft system was calculated to be approximately 80 Hz.

Calibration

Comprehensive static calibration tests were carried out to determine the measurement linearity between applied torque with output strain and measurement accuracy between applied torque and measured torque. The test was conducted by fixing the transducer between the rim the concave disk and tractor rear axle simulator. A rectangular bar was bolted horizontally to wheel rim concave disc. The whole assembly was mounted to a loading frame that is equipped with manual hydraulic power pack. A load cell that was located in between the piston end of the hydraulic cylinder of the power pack and the free of the rectangular bar to measure the applied torsional force. A known torque was applied to the transducer and shaft simulator by manually operating the hydraulic pack on the loading frame. A data acquisition system running on DeCipher plus command program was used to scan and record the output strain from the drive wheel torque transducer. The test was conducted under the loading range from 0 to 5.0 kNm at 0.5 kNm intervals. Each drive wheel transducer was calibrated under two loading directions (i.e. clockwise and anticlockwise) and two loading conditions (i.e. increasing and decreasing). Each measurement at any applied load was repeated four times and each test at any loading direction-combination was replicated three times. A similar test was conducted to obtain the relationship between the measured torque by the data acquisition system and the applied torque for the purpose of checking the measurement accuracy of the transducer. The involved test was only conducted to the left drive wheel torque transducer under clockwise loading direction and the test procedure was similar to the before. Both transducers were mounted to tractor rear drive axles upon the completion of the calibration test. The displacement of the tractor rear wheel width caused by the installation of the transducers was minimized to 7 cm at each side. This is achieved by bolting the wheel rim concave disc to the outside of bolt clamp brackets on the wheel rim for both rear wheels.

Statistical Analysis

A four way factorial statistical design was employed, consisting of two sides of the wheel (i.e. left and right), two levels of wheel rotation (i.e. clockwise and

anticlockwise), two modes of loading (i.e. loading and unloading), eleven levels of applied torque and four replications; resulting in a total of 352 tests. For simplicity, the following linear additive model was utilized (Steel and Torrie 1996):

$$Y_{ijklm} = \mu + \alpha_i + \beta_j + \gamma_k + \delta_l + (\alpha\beta)_{ij} + (\alpha\gamma)_{ik} + (\alpha\delta)_{il} + (\beta\gamma)_{jk} + (\beta\delta)_{jl} + (\gamma\delta)_{kl} + (\alpha\beta\gamma)_{ijk} + (\alpha\beta\delta)_{ijl} + (\alpha\gamma\delta)_{ikl} + (\beta\gamma\delta)_{jkl} + (\alpha\beta\gamma\delta)_{ijkl} + e_{ijklm} \quad (6)$$

where Y_{ijklm} is the output strain made in i^{th} level of wheel, j^{th} level of rotation, k^{th} level of loading, l^{th} level of applied torque, and in the m^{th} replications, μ is the mean, α_i, β_j, γ_k and δ_l are the main effects of wheel, rotation, loading and applied torque, respectively, $(\alpha\beta)_{ij}$, $(\alpha\gamma)_{ik}$ ..... $(\beta\gamma\delta)_{jkl}$ and $(\alpha\beta\gamma\delta)_{ijkl}$ are first and higher order interaction effects of wheel, rotation, loading and applied torque, and ε_{ijklm} is the random error.

The General Linear Model procedure in PC SAS software package (SAS 1996) was employed to determine the relationship of output measured strain with applied torque.

Demonstration Test

Field demonstration trials on complete instrumentation and data acquisition system were conducted for verifying wheel torque measurements of the Massey Ferguson 3060 tractor. The tractor was used to pull at its drawbar a FIAT 540 tractor under brake on a dry asphalt surface at an average traveled speed of 2 km/hr (*Fig. 6*). During the test, the tractor differential lock was engaged to ensure equal torque and travel reduction at each wheel. The instrumentation system and data acquisition system on the tractor was set to run at sampling means at one-second intervals. The collected data during field demonstration was downloaded into the host computer with the aid of Datataker 605 memory card reader for further analysis.

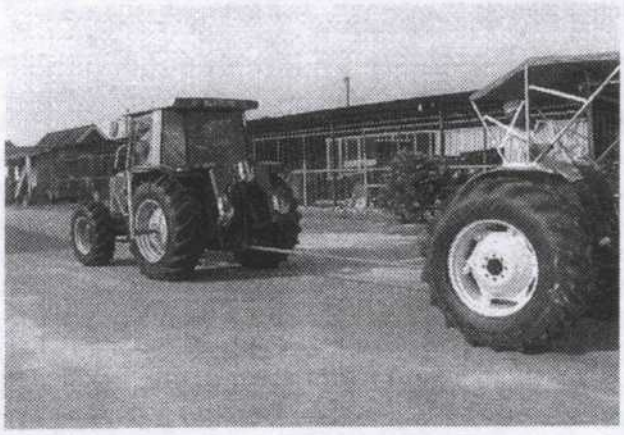

Fig. 6: Wheel torque transducer demonstration test

RESULTS AND DISCUSSIONS

ANOVA on the calibration for wheel torque transducer in Table 1 shows that the entire tested main effects and interactions with the exception of applied torque had no significant ($P>0.05$) effects on measured output strain. The insignificance of rotation implies no differences on the measured output strain between clockwise and anticlockwise wheel rotation. The insignificance of loading indicates no hysteresis effect on the measured output strain under loading and unloading modes. Again, the insignificance of wheel explains similar measured output strain from both wheel sides. All these obtained findings supported the use of one calibration equation for wheel torque transducer measurement.

TABLE 1
ANOVA on the calibration for wheel torque transducer

Source of variation	SS	MS	F-value
Replication	4.8933	1.6311	2.25NS
Wheel	12.5340	12.5340	17.32NS
Rotation	0.4305	0.4305	0.60NS
Loading	0.0707	0.0707	0.10NS
Torque	179916.7807	179916.7807	24867.65**
Wheel (Rotation	0.0041	0.0041	0.01NS
Wheel (Loading	3.2359	3.2359	4.47NS
Wheel (Torque	14.3287	14.3287	1.98NS
Rotation (Loading	0.0001	0.0001	0.00NS
Rotation (Torque	5.2415	0.5241	0.72NS
Loading(Torque	18.4511	1.8451	2.55NS
Wheel(Rotation(Loading	1.4114	1.4114	1.95NS
Wheel(Rotation(Torque	6.2343	6.2343	0.86NS
Wheel (Loading(Torque	3.4713	0.3471	0.48NS
Rotation(Loading(Torque	1.9759	0.1975	0.27NS
Wheel (Rotation(Loading(Torque	3.5036	0.3503	0.48NS
Error	188.8328	0.7235	

** Significant at 1% probability level
NS Not Significant

The plotted calibration graph in *Fig. 7* shows that applied torque and measured output strain were highly correlated. The linearity equation is expressed by:

$$S = 14.492T \quad \text{with} \quad R^2 = 0.9994 \tag{7}$$

where S represents the measured output strain in μStrain and T is the applied torque in kNm. The equation was used in the programming of Datataker 605 to read the measured output strain from the tractor's drive wheels in kNm.

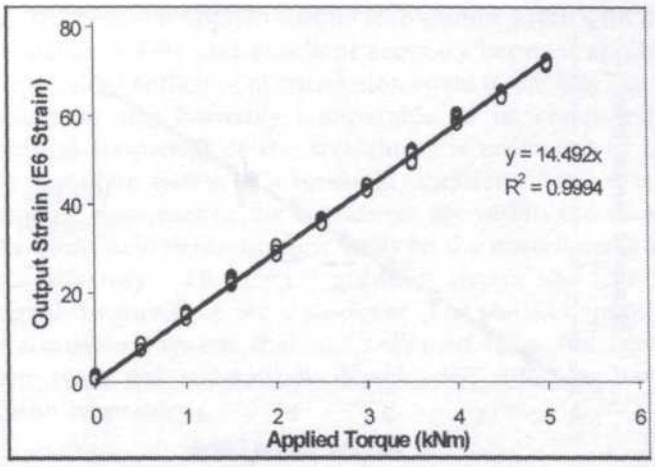

Fig. 7: Calibration curve for wheel torque transducer

The measured strain gauge sensitivity was 14.492 μStrain/kNm. This value was 0.45 times lower than earlier computed theoretical sensitivity (i.e 30.41μStrain/kNm). This difference was due to gain multiplier effect that was set automatically during autoranging by the Datataker 605.

The plotted measurement accuracy graph in *Fig. 8* shows a high degree of linearity between applied torque and measured torque. Their relationship is best expressed by the following formula:

$$T_M = 0.998T \quad \text{with} \quad R^2 = 0.9994 \tag{8}$$

where T_M represents the measured output torque in kNm and T is the applied torque in kNm. The transducer is rated to give a measurement accuracy within ± 0.20% range. This factor was used for computing and documenting the measured output torque by the transducer.

The natural frequency of wheel torque transducer based on torsional vibration of two mass shaft systems was estimated to be 80 Hz while the working frequency of a typical tractor operating in the field as indicated by Claar *et al.* (1982) and Erickson and Larsen (1983) was around 2 Hz. Fortunately, with this frequency ratio of less than 0.1 (i.e. 0.025 to be exact) resulted with a transmissibility value of less than 1.01 and torque measurement error of no more than 1% of the excitation torque (Timoshenko *et al.* 1990). Consequently, the conducted static calibration on the transducer was acceptable for dynamic torque measurement. Besides that, it also ensured that the dynamic torque measured by the transducer would not be attenuated or distorted.

Fig. 9 indicates a sample data of the measured wheel torque at the tractor left drive wheel. The computed 95% confidence interval for the measured torque was found to be 3.46 ± 0.63 kNm. The dynamic variability was reasonably synchronized with the sampling frequency pattern of instrumentation and data

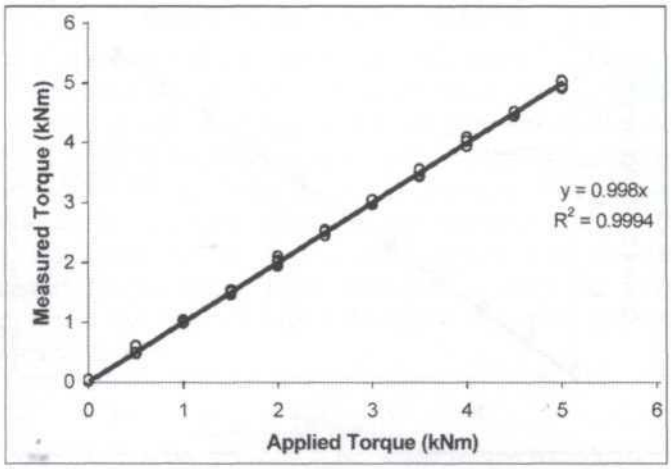

Fig. 8: Verification curve for measurement accuracy of wheel torque transducer

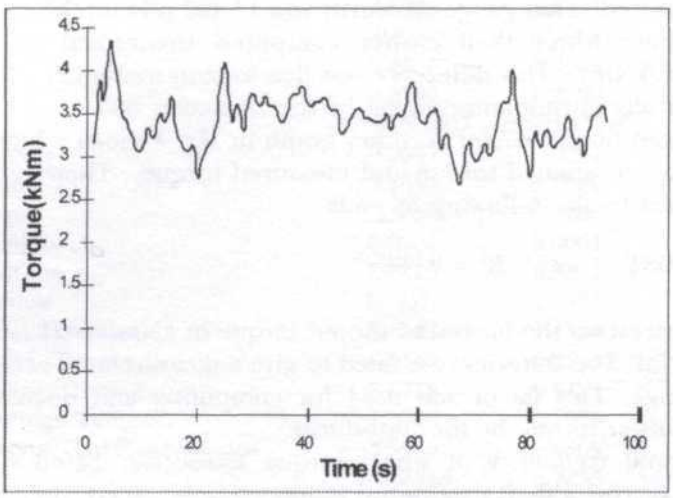

Fig. 9: Torque measurements at left rear drive wheel

acquisition system. The instrumentation and data acquisition system was able to scan the transducer signals without difficulties. The stored data in the memory card of the Datataker 605 was downloaded and recovered into the hard disk of the computer at the end of the trials.

CONCLUSION

A wheel torque transducer was designed and developed to measure the tractor's rear wheel torque output up to 32 kNm at a sensitivity of 14.492 μStrain/kNm. The transducer unit adopts a design having extension shaft mounted between wheel axle flange and wheel rim. Static calibration of the transducer revealed

excellent linearity between applied torque with output strain with coefficient of correlation equal to 0.9994 and excellent accuracy between applied load with measured torque with coefficient of correlation equal to 0.9994. The transducer's measured sensitivity was favorably comparable to its computed theoretical sensitivity. Natural frequency of the transducer is estimated to be 80 Hz by modeling the complete system as a torsional vibration of two mass-shafts. The static and dynamic responses of the transducer are within the acceptable error limit. Measurements field demonstration trials on the transducer and acquisition system were satisfactory. The data acquisition system was able to scan and record the signal measured by the transducer. The stored data in the memory card of the acquisition system that was collected from the conducted field demonstration trials was successfully downloaded into the hard disk of a computer at the laboratory.

ACKNOWLEDGMENT

This research project is classified under RM7-IRPA Project No. 01-02-04-0138. The authors are very grateful to the Ministry of Science, Environment and Technology of Malaysia for granting the fund.

REFERENCES

CLAAR, P. W., P. N. SHETH, W. F. BUCHELE and S. J. MARLEY. 1982. Simulated tractor chassis suspension system. *Transactions of the ASAE* **25(3)**: 590-594.

DATA ELECTRONIC (Aust.) Pty. Ltd. 1996. Datataker manual. Rowville, Australia.

EL-JANOBI, A., A. A. BEDRI, S. A. AL-SUHAINANI and A. S. SABBEIR. 1997. A precision wheel torque and weight transducer for most common agriculture tractor. *Agric. Mech. in Asia and Latin Am* **28(1)**:13-17, 22.

ERICKSON, L. R. and W. E. LARSEN. 1983. Four-wheel drive tractor field performance. *Transactions of the ASAE* **26(6)**:1346-1351.

GOERING, C. E. 1990. *Engine and Tractor Power.* 1st ed. Boston, Massachusetts: Prindle, Weber & Schmidt Publishers.

HINDHEDE, U., J. R. ZIMMERMAN, R. B. HOPKINS, R. J. ERISMAN, W. C. HULL and J. D. LANG. 1987. *Machine Design Fundamental, A Practical Approach.* 1st ed. New Jersey: Prentice-Hall, Inc.

KHEIRALLA, A. F. and A. YAHYA. 2001. A tractor data acquisition system for power and energy demand monitoring of agricultural field operations. *Pertanika J. Sci. & Technol.* **9(1)**: 51-67.

LIJEDAHL, J. B., P. K TURNQUIST, D. W. SMITH and M. HOKI. 1989. *Tractor and Their Power Units.* ASAE. 4th ed. New York: Van Nostrand Reinhold.

MCLAUGHLIN, N. B., L. C. HESLOP, D. J. BUCKLEY. G. R. AMOUR, B. A. COMPTON, A. M. JONES and P. V. BODEGOM. 1993. A general purpose tractor instrumentation and data logging system. *Transaction of the ASAE* **36(2)**: 265-273.

PALMER, J. 1985. Automatic collection of data on practical use of field machines. *Agric. Engng.* **40**: 42-49.

SAS. 1996. *SAS User's Guide: Statistics*. North Carolina: Statistical Analysis System Inc.

SNYDER, K. A. and N. L. BUCK. 1990. Axle instrumentation for tractive performance parameters measurement. *Transaction in Agriculture* **33(1)**: 290-297.

STEEL, R. G. D. and J. H. TORRIE. 1996. *Principles and Procedures of Statistics*. 3rd ed. New York: McGraw- Hill.

TIMOSHENKO, S. and J. M. GERE. 1990. *Mechanics of Materials*. 3rd ed. New York: Van Nostrand Reinhold.

Pertanika Journal of Science and Technology

Subject Index for Vol. 11, Nos. 1 and 2, 2003

Pertanika Journal of Science & Technology

Author Index for Volume 11, Nos. 1 & 2, 2003

ACKNOWLEDGEMENTS

The Editorial Board acknowledges the assistance of the following reviewers in the preparation of Volume 11, Numbers 1 & 2 of this journal

Dr. Abu Bakar Mohamad
Prof. Dr. Abdul Halim Shaari
Prof. Dr. Abdul Kariem Arof
Dr. Ahmad Md. Noor
Prof. Dr. Anuar Kassim
Dr. Ashaari Abd. Jalil
Dr. Chong Fai Kait
Assoc. Prof. Dr. Desa Ahmad
Dr. F. Faez Osuna
Dr. Harbant Singh
Dr. Hishamudin Zainudin
Assoc. Prof. Dr. Husaini Omar
Assoc. Prof. Dr. Ibrahim Jantan
Dr. Jumiah Hassan
Assoc. Prof. Dr. Karen Badri
Prof. Dr. Karsono Ahmad Dasuki
Assoc. Prof. Dr. Khairudin Omar
Dr. Mohd. Khazani Abdullah
Assoc. Prof. Dr. Khoo Khay Huat
Assoc. Prof. Dr. Khozirah Shaari
Dr. Lee Pat Moi
Ir. Dr. Lee Teang Shui
Prof. Dr. Liew Kong Yong
Assoc. Prof. Dr. Lim Poh Eng
Assoc. Prof. Dr. Mat Johar Abdullah
Prof. Dr. Mohamad Ridza Wahidin
Assoc. Prof. Dr. Mohd. Alaudin Mohd Ali
Assoc. Prof. Dr. Mohd. Amin Mohd. Som
Assoc. Prof. Dr. Mohd Jelas Haron
Assoc. Prof. Dr. Mohd. Radzi Abas
Assoc. Prof. Dr. Mohd. Zaizi Desa
Assoc. Prof. Dr. Muhamad Deraman
Prof. Dr. Muhammad Mat Salleh
Prof. Dr. Muhammad Yahya
Assoc. Prof. Dr. Noriah Bidin
Assoc. Prof. Dr. Ir. Norman Mariun
Assoc. Prof. Dr. Othman Karim
Dr. Rosalina Abdul Salam
Assoc. Prof. Dr. Salim Said
Assoc. Prof. Dr. Salmijah Sarif
Assoc. Prof. Dr. Tan Guat Huat
Assoc. Prof. Dr. Tan Wee Tee
Dr. Thamer Ahmed
Assoc. Prof. Dr. Wan Azlina Ahmad
Assoc. Prof. Dr. Yousif Khalid
Assoc. Prof. Dr. Zainal Abidin Talib
Assoc. Prof. Dr. Zulkarnain Zainal

Preparation of Manuscript

General
The manuscript, including footnotes, tables, and captions for illustrations, should be typewritten double spaced on paper 210 x 297 mm in size, with margins of 40 mm on all sides. Three clear copies are required. Typing should be on one side of the paper only. Each page of the manuscript should be numbered, beginning with the title page.

Title page
The title of the paper, name of author and full address of the institution where the work was carried out should appear on this page. A short title not exceeding 60 characters should be provided for the running headline.

Abstract
Abstracts in Bahasa Melayu and English of not more than 200 words each are required for full articles and communications. No abbreviation should appear in the abstract. Manuscripts from outside of Malaysian may be submitted with an English abstract only.

Keywords
Up to a maximum of ten keywords are required and they should be placed directly below the abstract.

Footnotes
Footnotes to material in the text should not be used unless they are unavoidable. Where used in the text, footnotes should be designated by superscript Arabic numerals in serial order throughout the manuscript. Each footnote should be placed at the bottom of the manuscript page where reference to it is made.

Equations
These must be clearly typed, triple-spaced and should be identified by numbers in square brackets placed flush with the right margin. In numbering, no distinction is made between mathematical and chemical equations. routine structural formulae can be typeset and need not be submitted as figures for direct reproduction but they must be clearly depicted.

Tables
Tables should be numbered with Arabic numerals, have a brief title, and be referred to in the text. Columns headings and descriptive matter in tables should be brief. Vertical rules should not be used. Footnotes in tables should be designated by symbols or superscripts small italic letters. Descriptive materials not designated by a footnote may be placed under a table as a *note.*

Illustrations & Photographs
Illustration including diagrams and graphs are to be referred to in the text as 'figures' and photographs as 'plates' and numbered consecutively in Arabic numerals. All photographs (gloosy black and white prints) should be supplied with appropriate scales.

Illustrations should be of print quality; outputs from dotmatrix printers are not acceptable, Illustrations should be on separate sheets, about twice the size of the finished size in print. All letters, numbers and legends must be included on the illustration with the author's name, short title of the paper, and figure number written on the vereso. A list of captions should be provided on a separate sheet.

Unit of Measure
Metric units must be used for all measurements.

Citations and References
Items in the reference list should be referred to in the text by inserting, within parentheses, the year of publication after the author's name. If there are more than two authors, the first author should be cited followed by '*et al*'. The names of all authors, however, will appear in the reference list.

In the case of citing an author who has published more than one paper in the same year, the papers should be distinguished by addition of a small letter, e.g. Choa (1979a); Choa (1979b); Choa (1979c).

In the reference list, the names should be arranged alphabetically according to the name of the first author. Serials are to be abbreviated as in the *World List of Scientific Periodicals.*

The abbreviation for Pertanika Journal of Science and Technology is *Pertanika J. Sci. Technol.*

The following reference style is to be observed:

Monograph
Alefed, G. and J. Herzberger. 1983. *Introduction to Interval Computations.* New York: Academic Press.

Chapter in Edited Book
Muzzarell, R.A.A. 1980. Chitin. In *Polymers in Nature,* ed. E.A. MacGregor and C.T. Greenwood, p. 417-449. New York: John Wiley.

Serials
Kamaruzaman Ampon. 1991. The effect of attachment of hydrophobic imidoesters on the catalytic activity of trypsin. *Pertanika* **14(2)**: 18-185.

Proceedings
Mokhtaruddin, A.M. and L.M. Maene. 1981. Soil erosion under different crops and management practices. In *Agricultural Engineering in National Development,* ed. S.L. Choa, Mohd Zohdie Bardaie, N.C. Saxena and Van Vi Tran, p. 245-249. Serdang, Malaysia: Universiti Pertanian Malaysia Press.

Unpublished Materials (e.g. theses, reports & documents)

Sakri, 1. 1990. Proper construction set-up of Malaysian Fish Aggregating Devices (Unjam). Ph.D. Thesis, Universiti Pertanian Malaysia, Serdang, Selangor.